Title

Development of Strategies for Targeting Voltage-Sensitive Fluorescent Dyes to Subcellular Organelles

Author

Klier, Pavel Erich Zivanovic

Publication Date

2021

Peer reviewed|Thesis/dissertation

Development of Strategies for Targeting Voltage-Sensitive Fluorescent Dyes to Subcellular Organelles

By
Pavel Erich Klier

A Dissertation submitted in partial satisfaction of the
Requirements for the degree of
Doctor of Philosophy
In
Chemistry
In the
Graduate Division
of the
University of California, Berkeley

Committee in charge:

Professor Evan W. Miller, Chair
Professor Christopher J. Chang
Professor Stephen Brohawn

Fall 2021

Development of Strategies for Targeting Voltage-Sensitive Fluorescent Dyes to Subcellular Organelles

By Pavel Erich Klier

Abstract

Development of Strategies for Targeting Voltage-Sensitive Fluorescent Dyes to Subcellular Organelles

By

Pavel Erich Klier

Doctor of Philosophy in Chemistry

University of California, Berkeley

Professor Evan W. Miller, Chair

Membrane potential is a crucial signaling factor in many biological processes and understanding these processes requires measurements of membrane potential in a normal physiological environment. Voltage-sensitive fluorophores provide a non-invasive tool for high throughput optical measurements of membrane potential. In the Miller lab, we focus on a class of voltage-sensitive fluorophores known as VoltageFluors which rapidly modulate their fluorescence in response to changes in membrane potential via changes in the rate of photoinduced electron transfer from an electron-rich aniline. Prior to this work, VoltageFluors had only been targeted to the extracellular surface of plasma membranes. This work reports the development of new strategies for targeting of VoltageFluors to specific membranes including those of subcellular organelles. Chapter 1 provides background material on methods of targeting fluorescent probes to organelles. Chapter 2 describes the targeting and methods for use of a novel VoltageFluor, SPIRIT RhoVR, that localizes to the mitochondrial inner membrane via electrostatic accumulation followed by unmasking of an ester for retention in mitochondria. Chapter 3 describes a tetrazine-transcyclooctene click chemistry strategy for targeting of a novel VoltageFluor, LUnAR RhoVR, to multiple cellular locations with the primary focus being the endoplasmic reticulum (ER). Using LUnAR RhoVR, we were able to monitor ER membrane potential during calcium release and establish the directionality of ER-plasma membrane electrical coupling. Chapter 4 focuses on the physics behind energy transfer in fluorescent dyes, provides a computational description of VoltageFluor sensitivity, and proposes an approach for using VoltageFluors as ratiometric sensors of membrane potential. This dissertation follows this main body of work with two appendices describing initial steps towards synthesizing water-soluble and enzymatically uncageable dyes that would enhance targeting of fluorescent dyes to specific membranes in complex samples.

Dedications

Note: my full legal name is Pavel Erich Zivanovic Klier and not Pavel Erich Klier, a truncated name by which I have never appeared on any legal document.

To MAAAA!!!, Daddy, and Pipsqueak, Baka, and Deka for their unwavering love and support not just during this thesis but through my whole life (minus 3 years 9 months for you Nikola but I won't hold it against you).

To Amber and Shadow, for meow meow purrrrr meow purr meow meow.

To Julia, my partner in crime on SPIRIT RhoVR and who might as well be co-author on the whole thesis, for being there whenever I needed her inside or outside of lab. GET THAT BREAD!!

To Molly, my emotional support graduate student, for excellent scientific discussions and just generally being a fun person to be around.

To Brittany, cohort buddy, purveyor of fine lunchtime discussions, and general sarcasm appreciator.

To Anneliese, for coming in clutch to finish LUnAR RhoVR at the end of it all and for being my fellow gossipy old grad student with Opinions.

To Thomas and Ryan, for all of the hard work they put in and for letting me watch them learn.

To Parker, for being my early guide in the ways of the Miller lab.

To Evan, for mentoring me through the degree process.

And to the whole lab for being a wonderful and supportive group of people who have helped me grow in the ways of science.

Table of Contents

Chapter 1: Methods for targeting fluorescent probes to and measuring membrane potential of subcellular organelles

1.0 Introduction

Eukaryotic cells isolate key biochemical processes by selectively partitioning metabolites, enzymes, and ions within membrane-bound compartments known as organelles. The separation of ions results in electrical potentials across organelle membranes. Visualizing these compartments and accessing them for electrophysiological measurements poses unique challenges in cell biological research. Typically in cell biology, membrane potentials are measured through patch-clamp electrophysiology in which an electrode contained within a glass pipet is put in direct electrical contact with the interior of a membrane for measurements of relative membrane potential. Although these experiments are typically executed on the plasma membrane of cells, approaches have been developed to perform these measurements on organelle membranes. Seductive though these methods may be, they involve isolating the organelle from its physiological environment in order to perform electrical measurements on the organelle's membrane. Fluorescent probes for membrane potential provide an attractive alternative to electrophysiological measurements of subcellular membrane potential. Although many useful fluorescent probes for membrane potential exist, their use is predominantly confined to the plasma membranes of cells. The work presented in this dissertation serves to enable optical measurements of subcellular membrane potential by targeting an established voltage-sensitive fluorescent probe, a Rhodamine Voltage Reporter (RhoVR), to multiple subcellular locations of interest. The purpose of this first chapter is to provide a survey of the methods that can be used to target fluorescent probes to subcellular locations of interest, as well as highlight the tools used for measurements of subcellular membrane potential at the time of this dissertation.

1.1 Targeting fluorescent dyes to organelles via organelle properties

A key method for targeting fluorescent dyes to an organelle is to use the intrinsic properties of that organelle to promote dye accumulation, enhance dye fluorescence, or retain the dye in location. The following is a breakdown of the properties of specific organelles that have been used to target fluorescent dyes to that location:

Mitochondria: Mitochondria have an outer and an inner membrane (**Figure 1.1.1a**). The space between these membranes is known as the intermembrane space and the region inside the inner membrane is known as the mitochondrial matrix. The electron transport chain, a crucial series of membrane-bound enzymes used in oxidative metabolism, is located on the mitochondrial inner membrane and moves protons from inside the mitochondrial matrix to the intermembrane space to contribute to an electrochemical gradient used to drive oxidative phosphorylation[1]. The inner membrane is also naturally semi-permeant to protons which contributes to overall equilibrium of protons across the membrane. The reduction of proton concentration in the matrix makes it more alkaline, with a pH of approximately 8, and creates a net negative charge relative to the cytosol[2].

Lipophilic cations are generally membrane permeant and, when added to the bath solution of cells, diffuse across the plasma membrane, mitochondrial outer membrane, and mitochondrial inner membrane to accumulate in the mitochondrial matrix due to charge-charge attraction. Some common examples of stains for mitochondria that operate using this principle are rhodamine esters such as tetramethylrhodamine methyl ester (TMRM) and Rhodamine 123 (Rhod123) and certain classes of cyanine dyes such as JC-1 and the FM dyes used in the commercially available MitoTracker series. Some mitochondrial stains such as the MitoTracker series also contain benzyl chloride groups which react with nucleophiles in mitochondria to covalently tether them to the mitochondrial matrix[3].

Nucleus: The primary purpose of the nucleus is to contain DNA, which is often the target of nuclear fluorescent stains (**Figure 1.1.1b**). DNA is highly negatively charged due to its phosphate backbone and has aromatic nitrogenous bases that stack in a planar fashion. Nuclear stains typically have both an affinity for DNA and a fluorogenic response upon intercalating between bases or binding to the backbone or grooves in DNA structure[4]. Perhaps the most famous example of DNA binding dyes used as nuclear stains is the Hoechst series, which can bind to the phosphate backbone or minor groove of DNA to elicit a fluorogenic response due to suppression of rotational relaxation. Fluorogenic binding to DNA is key in nuclear stains because many of them are cationic and localize to the nucleus due to attraction between the positive charge of the probe and the negative charge of the DNA backbone. However, as noted above, this will cause the dye in question to also localize to mitochondria. A fluorescence increase upon DNA binding ensures that the nuclear signal will predominate over off-target mitochondrial signal[5].

Lysosomes: Lysosomal pH is significantly more acidic than other subcellular compartments, averaging a pH of approximately 5[6]. Most fluorescent stains for lysosomes have pH-sensitive groups with a pKa lower than cytosolic pH (**Figure 1.1.1c**). This means that these dyes will be minimally protonated at cytosolic pH and freely permeate across cell membranes. However, when the dyes diffuse into lysosomes, the basic group becomes protonated, discouraging transit across the lysosomal membrane back into the cytosol and allowing accumulation. This protonation is sometimes accompanied by a fluorogenic response that results in brighter fluorescence inside the acidic lysosomal compartment. Key examples of this strategy for lysosomal targeting include the LysoTracker series of dyes[7]. Another strategy for targeted lysosomes involves attaching ligands to the fluorescent dye that allow it to be endocytosed, travel through the endocytotic pathway, and eventually end up in lysosomes[8].

Endoplasmic Reticulum (ER): Most stains for the endoplasmic reticulum are common lipophilic fluorophores such as BODIPYs conjugated to groups that react with membrane-bound proteins of the endoplasmic reticulum (**Figure 1.1.1d**)[9]. Notable examples of such groups include sulfonylurea groups used to target endoplasmic reticulum potassium channels[10].

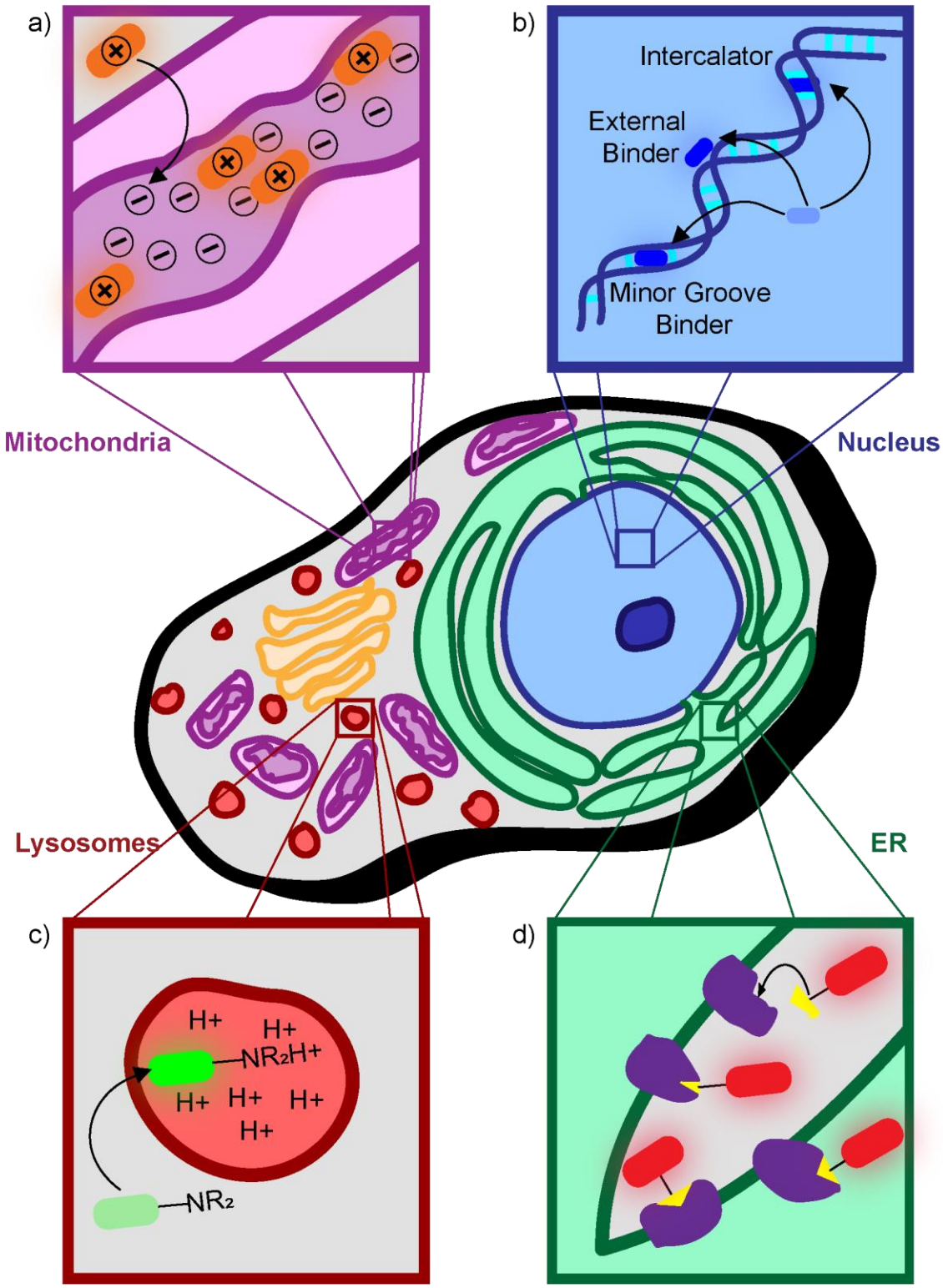

Figure 1.1.1 Common strategies for subcellular targeting of fluorescent probes to mitochondria (**a**), nucleus (**b**), lysosomes (**c**), and endoplasmic reticulum (**d**)

1.2 Targeting fluorescent dyes to organelles via bioorthogonal reactions

Another strategy for targeting fluorescent dyes to organelles is to target a reactive group to an organelle of interest and then add its reaction partner to the dye that is to be targeted. This strategy is advantageous because it enables flexibility in both staining color and location by using different combinations of dyes and targeting groups. Additionally, the reactive groups attached to the dyes can be designed to minimally affect the properties of the dyes or quench the fluorescence of the dye until it reacts with the targeted reaction partner leading to higher fluorescence intensity in the desired organelle and lower fluorescence intensity in off-target locations.

Although many bioorthogonal reactions have been used for subcellular targeting of fluorescent dyes and are reviewed elsewhere[11], this chapter will focus on inverse electron demand Diels-Alder (IEDDA) reactions between strained alkenes and tetrazines. In this reaction, the Lowest Unoccupied Molecular Orbital (LUMO) of an electron deficient tetrazine reacts with the Highest Occupied Molecular Orbital (HOMO) of a strained or electron rich alkene to form a cyclic intermediate which then rearranges to lose nitrogen gas and form a cyclic product which rapidly oxidizes to form a nitrogen containing aromatic ring that covalently binds the two molecules together[12]. This reaction is bioorthogonal, meaning that it can take place in cells, tissues, or whole organisms with minimal reactivity to endogenous molecules. The tetrazines and alkenes used for these reactions are stable for hours in aqueous environments at 37 degrees Celsius which makes them suitable for imaging in live cells[13].

One important property of the IEDDA reaction between tetrazines and alkenes are the kinetics, which are both rapid compared to many other bioorthogonal reactions and easily tunable by altering the electronics of the reaction partners. Adding electron withdrawing groups to the carbon atoms in a tetrazine lowers the LUMO and increases the rate of reaction. Adding electron donating groups to the alkene raises its HOMO and also increases the rate of the reaction; however, installing these groups can be synthetically challenging and lead to unstable alkenes[14]. A common alternative to adding electron donating groups to the alkene is raising the alkene HOMO by putting the alkene in a strained ring, such as a norbornene or the ubiquitous trans-cyclooctene which has extremely rapid reaction kinetics with tetrazines and is very stable in a biological environment and thus is used frequently for *in cellulo* and *in vivo* bioorthogonal labeling[15].

The typical strategy used to employ an IEDDA reaction between and tetrazine and a strained alkene is as follows: a fluorescent dye or probe is conjugated to a tetrazine. Depending on the linkage between the fluorophore and the tetrazine, the tetrazine can quench the fluorescence of the dye anywhere from 2-fold to over 100-fold[16], meaning that in the absence of an alkene reaction partner, the dye may stain multiple subcellular locations but have minimal fluorescence. To target the fluorescent dye-tetrazine conjugate to a specific subcellular location, a strained alkene, typically a transcyclooctene (TCO), is then conjugated to a group that will allow it to chemically target to a subcellular

location of interest, either by taking advantage of the organelle-specific properties listed above or by covalently binding to a genetically expressed protein targeted to a subcellular location of interest.

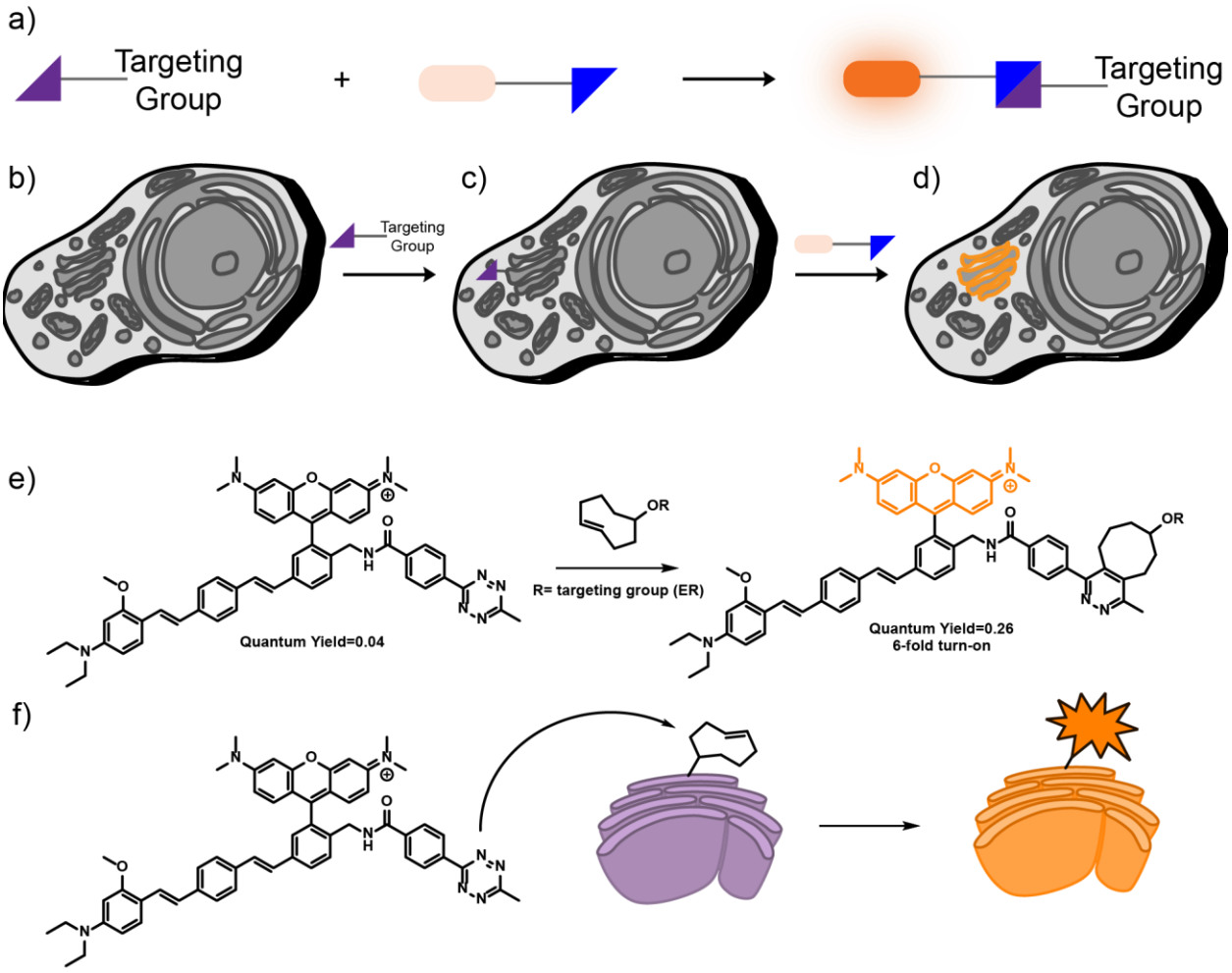

Figure 1.2.1 Click chemistry strategies for targeting fluorescent probes to organelles. **a**) general schematic of an in vitro reaction between a targeted reaction partner and a fluorescent dye conjugated to the other reaction partner resulting in a turn-on in dye fluorescence. A cell (**b**) treated with one click chemistry reaction partner targeted to a subcellular location of interest will label that subcellular location with that reaction partner (**c**). The cell can then be treated with a dye conjugated to the other reaction partner resulting in an in cellulo reaction between the two and dye labeling at the targeted subcellular location (**d**). A schematic of an *in vitro* (**e**) and *in cellulo* (**f**) reaction between a fluorescent probe conjugated to a tetrazine and a transcyclooctene with a targeting group for the endoplasmic reticulum to demonstrate an example of this labeling strategy.

Targeting a TCO and subsequently reacting it *in vivo* with a dye-tetrazine conjugate has a few advantages over directly attaching a targeting group to a dye. Firstly, TCO and its

derivatives are small and hydrophobic, meaning they are highly cell-permeant, whereas many fluorescent dyes are larger and sometimes charged, reducing their permeability; thus, a TCO-targeting group conjugate is much more likely to be cell permeant than a dye-targeting group conjugate, and adding a tetrazine to a dye will minimally affect its permeability. Secondly, when making a fluorescent probe, adding large targeting groups may alter the efficacy of the probe by affecting binding properties to the analyte of interest or adding non-radiative decay pathways which can reduce the quantum yield of the fluorophore. Conversely, the TCO reactivity to tetrazines will only be minimally affected by the addition of targeting groups because they will rarely substantially alter the strain of the TCO which is the major factor driving the reaction rate. Furthermore, the reaction rate and is very rapid, so reductions in its reaction kinetics will not substantially affect the targeting efficacy. Finally, off-target fluorescence will be reduced because low concentrations of targeted TCOs will react much slower with off-target dye-tetrazine conjugates than the high concentrations present at the desired subcellular location. Thus, targeting a TCO and subsequently reacting it *in vivo* with a tetrazine-dye conjugate with quenched fluorescence provides a highly effective strategy for specific subcellular localization of fluorescent dyes and probes.

Many chemical biology researchers have used tetrazine-TCO reactions for targeting of fluorescent dyes and functional probes. One approach involves targeting fluorescein, tetramethylrhodamine, and BODIPY derivatives by conjugating them to a methyl tetrazine via a styrene linkage. These dyes exhibit 400 fold, 76 fold, and 200 fold turn on in fluorescence respectively after reaction with transcyclooctene. These probes can be used with TCO conjugated antibodies for selective targeting of membranes[17]. Superresolution STED probes have also been targeted to the Golgi apparatus[18], ER[19], and mitochondria[20] used targeted lipids that localize a TCO to the membrane of the organelle of interest with high selectivity and high density of labeling. An example of targeting functional fluorescent probes using tetrazine click chemistry targets magnesium sensors to subcellular locations by using a strained alkyne targeted via a HaloTag protein to a specific subcellular location as one reaction partner and a tetrazine-conjugated magnesium sensor as the other[21]. A twist on the typical tetrazine conjugated dye approach involves sequence-specific RNA sensors in which a fluorophore is capped with an alkene that quenches the fluorescence. Upon reaction with a tetrazine and subsequent oxidation, the fluorophore is ejected as a leaving group, uncaging fluorescence. The proximity induced by selective duplex formation enables the reaction to occur[22].

1.3 Electrophysiology in organelles

The approach highlighted above for selectively targeting metal ion sensors to subcellular locations highlights the importance of ionic compartmentalization in subcellular organelles. This ionic compartmentalization creates an electrical potential across

organelle membranes that is crucial for many biological signaling processes, but is difficult to study due to a lack of effective tools for measuring membrane potential in organelles.

The gold standard in membrane potential measurements in biology is patch-clamp electrophysiology, in which a pipet containing an electrode is attached to a cell membrane to allow the electrode to be put in direct electrical contact with the interior of the membrane. The voltage difference between the solution on the outside of the membrane and the solution on the inside can then be directly measured electrically. While this technique provides extremely accurate readings of membrane potential with high temporal resolution, it is highly invasive and thus does not provide a good representation of the natural cell environment. Patch-clamp electrophysiology is also difficult to accomplish in practice especially when dealing with intracellular membranes which are extremely small relative to the size of the pipet.

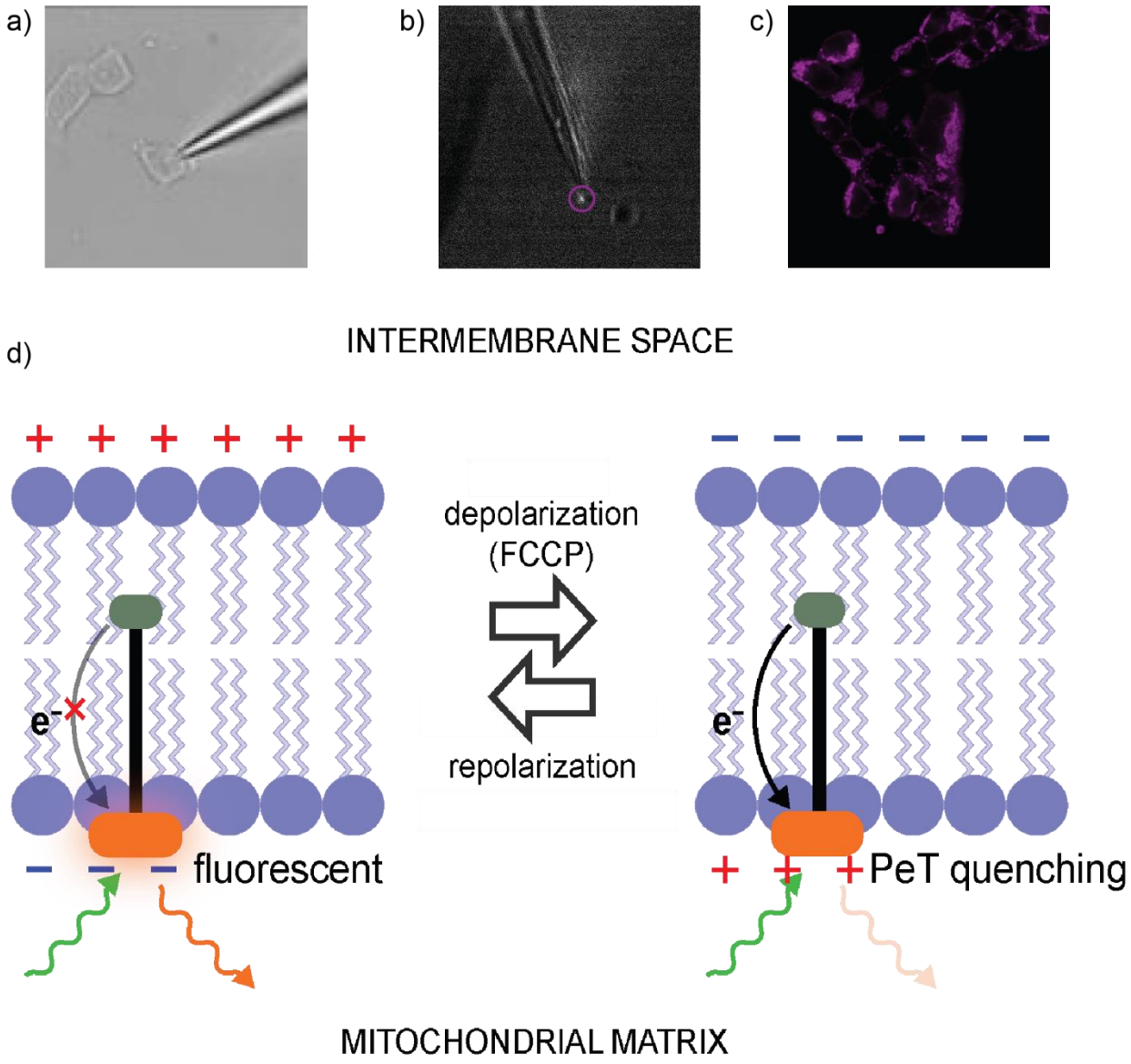

Figure 1.3.1 Electrophysiological vs optical measurements of membrane potential. Images of patch-clamp electrophysiology on a whole cell (**a**) and an isolated mitoplast (**b**). Mitoplast is indicated by magenta circle. A mitochondrially targeted voltage-sensitive dye developed in this work (**c**) enables high throughput measurements of membrane potential of large numbers of mitochondria inside of their cellular environment via the mechanism diagrammed in (**d**)

Despite these limitations, some approaches to direct electrophysiological measurements of membrane potential in organelles exist and are used mainly to characterize the properties of subcellular ion channels. Mitochondrial inner membrane patch-clamp electrophysiology is enabled through the isolation of structures called mitoplasts[23].

Mitoplasts are created by isolating mitochondria from cell lysate, perforating their outer membrane, and then treating them with a hypotonic solution to allow the matrix to swell, pushing the inner membrane through holes in the outer membrane. The inner membrane can then be patched to measure the properties of ion channels[23]. Lysosomal patch clamp electrophysiology typically occurs on enlarged lysosomes, which similar to the generation of mitoplasts, are swollen via vacuolin treatment after lysis of the plasma membrane[24]. Two strategies have been used to patch the ER membrane. In the first, cells are lysed via a mechanical tissue homogenizer and then the nuclei are isolated from cell debris, leaving the portion of the ER that is connected to the nuclear envelope intact and available for access via a patching pipet[25]. In the second strategy, a second pipet was used to encapsulate a patch-clamp electrophysiology pipet. The outer pipet seals onto and punctures the plasma membrane which then gives the inner pipet access to the interior of the cell for patch-clamp electrophysiology. This strategy is most easily adapted for the ER because the ER membrane occupies a large volume of the cell[26].

1.4 Optical measurements of membrane potential in organelles

The electrophysiological measurements described above for measuring membrane potential in organelles all involve substantially altering the organelle in question, isolating it from its cellular environment, significantly perturbing its cellular environment, or some combination of the three, which make them less than ideal for physiologically relevant measurements of subcellular membrane potential. Optical measurements of membrane potential are an attractive alternative, as they are much less invasive than patch-clamp electrophysiology, enable imaging of intact cells, and are much higher throughput as all the organelles in a single cell or in multiple cells can be measured simultaneously. Although optical measurements of plasma membrane potential have become commonplace, few examples exist of tools for optical measurements of membrane potential in organelles beyond mitochondria. Below is a comprehensive summary of the currently existing fluorescent probes for optical measurements of membrane potential in organelles

Mitochondria: The mitochondria is the powerhouse of the cell because it generates adenosine triphosphate (ATP) to fuel cellular processes. The synthesis of ATP is driven by a proton gradient across the inner mitochondrial membrane. This gradient results in an electrical potential difference across the mitochondrial inner membrane of approximately 160 mV with the matrix negative relative to the intermembrane space[27]. This membrane potential is indicated to have a role in regulating ATP synthesis[28], calcium release[29], and is misregulated in carcinoma lines[30]. Because of its relevance to a broad spectrum of biological processes, measuring mitochondrial inner membrane potential is of interest to cell biologists. This combined with the ease of targeting fluorescent probes to mitochondria due to the relative negative charge of the mitochondrial matrix means

that there are far more tools for optically measuring mitochondrial membrane potential than for other organelles.

A fluorescent probe for mitochondrial membrane potential must change one of its properties in response to a change in membrane potential such as the intensity of fluorescence, color of fluorescence, or physical localization. The simplest design for such a probe is simply a membrane-permeable dye that is positively charged and thus will accumulate in the mitochondria in proportion to the negative charge in the mitochondrial matrix. Two key classes of fluorescent indicators, cationic cyanines and rhodamine esters, emerged in the 1970s and 80s based on this principle[3231]. DiOC6(3) is an oxacarbocyanine dye that is lipophilic and has a net charge of +1. The intensity of mitochondrial fluorescence observed in microscopy images is directly proportional to how much dye has diffused into the mitochondria and thus is proportional to the amount of relative negative charge in the matrix[32]. However, DiOC6(3) is toxic to mitochondria at relatively low concentrations (nM) which makes it challenging to use in imaging experiments[33]. Despite this drawback, DiOC6(3) does find usage in flow cytometry experiments[34]. Rhodamine esters are also small, lipophilic, and cationic, and thus will accumulate in mitochondria in proportion to the negative charge in the matrix as well; however, Rhodamine esters are generally less toxic to mitochondria. Three rhodamine esters are commonly used to measure mitochondrial membrane potential, each with their own properties: Rhodamine 123 (Rho123, cyan absorbance, green fluorescence), Tetramethylrhodamine Methyl ester (TMRM, green absorbance, orange fluorescence), and Tetramethylrhodamine Ethyl ester (TMRE, green absorbance, orange fluorescence)[35]. Of these three, TMRE binds the most to the electron transport chain and thus is often eschewed in favor of TMRM since they have similar equilibration kinetics and spectral properties[35]. All three of these dyes can be operated under two sets of conditions: quenching and non-quenching mode. In non-quenching mode, usually at concentrations of 10s of nM, the intensity of dye fluorescence in the mitochondria increases as the mitochondrial inner membrane becomes more hyperpolarized as dye continues to accumulate. In quenching mode, typically at low micromolar concentrations, so much dye is accumulated in the mitochondria that it forms aggregates with severely reduced fluorescence. Thus, as mitochondria hyperpolarize, quenching increases and fluorescence decreases, and as they depolarize, dye is released into the cytoplasm and the dye remaining in the mitochondria is unquenched and increases its fluorescence. TMRM is typically used in non-quenching mode to look at slow changes in mitochondrial inner membrane potential or resting inner membrane potential due to its fast equilibration kinetics and low electron transport chain toxicity. Rho123 is best suited for use in quenching mode to look at rapid changes in inner membrane potential because it is slow to equilibrate, meaning that it is unresponsive to changes in plasma membrane potential over short time scales[36].

One drawback of lipophilic cationic dyes that accumulate in mitochondria based on their electrochemical gradient is that the measurements are intensity based, which can be

confounded by many factors including small differences in concentration and diffusion out of mitochondria along a concentration gradient as well as photobleaching and other degradation pathways. Ratiometric probes can circumvent these issues by allowing measurements via changes in intensity at two wavelengths which can be normalized to each other. One commonly used ratiometric probe for mitochondrial membrane potential is JC-1[37], which is a cationic carbocyanine dye that accumulates in mitochondria similarly to DiOC6(3). However, as JC-1 concentration increases, it forms J-aggregates which redshift the emission spectrum of the dye. This allows for a ratiometric readout of JC-1 concentration by measuring the relative emission of the monomeric dye and the J-aggregates, which then is a proxy for mitochondrial membrane potential[37]. Although this in theory allows for the readout of absolute mitochondrial membrane potential, because the ratiometric readout depends on local aggregation, it is sensitive to loading concentration and equilibration time, which is significantly longer for the J-aggregate than for the monomeric form[36].

Resonance Energy Transfer (RET)-based probes offer an alternative approach to ratiometric measurements of mitochondrial membrane potential. In these systems, two mitochondrially targeted dyes that comprise a RET donor-acceptor pair are stained onto cells. Typically, one of these dyes will remain in mitochondria even during changes in membrane potential whereas the other will diffuse in and out in response to changes in membrane potential. The RET efficiency between these two dyes then provides a readout of mitochondrial membrane potential. A classic approach uses MitoTracker green as a RET donor and TMRM as a RET acceptor[38]. MitoTracker green is a cyanine-based cationic dye with benzyl chloride groups that covalently link to reactive cysteines in mitochondrial proteins. MitoTracker green fluorescence is insensitive to changes in inner membrane potential that induce changes in Rho123 fluorescence[39]. The MitoTracker green-TMRM RET pair with washout of excess dye can differentiate between individual polarized and depolarized mitochondria in living cells. Both JC-1 and the MitoTracker green-TMRM RET pair have a spectral separation of around 70 nm which can result in crosstalk which reduces signal-to-noise ratio in some imaging experiments. A novel dye pair dubbed FixD and LA1 have large Stokes shifts and good spectral overlap and allow for measurements using the same principles. FixD has a benzyl chloride group for retention in mitochondria whereas LA1 is free to diffuse. This system results in excitation at 405 nm with readout at 565 and 675 nm for a 110 nm spectral separation between the two dyes[40].

Another emerging approach for measuring mitochondrial membrane potential is the synthesis of probes that partition between the mitochondrial matrix and another subcellular location which can then be read out by looking at the relative fluorescence of these locations. A key benefit of these systems is reversibility, because when the indicator diffuses out of mitochondria it becomes trapped in another subcellular location rather than diffusing out of the cell entirely. In one such approach, lipophilic cationic dyes with an affinity for both mitochondria and nucleic acids are synthesized in order to create a

partition between the mitochondrial matrix and the nucleus or nucleolus. These are often based on polystyryl pyridinium systems which are fluorescent and cationic, but have enough aromatic character to have an affinity for base stacking in RNA and DNA. The relative amount of dyes in these locations are then quantified to determine whether the mitochondria are in a hyperpolarized, depolarized, or intermediate state. These dyes have been successfully used to pick apoptotic cells out of a population[41]. Additionally, the authors have extended their work to make red-emitting, two-photon active dyes that would be of great use in tissues due to the enhanced penetration of red and IR light compared to blueshifted wavelengths[42].

A much more recent approach to mitochondrial membrane potential measurements is to target a fluorescent probe that modulates its fluorescence in response to voltage changes via photoinduced electron transfer (PeT). PeT occurs when the excited state of a fluorophore acts as an electron donor or acceptor for an electron poor or electron rich group nearby, typically on the same molecule and linked via a bond structure that enables efficient electron transfer. PeT based voltage probes insert themselves into membranes where the rate of PeT is modulated by the electrical field across the membrane (which is proportional to membrane potential), thus altering the fluorescence of the chromophore as a function of the electric field. This work reports the synthesis, characterization, and protocols for use in functional imaging of the first ever PeT-based mitochondrial voltage indicator in Chapter 2 and Chapter 4 contains a more thorough description of the parameters involved in electron transfer and energy transfer in chromophores in Chapter 4 with a focus on VoltageFluors, a class of PeT-based membrane potential indicators. Since the publication of the results in Chapter 2, another group has reported a PeT-based mitochondrial voltage sensor masked with an ester group that is cleaved in mitochondria, allowing it to insert into the mitochondrial inner membrane and report membrane potential via modulation of PeT quenching of the chromophore[43].

Lysosomes: The highly acidic lumen of lysosomes leads to a large charge gradient across the lysosomal membrane and thus a significant membrane potential with the lumen positive relative to the cytosol. Ions such as sodium and potassium are also found to be important contributors to lysosomal membrane potential[44]. One approach to measuring lysosomal membrane potential is to use a two-piece system consisting of a lysosomal membrane targeted fluorophore and a charged small molecule that can interact with the fluorophore spectrally via resonance energy transfer (RET). When the membrane potential changes, the distribution of the charged small molecule will change in response. Because RET is distance dependent, this will change the RET efficiency between the fluorophore and the charged small molecule and result in a change in fluorescence. One demonstration of this technique in lysosomes uses l-α-phosphatidylethanolamine as a targeting group for conjugated tetraethylrhodamine and 7-diethyaminocoumarin derivatives as the lysosomally targeted fluorophore coupled with $DiBAC_4(3)$ and

$DiSBAC_2(3)$ as the charged groups, respectively. $DiBAC_4(3)$ and $DiSBAC_2(3)$ are anionic oxonol dyes which will redistribute in response to membrane potential, and $DiBAC_4(3)$ acts as a good RET donor to tetraethylrhodamine and $DiSBAC_2(3)$ as a good acceptor for 7-diethyaminocoumarin, enabling a measurement of lysosomal membrane potential by measuring the donor/acceptor fluorescence ratio[45]. Another example of this technique targets enhanced green fluorescent protein (EGFP) to the lysosomal membrane by fusing it with LAMP1, a lysosomal membrane protein, and dipicrylamine (DPA), a lipophilic anion that quenches the fluorescence of EGFP via RET, was added exogenously. This system was able to report changes in lysosomal membrane potential via the intensity of EGFP fluorescence and was extended to targeting other organelles including the golgi apparatus and ER[46]. A more recent approach involves assembling *in cellulo* a 3-component system consisting of an endolysomal membrane targeting group that takes advantage of the natural endocytosis of DNA duplexes, the membrane-bound voltage-sensitive fluorophore RVF[47], and Atto647N as a reference dye in living cells. Each of these components are bound to single-stranded DNA such that two components are each complementary to half of the third component, ensuring a 1:1:1 stoichiometry of the assembled reagents on the endolysosomal membrane. The resulting probe, Voltair, is used for ratiometric measurements of membrane potential changes along the endolysosomal pathway[48].

Endoplasmic Reticulum: The major ionic players in the ER are Ca^{2+} and K^{+}[49]. The ER is one of the two major intracellular stores of calcium, and releases calcium from the ER lumen into the cytosol during signaling processes that require an increase in cytosolic calcium concentration. The predominant hypothesis is that despite the large outward flux of calcium from the ER lumen during calcium release, ER membrane potential remains largely static due to a concurrent influx of potassium which compensates for the outward flux of calcium[49]. The function and dynamics of ER membrane potential are minimally studied because there are few tools for measuring ER membrane potential. Conflicting reports exist as to the resting membrane potential of the ER membrane with some reports indicating it is electrically neutral at rest[50] and other reports indicating that it is hyperpolarized relative to the cytosol[51]. One approach to optically measuring ER membrane potential is to use highly lipophilic, charged dyes such as 3,3'-diethyl-2,2'-indodicarbocyanine, oxonol VI, or diS-C3-(5) and rely on their lipophilicity to stain the ER membrane over other subcellular locations. Their charge will then make them respond to voltage changes through Nernstian redistribution[52,53]. Carbocyanines have been used to show that in skeletal muscle sarcoplasmic reticulum[54] and fragmented sarcoplasmic reticulum[55], sarcoplasmic reticulum membrane potential does not change during calcium release. A genetically encoded voltage indicator (GEVI) has also been developed for measuring sarcoplasmic reticulum membrane potential in intact skeletal muscle is based on Mermaid[56] which has response kinetics of 10s of milliseconds to voltage transients and the internally targeted variant has a response time of 25-150 ms depending on

voltage[54]. Another attempt at making a GEVI for sensing voltage in the ER attempts to target an ArcLight[57] derivative to the ER membrane instead of the plasma membrane by modifying the transmembrane domain for ER targeting. Although this voltage sensor was used to demonstrate that the plasma membrane and ER membrane are electrically coupled, the voltage sensor mostly targets the plasma membrane over the ER which makes functional measurements difficult and the direction of the relationship between fluorescence response and membrane potential is unknown[58].

1.5 Conclusion and outlook

The methods reported above represent the current state of the art in targeting fluorescent probes to organelles and measuring subcellular membrane potential at the time of writing of this thesis. The remainder of this thesis presents new tools developed in this dissertation for achieving optical measurements of subcellular membrane potential. Chapter 2 describes the targeting a VoltageFluor known as Rhodamine Voltage Reporter (RhoVR) to mitochondria via cationic/anionic attraction followed by unmasking of an ester to visualize reversible mitochondrial membrane potential changes. Chapter 3 describes the development of a fluorogenic, bioorthogonal, click chemistry targeting strategy to localize RhoVRs to the endoplasmic reticulum and other organelles. Chapter 4 details the physical mechanism behind the voltage sensing of VoltageFluors as well as providing a computational description of their properties and initial experiments towards the development of ratiometric measurements of membrane potential. Appendix α describes progress in a new synthetic route for tetrasulfonated rhodamines which could have applications in targeting voltage sensors and other probes in complex biological tissues. Appendix β describes progress towards a caged RhoVR which could be selectively uncaged enzymatically for targeting to specific membranes.

1.6 References

1. Lehninger, A. L.; Cox, M. M.; Nelson, D. L. *Lehninger Principles of Biochemistry*. W.H. Freeman: New York, **2008**
2. Abad, M.F.; Di Benedetto. G.; Magalhães, P.J.; Filippin, L.; Pozzan, T. Mitochondrial pH monitored by a new engineered green fluorescent protein mutant. *J Biol Chem*. **2004**, *279* (12), 11521-11529
3. Thermo Fisher. Molecular Probes Handbook. **2010**, 495-543
4. Thermo Fisher. Molecular Probes Handbook. **2010**, 303-360
5. Bucevičius, J.; Lukinavičius, G.; Gerasimaitė, R. The Use of Hoechst Dyes for DNA Staining and Beyond. Chemosensors **2018**, *6* (2), 18-29 https://doi.org/10.3390/chemosensors6020018
6. Grabe, M.; Oster, G. Regulation of Organelle Acidity*. J. Gen.*

Physiol. **2001**, *117* (4), 329−344
7. Pierzyńska-Mach, A.; Janowski, P.A.; Dobrucki, J.W. Evaluation of acridine orange, LysoTracker Red, and quinacrine as fluorescent probes for long-term tracking of acidic vesicles. *Cytometry A*. **2014**, *85* (8), 729-737
8. Yapici, N.B.; Bi, Y.; Li, P.; Chen, X.; Yan, X.; Mandalapu, S.R.; Faucett, M.; Jockusch, S.; Ju, J.; Gibson, K.M.; Pavan, W.J.; Bi, L. Highly stable and sensitive fluorescent probes (LysoProbes) for lysosomal labeling and tracking. *Sci Rep*. **2015**, *5* 8576-8583
9. Xu, W.; Zeng, Z.; Jiang, J.H.; Chang, Y.T.; Yuan L. Discerning the Chemistry in Individual Organelles with Small-Molecule Fluorescent Probes. *Angew Chem Int Ed Engl.* **2016**, *55* (44), 13658-13699
10. Terasaki, M.; Fluorescent and Luminescent Probes for Biological Activity **1993**, 120–123
11. Cañeque, T.; Müller, S.; Rodriguez, R. Visualizing biologically active small molecules in cells using click chemistry. *Nat Rev Chem.* **2018**, *2***,** 202–215
12. Knall, A.C.; Slugovc, C. Inverse electron demand Diels-Alder (iEDDA)-initiated conjugation: a (high) potential click chemistry scheme. *Chem Soc Rev*. **2013**, *42* (12) 5131-5142
13. Devaraj, N.K.; Weissleder, R.; Hilderbrand, S.A. Tetrazine-based cycloadditions: application to pretargeted live cell imaging. *Bioconjug Chem*. **2008** *19* (12) 2297-2299
14. Karver, M.R.; Weissleder, R.; Hilderbrand, S.A. Synthesis and evaluation of a series of 1,2,4,5-tetrazines for bioorthogonal conjugation. *Bioconjug Chem*. **2011**, *22* (11) 2263-2270
15. Chen, W.; Wang, D.; Dai, C.; Hamelberg, D.; Wang, B. Clicking 1,2,4,5-tetrazine and cyclooctynes with tunable reaction rates*. Chem Commun (Camb)*. **2012**, *48* (12); 1736-1738
16. Wieczorek, A.; Werther, P.; Euchner, J.; Wombacher, R. Green- to far-red-emitting fluorogenic tetrazine probes - synthetic access and no-wash protein imaging inside living cells. *Chem Sci.* **2017**, *8* (2) 1506-1510
17. Wu, H.; Yang, J.; Šečkutė, J.; Devaraj, N.K. In situ synthesis of alkenyl tetrazines for highly fluorogenic bioorthogonal live-cell imaging probes*. Angew Chem Int Ed Engl.* **2014**, *53* (23) 5805-5809
18. Erdmann, R.S.; Takakura, H.; Thompson, A.D.; Rivera-Molina, F.; Allgeyer, E.S.; Bewersdorf, J.; Toomre, D.; Schepartz, A. Super-resolution imaging of the Golgi in live cells with a bioorthogonal ceramide probe. *Angew Chem Int Ed Engl*. **2014**, *53* (38) 10242-10246
19. Takakura, H.; Zhang, Y.; Erdmann, R.S.; Thompson, A.D.; Lin, Y.; McNellis, B.; Rivera-Molina, F.; Uno, S.N.; Kamiya, M.; Urano, Y.; Rothman, J.E.; Bewersdorf, J.; Schepartz, A.; Toomre, D. Long time-lapse nanoscopy with spontaneously blinking membrane probes. *Nat Biotechnol*. **2017**, *35* (8) 773-780

20. Chu, L.; Tyson, J.; Shaw, J.E.; Rivera-Molina, F.; Koleske, A.J.; Schepartz, A.; Toomre, D.K. Two-color nanoscopy of organelles for extended times with HIDE probes. *Nat Commun*. **2020**,*11* (1), 4271-4278
21. Gruskos, J.J.; Zhang, G.; Buccella, D. Visualizing Compartmentalized Cellular Mg2+ on Demand with Small-Molecule Fluorescent Sensors. *J Am Chem Soc*. **2016**, *138* (44), 14639-14649
22. Wu, H.; Alexander, S.C.; Jin, S.; Devaraj, N.K. A Bioorthogonal Near-Infrared Fluorogenic Probe for mRNA Detection. *J Am Chem Soc*. **2016**, *138* (36), 11429-11432
23. Kirichok, Y.; Krapivinsky, G.; Clapham, D.E. The mitochondrial calcium uniporter is a highly selective ion channel. *Nature*. **2004**, *427* (6972), 360-364
24. Schieder, M.; Rötzer, K.; Brüggemann, A.; Biel, M.; Wahl-Schott, C. Planar patch clamp approach to characterize ionic currents from intact lysosomes. *Sci Signal.* **2010**, *3* (151), pl3
25. Mak D.O.; Vais, H.; Cheung, K.H.; Foskett, J.K. Patch-clamp electrophysiology of intracellular Ca2+ channels. *Cold Spring Harb Protoc*. **2013**, *2013* (9), 787-797
26. Jonas, E.A.; Knox, R.J.; Kaczmarek, L.K. Giga-ohm seals on intracellular membranes: a technique for studying intracellular ion channels in intact cells. *Neuron*. **1997**, *19* (1), 7-13
27. Gerencser, A.A.; Chinopoulos, C.; Birket, M.J.; Jastroch, M.; Vitelli, C.; Nicholls, D.G.; Brand, M.D. Quantitative measurement of mitochondrial membrane potential in cultured cells: calcium-induced de- and hyperpolarization of neuronal mitochondria. *J Physiol*. **2012**, *590* (12), 2845-2871
28. Nicholls, D. G. Mitochondrial membrane potential and aging. *Aging Cell* **2004**, *3*, 35−40
29. Hoppe, U. C. Mitochondrial calcium channels. *FEBS Lett.* **2010**, *584*, 1975−1981
30. Summerhayes,I.C.; Lampidis,T.J.; Bernal,S.D.; Nadakavukaren, J. J.; Nadakavukaren, K. K.; Shepherd, E. L.; Chen, L. B. Unusual retention of rhodamine 123 by mitochondria in muscle and carcinoma cells. *Proc. Natl. Acad. Sci.* **1982**, *79*, 5292−5296
31 https://www.pnas.org/content/77/2/990
32. Korchak, H.M.; Rich, A.M.; Wilkenfeld, C.; Rutherford, L.E.; Weissmann, G. A carbocyanine dye, DiOC6(3), acts as a mitochondrial probe in human neutrophils. *Biochem Biophys Res Commun*. **1982**, *108* (4), 1495-1501
33. Lemasters, J.J.; Ramshesh, V.K. Imaging of mitochondrial polarization and depolarization with cationic fluorophores. *Methods Cell Biol.* **2007**, *80*, 283-295
34. Kalbácová, M.; Vrbacký, M.; Drahota, Z.; Melková, Z. Comparison of the effect of mitochondrial inhibitors on mitochondrial membrane potential in two different cell lines using flow cytometry and spectrofluorometry. *Cytometry A*. **2003**, *52* (2) 110-116
35. Scaduto, R.C. Jr; Grotyohann, L.W. Measurement of mitochondrial membrane potential using fluorescent rhodamine derivatives. *Biophys J*. **1999**, *76* (1 Pt 1) 469-477

36. Perry S.W.; Norman, J.P.; Barbieri, J.; Brown, E.B.; Gelbard, H.A. Mitochondrial membrane potential probes and the proton gradient: a practical usage guide. *Biotechniques*. **2011**, *50* (2), 98-115
37. Reers, M.; Smith, T.W.; Chen, L.B. J-aggregate formation of a carbocyanine as a quantitative fluorescent indicator of membrane potential. *Biochemistry*. **1991**, *30* (18), 4480-4486
38. Elmore, S.P.; Nishimura, Y.; Qian, T.; Herman, B.; Lemasters, J.J. Discrimination of depolarized from polarized mitochondria by confocal fluorescence resonance energy transfer. *Arch Biochem Biophys*. **2004**, *422* (2) 145-152
39. Cottet-Rousselle, C.; Ronot, X.; Leverve, X.; Mayol, J.F. Cytometric assessment of mitochondria using fluorescent probes. *Cytometry A*. **2011**, 79 (6) 405-425
40. Feng, R.; Guo, L.; Fang, J.; Jia, Y.; Wang, X.; Wei, Q.; Yu, X. Construction of the FRET Pairs for the Visualization of Mitochondria Membrane Potential in Dual Emission Colors. *Anal Chem*. **2019**, 91 (5), 3704-3709
41. Zhao, Y.; Zhang, C.; Liu, J.; Li, D.; Tian, X.; Wang, A.; Li, S.; Wu, J.; Tian, Y. Dual-channel fluorescent probe bearing two-photon activity for cell viability monitoring. *J. Mater. Chem. B.* **2019**, *7*, 3633–3638
42. Seki, H.; Onishi, S.; Asamura, N.; Suzuki, Y.; Kawamata, J.; Kaneno, D.; Hadano, S.; Watanabe, S.; Niko, Y.; Bright and two-photon active red fluorescent dyes that selectively move back and forth between the mitochondria and nucleus upon changing the mitochondrial membrane potential. *J Mater Chem B*. **2018**, *6* (45), 7396-7401
43. *Hernández-Juárez*, C.; *Flores-Cruz*, R.; *Jiménez-Sánchez, A*. Fluorescent probe for early mitochondrial voltage dynamics. Chem. Comm. 2021, 57 (45), 5526-5529
44. Xiong, J;, Zhu, M.X. Regulation of lysosomal ion homeostasis by channels and transporters. Sci *China Life Sci.* **2016**, *59* (8), 777-791
45. Koivusalo, M.; Steinberg, B.E.; Mason, D.; Grinstein, S. In situ measurement of the electrical potential across the lysosomal membrane using FRET. *Traffic*. **2011**, *12* (8) 972-982
46. Matamala, E.; Castillo, C.; Vivar, J.P.; Rojas, P.A.; Brauchi, S.E. Imaging the electrical activity of organelles in living cells. *Commun Biol*. **2021**, 4 (1), 389-400
47. Kulkarni, R.U.; Kramer, D.J.; Pourmandi, N.; Karbasi, K.; Bateup, H.S.; Miller, E.W. Voltage-sensitive rhodol with enhanced two-photon brightness. *Proc Natl Acad Sci U S A.* **2017**, *114* (11), 2813-2818
48. Saminathan, A.; Devany, J.; Veetil, A.T.; Suresh, B.; Pillai, K.S.; Schwake, M.; Krishnan, Y. A DNA-based voltmeter for organelles. *Nat Nanotechnol*. **2021**, *16* (1), 96-103
49. Kuum, M;, Veksler, V.; Kaasik, A. Potassium fluxes across the endoplasmic reticulum and their role in endoplasmic reticulum calcium homeostasis. *Cell Calcium*. **2015**, *58* (1), 79-85
50. Lam, A.K.; Galione, A. The endoplasmic reticulum and junctional membrane communication during calcium signaling. *Biochim Biophys Acta*. **2013**, *1833* (11) 2542-2559

51. Burdakov, D.; Petersen, O.H.; Verkhratsky, A. Intraluminal calcium as a primary regulator of endoplasmic reticulum function. *Cell Calcium*. **2005**, *38* (3-4), 303-310
52. Beeler T.J.; Farmen, R.H.; Martonosi, A.N. The mechanism of voltage-sensitive dye responses on sarcoplasmic reticulum. *J Membr Biol*. **1981**, *62* (1-2) 113-137
53. Cabrini, G.; Verkman, A.S. Potential-sensitive response mechanism of diS-C3-(5) in biological membranes. *J Membr Biol*. **1986**, *92* (2), 171-182
54. Sanchez, C.; Berthier, C.; Allard, B.; Perrot, J.; Bouvard, C.; Tsutsui, H.; Okamura, Y.; Jacquemond, V. Tracking the sarcoplasmic reticulum membrane voltage in muscle with a FRET biosensor. *J Gen Physiol*. **2018**, *150* (8), 1163-1177
55. Koshita, M.; Hotta, K. Relationship between membrane potential and calcium ion fluxes in the fragmented sarcoplasmic reticulum. *Jpn J Physiol*. **1981**, *31* (1), 109-120
56. Tsutsui, H.; Karasawa, S.; Okamura, Y.; Miyawaki, A. Improving membrane voltage measurements using FRET with new fluorescent proteins. *Nat Methods*. **2008**, *5* (8), 683-685
57. Jin, L.; Han, Z.; Platisa, J.; Wooltorton, J.R.; Cohen, L.B.; Pieribone, V.A. Single action potentials and subthreshold electrical events imaged in neurons with a fluorescent protein voltage probe. *Neuron*. **2012**, *75* (5) 779-785
58. Sepehri Rad, M.; Cohen, L.B.; Braubach, O.; Baker, B.J. Monitoring voltage fluctuations of intracellular membranes. *Sci Rep*. **2018**, 8 (1), 6911

Chapter 2: Imaging Reversible Mitochondrial Membrane Potential Dynamics with a Masked Rhodamine Voltage Reporter

With Julia G. Martin

Portions of this work were published in: Klier, P.E.Z.; Martin, J.G.; Miller, E.W. Imaging Reversible Mitochondrial Membrane Potential Dynamics with a Masked Rhodamine Voltage Reporter. *J. Am. Chem. Soc.* **2021**, *143* (11), 4095–4099

2.0 Introduction

Membrane-bound organelles maintain gradients of ions across their membranes resulting in a membrane potential (V_{mem}), or voltage, difference relative to the cytosol.[1] Mitochondria are perhaps the most well-known example of this phenomenon: as the locus of oxidative phosphorylation,[2] the chemical potential energy in cellular fuel sources is used to pump H^+ across the mitochondrial inner membrane and into the intermembrane space. In normally respiring mitochondria, this results in a voltage gradient of approximately 160 mV with the matrix negative relative to the intermembrane space. The magnitude of this mitochondrial electrochemical potential ($\Delta\Psi_m$) profoundly influences the rate of ATP synthesis,[3] is linked to calcium release,[4] and is often misregulated in cancer metabolism.[5]

Traditionally, V_{mem} is measured using patch-clamp electrophysiology, but the invasive nature of this technique, the small size of mitochondria, and the sequestration of the mitochondrial inner membrane within both the plasma membrane and outer mitochondrial membrane make electrode-based methods impossible to implement for mitochondria inside of living cells. Optical methods are a promising route for studying voltage in membrane-bound organelles because a membrane-permeable dye can be used in intact cells to provide a minimally invasive readout of the membrane potential of an organelle in its physiological niche.[6]

The vast majority of reported fluorescent sensors of $\Delta\Psi_m$ involve a lipophilic, cationic fluorophore that accumulates in mitochondria in proportion to the negative $\Delta\Psi_m$. The change in voltage is then read out by measuring the intensity of mitochondrial fluorescence,[7] the change in color as the dye forms spectrally shifted aggregates,[8-9] the RET efficiency between a static donor and a mobile acceptor,[10-11] or the physical partition of the dye between mitochondria and another subcellular compartment.[12-13] A commonly used class of dye is rhodamine esters (**Scheme 2.0.1**) which report change in $\Delta\Psi_m$ via the intensity of mitochondrial fluorescence. However, this approach has some technical limitations. First, at high concentrations, rhodamines and other lipophilic dyes will self-quench, confounding interpretation of intensity changes.[14] Second, dye must be continuously present in the bath solution to compensate for diffusion out of the mitochondria that occurs when no dye is present extracellularly. It is impossible to leave dye solution on the sample in some experimental configurations. Finally, because all of the mechanisms listed above rely on diffusion, rapid voltage changes on timescales of milliseconds will not be observed.[15]

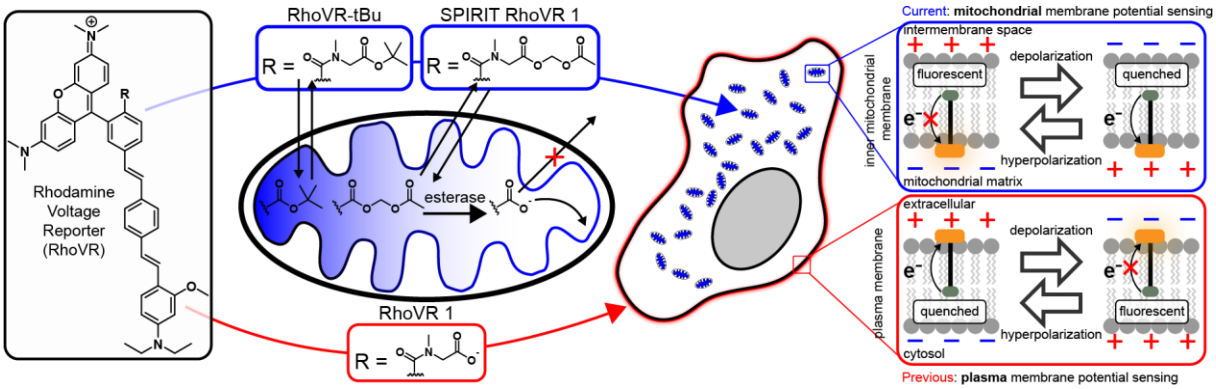

Scheme 2.0.1 Targeting Rhodamine Voltage Reporters to mitochondria

Voltage-sensitive fluorophores that sense changes in V_{mem} via a photoinduced electron transfer (PeT) mechanism,[16] can address some of the limitations of diffusion-based rhodamine esters. The lipophilic molecular wire of VF dyes drives membrane localization, and anionic carboxylate or sulfonate groups prevent internalization. In the course of developing rhodamine based voltage-reporters (RhoVR dyes), we found that the tBu ester of RhoVR (**Scheme 2.0.1**) localized to internal structures, whereas the free carboxylate (RhoVR 1, **Scheme 2.0.1**) localized to plasma membranes.[17]

We hypothesized that RhoVR-tBu localized to mitochondria, on account of its overall cationic and lipophilic nature, and would show $\Delta\Psi_m$-dependent accumulation in these structures, similar to classic rhodamine esters. We wondered whether a labile ester, like acetoxymethyl (AM) esters, would allow RhoVR to accumulate in the mitochondria matrix, where esterases[18] could hydrolyze the ester, trapping RhoVR 1 and enabling it to insert to the inner membrane. The revealed carboxylate would prevent it from acting like an “accumulation” type rhodamine ester, and it would then sense voltage via a PeT-based mechanism. This Small molecule, Permeable, Internally Redistributing for Inner membrane Targeting RhoVR, or SPIRIT RhoVR 1, represents the first of a new class of $\Delta\Psi_m$ indicators that does not rely on molecular accumulation for voltage sensing.

2.1 Synthesis of SPIRIT RhoVRs

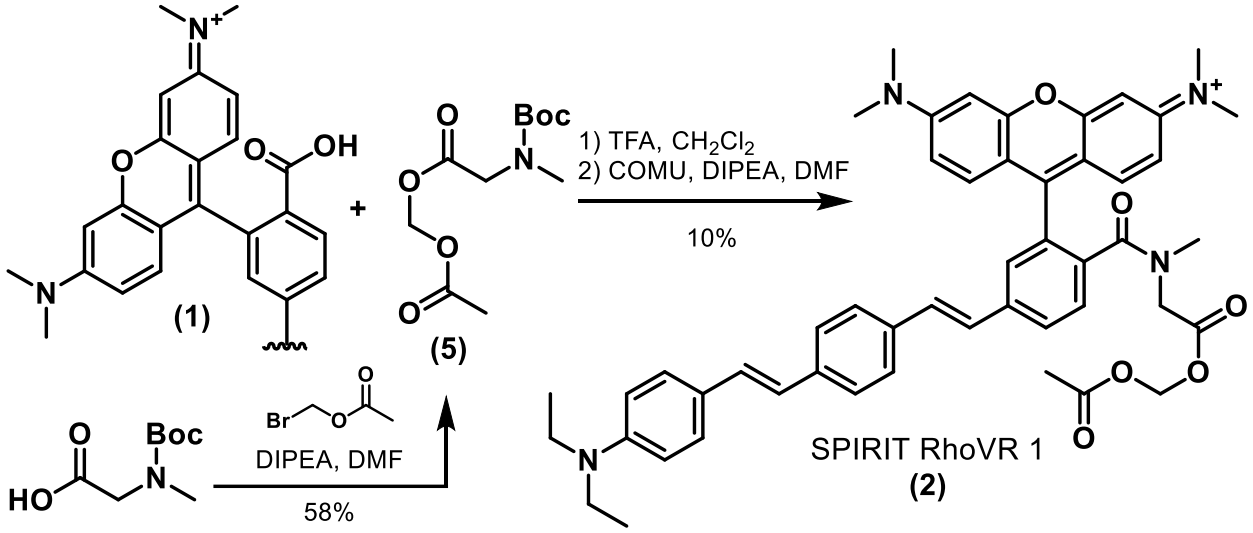

Scheme 2.1.1 Synthesis of SPIRIT RhoVRs

SPIRIT RhoVR1 is synthesized in 3 steps (**Scheme 2.1.1**). Esterification of *N-tert*-butyloxycarbonyl sarcosine (Boc-sarc, **5**) with bromomethylacetate provides the acetoxymethylester (AM ester) of **5** in 58% yield. Removal of the *N*-Boc protecting group with trifluoroacetic acid (TFA), followed immediately by peptide bond formation with carboxy-RhoVR (**1**) mediated by HATU produces SPIRIT RhoVR 1 (**2**) in 10% yield. A control compound, SPIRIT RhoVR 0 (**4**) is synthesized via a similar route from RhoVR 0 carboxylate **3** (**Scheme S4**). RhoVR 0 derivatives lack the aniline group required for voltage sensitivity. RhoVR 0, like RhoVR 1, localizes to the plasma membrane but is not voltage-sensitive.[19] SPIRIT RhoVR 0 provides an important negative control for characterization of mitochondrial voltage responses in cells.

2.2 Spectroscopic characterization of RhoVRs

The new SPIRIT RhoVR derivatives possess emission and excitation profiles nearly identical to the parent RhoVR compounds (**Figure 2.2.1**, **Table 2.2.1**).

Table 2.2.1. Spectroscopic Properties of RhoVR Derivatives.

Dye	Rhod Abs λ_{max} (nm)[a]	Rhod Emission λ_{max} (nm)[a]	Wire Abs λ_{max} (nm)[a]	Φ_{fl}[a]	$\varepsilon_{557\ nm}$ (M^{-1} cm^{-1})[a]

RhoVR 1	557	579	417	0.037	8.5×10^4
RhoVR 0	557	574	364	0.16	5.8×10^4
SPIRIT RhoVR 1	558	580	418	0.011	7.8×10^4
SPIRIT RhoVR 0	557	578	362	0.14	1.2×10^5

[a] Determined in EtOH.

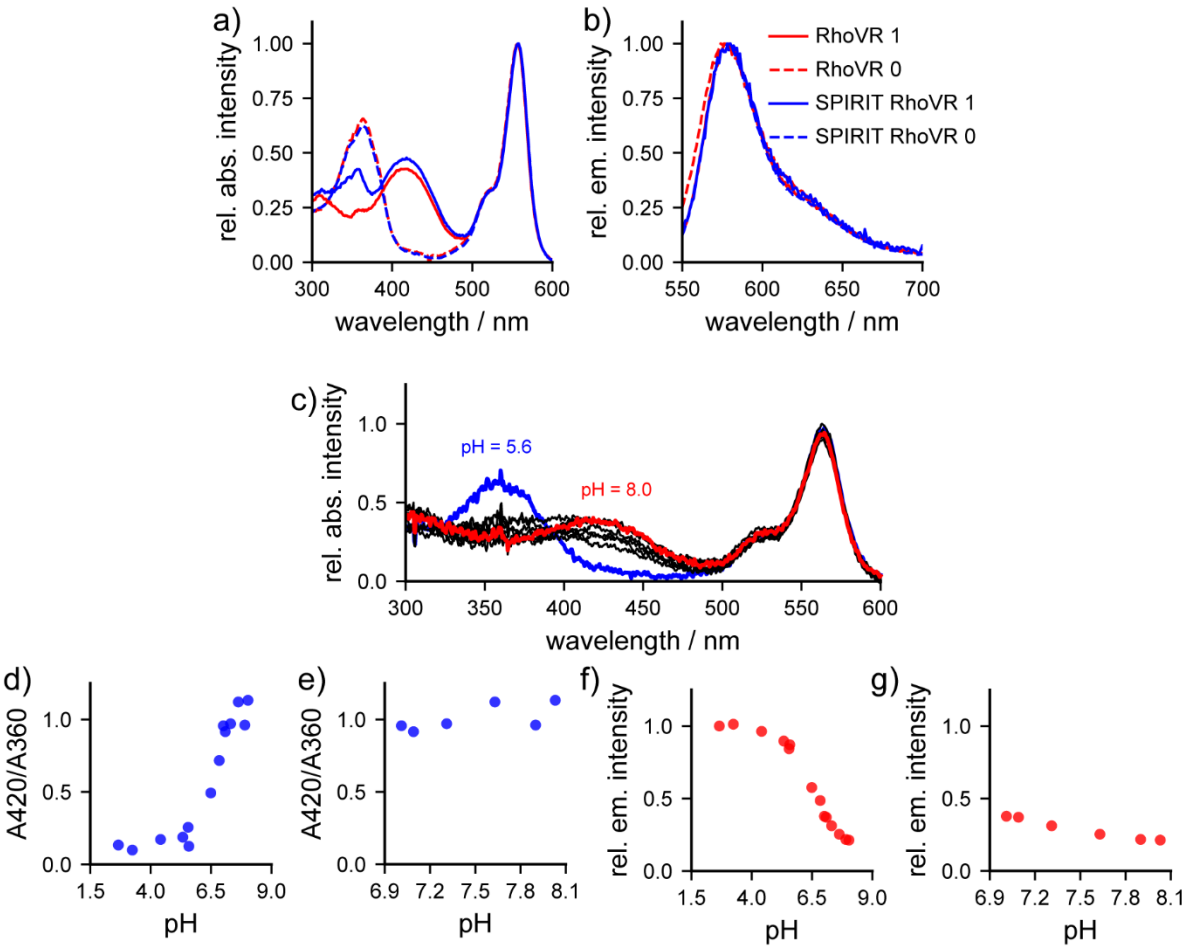

Figure 2.2.1 Spectroscopic Characterization of SPIRIT RhoVR 1 and SPIRIT RhoVR 2.

Plots of **a)** relative absorbance intensity and **b)** relative emission intensity vs wavelength for RhoVR 1 (solid red line), RhoVR 0 (dashed red line), SPIRIT RhoVR 1 (solid blue line), and SPIRIT RhoVR 0 (dashed blue line). All spectra were acquired in EtOH at a concentration of 500 nM. For emission scans, excitation was provided at 525 nm and emission was collected from 500 nm to 700 nm.

c) Plot of RhoVR 1 (500nM) absorbance intensity vs. wavelength at pH values of 5.6, 6.5, 6.8, 7.0, 7.10, 7.3, 7.6, 7.9, and 8.0. The spectrum in blue was acquired at pH = 5.6; the spectrum in red was acquired at pH = 8.0; intermediate pH values are in black.

Plot of **d)** the ratio of RhoVR 1 absorbance at 420 nm to absorbance at 360 nm (A420/A360) vs pH. **e)** A zoomed-in view of A420/A360 from pH 6.8 to 8.0. Plots of **f)** relative emission intensity of RhoVR 1 (excitation provided at 525 nm, emission integrated from 550 nm to 700 nm) vs pH. **g)** A zoomed-in view of relative emission intensity vs. pH for RhoVR 1 from pH 6.8 to 8.0.

Because the major contributor to mitochondrial membrane potential is protons, we characterized the pH sensitivity of RhoVR1, the parent dye which is unmasked in mitochondria to allow for voltage sensing. We measured the pKa of RhoVR1 using both fluorescence and absorbance. To measure the pKa via fluorescence, we made the following assumptions:

1. RhoVR1 exists in an equilibrium of states with two different quantum yields; a state where the aniline is protonated with Φ_a and a state where the aniline is deprotonated with Φ_b
2. These two states only differ in their quantum yields
3. No other spectroscopically relevant states exist; although the carboxylic acid on the sarcosine can protonate/deprotonate, this is assumed to be irrelevant to pKa calculations
4. At pH 2.66, RhoVR1 with deprotonated aniline exists in negligible concentrations and at pH 8.03, RhoVR1 with protonated aniline exists in negligible concentrations

The Hendersson-Hasselbach equation gives that:

$$pH = pKa + \log\left(\frac{[base]}{[acid]}\right)$$

Furthermore, the measured fluorescence will be proportional to the concentration of the fluorescent species via the following relationship:

$$F = \epsilon_{fl} * l * \Phi * c$$

Where F represents the total fluorescence, ϵ_{fl} is the emissivity coefficient, l is the path length, Φ is the quantum yield of fluorescence, and c is the concentration of the

fluorescent species. Writing this according to the above assupmtions with two fluorescent species in solution this becomes:

$$F = \epsilon_{fl} * l * (\Phi_a * c_a + \Phi_b * c_b)$$

Where the subscripts a and b denote the contributions from the acidic and basic species, respectively. Thus Φ_a represents the quantum yield of RhoVR1 with a protonated aniline, c_a represents the concentration of the protonated species, and Φ_b and c_b model RhoVR1 with a deprotonated aniline.

Normalizing the fluorescence to its value at the most acidic pH measured allows us to see what the fluorescence of a given pH is relative to the fully protonated state and will normalize for other factors such as the quantum yield of the detector. This gives us an equation for normalized fluorescence of:

$$F_{norm} = \frac{\epsilon_{fl} * l * (\Phi_a * c_a + \Phi_b * c_b)}{\epsilon_{fl} * l * \Phi_a * c_{tot}}$$

Where F_{norm} is the normalized fluorescence and c_{tot} is the total concentration of RhoVR1. Rearranging this equation and recognizing that $c_{tot} = c_a + c_b$ gives the relationship:

$$F_{norm} = \frac{\frac{\Phi_b}{\Phi_a} * \frac{c_b}{c_a} + 1}{\frac{c_b}{c_a} + 1}$$

For convenience, denote $\frac{\Phi_b}{\Phi_a}$ as Φ_{corr} and $\frac{c_b}{c_a}$ as R. R also represents the $\frac{[base]}{[acid]}$ ratio that is present in the Hendersson-Hasselback equation. Rearranged to solve for R gives:

$$R = \frac{1 - F_{norm}}{F_{norm} - \Phi_{corr}}$$

R is the quantity needed to fit to the Hendersson-Hasselbach equation. F_{norm} is the normalized fluorescence measured in the experiment (normalized to the estimated maximum fluorescence at acidic pH). Φ_{corr} represents the ratio of the quantum yield with a fully deprotonated aniline to the quantum yield with a fully protonated aniline and is thus approximated by dividing the fluorescence at the most basic pH by the fluorescence at the most acidic pH

This relationship along with the measured F_{norm} values at a variety of pHs and the approximated Φ_{corr} allows the calclulation of R at each pH from the data. The Hendersson-Hasselbach equation then becomes:

$$pH = pKa + \log(R)$$

Taking the log(R) and fitting linearly to find the y-intercept gives **pKa = 6.2** for the aniline on RhoVR1 using this method.

To measure the pKa of RhoVR1 via absorption, we made the following assumptions:

1. The absorbance at 360 nm is due primarily to the absorbance of the wire with a protonated aniline
2. The absorbance at 420 nm is due primarily to the absorbance of the wire with a deprotonated aniline
3. At pH 2.66, RhoVR1 with deprotonated aniline exists in negligible concentrations and at pH 8.03, RhoVR1 with protonated aniline exists in negligible concentrations

The Hendersson-Hasselbach equation gives that:

$$pH = pKa + \log\left(\frac{[base]}{[acid]}\right)$$

And Beer's law gives that:

$$A_\lambda = \epsilon_\lambda * c * l$$

Where A_λ is the absorbance at wavelength λ, ϵ_λ is the molar absorptivity coefficient at wavelength λ, c is the concentration of the species responsible for the absorbance, and l is the path length.

Per assumptions 1 and 2, this gives:

$$A_{420} = \epsilon_{420} * c_b * l$$

And

$$A_{360} = \epsilon_{360} * c_a * l$$

Where c_b and c_a represent the concentrations of the deprotonated and protonated species, respectively. Thus,

$$\frac{A_{420}}{A_{360}} = \frac{\epsilon_{420} * c_b * l}{\epsilon_{360} * c_a * l}$$

Rearranging gives:

$$\frac{A_{420} * \epsilon_{360}}{A_{360} * \epsilon_{420}} = \frac{c_b}{c_a}$$

Where A_{420} represents the absorbance of the molecule at 420 nm at a given pH minus the minimum absorbance at 420 observed at acidic pH to account for background signal. Similarly, A_{360} represents the absorbance of the molecule at 360 nm at a given pH minus the minimum absorbance at 360 observed at basic pH to account for background signal.

The ratio $\frac{\epsilon_{360}}{\epsilon_{420}}$ is approximated using assumption #3 and dividing the background subtracted absorbance at 360 nm by the background subtracted absorbance at 420 nm to calculate the ratio of the molar absorptivities of the two different species at two different wavelengths.

These parameters can then be used to calculate $\frac{c_b}{c_a}$ at a given pH which represents the term inside the logarithm in the Hendersson-Hasselbach equation. Plotting pH vs. the log and fitting to a line gives an intercept at **pKa = 6.2** which is consistent with the pKa derived from fluorescence measurements.

2.3 Cellular localization of RhoVR esters

Both SPIRIT RhoVR 1 and RhoVR-tBu localize to mitochondria.

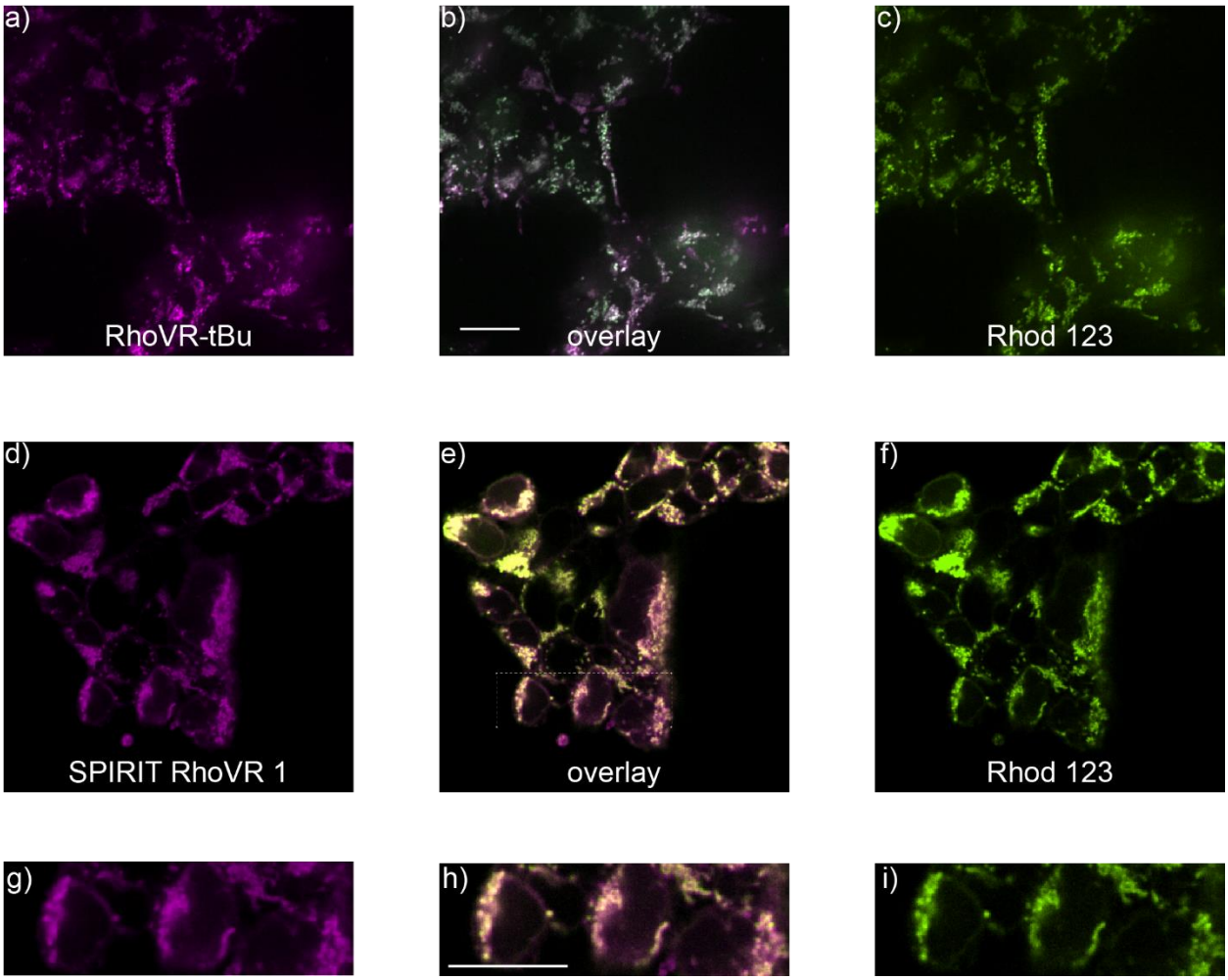

Figure 2.3.1 SPIRIT RhoVR 1 localizes to mitochondria in mammalian cells. Confocal fluorescence microscopy images of HEK cells stained with either **a)** RhoVR-tBu (250 nM) or **d)** SPIRIT RhoVR 1 (250 nM) and rhodamine 123 (250 nM, **c** and **f**). Overlay image of rhodamine 123 and either **b)** RhoVR-tBu or **e)** SPIRIT RhoVR 1. **g-i**) Expanded view of the boxed region in panel (**e**). Scale bar is 20 μm (**a-f**)

Confocal imaging of HEK 293T cells stained with SPIRIT RhoVR 1 (**Figure 2.3.1a-c**) or RhoVR-tBu (**Figure 2.3.1d-f**) display punctate, intracellular staining that co-localizes with mitochondria-targeted rhodamine 123 and possess near-unity Pearson correlation (**Figure 2.3.2a**).

In contrast, RhoVR 1, which senses plasma membrane potential, does not co-localize with rhodamine 123 (**Figure 2.3.2 b-d**) and has a low Pearson correlation coefficient of 0.28 ± 0.04 (**Figure 2.3.2a**). SPIRIT RhoVR 1 and 0 localization in mitochondria is generalizable across a range of cell lines (**Figure 2.3.2e** and **f**).

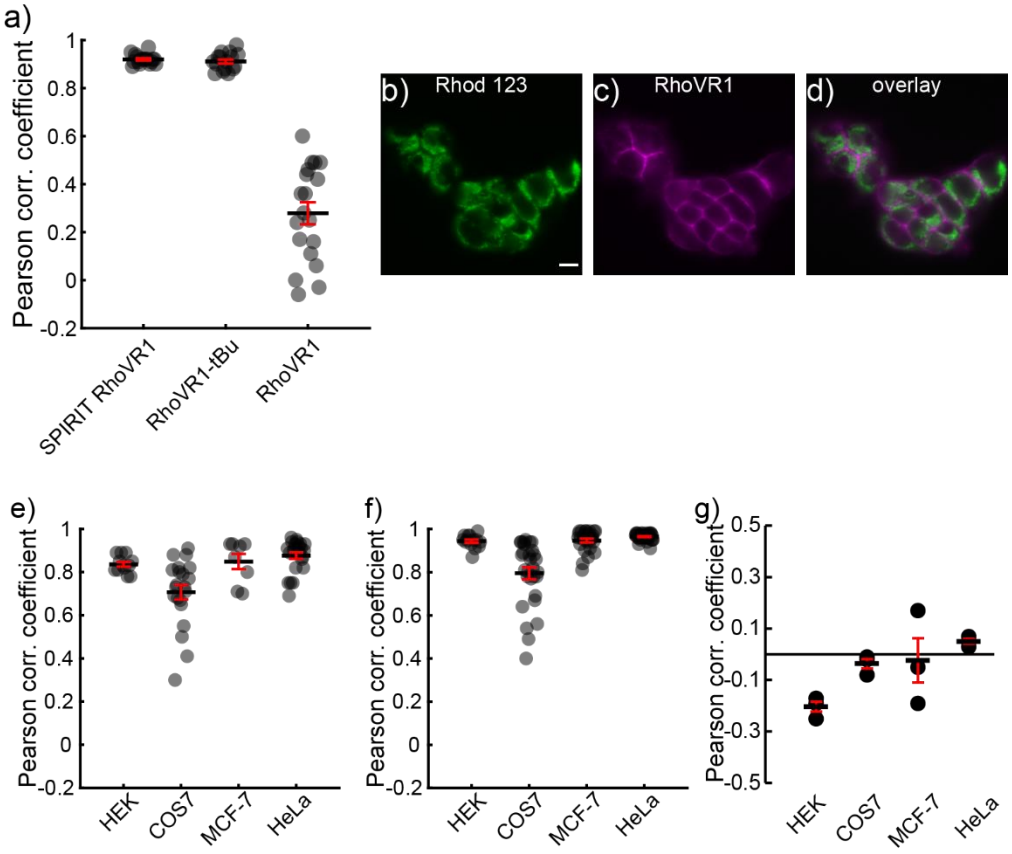

Figure 2.3.2 Localization of rhodamine esters and RhoVR derivatives in cells. **a)** Quantification of Pearson correlation coefficient between rhodamine 123 and the indicated RhoVR derivative. Data are mean ± S.E.M. Each data point represents the Pearson coefficient calculated for a cluster of 1 to 4 cells. Widefield fluorescence microscopy of HEK293T cells stained with both **b)** Rhodamine 123 (250 nM) and **c)** RhoVR1 (250 nM). **d)** Merged image shows rhodamine 123 (green) and RhoVR 1 (magenta) signals in the same cell and lack of colocalization. Scale bar is 10 μm. Plots of Pearson correlation coefficient between rhodamine 123 and either **e)** SPIRIT RhoVR 1 or **f)** SPIRIT RhoVR 0 in HEK, COS7, MCF-7, and HeLa cell lines. Each data point represents the Pearson correlation coefficient for a cluster of 1 to 4 cells. Data are mean ± S.E.M. **g)** Negative controls of colocalization of SPIRIT RhoVR1 acroos cell lines. Controls were generated by rotating the images from one channel of the colocalization images from **e)** and measuring the Pearson's correlation coefficient between the rotated and non-rotated channel. Each data point represents the Pearson's correlation coefficient for a 1028 × 1028 pixel region of an image. Data are mean ± S.E.M.

Although negative controls are reported above and are often reported in literature for colocalization by rotating and image 90 degrees and performing colocalization analysis, this method does not provide a physiologically relevant control. Rather, what this method establishes is that two unrelated images will not produce the same values when colocalization is quantified, and thus serves merely as a control to validate the quantification method itself. A much better control for colocalization is to costain with markers for cellular locations in which little to no dye staining should be observed and compare the quantification obtained of colocalization with these locations to the quantification obtained from the desired location. To this end, we costained HEK 293T cells with SPIRIT RhoVR1 and LysoTracker green and demonstrated that SPIRIT RhoVR 1 shows very little colocalization with lysosomes (**Figure 2.3.3**).

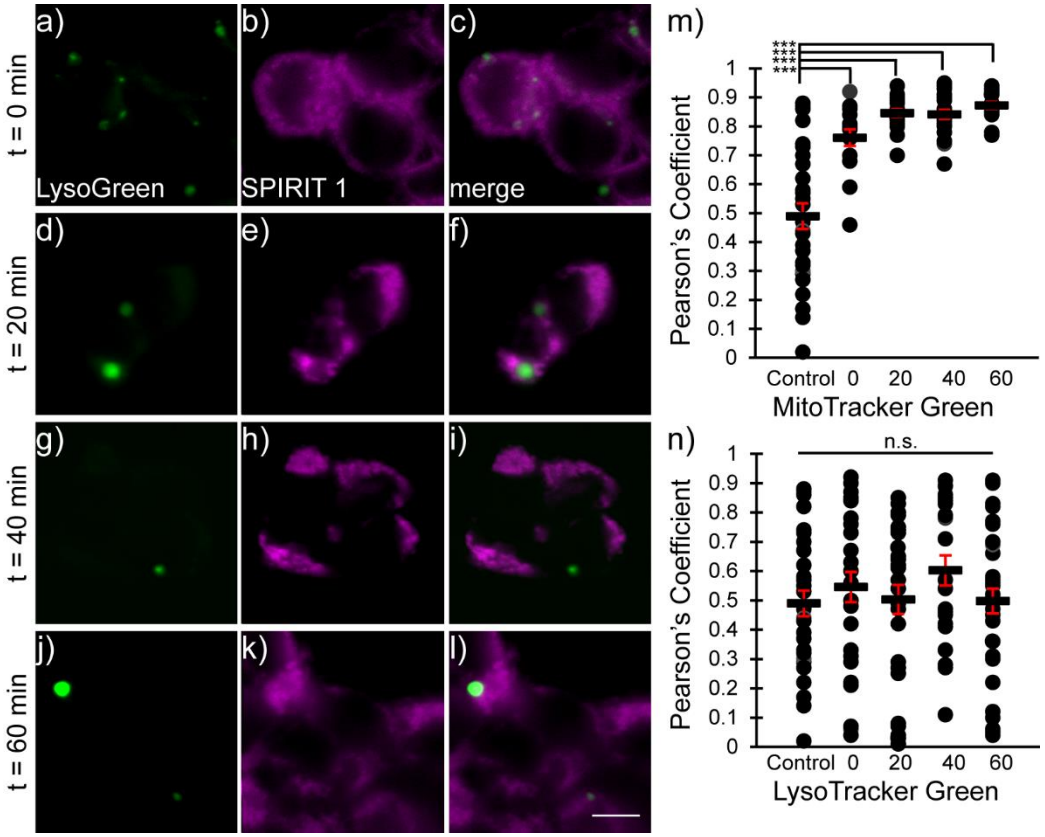

Figure 2.3.3 SPIRIT RhoVR1 does not colocalize with LysoTracker Green.

a-l) Widefield fluorescence microscopy of SPIRIT RhoVR 1 co-stained with LysoTracker Green and incubated in media for 0 **(a-c)**, 20 **(d-f)**, 40 **(g-i)**, or 60 **(j-l)** minutes. Left hand column is LysoTracker Green signal, middle is SPIRIT RhoVR1 signal, and right is an overlay. Scale bar is 10 µm.

Plots of Pearson's Correlation Coefficient for **m)** SPIRIT RhoVR 1 (150 nM) and MitoTracker Green or **n)** SPRIT RhoVR 1 (150 nM) and LysoTracker Green (75 nM) after 0, 20, 40, and 60 minutes of incubation in media after dye loading compared to a control co-stain of MitoTracker Red (100 nM) and LysoTracker Green (75 nM). Data represented as mean ± Standard Error of the Mean. Each data point is the correlation coefficient determined for a group of 2-4 cells for MitoTracker costains and regions approximately 5-15 µm in diameter surrounding lysosomes for LysoTracker images; *** denotes $p<0.001$ and n.s. denotes $p>0.05$ (t-test, two-tailed)

Unlike traditional rhodamine esters, SPIRIT RhoVR 1 remains localized to mitochondria following depolarization. Mitochondrial depolarization causes accumulation-based dyes like rhodamine 123 to diffuse out of mitochondria,[20] whereas SPIRIT RhoVR1 should be retained in mitochondria, since loss of AM ester reveals a charged carboxylate which prevents RhoVR-type molecules from crossing cellular membranes (**Scheme 2.0.1**).[17] In contrast, intact esters of RhoVR-type molecules should accumulate in hyperpolarized mitochondria and diffuse out of depolarized mitochondria. We loaded HEK 293T cells with rhodamine esters rhodamine 123, RhoVR-tBu, and SPIRIT RhoVR 1 and induced mitochondrial membrane depolarization (**Figure 2.3.4**) with antimycin A[21] (**Figure 2.3.5**).

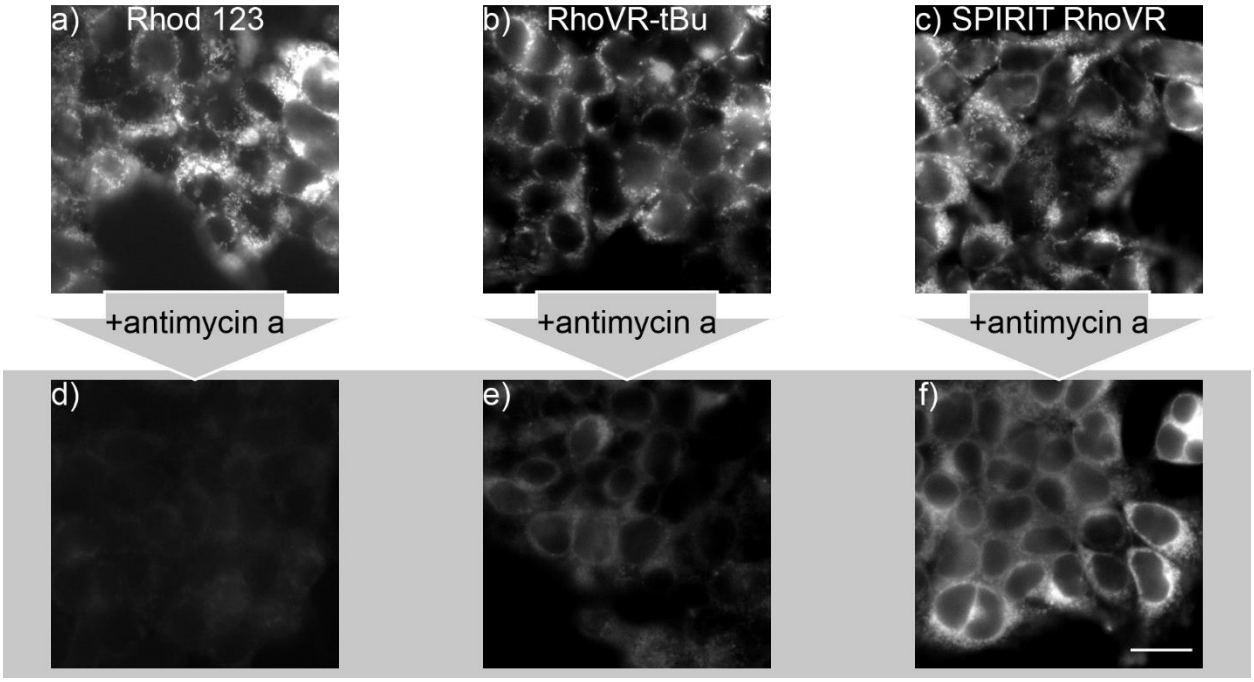

Figure 2.3.4 SPIRIT RhoVR1 is retained in mitochondria after dissipation of $\Delta\Psi_m$ with antimycin A. Widefield fluorescence microscopy of rhodamine or RhoVR derivative (250 nM) in the **a-c)** absence or **d-f)** presence of antimycin A (5 µg/mL). Widefield fluorescence microscopy of SPIRIT RhoVR1 in the **c)** absence or **d)** presence of 5 µg/mL antimycin A for 90 min. Scale bar is 20 µm.

Antimycin A inhibits complex III, preventing electron transfer into cytochrome c and abolishing H^+ transfer from the matrix to the inner membrane space, resulting in a loss of $\Delta\Psi_m$.

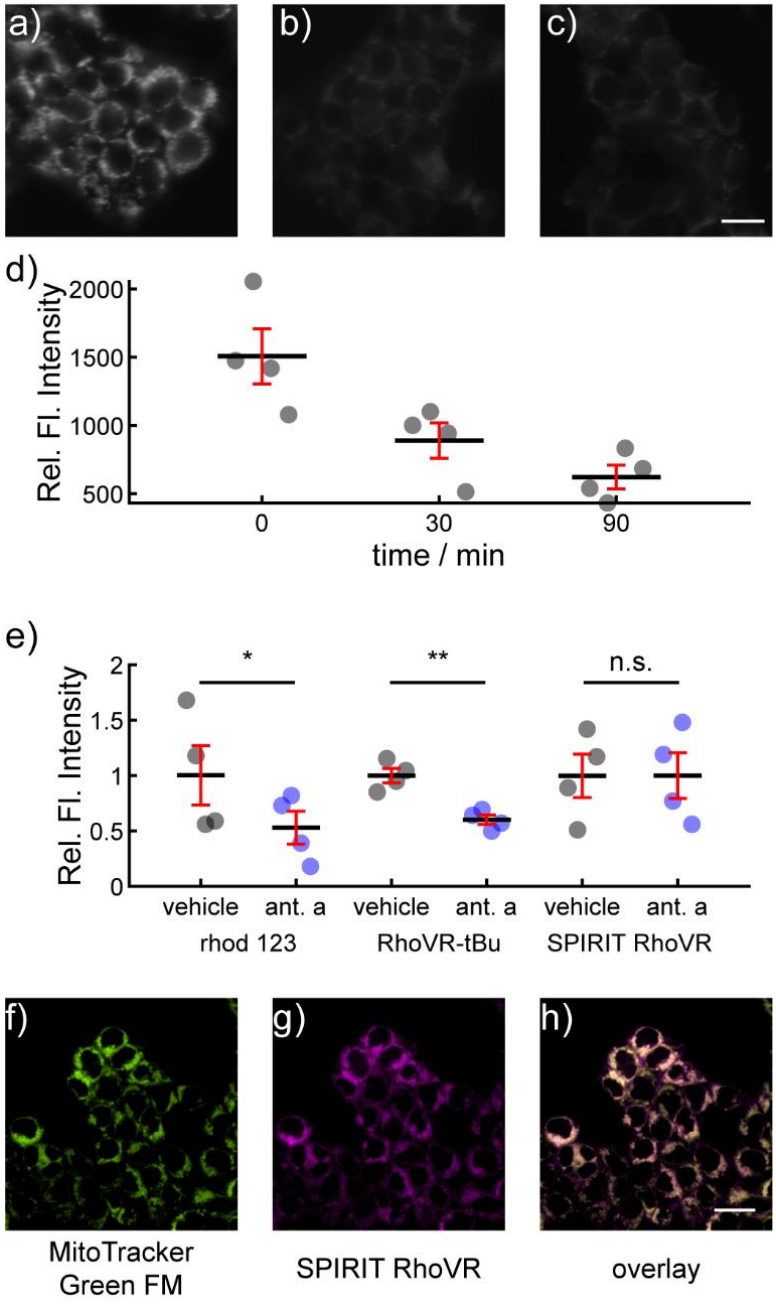

Figure 2.3.5 Antimycin A treatment alters distribution of rhodamine esters, but not SPIRIT RhoVR. **a-c)** Widefield fluorescence microscopy images of HEK 293T cells stained with rhodamine 123 (100 nM) and then treated with antimycin A (5 µg/mL) for **a)** 0 min, **b)** 30

min, or **c)** 90 min. The histogram display limits of the images are identical to allow for direct comparison. Scale bar is 20 μm. **d)** Quantification of fluorescence intensity vs time of antimycin A treatment, from panels **a-c**. Data are mean ± S.E.M. Each data point represents a region of interest containing (20-40 cells).

e) Quantification of data from **Figure 2.3.4**. Plot of fluorescence intensity of HEK293T cells loaded with rhodamine 123, SPIRIT RhoVR 1, or RhoVR-tBu (250 nM, all dyes) and then treated with antimycin A (5 μg/mL, 90 min) for the indicated time. Data are mean ± S.E.M. Each data point represents the average fluorescence intensity from an independent experimental determination (20 to 40 cells per experiment). * denotes p = 0.04; ** denotes p = 0.02; n.s. denotes p > 0.95; t-test, two-tailed.

SPIRIT RhoVR retains mitochondrial localization after antimycin A poisoning. Confocal fluorescence images of HEK293T cells stained with **f)** MitoTracker Green FM (100 nM) and **g)** SPIRIT RhoVR (250 nM) and then poisoned with antimycin A (5 μg/mL, 90 min). MitoTracker Green contains chloromethyl groups which react with nucleophiles in mitochondria allowing it to be retained during depolarizations The **h)** overlay between the two signals indicates retention of SPIRIT RhoVR in mitochondria. Scale bar is 20 μM.

Rhodamine 123 and RhoVR-tBu exhibit significant (p = 0.04 and 0.02, **Figure 2.3.5e**) washout from mitochondria and dilution into the dye-free external solution upon antimycin A treatment (**Figure 2.3.4a/d** and **b/e**), displaying fluorescence approximately 50% and 60% as bright as cells treated with vehicle (**Figure 2.3.5e**). By comparison, SPIRIT RhoVR 1 fluorescence is retained (**Figure 2.3.4c/f**) at levels nearly identical to vehicle controls (**Figure 2.3.5e**). SPIRIT RhoVR 1 remains localized to mitochondria, even after antimycin A-induced depolarization (**Figure 2.3.5f-h**).

2.4 Voltage sensitivity of SPIRIT RhoVR1 in the inner mitochondrial membrane

SPIRIT RhoVR 1 tracks depolarizations and hyperpolarizations in $\Delta\Psi_m$ with high fidelity. HEK 293T cells loaded with SPIRIT RhoVR 1 and treated with the protonophore carbonyl cyanide 4-(trifluoromethoxy)phenylhydrazone[22] (FCCP, 500 nM) to collapse the $\Delta\Psi_m$ show a decrease in fluorescence (**Figure 2.4.2a, red**), consistent with a depolarization of the inner mitochondrial membrane, which results in an increased rate of PeT, and subsequent decrease in fluorescence intensity (**Scheme 2.0.1**). Fluorescence intensity is restored to baseline levels upon washout of FCCP (**Figure 2.4.2a, c-e**). Cells loaded with SPIRIT RhoVR 1 and treated identically, but with a vehicle control (EtOH), show no change in fluorescence intensity (**Figure 2.4.2a, blue**). Identical experiments using cells loaded with SPIRIT RhoVR 0 (which lacks an aniline and is therefore not voltage-sensitive via a PeT-based mechanism)[17] show no change in fluorescence (**Figure 2.4.2b**),

consistent with a PeT mechanism of voltage sensing. The slow decay of fluorescence, even in vehicle controls, is likely due to a combination of photobleaching and slow leakage of unhydrolyzed SPIRIT RhoVR. TMRM a traditional, accumulation-based $\Delta\Psi_m$ indicator, cannot report on reversible changes under these conditions (**Figure 2.4.1**).

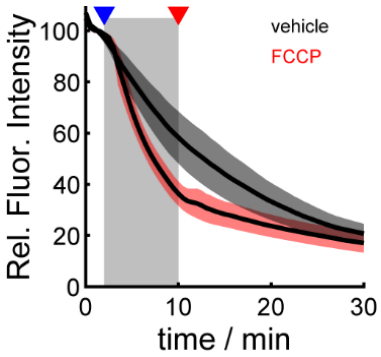

Figure 2.4.1 TMRM does not respond reversibly to mitochondrial membrane potential fluctuations. Plot of fluorescence intensity vs. time for HEK cells stained with tetramethylrhodamine methyl ester (TMRM, 20 nM). At 2 minutes into the experiment (beginning of grey box, blue arrowhead) cells were perfused with either vehicle (ethanol, grey) or FCCP (500 nM, red). At 10 minutes (end of grey box, red arrowhead) cells were perfused with HBSS to washout FCCP. Data are mean (black line) ± S.E.M. (shading) for 3 separate experiments.

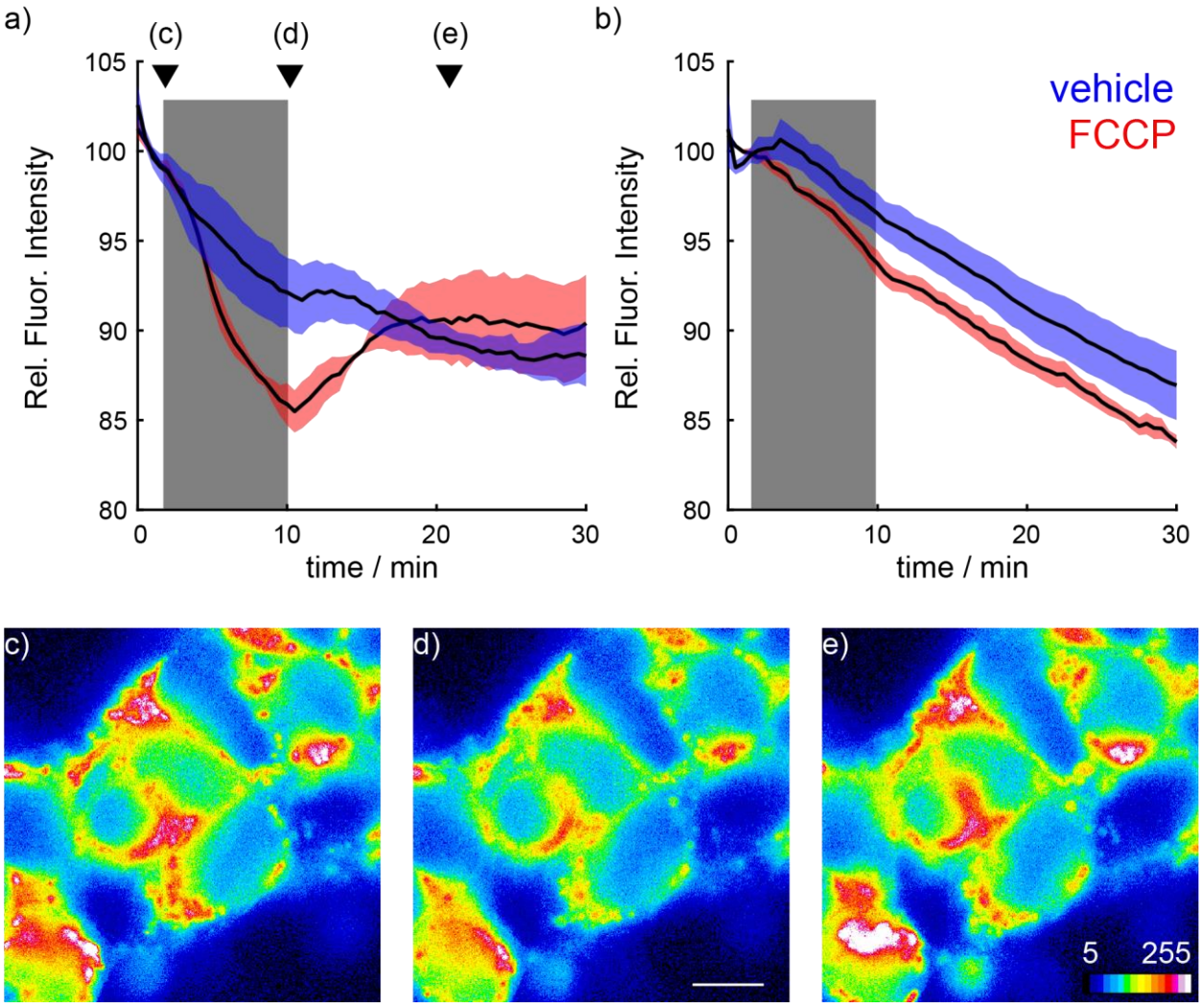

Figure 2.4.2. SPIRIT RhoVR 1 reports on $\Delta\Psi_m$ dynamics in HEK cells. Plot of fluorescence intensity vs. time for HEK cells stained with **a)** SPIRIT RhoVR 1 (150 nM) or **b)** SPIRIT RhoVR 0(150 nM). At 2 minutes into the experiment (beginning of grey box) cells were perfused with either vehicle (ethanol, blue) or FCCP (500 nM, red). At 10 minutes (end of grey box) cells were perfused with HBSS. Data are mean (black line) ± S.E.M. (colored shading) for 3 separate experiments. Representative pseudocolor images of SPIRIT RhoVR 1-loaded HEK cells **c)** before, **d)** during, and **e)** after treatment with FCCP (500 nM). Scale bar is 10 µm for all images. Arrowheads in panel (a) indicate the timepoints of the representative images in panels c-e.

Higher concentrations of FCCP (>500 nM) should not be used. Although concentrations of FCCP of up to 50 µM are often used to induce mitochondrial depolarizations, the micromolar levels of FCCP reported in the literature[14, 23] may cause artifacts in dyes that should not have a voltage response (**Figure 2.4.3**). Fluorescence measurements of mitochondrial membrane potential obtained using micromolar concentrations of FCCP in

conjunction with tetramethylrhodamine-based dyes in particular should be viewed with skepticism.

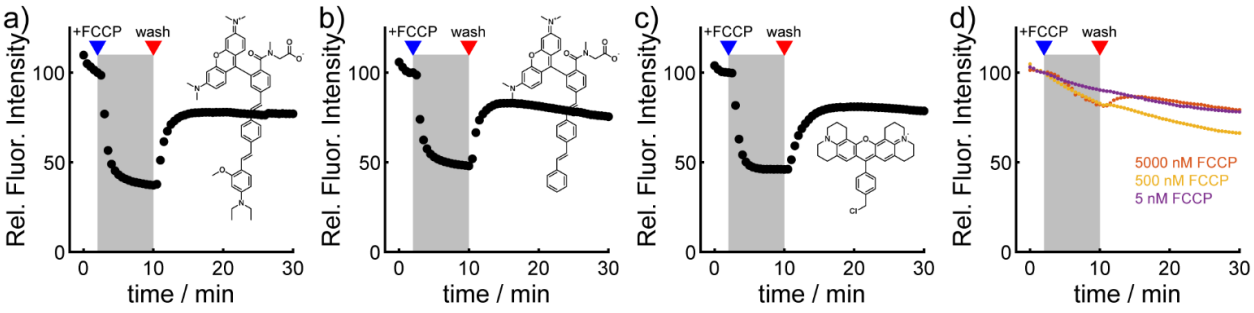

Figure 2.4.3 High concentrations of FCCP cause experimental artifacts. Plots of fluorescence intensity vs. time in HEK293T cells stained with **a)** RhoVR1 (500 nM), **b)** RhoVR0 (500 nM), or **c)** Mitotracker Red (100 nM) and treated with 50 µM FCCP perfused on at 2 minutes (blue arrow) and HBSS with vehicle perfused on at 10 minutes (red arrow). Images taken every 30 seconds. Although doses ranging from 5 to 50 µM FCCP are commonly reported in the literature,[2-3] we found that treatment with 50 µM FCCP results in large fluorescence decreases in cells loaded with RhoVR 1 (panel **a**). The fluorescence decrease of RhoVR 1 in response to membrane depolarization induced by FCCP[4] is the opposite of the fluorescence brightening that occurs in plasma membrane-localized RhoVR 1 during depolarization,[1] suggesting an artifact at this high concentration of FCCP. Furthermore, the voltage insensitive RhoVR 0 (panel **b**), which stains the plasma membrane,[5] shows a similar fluorescence decrease when treated with 50 µM FCCP. Finally, even MitoTracker Red, whose fluorescence remains localized within mitochondria even after cellular fixation, on account of reactive chloromethyl groups, shows a fluorescence decrease in response to 50 µM FCCP (panel **c**).

d) Plot of fluorescence intensity vs. time in HEK 293T cells stained with RhoVR-0 (500 nM) and treated with various concentrations of FCCP at 2 minutes, followed by washout at 10 minutes. Sub-micromolar doses of FCCP were required to avoid experimental artifacts. By titrating down the concentration of FCCP in cells loaded with voltage insensitive RhoVR 0, concentrations of up to 500 nM FCCP does not produces a fluorescence decrease artifact, confirming that 500 nM FCCP is an appropriate dosage to use in our cellular studies with SPIRIT RhoVR 1. Together, these data suggest that care should be taken when interpreting fluorescence signals obtained from mitochondrial dyes when used in conjunction with micromolar concentrations of FCCP.

In addition to HEK 293T cells, SPIRIT RhoVR 1 can track reversible changes in $\Delta\Psi_m$ across several common cell lines. These include COS7, commonly used in organelle imaging experiments due to their relatively large subcellular compartments including mitochondria; MCF-7, a common breast cancer model cell line; and HeLa, which is used frequently as a generic human cell line in many experiments. (**Figure 2.4.4**)

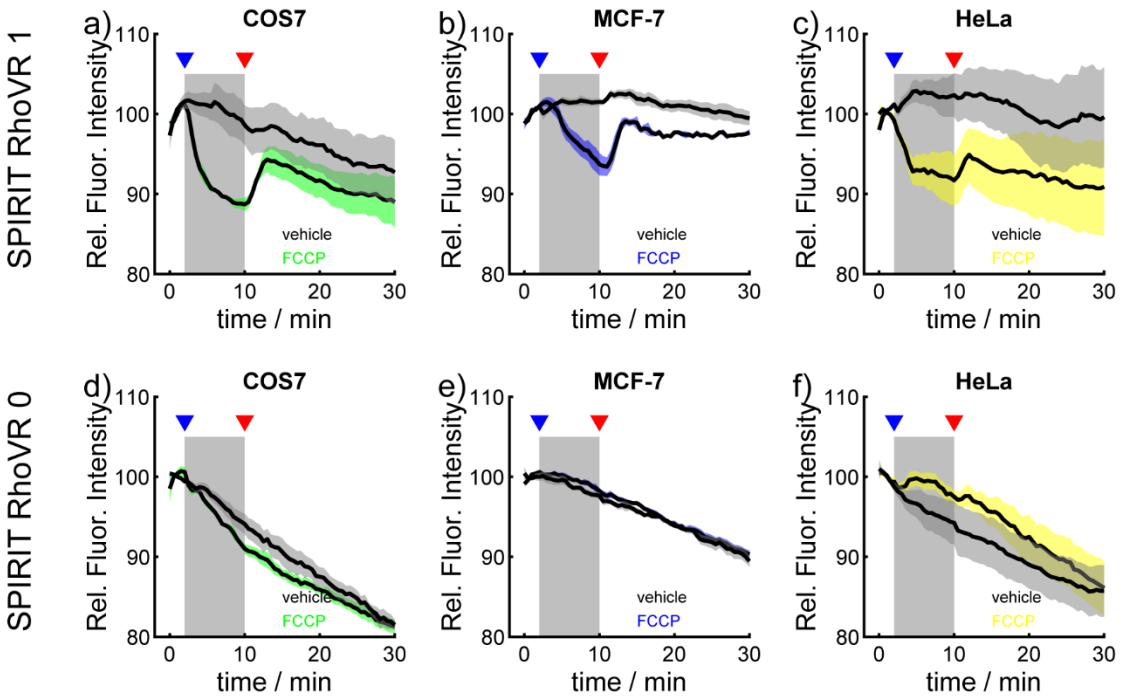

Figure 2.4.4 SPIRIT RhoVR 1 monitors reversable mitochondrial membrane potential dynamics across many cell lines.

Plots of fluorescence intensity of SPIRIT RhoVR 1 vs. time for **a)** COS7, **b)** MCF-7, or **c)** HeLa cells stained with 150 nM SPIRIT RhoVR 1 and then treated with FCCP. At 2 minutes into the experiment (beginning of grey box, blue arrowhead) cells were perfused with either vehicle (ethanol, grey) or FCCP (500 nM, colored). At 10 minutes (end of grey box, red arrowhead) cells were perfused with HBSS. Data are mean (black line) ± S.E.M. (colored shading) for 3 separate experiments.

Plot of fluorescence intensity of SPIRIT RhoVR 0 vs. time for **d)** COS7, **e)** MCF-7, or **f)** HeLa cells stained with 150 nM SPIRIT RhoVR 1 and then treated with FCCP. At 2 minutes into the experiment (beginning of grey box, blue arrowhead) cells were perfused with either vehicle (ethanol, grey) or FCCP (500 nM, colored). At 10 minutes (end of grey box, red arrowhead) cells were perfused with HBSS. Data are mean (black line) ± S.E.M. (colored shading) for 3 separate experiments.

2.5 Multicolor imaging of mitochondrial membrane potential and other parameters

SPIRIT RhoVR 1 responds reversibly to changes in $\Delta\Psi_m$, allowing the real-time observation of voltage dynamics without the need for an extracellular pool of indicators and can be used to detect $\Delta\Psi_m$ changes induced by nanomolar concentrations of FCCP. Because of its robust response to $\Delta\Psi_m$ dynamics, we thought that SPIRIT RhoVR 1 could be an important component of methods to monitor multiple cellular physiological parameters simultaneously. We stained HEK 293T cells with Oregon Green BAPTA (OGB, to monitor intracellular Ca^{2+}),[24] BeRST 1, a far-red plasma V_{mem} indicator,[25] and SPIRIT RhoVR 1 individually to verify that no more than 10% of their fluorescence bled through into the other channels (**Figure 2.5.1**) after which we costained HEK 293T cells with all three indicators to perform multicolor imaging experiments for simultaneous measurement of intracellular Ca^{2+}, plasma membrane potential, and mitochondrial inner membrane potential.

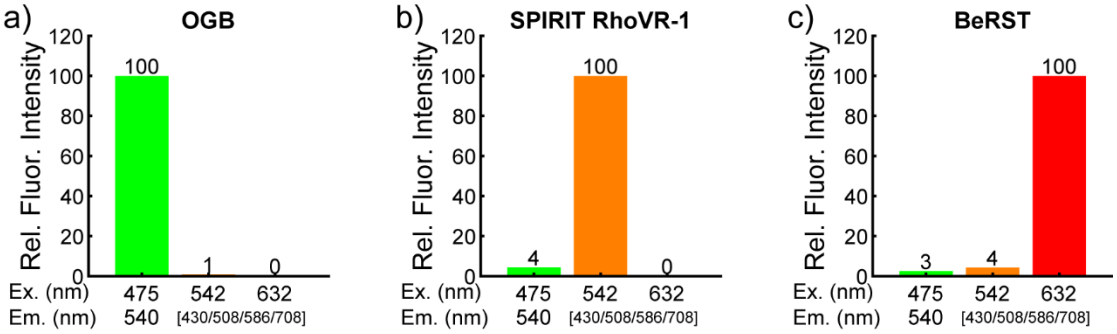

Figure 2.5.1 Crosstalk between channels for multicolor imaging experiment. Normalized fluorescence intensity of HEK cells stained with either **a)** Oregon Green BAPTA AM (OGB, 500 nM), **b)** SPIRIT RhoVR-1 (150 nM), or **c)** BeRST (50 nM) vs. LED excitation light (Ex.) and emission filter (Em.) combination.

Cells loaded with these three indicators show clear cytosolic fluorescence in the OGB channel (**Figure 2.5.2a**), mitochondrial-localized tetramethyl rhodamine fluorescence from SPIRIT RhoVR 1 (**Figure 2.5.2b**), and plasma membrane-localized fluorescence in the far-red channel from BeRST 1 (**Figure 2.5.2c**). Importantly, we are able to isolate the excitation and emission spectrum of each indicator, minimizing excitation and emission cross-talk (**Figure S8**) to allow real-time, three-color imaging (**Figure 2.5.2d**).

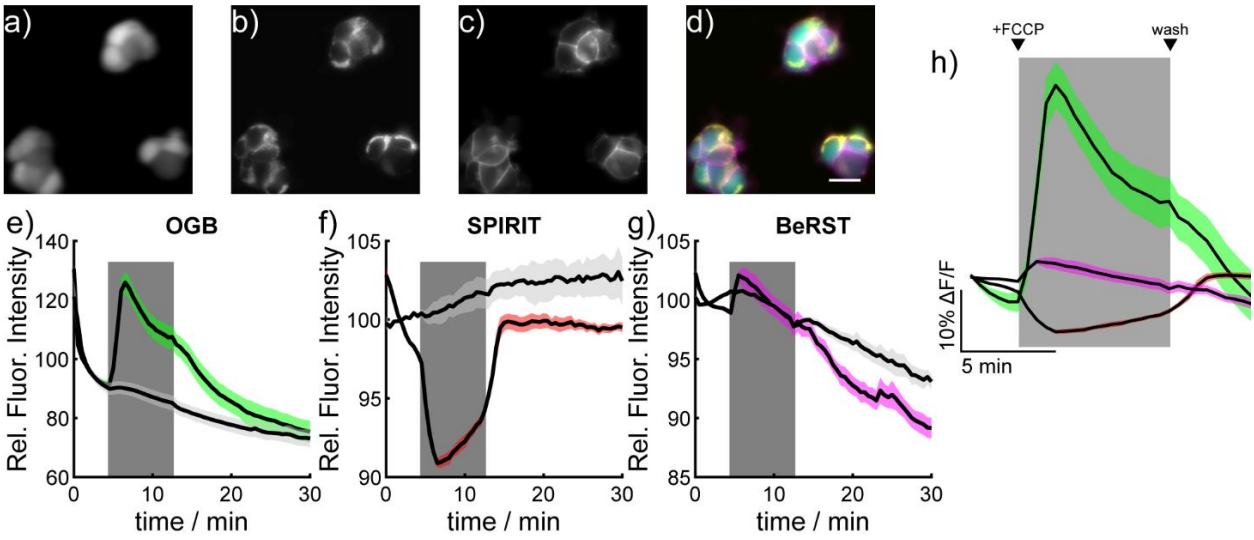

Figure 2.5.2 Simultaneous, multicolor imaging of mitochondrial membrane potential, cytosolic Ca^{2+}, and plasma membrane potential in mammalian cells. Widefield epifluorescence image of HEK cells stained with **a)** Oregon Green BAPTA-AM (OGB, 500 nM), **b)** SPIRIT RhoVR 1 (SPIRIT, 150 nM), **c)** and BeRST 1 (50 nM). **d)** An overlay of the images cytosolic localization of OGB (green), mitochondrial localization of SPIRIT RhoVR 1 (yellow), and plasma membrane localization of BeRST (magenta). Scale bar is 20 μm. Plots of fluorescence vs. time from HEK cells stained with **e)** OGB, **f)** SPIRIT RhoVR 1, or **g)** BeRST. At 4 minutes into the experiment (beginning of grey box) cells were perfused with either vehicle (ethanol, light grey) or FCCP (500 nM, colored trace). At 4 minutes (end of grey box) cells were recovered by perfusion with HBSS. Data are mean (black line) ± S.E.M. (colored shading) for 3 separate experiments. h) Shows a zoomed-in plot of the response of OGB (green), SPIRIT RhoVR 1 (red), and BeRST 1 (magenta). The grey box indicates the start and end of FCCP perfusion.

FCCP perfusion of cells with the three indicators gives an increase in OGB fluorescence with a peak change of nearly 30% over baseline, followed by a decay to steady-state levels of ~20% before returning to baseline upon removal of FCCP (**Figure 2.5.2e**), consistent with reports of Ca^{2+} release from mitochondrial stores in response to FCCP.[26] Perfusion of vehicle control gives no change to OGB fluorescence (**Figure 2.5.2e**, light grey). The increase in cytosolic Ca^{2+} occurs simultaneously with the depolarization of $\Delta\Psi_m$, as measured by SPIRIT RhoVR 1 (**Figure 2.5.2f,h**). At the same time, BeRST fluorescence indicates a small FCCP-induced depolarization at the plasma membrane (**Figure 2.5.2g**, magenta).[27-28] Analysis of individual cell responses allows examination of the similarity of responses across all imaged cells (**Figure 2.5.3**).

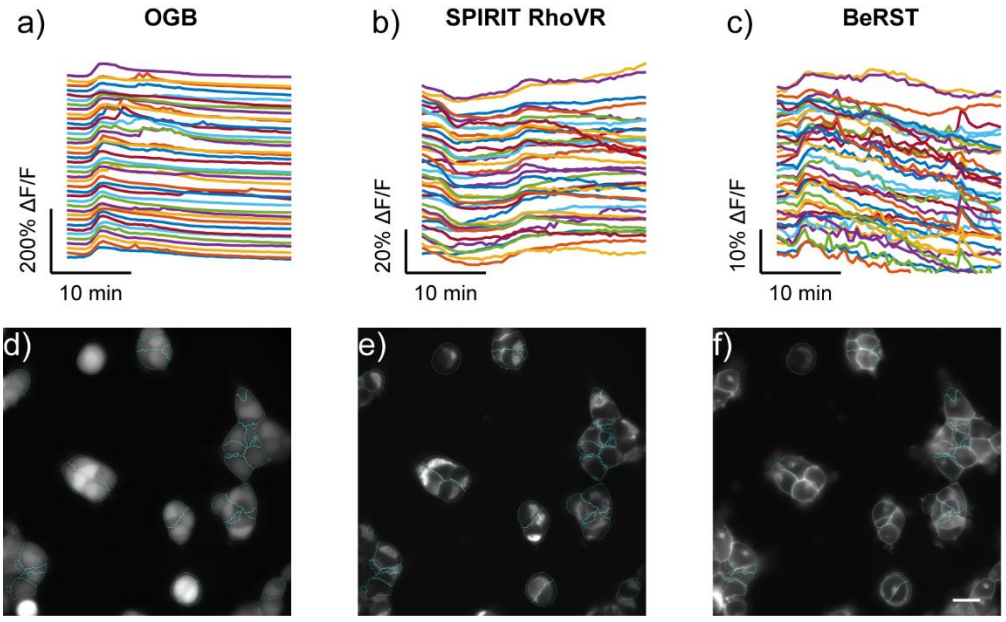

Figure 2.5.3 Individual cell fluorescence traces for multicolor experiment. Top: Normalized fluorescence intensity for individual cells over time in OGB (**a**), SPIRIT RhoVR1 (**b**) and BeRST1 (**c**) channels. Bottom: ROIs overlaid with OGB (**d**), SPIRIT RhoVR1 (**e**), and BeRST (**f**) fluorescence images from t=0 min timepoint. ROIs were generated via CellProfiler using the t=0 min timepoint in the OGB channel. 500 nM FCCP perfused on at 4 minutes followed by HBSS washout at 12 minutes.

2.6 Conclusions and Outlook

In summary, we present the design, synthesis, and application of SPIRIT RhoVR 1, the first in its class of voltage-sensitive fluorophores that report on changes to $\Delta\Psi_m$ via a PeT-based mechanism. SPIRIT RhoVR 1 shows excellent localization to mitochondria, is retained within the mitochondria even after the dissipation of $\Delta\Psi_m$, and can reversibly respond to both hyper- and depolarization of $\Delta\Psi_m$ without the need for exogenous pools of dye in solution. In the future, we envision a palette of mitochondrial-targeted indicators, pairing with non-native enzymes to achieve enhanced targeting to mitochondria and other organelles, and development of indicators with improve brightness for monitoring rapid organelle membrane potential changes.

2.7 Details of synthesis, characterization, and image analysis

General method for chemical synthesis and characterization

Chemical reagents and solvents (dry) were purchased from commercial suppliers and used without further purification. Synthesis of RhoVR carboxylate (compound 1) and RhoVR-tBu were carried out as previously reported.[29] Thin layer chromatography (TLC) (Silicycle, F254, 250 µm) and preparative thin layer chromatog-raphy (PTLC) (Silicycle, F254, 1000µm) were performed on glass backed plates pre-coated with silica gel and were visualized by fluorescence quenching under UV light. Flash column chromatography was performed on Silicycle Silica Flash F60 (230–400 Mesh) using a forced flow of air at 0.5–1.0 bar. NMR spectra were measured on Bruker AVB-400 MHz, 100 MHz, AVQ-400 MHz, 100 MHz, Bruker AV-600 MHz, 150 MHz. Variable temperature NMR experiments were measured on the Bruker AV-600 with the assistance of Hasan Celik. Chemical shifts are expressed in parts per million (ppm) and are referenced to CDCl3 (7.26 ppm, 77.0 ppm) or DMSO (2.50 ppm, 40 ppm). Coupling constants are reported as Hertz (Hz). Splitting patterns are indicated as follows: s, singlet; d, doublet; t, triplet; q, quartet; dd, doublet of doublet; m, multiplet. High-resolution mass spectra (HR-ESI-MS) were measured by the QB3/Chemistry mass spectrometry service at University of California, Berkeley. High performance liquid chromatography (HPLC) and low resolution ESI Mass Spectrometry were performed on an Agilent Infinity 1200 analytical instrument coupled to an Advion CMS-L ESI mass spectrometer. The column used for the analytical HPLC was Phenomenex Luna 5 µm C18(2) (4.6 mm I.D. × 150 mm) with a flow rate of 1.0 mL/min. The mobile phases were MQ-H2O with 0.05% trifluoroacetic acid (eluent A) and HPLC grade acetonitrile with 0.05% trifluoroacetic acid (eluent B). Signals were monitored at 254, 380 and 545 nm over 10 min with a gradient of 10-100% eluent B. The column used for preparative HPLC was Phenomenex Luna 10 µm C18(2) (21.2 mm I.D. x 250 mm) with a flow rate of 30.0 mL/min. The mobile phases were MQ-H2O with 0.05% trifluoroacetic acid (eluent A) and HPLC grade acetonitrile with 0.05% trifluoroacetic acid (eluent B). Signals were monitored at 254 nm over 40 min with a gradient of 30-70% eluent B. Alternately, mobile phases of 10 mM ammonium bicarbonate in MilliQ H2O acidified to pH 6.7 with formic acid (eluent A) and 10 mM ammonium bicarbonate in a mixture of 10% MilliQ H2O and 90% acetonitrile acidified to pH 6.7 with formic acid (eluent B) were used. Signals were monitored at 545 nm over 40 min with a gradient of 60-100% eluent B.

Spectroscopic Studies

For pH studies, a stock solution of RhoVR1 was prepared in DMSO (500 µM) and diluted with PBS (10 mM K_2HPO_4, 2 mM KH_2PO_4, 50 mM Trizma, pH adjusted to indicated value with HCl and NaOH) solution containing 0.10 % (w/w) SDS (1:100-1:1000 dilution). For quantum yield studies, stock solutions of RhoVRs were prepared in DMSO (500 µM) and

diluted in ethanol. UV-Vis absorbance and fluorescence spectra were recorded using a Shimadzu 2501 Spectrophotometer (Shimadzu) and a Quantamaster Master 4 L-format scanning spectrofluorometer (Photon Technologies International). The fluorometer is equipped with an LPS-220B 75-W xenon lamp and power supply, A-1010B lamp housing with integrated igniter, switchable 814 photon-counting/analog photomultiplier detection unit, and MD5020 motor driver. Samples were measured in 1-cm path length quartz cuvettes (Starna Cells)

Cell Culture

Human embryonic kidney 293T (HEK) cells, COS7 cells, and MCF-7 cells were passaged and plated onto 12 mm glass coverslips pre-coated with Poly-D-Lysine (PDL; 0.1 mg/ml; in 10 mM Na_3BO_3; Sigma-Aldrich) to provide a confluency of ~50% for imaging. HeLa cells were plated directly onto 12 mm glass coverslips with no pre-coating. HEK, COS7, and HeLa cells were plated and maintained in Dulbecco's modified eagle medium (DMEM) supplemented with 4.5 g/L D-glucose, 10% FBS and 1% Glutamax. MCF-7s were plated and maintained in DMEM supplemented with 4.5 g/L D-glucose, 10% FBS, 2mM Glutamax, 1x non-essential amino acid solution (NEAA), and 1mM sodium pyruvate. Unless stated otherwise, for loading of all cell lines, dyes were diluted in DMSO to 1000x the final indicated concentration and then diluted 1:1000 in HBSS. All imaging experiments were performed in HBSS.

Imaging Parameters

Epifluorescence imaging was performed on an AxioExaminer Z-1 (Zeiss) equipped with a Spectra-X Light engine LED light (Lumencor), controlled with Slidebook (v6, Intelligent Imaging Innovations). Images were acquired with either a W-Plan-Apo 20x/1.0 water objective (20x; Zeiss) or a W-Plan-Apo 63x/1.0 water objective (63x; Zeiss). Images were focused onto an OrcaFlash4.0 sCMOS camera (sCMOS; Hamamatsu). More detailed imaging information for each experimental application is expanded below. Confocal imaging was performed with a Nikon Inverted Yokogawa spinning disk confocal microscope with 405nm, 488nm, 561nm, and 637nm laser lines and incubation/CO2 for live-cell imaging controlled via Nikon imaging elements. Images were acquired with a 60x oil objective. In multicolor experiments, filter sets were selected to ensure that bleedthrough contributed <10% of the signal in any given channel by measuring the relative fluorescence of cells stained with a single dye in each excitation/emission path.

Epifluorescence colocalization of RhoVRs with Mitotracker Green and LysoTracker Green

HEK, COS7, MCF-7, or HeLa cells were incubated at 37 ˚C with an HBSS solution (Gibco) containing 150 nM SPIRIT RhoVR1 or SPIRIT RhoVR0 and 100 nM MitoTracker Green FM (Invitrogen) or 250 nM Rhodamine 123 (Sigma) for 20 minutes and then transferred to fresh HBSS (no dye) for imaging. For time courses, HEK 293T cells were incubated with 150 nM SPIRIT RhoVR1 or 100 nM MitoTracker Red CMXRos (Invitrogen) co-loaded with 75 nM LysoTracker Green DND-26 (Invitrogen) or 100 nM MitoTracker Green for 20 minutes in HBSS. After 20 minutes, HBSS was aspirated off and replaced with media for 0, 20, 40, or 60 minutes and then transferred to a separate dish in HBSS for imaging. Images were acquired with a W-Plan-Apo 63x/1.0 water objective (Zeiss) and OrcaFlash4.0 sCMOS camera (Hamamatsu). For RhoVR images, the excitation light was delivered from an LED (70 mW/mm^2; 100 ms exposure time) at 575/35 (bandpass) nm and emission was collected with a bandpass emission filter (650/60 nm) after passing through a dichroic mirror (594 nm LP). For MitoTracker images, the excitation light was delivered from an LED (67 mW/mm^2) at 475/34 nm and emission was collected with a bandpass emission filter (540/50 nm) after passing through a dichroic mirror (510 nm LP).

Confocal colocalization of RhoVRs with Mitotracker Green or Rhodamine 123

HEK cells were incubated at 37 ˚C with an HBSS solution containing 250 nM SPIRIT RhoVR1 or RhoVR-tBu and 250 nM Rhodamine 123 (Sigma) or 100 nM MitoTracker Green FM (Invitrogen) for 20 minutes and then transferred to fresh HBSS (no dye) for imaging. Images were acquired across multiple Z-planes at 0.2 µm intervals beginning at the cell-coverslip interface and processing for 20 µm upwards through the cell, first with a 561 nm laser for RhoVR images and next with a 488 nm laser for MitoTracker/Rhodamine 123 images.

Antimycin A treatment

HEK cells were incubated at 37 ˚C with an HBSS solution containing 250 nM SPIRIT RhoVR1, RhoVR-tBu, or Rhodamine 123. Cells were then washed 1x with fresh HBSS and incubated at 37 ˚C in an HBSS solution containing either 5 µg/mL antimycin A (Millipore Sigma) or vehicle for 90 minutes unless stated otherwise. Cells were then washed 1x with fresh HBSS and imaged. Images were acquired with a W-Plan-Apo 63x/1.0 water objective (Zeiss) and OrcaFlash4.0 sCMOS camera (Hamamatsu). For RhoVR images, the excitation light was delivered from an LED (73 mW/mm^2; 100 ms exposure time) at 542/33 (bandpass) nm and emission was collected with a quadruple emission filter (430/32, 508/14, 586/30, 708/98 nm) after passing through a quadruple dichroic mirror (432/38, 509/22, 586/40, 654 nm LP).

FCCP perfusion

HEK, COS7, MCF-7, or HeLa cells were incubated at 37 ˚C for 20 minutes with an HBSS solution containing 150 nM SPIRIT RhoVR1 or SPIRIT RhoVR0. Cells were then washed 1x with HBSS and incubated in fresh DMEM supplemented with 4.5 g/L D-glucose, 10% FBS and 1% Glutamax for 60 minutes. Cells were then washed 1x with DMEM, 1x with HBSS, and transferred to a perfusion chamber in HBSS. Cells were then imaged under continuous perfusion in HBSS with no additives, vehicle, or FCCP (TCI chemicals) at ~3 mL/min. Except where indicated otherwise, FCCP was weighed out dry and dissolved in ethanol to make a solution of 500 µM which was then diluted 1000x in HBSS for a final working concentration of 500 nM. Cells were imaged every 30 seconds for 30 minutes at room temperature. The excitation light was delivered from an LED (73 mW/mm^2; 100 ms exposure time) at 542/33 (bandpass) nm and emission was collected with a quadruple emission filter (430/32, 508/14, 586/30, 708/98 nm) after passing through a quadruple dichroic mirror (432/38, 509/22, 586/40, 654 nm LP). For FCCP concentration screens and ester hydrolysis time course, HEK cells were incubated for 20 minutes at 37 ˚C with HBSS solution containing the concentration of dye indicated.

Multicolor imaging of FCCP perfusion

HEK cells were incubated for 20 minutes at 37 ˚C with a solution of 150 nM SPIRIT RhoVR1 in HBSS. Cells were then washed 1x with HBSS and incubated for 40 minutes at 37 °C in fresh DMEM supplemented with 4.5 g/L D-glucose, 10% FBS and 1% Glutamax. DMEM was then replaced with a solution of 50 nM BeRST1 and 500 nM Oregon Green Bapta (OGB) with 0.01% Pluronic F-127 in fresh DMEM supplemented with 4.5 g/L D-glucose, 10% FBS and 1% Glutamax and cells were incubated for another 20 minutes at 37 °C. OGB was premixed in a 1:1 ratio with Pluronic F-127 in DMSO before 1000x dilution to its final concentration. Cells were then imaged under continuous perfusion in HBSS with no additives, vehicle, or FCCP (TCI chemicals) at ~3 mL/min. In monocolor experiments, FCCP or vehicle was perfused on at 2 minutes and switched back to HBSS perfusion at 10 minutes. In multicolor experiments, FCCP was perfused on at 4 minutes and switched back to HBSS perfusion at 12 minutes. FCCP was weighed out dry and dissolved in ethanol to make a solution of 500 µM which was then diluted 1000x in HBSS for a final working concentration of 500 nM except where indicated otherwise. Cells were imaged every 30 seconds for 30 minutes at room temperature. For OGB images, the excitation light was delivered from an LED (67 mW/mm^2) at 475/34 nm and emission was collected with a bandpass emission filter (540/50 nm) after passing through a dichroic mirror (510 nm LP). For SPIRIT RhoVR1 images, the excitation light was delivered from an LED (73 mW/mm^2; 100 ms exposure time) at 542/33 (bandpass) nm and emission was collected with a quadruple emission filter (430/32, 508/14, 586/30, 708/98 nm) after passing through a quadruple dichroic mirror (432/38, 509/22, 586/40, 654 nm LP). For BeRST1 images, the excitation light was delivered from an LED (95

mW/mm^2; 100 ms exposure time) at 631/28 (bandpass) nm and emission was collected with a quadruple emission filter (430/32, 508/14, 586/30, 708/98 nm) after passing through a quadruple dichroic mirror (432/38, 509/22, 586/40, 654 nm LP).

Image analysis

Unless stated otherwise, images were analyzed in ImageJ to extract raw fluorescence values which were then transferred to Excel (Microsoft) or MatLab (MathWorks) for further analysis. ROIs were selected manually to encompass cellular regions containing mitochondria within the region imaged. Background fluorescence was measured and subtracted from measured fluorescence intensities before intensities were analyzed.

Colocalization analysis

ROIs were selected manually to each include contiguous clusters of 1-4 cells. Pearson's values were then assessed individually for each cluster using the coloc2 plugin in ImageJ. In confocal image stacks, slices that did not contain fluorescence were eliminated before submitting the whole stack for colocalization analysis. Graphs of Pearson's coefficients depict the average Pearson's value as a horizontal bar overlaid with each individual measured Pearson's value. Error bars represent +/- standard error of the mean.

Antimycin A analysis

Background subtracted fluorescence intensities for each coverslip were normalized to the average intensity of the vehicle coverslips. Graphs of antimycin experiments depict the average normalized intensity of each condition as a horizontal bar overlaid with each individual normalized fluorescence intensity. Error bars represent +/- standard error of the mean.

Perfusion analysis

Background subtracted fluorescence intensities for each coverslip were normalized to the average intensity of the time point before FCCP perfusion began for that coverslip and then represented as a percent of this initial average. Average traces depict the average percent of initial average fluorescence of n=3 coverslips +/- standard error of the mean. For multicolor imaging, ROIs were selected to represent whole cells in the OGB channel or background and these ROIs were used to measure fluorescence in all channels.

CellProfiler analysis

Time course stacks from multicolor experiments were split into individual images. Traces were generated using an imaging pipeline in CellProfiler that automatically identifies primary objects from t=0 OGB image and uses these ROIs to measure integrated intensity across each time point in the other channels.

Scheme 2.7.1 Structures of compounds used in this study

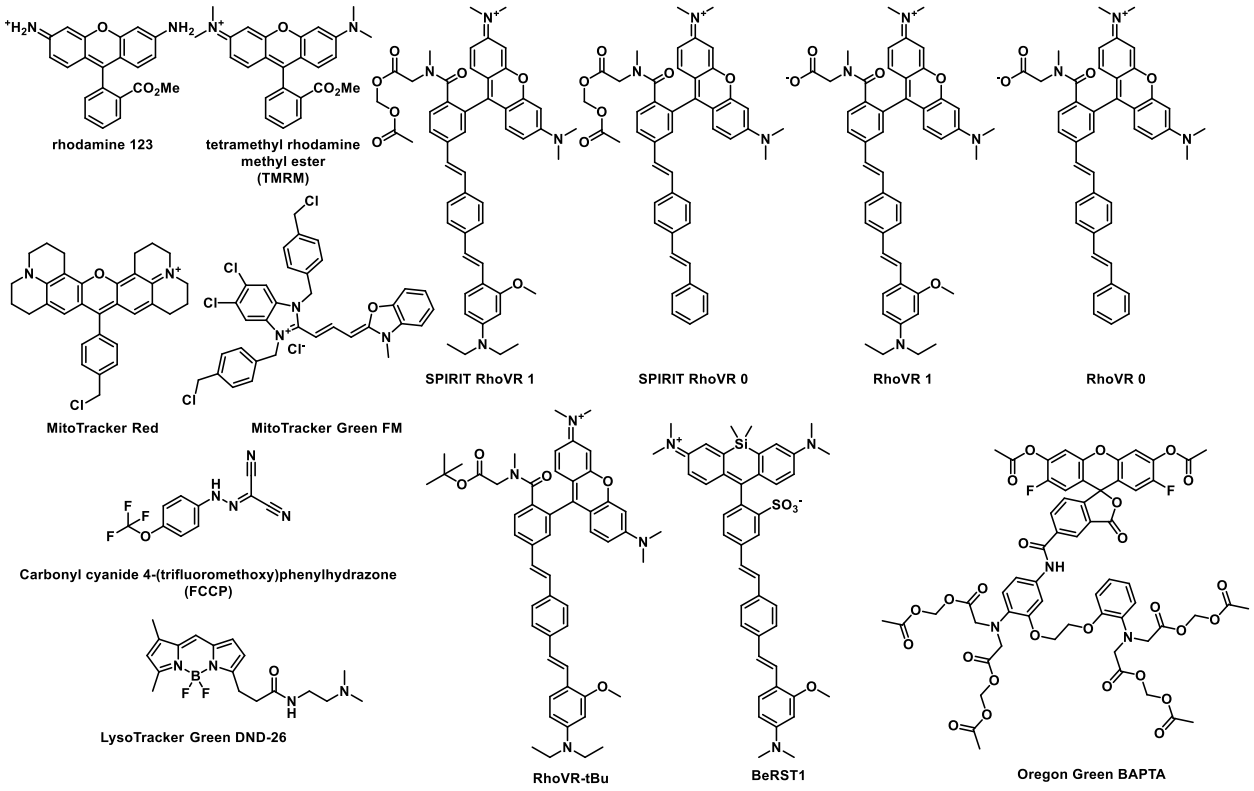

Scheme 2.7.2

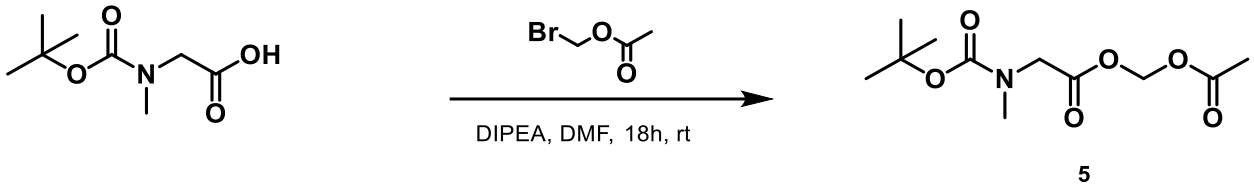

Synthesis of BOC-sarcosine-AM ester, 5:

A Schlenk flask was evacuated and backfilled 3x with nitrogen. N-BOC sarcosine (510 mg, 2.70 mmol) and anhydrous DMF were added and stirred at room temperature. 2.4 mL (13.8 mmol) of DIPEA and 1.2 mL (12.1 mmol) of bromomethyl acetate were added and the reaction was stirred overnight at room temperature under nitrogen. The reaction was then extracted 3x with brine and DCM, concentrated under reduced pressure, and purified by flash chromatography (9:1 – 2:1 hexanes:ethyl acetate) to yield compound **5** (406 mg, 58% yield).

^{1}H NMR (300 MHz, CD_3Cl) δ 5.80 (d, J = 3.4 Hz, 2H), 4.01 (d, J = 26.3 Hz, 2H), 2.95 (d, J = 5.5 Hz, 3H), 2.14 (s, 3H), 1.46 (d, J = 12.7 Hz, 9H).

Scheme 2.7.3

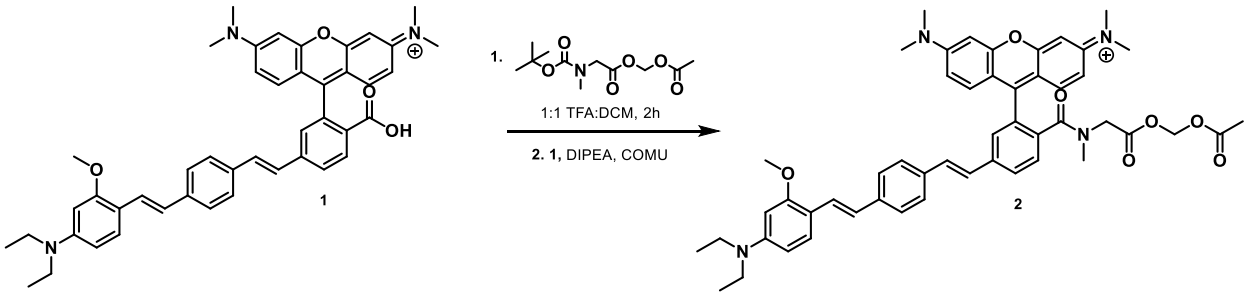

Synthesis of SPIRIT RhoVR1, 2:

BOC-sarcosine acetoxymethyl ester (compound **5,** 71 mg, 0.270 mmol) was stirred in 1:1 TFA:DCM for 1 hour. Solvent was then evaporated under a stream of nitrogen and the resulting solid basicified with DIPEA. In a separate vial, compound **1** (108 mg, 0.156 mmol) was stirred in DMF with 200 µL DIPEA at room temperature for 5 minutes. This

vial was then cooled to 0 ˚C and HATU (72 mg, 0.189 mmol) and all of the product from compound **5** were added and the reaction stirred for 30 minutes until complete by LC/MS. The reaction was then extracted 5x with 0.1M HCl and DCM, concentrated under reduced pressure, and then purified by preparative HPLC (60-100% acetonitrile in water w/ 10 mM ammonium bicarbonate, pH adjusted to 6.7 with formic acid) to yield compound **2** (13 mg, 10% yield)

^{1}H NMR (600 MHz, CDCl3) δ 7.80 (dd, J = 8.0, 1.7 Hz, 1H), 7.60 (d, J = 8.1 Hz, 1H), 7.50 (s, 1H), 7.49 (s, 1H), 7.47 (d, J = 5.1 Hz, 3H), 7.45 – 7.42 (m, 1H), 7.41 (s, 1H), 7.33 (d, J = 9.5 Hz, 1H), 7.22 (d, J = 16.3 Hz, 1H), 7.12 (d, J = 16.3 Hz, 1H), 6.98 – 6.92 (m, 3H), 6.85 (d, J = 2.5 Hz, 2H), 6.32 (dd, J = 8.8, 2.4 Hz, 2H), 6.20 (d, J = 2.4 Hz, 1H), 5.58 (s, 2H), 3.97 (s, 1H), 3.88 (s, 2H), 3.39 (q, J = 7.1 Hz, 4H), 3.32 (s, 12H), 2.91 (s, 2H), 2.69 (s, 1H), 2.06 (s, 3H), 1.19 (t, J = 7.1 Hz, 6H).

HRMS (ESI+) Calculated for $C_{51}H_{55}N_4O_7$+ $[M]^+$: 835.4065; found 835.4052

Scheme 2.7.4

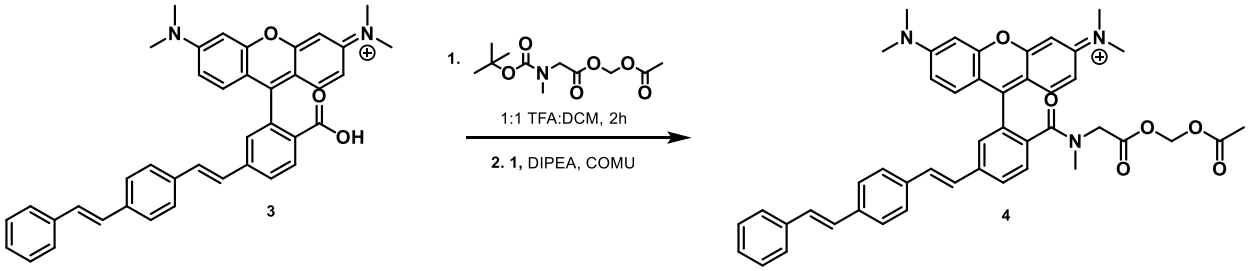

Synthesis of SPIRIT RhoVR0, 4:

BOC-sarcosine acetoxymethyl ester (compound **5,** 35 mg, 0.134 mmol) was stirred in 1:1 TFA:DCM for 2 hours. Solvent was then evaporated under a stream of nitrogen and the resulting solid basicified with DIPEA. In a separate vial, compound **3** (53 mg, 0.0896 mmol) was stirred in DMF with 200 µL DIPEA at room temperature for 5 minutes. This vial was then cooled to 0 ˚C and COMU (44 mg, 0.103 mmol) and all of the product from compound **5** were added and the reaction stirred for 30 minutes until complete by LC/MS. The reaction was then extracted 3x with brine and DCM, concentrated under reduced pressure, and then purified by flash chromatography (0-5% MeOH in DCM) to yield compound **2** (15 mg, 33% yield).

^{1}H NMR (400 MHz, $CDCl_3$) δ 7.83 – 7.76 (m, 1H), 7.50 (dd, J = 15.4, 5.9 Hz, 9H), 7.37 (t, J = 7.5 Hz, 2H), 7.33 – 7.22 (m, 4H), 7.18 (d, J = 8.6 Hz, 1H), 7.09 (d, J = 6.7 Hz, 2H), 6.94 (dd, J = 9.5, 2.6 Hz, 2H), 6.71 (d, J = 2.4 Hz, 2H), 5.83 (d, J = 6.3 Hz, 1H), 5.59 (s, 2H), 4.25 (s, 1H), 4.00 (s, 2H), 3.27 (s, 17H), 2.99 (d, J = 4.7 Hz, 3H), 2.16 (s, 2H), 2.07 (s, 3H).

HRMS (ESI+) Calculated for $C_{46}H_{44}N_3O_6$+ $[M]^+$: 734.3225; Found 734.3216

Spectrum 2.7.1 ^{1}H spectrum of 5, BOC-sarcosine-AM ester

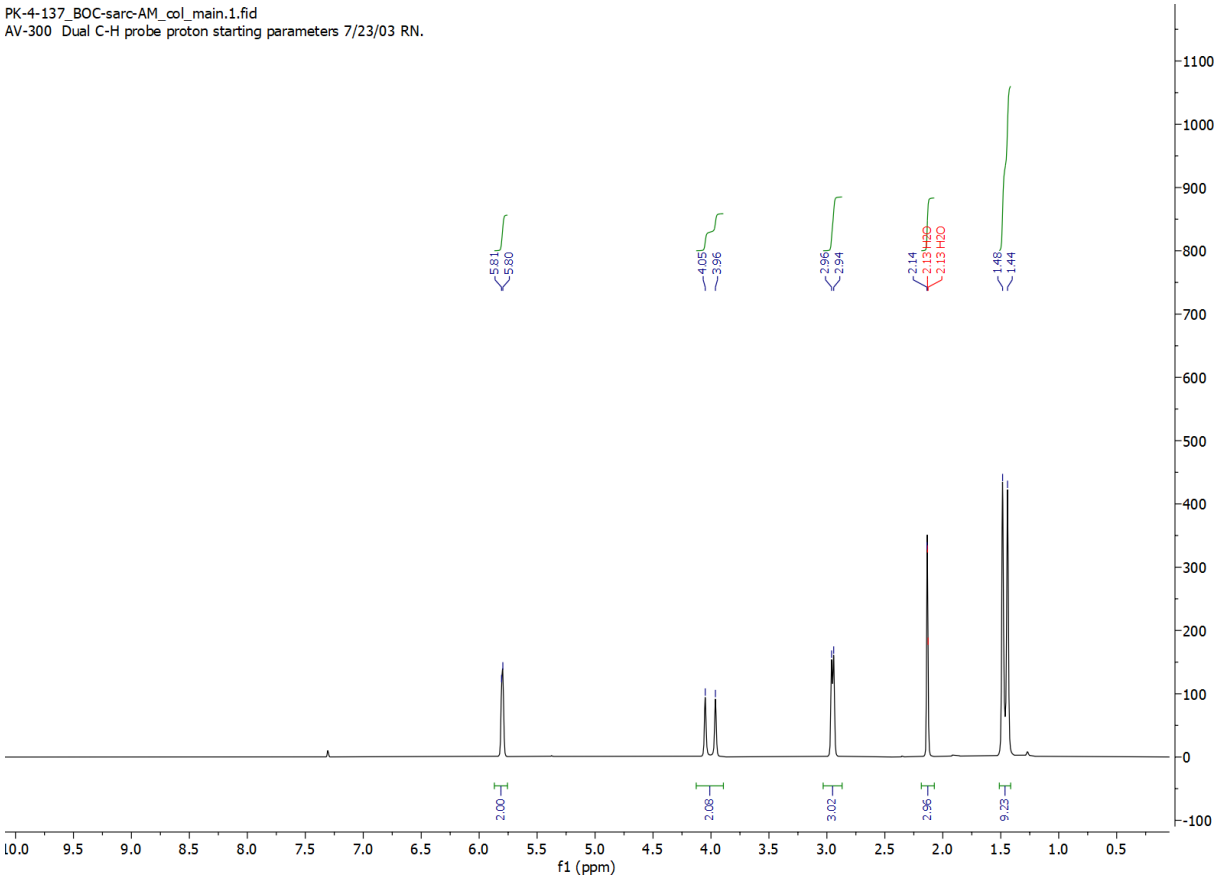

Spectrum 2.7.2 LC/MS spectrum of 2, SPIRIT RhoVR1

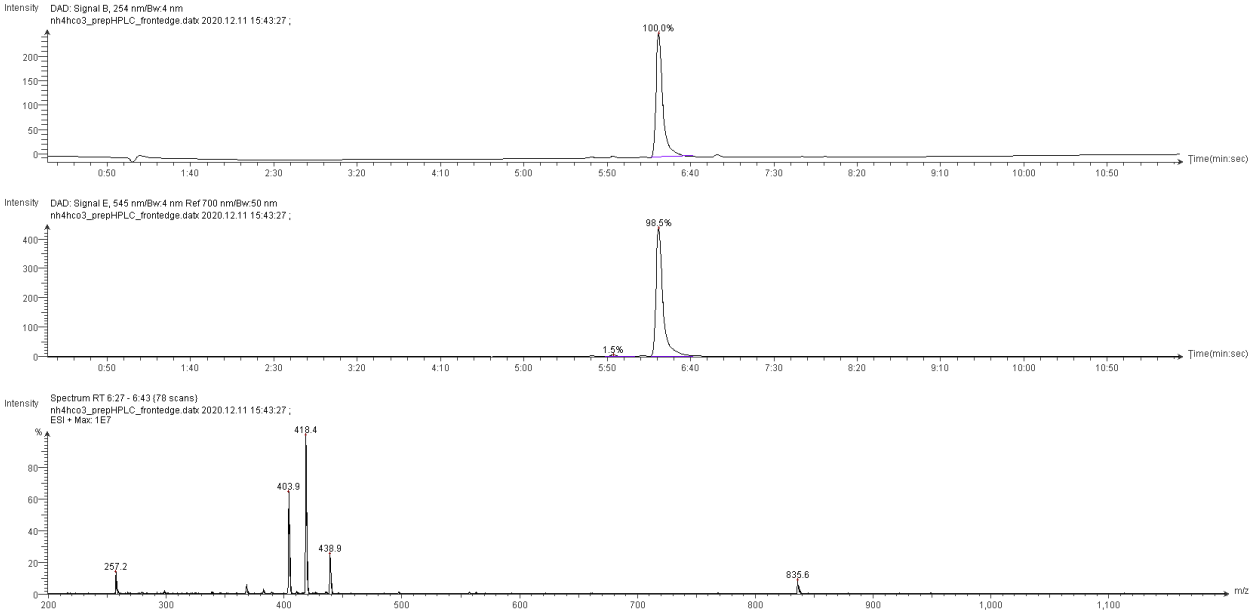

Low resolution ESI+ mass spectrum of **2** (SPIRIT RhoVR1):

Calculated for $[M]^{+}$: 835.41

Found: 835.6

Calculated for $[M+acetonitrile+H]^{2+}$: 438.72

Found: 438.9

Calculated for $[M+H]^{2+}$: 418.20

Found: 418.4

Calculated for $[M+H\text{-}ethyl\ (decomposition\ on\ MS)]^{2+}$: 404.19

Found: 403.9

Spectrum 2.7.3 ^{1}H spectrum of 2, SPIRIT RhoVR1

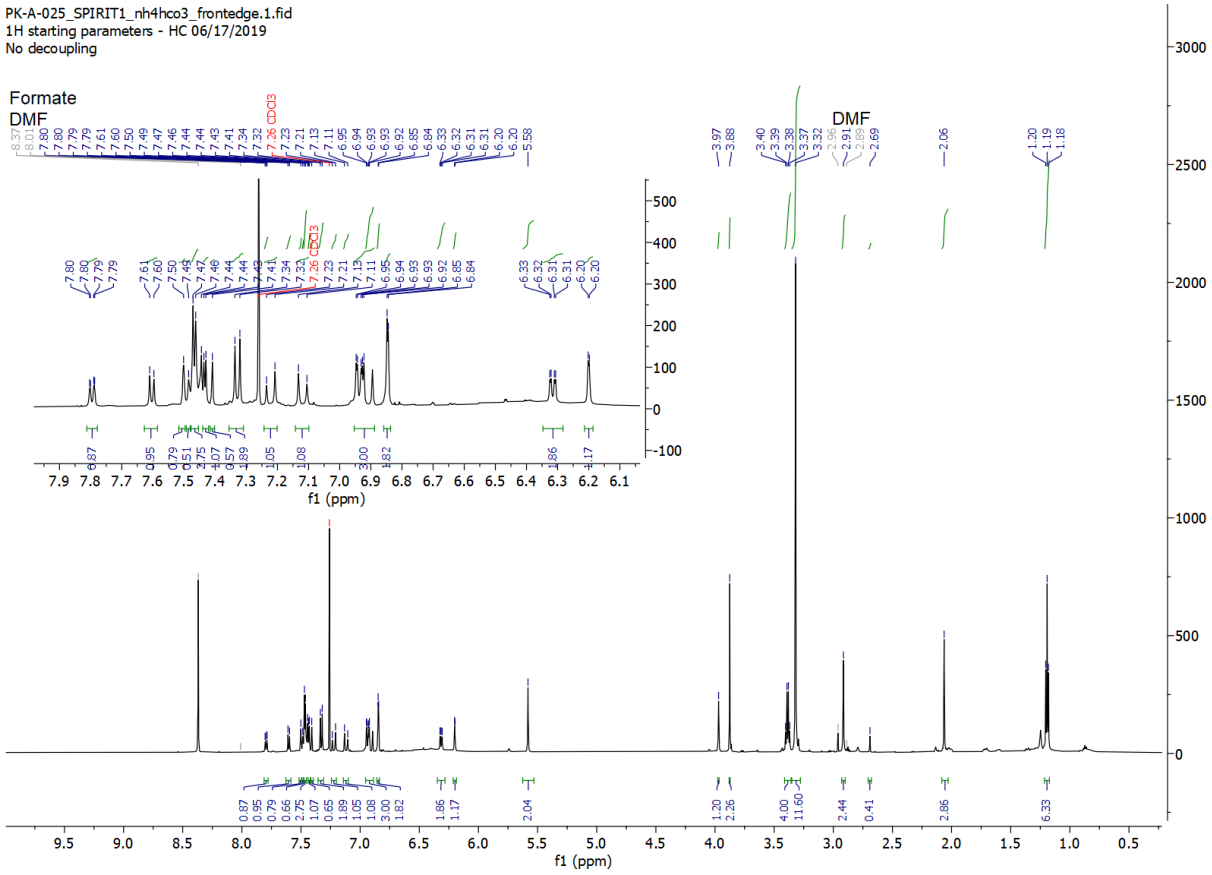

Spectrum 2.7.4 LC/MS spectrum of 4, SPIRIT RhoVR0

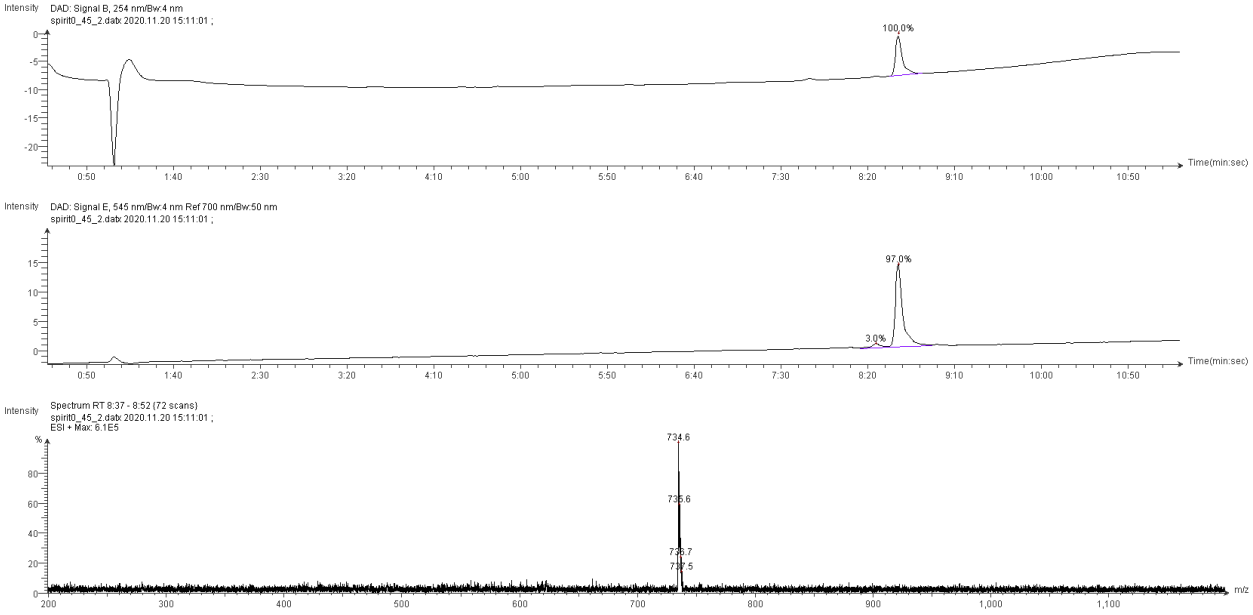

Low resolution ESI+ mass spectrum of **4** (SPIRIT RhoVR0):

Calculated for $[M]^+$: 734.32

Found: 734.6

Spectrum 2.7.5 ^{1}H spectrum of 4, SPIRIT RhoVR0

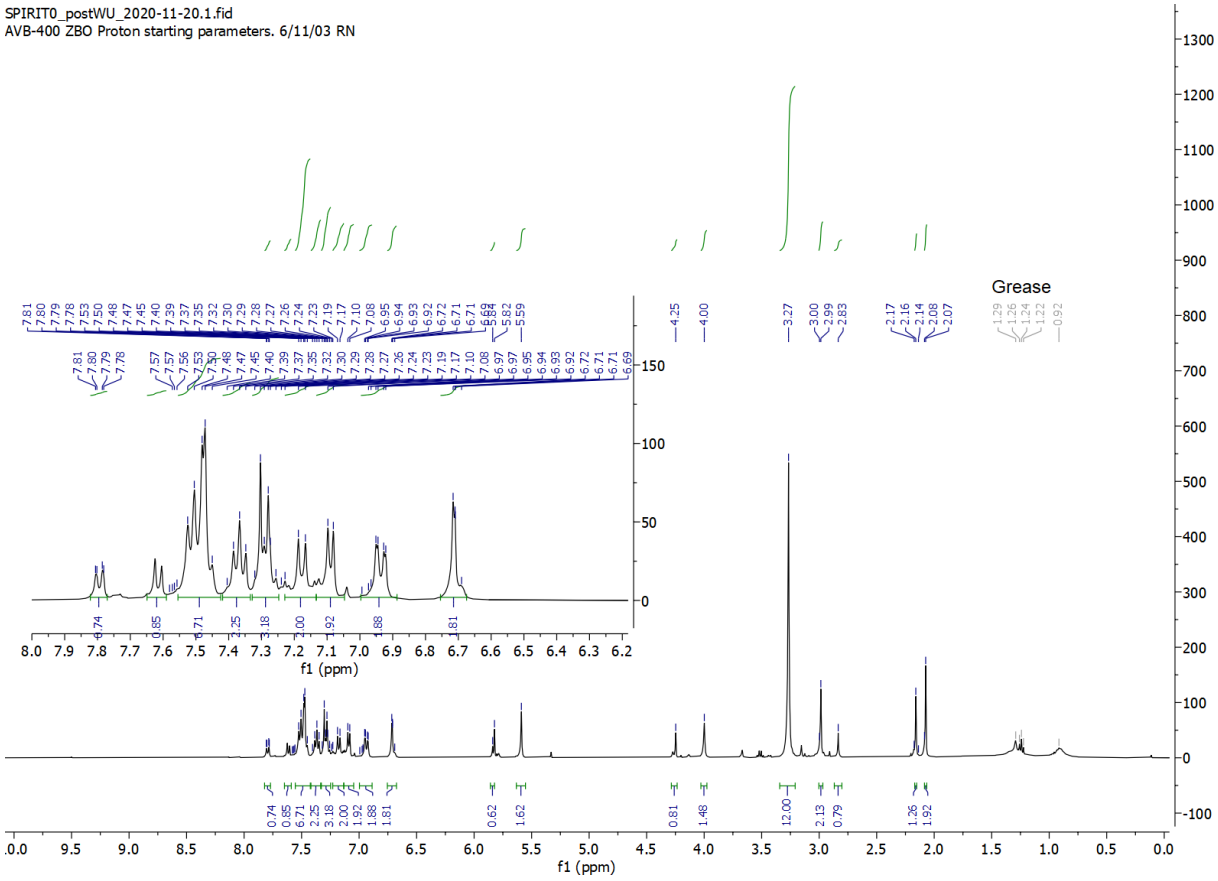

2.8 References

1. Grabe, M.; Oster, G., Regulation of Organelle Acidity. *Journal of General Physiology* **2001,** *117* (4), 329-344.
2. Lehninger, A. L.; Cox, M. M.; Nelson, D. L., *Lehninger Principles of Biochemistry*. W.H. Freeman: New York, 2008.
3. Nicholls, D. G., Mitochondrial membrane potential and aging. *Aging Cell* **2004,** *3*, 35-40.
4. Hoppe, U. C., Mitochondrial calcium channels. *FEBS Letters 584*, 1975-1981.
5. Summerhayes, I. C.; Lampidid, T. J.; Bernal, S. D.; Nadakavukaren, J. J.; Nadakavukaren, K. K.; Sheperd, E. L.; Chen, L. B., Unusual retention of rhodamine 123 by mitochondria in muscle and carcinoma cells. *Proceedings of the National Academy of Sciences* **1982,** *79*, 5292-5296.
6. Johnson, L. V.; Walsh, M. L.; Chen, L. B., Localization of mitochondria in living cells with rhodamine 123. *Proceedings of the National Academy of Sciences* **1980,** *77* (2), 990-994.
7. Scaduto, R. C.; Grotyohann, L. W., Measurement of Mitochondrial Membrane Potential Using Fluorescent Rhodamine Derivatives. *Biophysical Journal* **1999,** *76*, 469-477.
8. Reers, M.; Smith, T. W.; Chen, L. B., J-Aggregate Formation of a Carbocyanine as a Quantitative Fluorescent Indicator of Membrane Potential. *Biochemistry* **1991,** *30*, 4480-4486.
9. Zhao, N.; Li, M.; Yan, Y.; Lam, J. W. Y.; Zhang, Y. L.; Zhao, Y. S.; Wong, K. S.; Tang, B. Z., A tetraphenylethene-substituted pyridinium salt with multiple functionalities: synthesis, stimuli-responsive emission, optical waveguide and specific mitochondrion imaging. *Journal of Materials Chemistry C* **2013,** *1*, 4640-4646.
10. Elmore, S. P.; Nishimura, Y.; Qian, T.; Herman, B.; Lemasters, J. J., Discrimination of depolarized from polarized mitochondria by confocal fluorescence resonance energy transfer. *Biochemistry and Biophysics* **2004,** *422*, 145-152.
11. Feng, R.; Guo, L.; Fang, J.; Jia, Y.; Wang, X.; Wei, Q.; Yu, X., Construction of the FRET Pairs for the Visualization of Mitochondria Membrane Potential in Dual Emission Colors. *Analytical Chemistry* **2019,** *91*, 3704-3709.
12. Li, X.; Tian, M.; Zhang, G.; Zhang, R.; Feng, R.; Guo, L.; Yu, X.; Zhao, N.; He, X., Spatially Dependent Fluorescent Probe for Detecting Different Situations of Mitochondrial Membrane Potential Conveniently and Efficiently. *Analytical Chemistry* **2017,** *89*, 3335-3344.
13. Li, X.; Zhang, R.; Guo, L.; Zhang, H.; Meng, F.; Yang, R.; Li, C.; Liu, Z.; Yu, X., Colocalization Coefficients of a Target-Switchable Fluorescent Probe Can Serve As an Indicator of Mitochondrial Membrane Potential. *Analytical Chemistry* **2019,** *91*, 2672-2677.

14. Putti Perry, S. W.; Norman, J. P.; Barbieri, J.; Brown, E. B.; Gelbard, H. A., Mitochondrial membrane potential probes and the proton gradient: a practical usage guide. *Biotechniques* **2006,** *50* (2), 98-115.
15. Lemasters, J. J.; Ramshest, V. K., Imaging of Mitochondrial Polarization and Depolarization with Cationic Fluorophores. *Methods in Cell Biology* **2007,** *80*, 283-295.
16. Liu, P.; Miller, E. W., Electrophysiology, Unplugged: Imaging Membrane Potential with Fluorescent Indicators. *Acc Chem Res* **2020,** *53* (1), 11-19.
17. Deal, P. E.; Kulkarni, R. U.; Al-Abdullatif, S. H.; Miller, E. W., Isomerically Pure Tetramethylrhodamine Voltage Reporters. *Journal of the American Chemical Society* **2016,** *138* (29), 9085-9088.
18. Rutter, G. A.; Burnett, P.; Rizzuto, R.; Brini, M.; Murgia, M.; Pozzan, T.; Tavaré, J. M.; Denton, R. M., Subcellular imaging of intramitochondrial Ca2+ with recombinant targeted aequorin: significance for the regulation of pyruvate dehydrogenase activity. *Proceedings of the National Academy of Sciences* **1996,** *93* (11), 5489-5494.
19. Deal, P. E.; Liu, P.; Al-Abdullatif, S. H.; Muller, V. R.; Shamardani, K.; Adesnik, H.; Miller, E. W., Covalently Tethered Rhodamine Voltage Reporters for High Speed Functional Imaging in Brain Tissue. *Journal of the American Chemical Society* **2020,** *142* (1), 614-622.
20. Johnson, L. V.; Walsh, M. L.; Bockus, B. J.; Chen, L. B., Monitoring of Relative Mitochondrial Membrane Potential in Living Cells by Fluorescence Microsocpy. *Journal of Cell Biology* **1981,** *88*, 526-535.
21. Kim, H.; Esser, L.; Hossain, M. B.; Xia, D.; Yu, C.; Riso, J.; van der Helm, D.; Deisenhofer, J., Structure of Antimycin A1, a Specific Electron Transfer Inhibitor of Ubiquinol-Cytochrome c Oxidoreductase. *Journal of the American Chemical Society* **1999,** *121* (20), 4902-4903.
22. Kalbáčová, M.; Vrbacký, M.; Drahota, Z.; Mělková, Z., Comparison of the Effect of Mitochondrial Inhibitors on Mitochondrial Membrane Potential in Two Different Cell Lines Using Flow Cytometry and Spectrofluorometry. *Cytometry A* **2003,** *52A*, 110-116.
23. Baracca, A.; Sgarbi, G.; Solaini, G.; Lenaz, G., Rhodamine 123 as a probe of mitochondrial membrane potential: evaluation of proton flux through F0 during ATP synthesis. *Biochimica et Biophysica Acta (BBA) - Bioenergetics* **2003,** *1606* (1), 137-146.
24. Gee, K. R.; Poot, M.; Klaubert, D. H.; Sun, W.-C.; Haugland, R. P.; Mao, F. Fluorinated xanthene derivatives as fluorescent dyes and their use in staining biological materials. WO9739064A1, 1997.
25. Huang, Y. L.; Walker, A. S.; Miller, E. W., A Photostable Silicon Rhodamine Platform for Optical Voltage Sensing. *J Am Chem Soc* **2015,** *137* (33), 10767-76.
26. Luo, Y.; Bond, J. D.; Ingram, V. M., Compromised mitochondrial function leads to increased cytosolic calcium and to activation of MAP kinases. *Proceedings of the National Academy of Sciences* **1997,** *94* (18), 9705-9710.
27. Park, K. S.; Jo, I.; Pak, K.; Bae, S. W.; Rhim, H.; Suh, S. H.; Park, J.; Zhu, H.; So, I.; Kim, K. W., FCCP depolarizes plasma membrane potential by activating proton and

Na+ currents in bovine aortic endothelial cells. *Pflugers Archiv : European journal of physiology* **2002,** *443* (3), 344-52.
28. Kenwood, B. M.; Weaver, J. L.; Bajwa, A.; Poon, I. K.; Byrne, F. L.; Murrow, B. A.; Calderone, J. A.; Huang, L.; Divakaruni, A. S.; Tomsig, J. L.; Okabe, K.; Lo, R. H.; Cameron Coleman, G.; Columbus, L.; Yan, Z.; Saucerman, J. J.; Smith, J. S.; Holmes, J. W.; Lynch, K. R.; Ravichandran, K. S.; Uchiyama, S.; Santos, W. L.; Rogers, G. W.; Okusa, M. D.; Bayliss, D. A.; Hoehn, K. L., Identification of a novel mitochondrial uncoupler that does not depolarize the plasma membrane. *Molecular Metabolism* **2014,** *3* (2), 114-123.
29. Deal, P. E.; Kulkarni, R. U.; Al-Abdullatif, S. H.; Miller, E. W., Isomerically Pure Tetramethylrhodamine Voltage Reporters. *Journal of the American Chemical Society* **2016,** *138* (29), 9085-9088.

Chapter 3: A Click Chemistry Targeting Strategy for Subcellular Localization of Rhodamine Voltage Reporters

With Anneliese M.M. Gest, Ryan Roo, Lauren Lesiak, Julia G. Martin, Marisol X. Navarro, Parker E. Deal, Neville Dadina, and Jonathan Tyson

3.0 Introduction

Electrical potentials across biological membranes, including those that form membrane-bound organelles, regulate and initiate a host of physiological processes.[1] Although electrical potentials across external plasma membranes have been extensively studied, organelle membrane potentials remain relatively under-explored, by comparison. The membranes of organelles, ensconced within the confines of the cellular membrane, are difficult to access with electrodes, making determination of organelle membrane potential difficult.[2-4] While optical methods for monitoring changes in or measuring values of *plasma* membrane potentials are a powerful complement to electrode-based methods, delivering and targeting voltage-sensitive dyes to specific, internal organelle membranes for visualizing organelle membrane potential is an outstanding challenge.

A number of strategies exist to target mitochondria: most rely on lipophilic, cationic groups which accumulate in the mitochondrial matrix in a potential-dependent fashion. Approaches to other organelles are limited. Recent efforts to optically measure membrane potential of internal organelles have used DNA nanodevices[5] or genetic targeting with small molecule quenchers to target lysosomal membranes.[6] Alternative approaches using completely genetically encoded voltage-sensitive fluorescent proteins take advantage of expression in both external and internal membranes to track membrane potential.[7]

We wondered whether we might adapt VoltageFluor dyes for delivery to organelle membranes and take advantage of the photoinduced electron transfer (PeT) voltage-sensing mechanism to monitor membrane potential in organelles. Most existing VoltageFluors are designed to be cell impermeant for measuring cellular membrane potential and thus do not effectively stain organelle membranes.[8] However, we recently found that modifications to a rhodamine-based voltage reporter (RhoVR) enabled passage through cell membranes and localization to mitochondria.[9]

Fluorescent dyes can be targeted to subcellular locations either through charge,[10-12] covalently attached groups specific to a subcellular location,[13] genetic targeting of protein constructs,[14-18] or bioorthogonal chemistry in which one reaction partner is attached to a targeting group and another is attached to the fluorescent probe to allow targeting in living cells.[19] A VoltageFluor targeted using bioorthogonal chemistry would be targetable to multiple subcellular locations using different targeted reaction partners. We selected a transcyclooctene (TCO)/tetrazine click reaction to use for subcellular targeting of VoltageFluors due to its rapid reaction kinetics[20-22] and the ability of tetrazines to quench the fluorescence of xanthene dyes.[23-25] Fluorescence becomes unquenched after the tetrazine group reacts with a strained alkene to form a covalent adduct, tethering unquenched dye to the subcellular location targeted by the alkene.

3.1 Design of subcellularly targeted RhoVR

To realize this strategy, we made a **L**igation **Un**quenched for **A**ctivation and **R**edistribution **Rho**damine **V**oltage **R**eporter (LUnAR RhoVR). In this approach, a TCO is targeted to the membrane of interest using either a chemical targeting group or genetically targeted protein, after which the voltage reporter reacts with the targeted TCO to covalently bind it to the membrane of interest. Off-target background fluorescence is minimized because of quenching by the unreacted tetrazine group, (**Scheme 3.1.1**).

Scheme 3.1.1 Targeted transcyclooctenes enable tetrazine functionalized RhoVRs to organelle membranes.

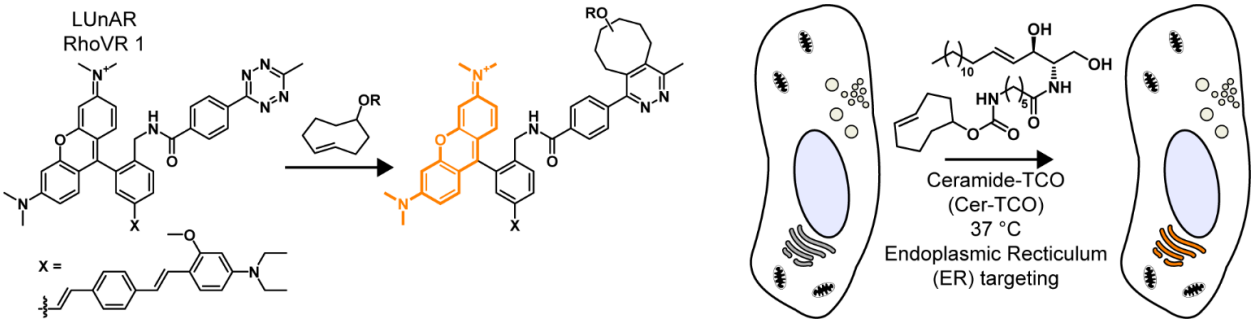

A small molecule rhodamine voltage sensor functionalized with a tetrazine quencher (LUnAR RhoVR 1) reacts with a targeted transcyclooctene (TCO) to form a covalent adduct with unquenched fluorescence. When this reaction is performed in live cells with a targeted transcyclooctene, for example ceramide-TCO, the small molecule voltage sensor is targeted to the membrane of interest with quenched fluorescence from any off-target localization.

After synthesizing and screening four different rhodamine-tetrazine linker chemistries for fluorescence turn-on (**Figure S1**), we settled on an amide linkage between the RhoVR and the tetrazine due to its superior turn-on and synthetic compatibility with published VoltageFluor syntheses (**Scheme 3.1.1**).

Figure 3.3.1 Amide linkages provide highest turn-on

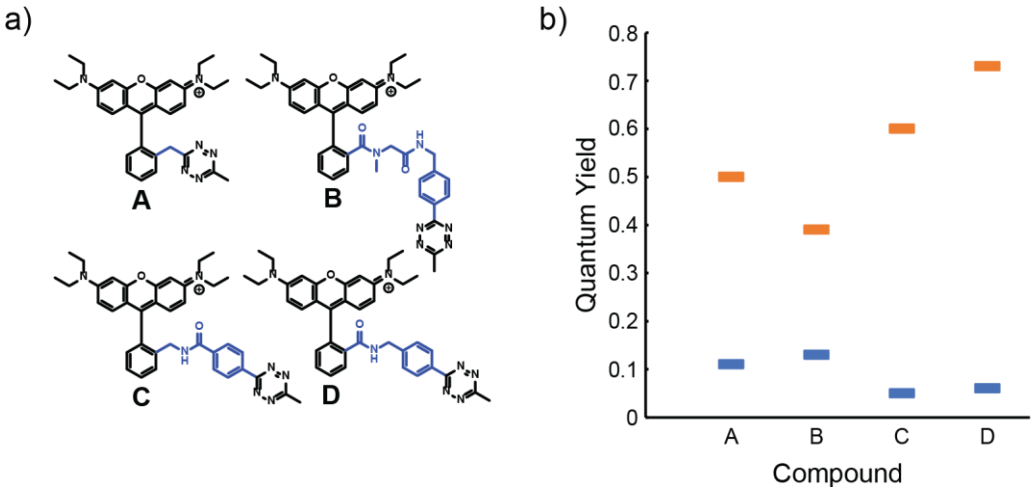

Figure S1. Amide linkages have best in-vitro turn on of parent dyes. **a)** Rhodamine B-tetrazine conjugates synthesized in this study and **b)** their measured in vitro quantum yields before (blue) and after (orange) reaction with 4-transcyclooctenol.

3.2 Synthesis and spectral characterization of LUnAR RhoVRs

The synthesis of tetrazine-containing LUnAR RhoVR proceeds from a reduction of a brominated carboxytetramethyl rhodamine (**1**)[8] to the corresponding alcohol (**2**) followed by a Heck reaction with a molecular wire. The alcohol is then converted to a primary amine and coupled using carbodiimide chemistry to 3-methyl-6-carboxyphenyl tetrazine (**24**)[26] to give LUnAR RhoVR 1 (**Scheme 3.2.1**). A similar synthesis with a molecular wire lacking aniline and methoxy groups gives LUnAR RhoVR 0, a voltage insensitive compound which serves as a useful control for cellular studies.[27-29]

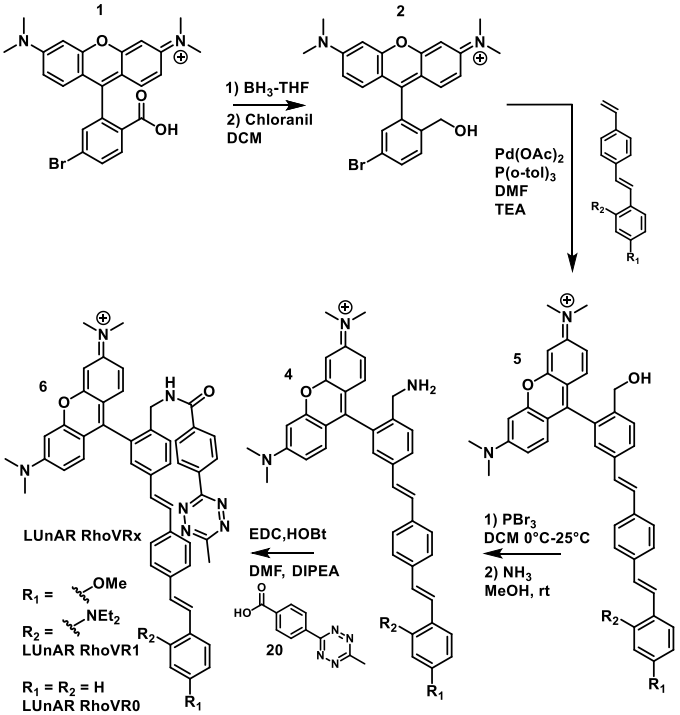

Scheme 3.2.1 (right) Synthesis of LUnAR RhoVRs

LUnAR RhoVR 1 and 0 possess absorbance and emission spectra characteristic of tetramethyl rhodamine, with absorbance centered at 557 nm and an emission maximum of 578 nm. The fluorescence of LUnAR RhoVR 1 increases 7-fold upon reaction with TCO-ol (**25**); LUnAR RhoVR 0 increases 10-fold (**Figure 3.2.1**, **Table 3.2.1**). Although the fluorescence increases, the absorbance shows very little change before and after reaction with TCO, indicating that the increase in brightness results primarily from a change in the quantum yield of fluorescence. Similar turn-on ratios are achieved with TCO compounds bearing HaloTag ligands and ceramide (**Table 3.2.1**).

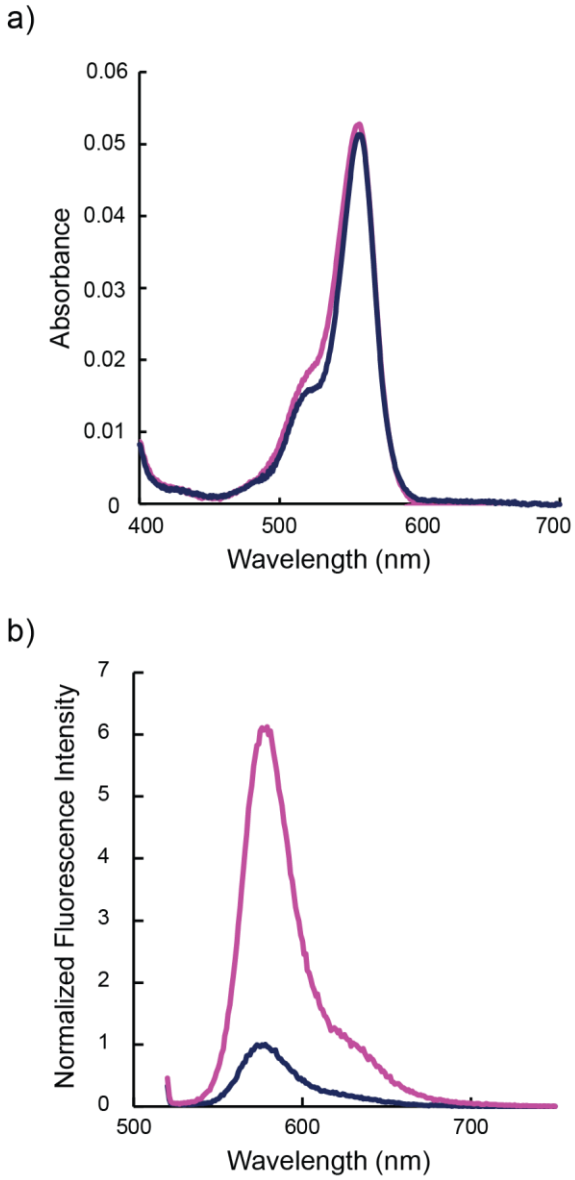

RhoVR [a]	**TCO**	**Φ_{fl}**
LUnAR 1	---	0.042
LUnAR 1	TCO-ol	0.26 (6.2×)
LUnAR 1	TCO-PEG$_{25}$-Halo	0.28 (6.7×)
LUnAR 1	Cer-TCO	0.20 (4.8×)
LUnAR 0	---	0.032
LUnAR 0	TCO-ol	0.32 (10.0×)
LUnAR 0	Cer-TCO	0.17 (5.3×)

Table 3.2.1 Turn-on repsonses of LUnAR RhoVRs and TCOs

Figure 3.2.1 Absorbance (**a**) and fluorescence (**b)** of LUnAR RhoVR before and after reaction with transcyclooctenol. **a.** plot of raw absorbance of representative samples of

LUnAR RhoVR1 before (dark blue) and after (magenta) reaction with transcycloocteneol. **b.** plot of normalized fluorescence emission vs. wavelength for LUnAR RhoVR 1 before (dark blue) and after (magenta) reaction with transcycloocteneol from the samples shown in **a**. Spectra were acquired in ethanol with 0.01% HCl. LUnAR RhoVR 1 (200 µM) was reacted with transcyclooctenol (10 mM) in 5:1 water:dioxane and then diluted to 500 nM for spectral measurements.

Although LUnAR RhoVRs can spirocyclize under conditions of high pH or low dielectric constant, their sensitivity to pH and polarity is identical before and after reaction with TCOs (**Figure 3.2.2)**

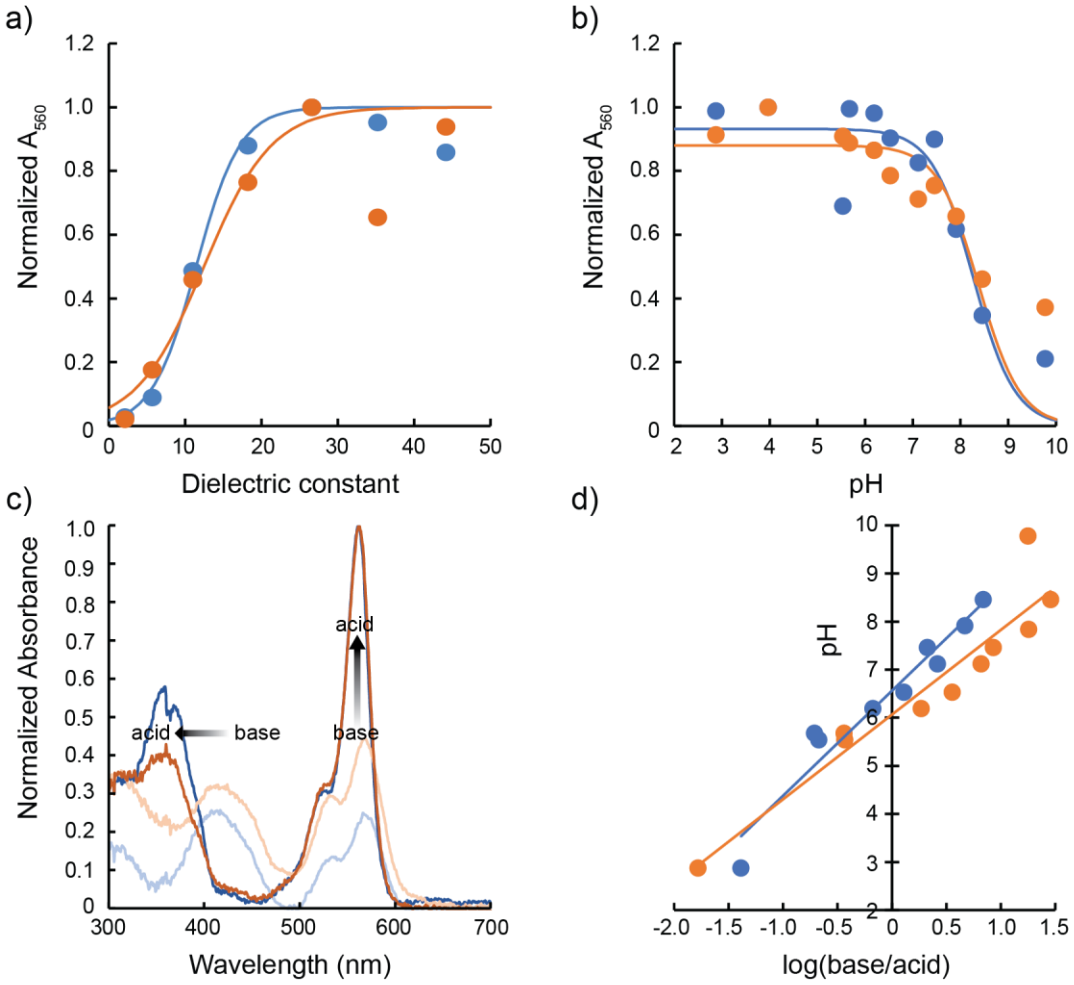

Figure 3.3.2 LUnAR RhoVR1 lactonizes in low dielectric solvents and high pH. **a**) Absorbance at 560 nm of 500 nM LUnAR RhoVR1 versus dielectric constant dioxane before (blue circles) and after (orange circles) reaction with transcycloocteneol. Solid lines represent fit to a sigmoidal curve to model the equilibrium for better comparison of

lactonization equilibria. **b**) Absorbance at 560 nm of LUnAR RhoVR1 as a function of pH before (blue circles) and after (orange circles) reaction with transcyloocteneol. Solid lines represent fit to a sigmoidal curve to model the open/closed equilibrium with participating proton for better comparison of lactonization equilibria. **c**) Absorption spectra of 500 nM LUnAR RhoVR1 before (blue traces) and after (orange traces) reaction with transcyclooctenol. Light blue and orange traces represent absorbance at pH 9.78 and dark blue and orange traces represent absorbance at pH 2.88. **d**) Hendersonn-Hasselbach plot of aniline protonation calculated from the ratio at 420 nm and 361 nm using previously reported methods[9]. Y-intercept of linear fit equals the pKa of the aniline before (blue, pK_a = 6.6) and after (orange, pK_a = 6.1) reaction with transcycloocteneol

3.3 Targeting LUnAR RhoVRs to specific cellular locations

We first tested a HaloTag targeting system for targeting LUnAR RhoVRs to both the exterior and interior leaflets of the plasma membrane. TCO tethered to a HaloTag chloroalkane ligand via a flexible polyethelenglycol (PEG) linker would first be localized to HaloTag. Then, treatment with LUnAR RhoVR would result in labeling of HaloTag proteins (**Figure 3.3.1a**).

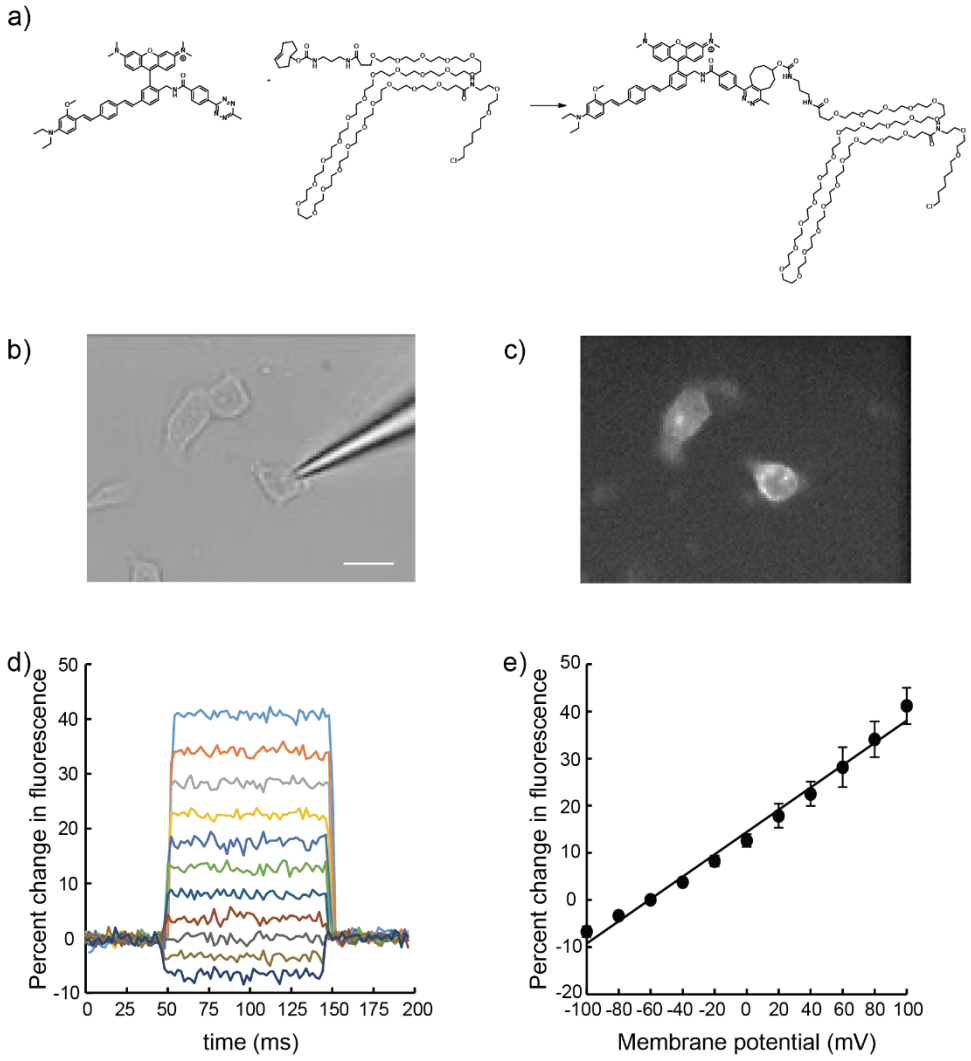

Figure 3.3.1 Patch clamp electrophysiology of LUnAR RhoVR1 pre-reacted with TCO-PEG$_{25}$-Halo. **a**) Schematic of the in-vitro reaction between LUnAR RhoVR1 and TCO-PEG$_{25}$-Halo. The reaction product on the right was used for the plasma membrane patch-clamp electrophysiology experiments. **b**) Visible and **c**) fluorescence images of a representative cell used for patch-clamp measurements. **d**) Concatenated traces of percent change in fluorescence from fluorescence at -60 mV of pre-reacted LUnAR RhoVR1. **e**) Plot of percent change in fluorescence from fluorescence at -60 mV of pre-reacted LUnAR RhoVR1 from n = 3 patches gives a voltage sensitivity of approximately 24% per 100 mV

LUnAR RhoVR1 labels the plasma membrane when HaloTag is localized to the outer leaftlet of the plasma membrane (**Figure 3.3.2a-c**); however, when HaloTag is localized to the inner leaflet of the plasma membrane via palmitoylation[51], we observe very low levels of cellular fluorescence, likely because the long PEG linkers used to ensure voltage

sensitivity of RhoVRs in HaloTag targeted systems[29] prevent substantial internalization of RhoVR (**Figure S2d-f**). Labeling of cells expressing the same inner leaflet-targeted HaloTag show robust fluorescence when labeled with the cell-permeable JF646-HaloTag ligand, supporting this hypothesis (**Figure S2f-h**).

We verified the voltage-sensitivity of the product of LUnAR RhoVR 1 and TCO by reacting TCO-PEG_{25}-Halo (**25**) with LUnAR RhoVR 1 *in vitro* and applying this to cells expressing outer leaflet HaloTag (**Figure 3.3.1**).[29] Patch clamp electrophysiology on these cells reveal that LUnAR RhoVR 1 / TCO conjugates respond to membrane potential change, with a sensitivity of approximately 21% (± 0.72%, S.E.M. for n = 3 cells, **Figure 3.3.1**).

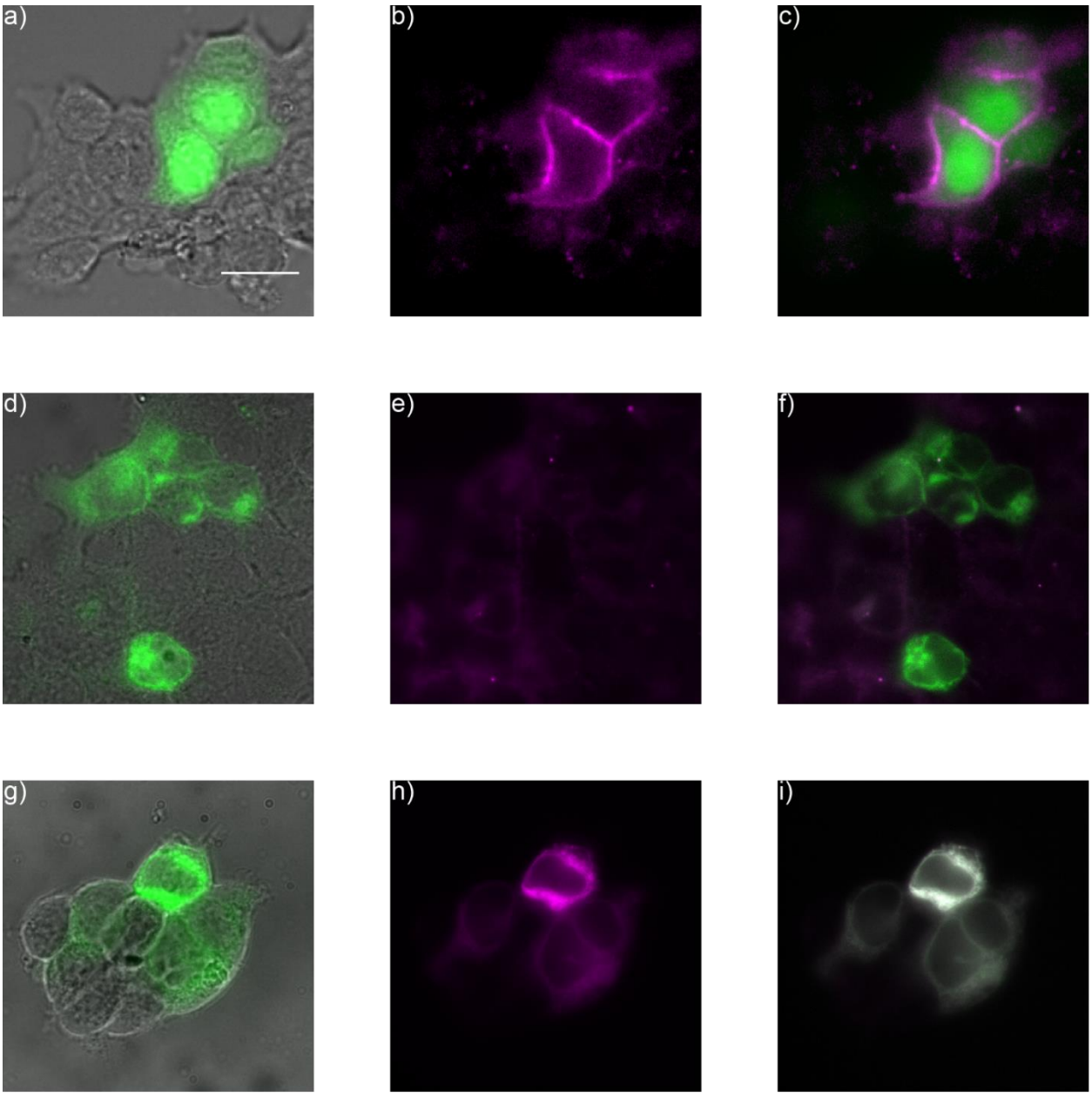

Figure 3.3.2 TCO-PEG25 HaloTag enables extracellular but not intracellular targeting of LUnAR RhoVR. Visible + GFP (**a**), LUnAR1 (**b**), and GFP + LUnAR1 (**c**) images of HEK cells transfected with a previously reported[29] outer-membrane targeting HaloTag protein and stained sequentially with TCO-PEG$_{25}$-Halo for 20 minutes followed by LUnAR RhoVR1 for 90 minutes in HBSS. Visible + GFP (**d**), LUnAR1 (**e**), and GFP + LUnAR1 (**f**) images of HEK cells transfected with an inner-membrane targeted HaloTag protein and stained equivalently do not show the same contrast between transfected and untransfected cells as in **c**. Visible + GFP (**g**), JF646 (**h**), and GFP + JF646 (**i**) images of HEK cells transfected with an inner-membrane targeted HaloTag protein and stained with

cell-permeant JaneliaFluor 646-HaloTag to verify that cell-permeant HaloTag ligands will stain the inner-membrane targeted construct.

After establishing the voltage sensitivity of LUnAR RhoVR1-TCO conjugates at the outer leaflet of the plasma membrane, we turned to the organelle specific lipid-TCO developed by the Schepartz lab for their High Density Environmentally-sensitive probes (HIDE probes)[30] to target LUnAR RhoVRs to organelles. We loaded HeLa cells with a ceramide-TCO that targets the endoplasmic reticulum (ER), followed by loading with LUnAR RhoVR 1 or LUnAR RhoVR 0. Cell treated with Cer-TCO followed by LUnAR RhoVR 1 show strong fluorescence associated with internal structures (**Figure 3.3.3a**, **Figure 3.3.4a**).

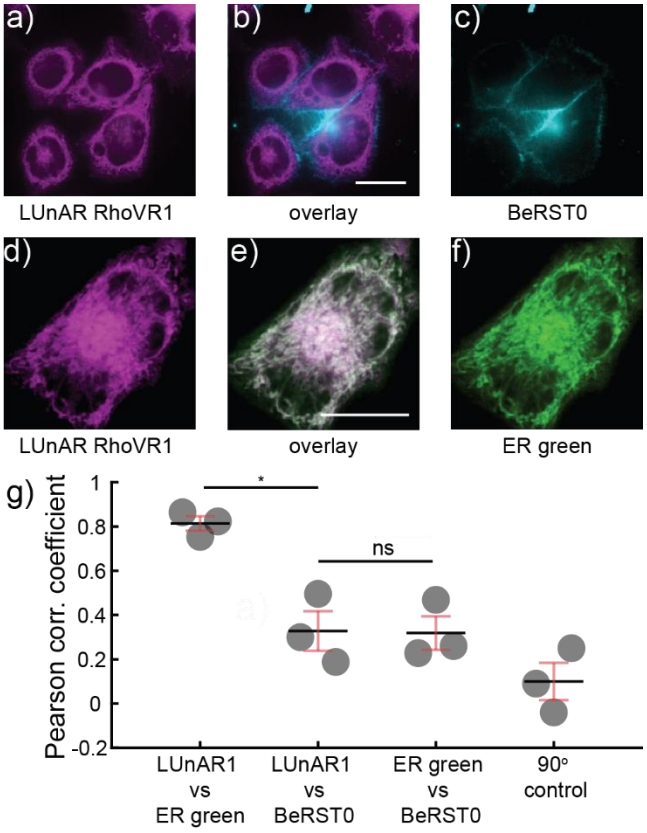

Figure 3.3.3 LUnAR RhoVR 1 + Cer-TCO localize to the endoplasmic reticulum of HeLa cells. Confocal slices of HeLa cells pre-incubated with Cer-TCO followed by labeling with **a)** LUnAR RhoVR 1 (magenta) and **c)** the plasma membrane marker BeRST (cyan). **b)** An overlay of the two signals shows minimal overlap. Scale bar is 20 μm. Confocal slices of HeLa cells pre-incubated with Cer-TCO followed by labeling with **d)** LUnAR RhoVR 1 (magenta) and **f)** ER Tracker Green (green). **e)** An overlay of the two signals shows overlap in white. Scale bar is 20 μm. **d)** Plot of Pearson's coefficients for colocalization analysis of LUnAR RhoVR 1 and ER green or BeRST. 90° control indicates analysis in which one of the images has been rotated 90° during the colocalization analysis. * marks $p < 0.05$; "ns" marks $p > 0.05$ (student's t-test)

LUnAR signal colocalizes with the ER (Pearson's coefficient of 0.8 with ER Tracker Green, **Figure 3.3.3d**) and shows negligible plasma membrane staining (Pearson's coefficient of 0.35 with membrane-associated BeRST,[31] **Figure 3.3.3d, Figure 3.3.4a**). Similar colocalization analysis reveals minimal colocalization with mitochondria (when using mitotracker deep red as a marker for mitochondria[10, 32]) or Golgi (using GalNAc –

BFP[50] as Golgi marker). The voltage insensitive control compound, LUnAR RhoVR 0, shows similar cellular localization (**Figure 3.3.4, 3.3.5, 3.3.6**).

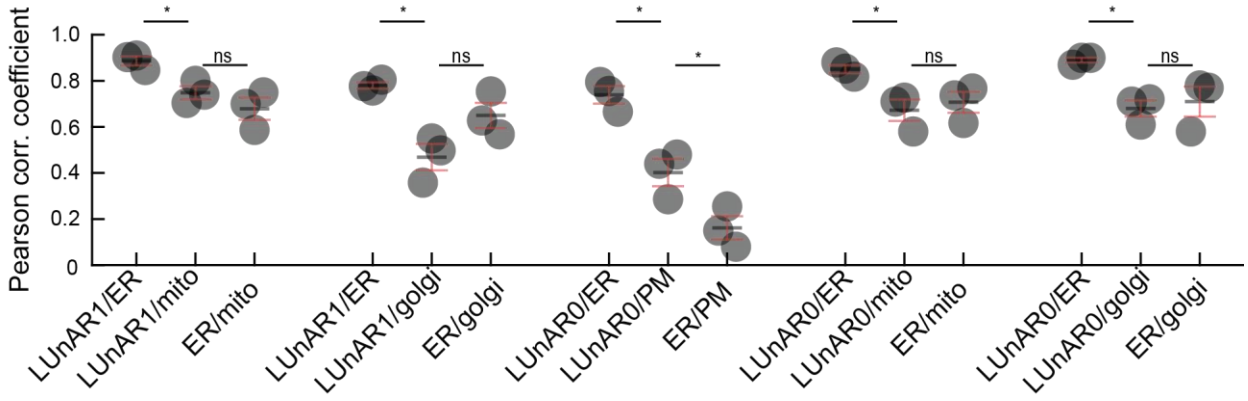

Figure 3.3.4 LUnAR RhoVRs colocalize significantly more with ER marker than with markers for other organelles. Pearson's correlation coefficients between the markers indicated on the x-axis of individual coverslips (gray circles) plotted with the coverslip average (black bar) and error bars denoting SEM across the 3 coverslips (red). * denotes $p<0.05$

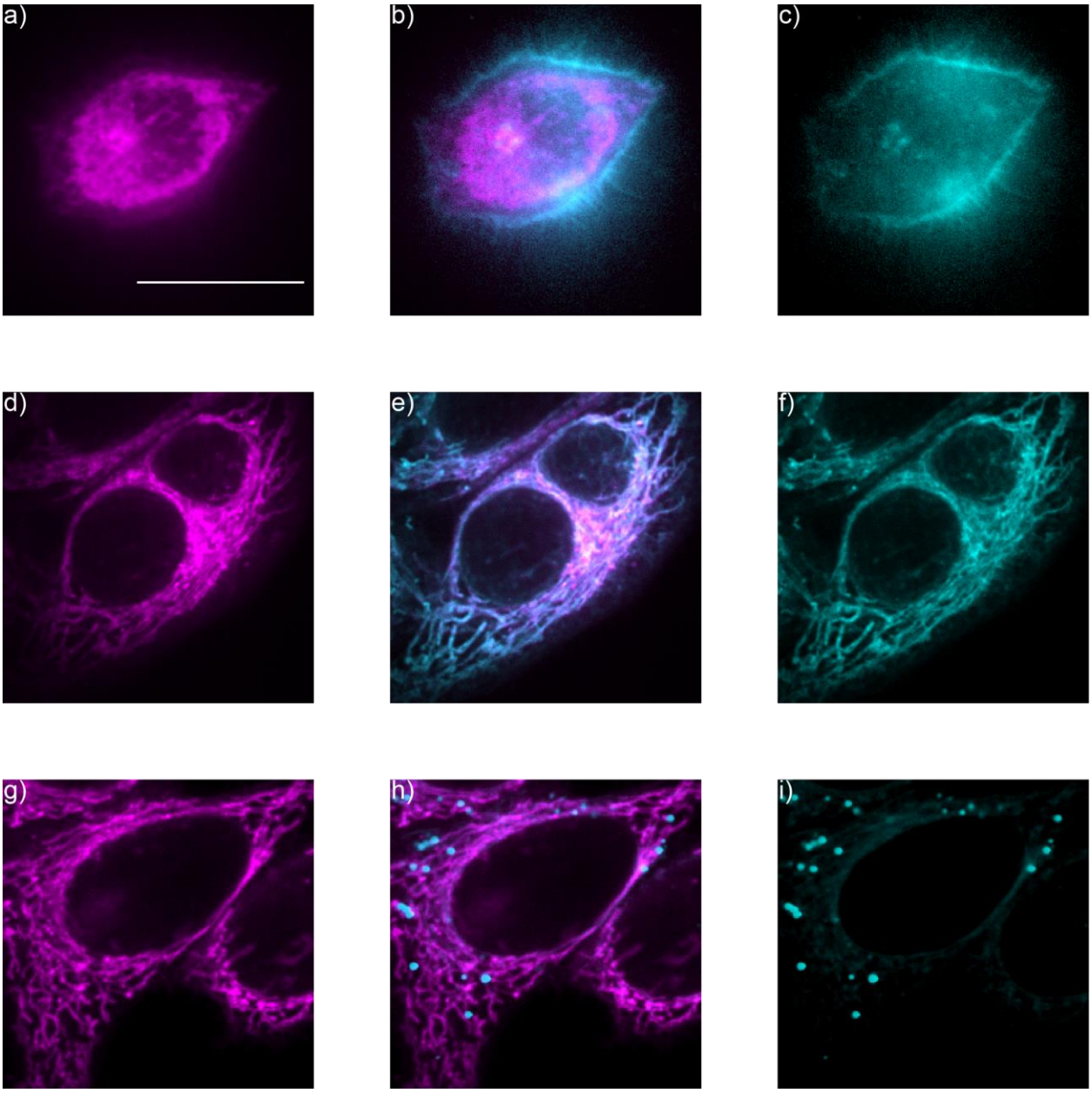

Figure 3.3.5 Visual colocalization of LUnAR RhoVR1 with organelle markers. Representative images of data taken for figure S3. Images of LUnAR RhoVR1 (**a, d,** and **g**) fluorescence merged with plasma membrane marker BeRST (**b**), MitoTracker deep red (**e**), and golgi marker GalNAc-BFP (**h**). Images of isolated fluorescence of plasma membrane marker BeRST (**c**), MitoTracker deep red (**f**), and golgi marker GalNAc-BFP (**i**).

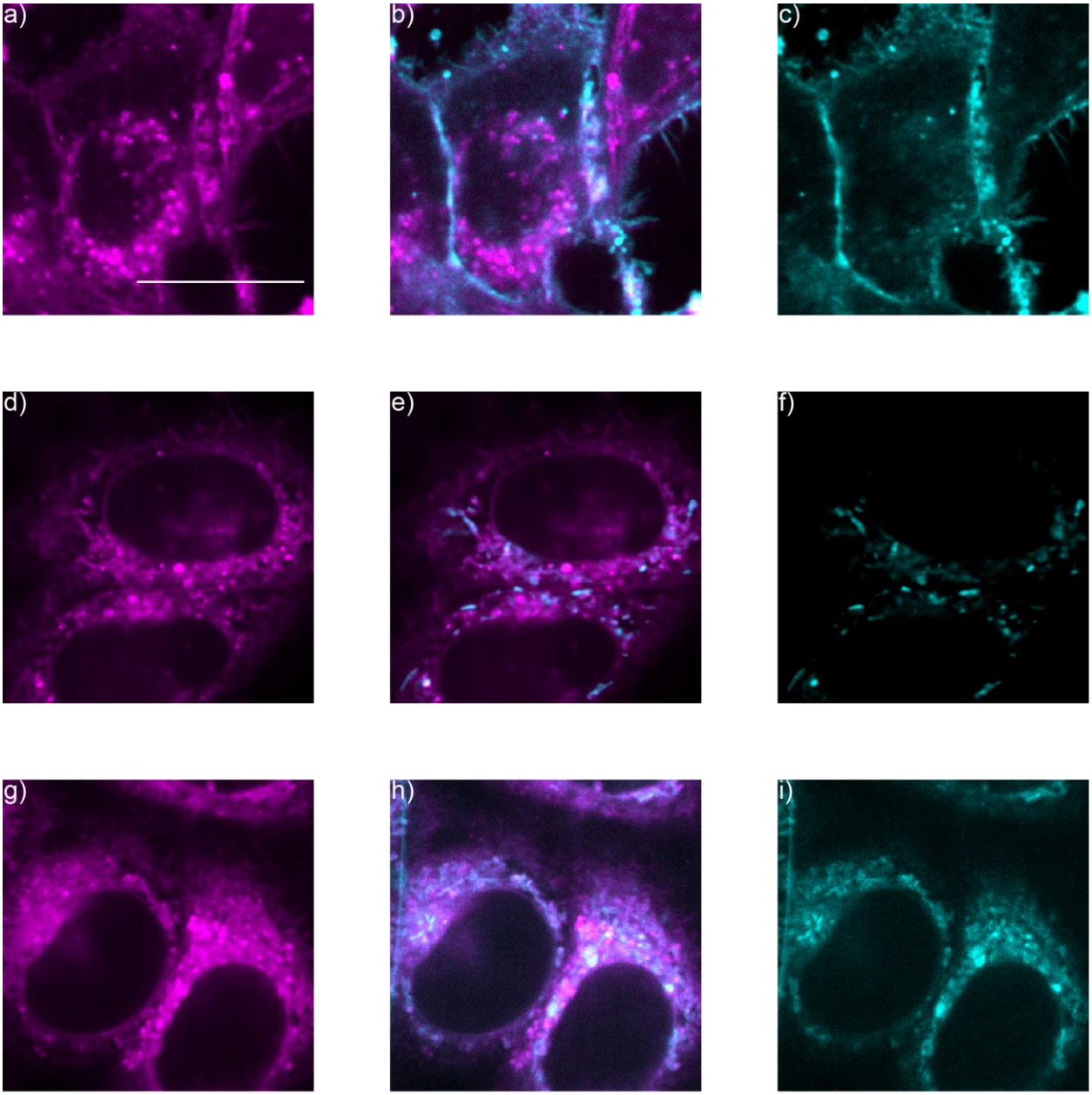

Figure S3B Visual colocalization of LUnAR RhoVR0 with organelle markers. Representative images of data taken for figure S3. Images of LUnAR RhoVR0 (**a, d,** and **g**) fluorescence merged with plasma membrane marker BeRST (**b**), MitoTracker deep red (**e**), and golgi marker GalNAc-BFP (**h**). Images of isolated fluorescence of plasma membrane marker BeRST (**c**), MitoTracker deep red (**f**), and golgi marker GalNAc-BFP (**i**).

3.4 Establishing voltage sensitivity in the ER membrane

Having established that LUnAR RhoVR 1 can label to ER via reacting with pre-localized Cer-TCO (**Figure 3.3.3**) and that the reaction product of LUnAR RhoVR 1 + TCO is voltage sensitive (**Figure 3.3.1**), we next sought to determine whether LUnAR RhoVR 1 is voltage sensitive in the ER membrane. Because of the difficulty associated with patch clamp electrophysiological calibration of ER membrane potential in living cells, we modified a previously reported literature method for inducing voltage changes in intracellular membranes.[6] In our method (**Figure 3.4.1**), cells loaded with LUnAR RhoVR1 targeted to the ER via Cer-TCO are first treated briefly with digitonin to selectively permeabilize the cell membrane, but not organelle membranes. Digitonin permeabilizes cholesterol-rich membranes.[33] The plasma membrane contains up to 50% cholesterol content;[34-35] while ER membranes contain only about 5% cholesterol content.[36-37] Thus, the digitonin treatment selectively permeabilizes the plasma membrane while leaving the ER membrane intact.

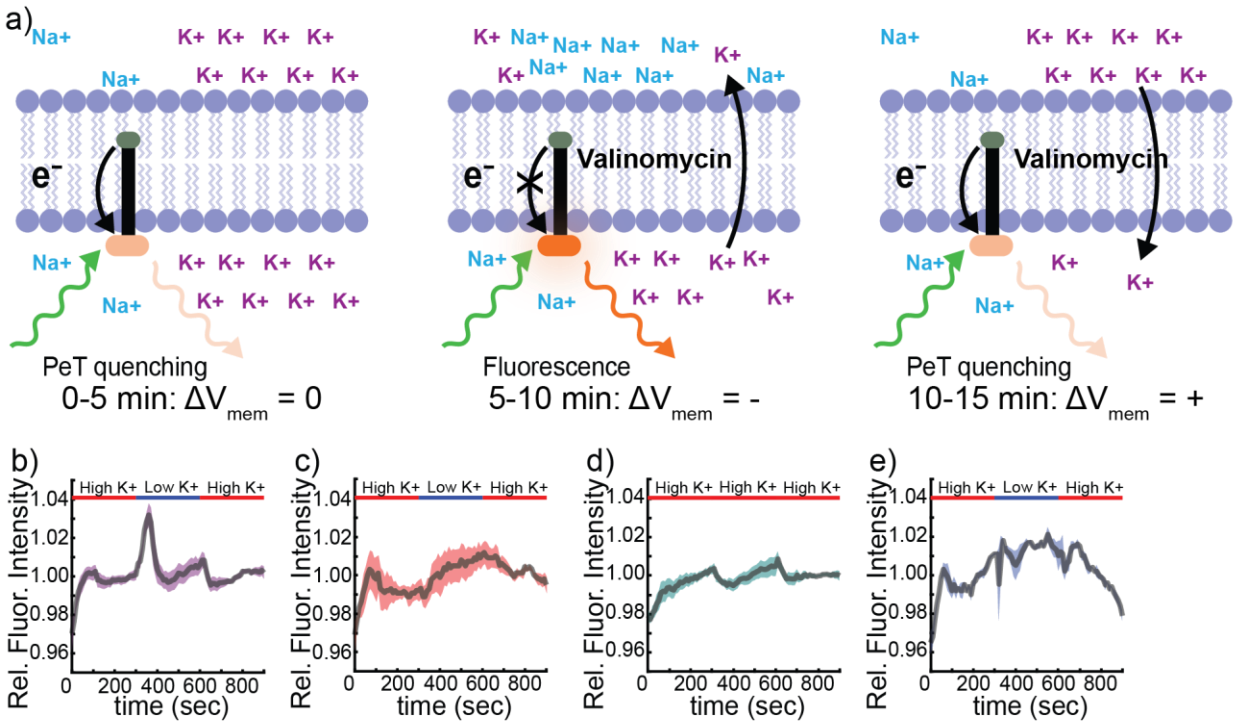

Figure 3.4.1 LUnAR RhoVR1 senses voltage changes across the ER membrane. **a)** Schematic representation of permeabilization, treatment with ionophores, and modulation of [K^+] to change ER membraen potential. Plots of relative RhoVR fluorescence intensity vs. time for Cer-TCO loaded, LUnAR RhoVR 1 stained HeLa cells with **b)** digitonin-

permeabilized plasma membranes or **c)** intact plasma membranes. Red bars indicate high external [K^+] (130 mM) during perfusion, while blue bars indicate low [K^+] (10 mM). **d)** Plot of relative RhoVR fluorescence intensity for cells as in (a), but with a constant high [K^+] (130 mM) perfusion. **e)** Plot of relative RhoVR fluorescence intensity for cells as in (a), but with voltage-insensitive LUnAR RhoVR 0 in place of LUnAR RhoVR 1. Data represent mean values (solid lines) ± error (S.E.M.) for n = 9, 5, 4, or 3 for conditions b, c, d, and e, respectively.

We established plasma permeability by co-incubation with calcein-AM: cells with intact cell membranes retained calcein-AM fluorescence, while cells with permeabilized calcein-AM showed little to no calcein fluorescence.[38] After treatment with digitonin, cells are incubated in a buffer mimicking the intracellular environment (high [K^+] of 130 mM) and containing the potassium ionophores valinomycin and nigericin which allows K^+ ions to equilibrate.

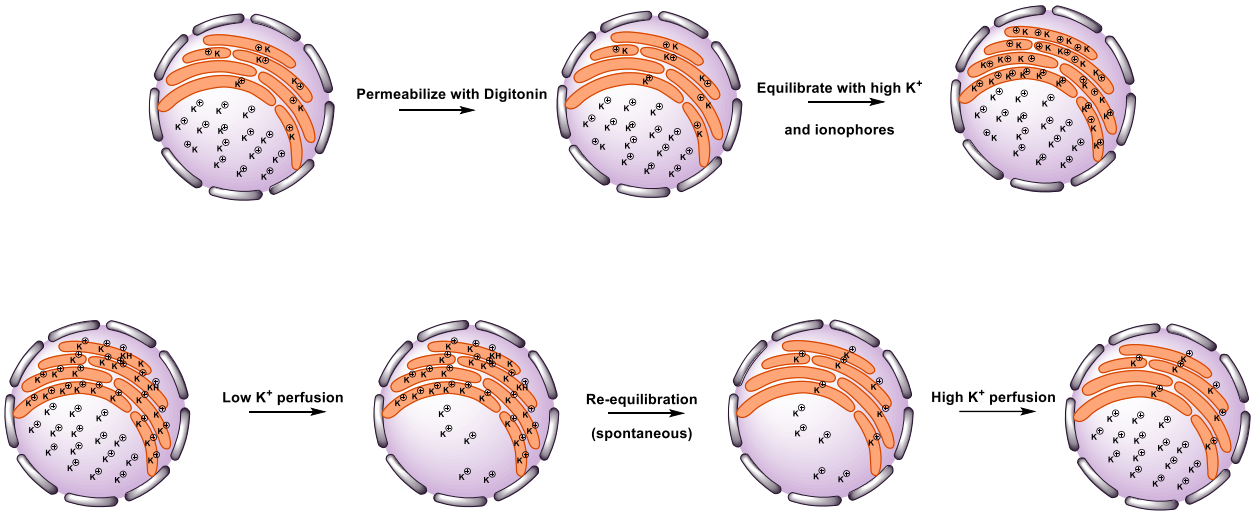

Figure 3.4.2. Schematic of potassium perfusion experiments showing the sequence of events that leads to an induced voltage change at the endoplasmic reticulum

Subsequently, a solution of low [K^+] (10 mM) is perfused onto the cells while fluorescence images are taken over time (**Figure 3.4.2**). A short voltage transient is induced due to the different K^+ concentrations on either side of the ER membrane and high K^+ permeability induced by valinomycin and nigericin, resulting in a net negative potential on the lumenal side of the ER. Accompanying this hyperpolarization is a transient increase in LUnAR RhoVR 1 fluorescence of approximately 5% after correcting for photoinduced fluorescence increases (**Figure 3.4.1b**, **Figure 3.4.3**). When high potassium is perfused back on the cells, a small decrease in fluorescence occurs (**Figure 3.4.1b**). This response is likely smaller due to incomplete equilibration with the low potassium solution and thus a smaller magnitude of the reverse voltage transient.

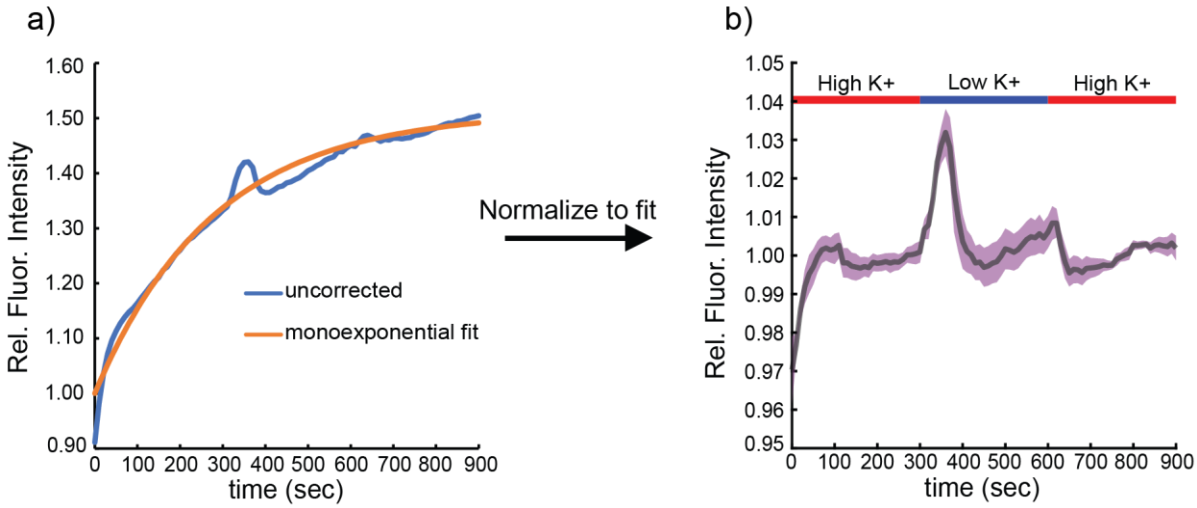

Figure 3.4.3 Photobleach correction facilitates detection of voltage transients in potassium perfusion experiments. Normalized but uncorrected fluorescence intensities of LUnAR RhoVR1 fluorescence during potassium perfusion (blue) and the fit of early and late data points to 1-c1*exp(-c2/t) (orange). Dividing the blue trace in **a** by the orange trace in **a** gives the voltage response traces shown in **b** and in **Figure 3.4.1**

The increase in fluorescence is only observed in cells with permeabilized plasma membranes; non-permeabilized cells in the same dish, identified by their high intracellular calcein fluorescence, do not respond to differing [K^+] perfusion (**Figure 3.4.1c**, **Figure 3.4.4**). In separate control experiments, perfusion with identical high [K^+] solutions results in no fluorescence change (**Figure 3.4.1d**). Finally, if the high/low [K^+] perfusion is repeated with voltage insensitive LUnAR RhoVR 0 instead, we observe no change in fluorescence (**Figure 3.4.1e**).

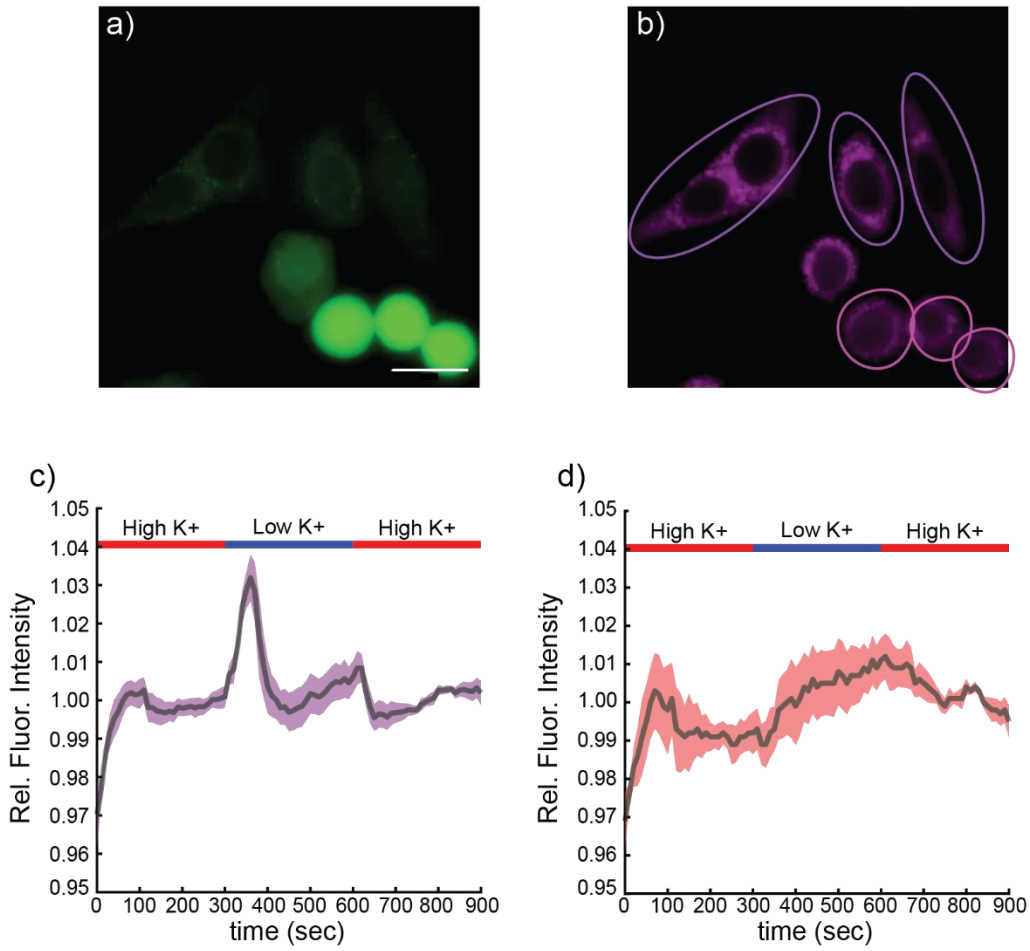

Figure 3.4.4 Calcein control enables selective analysis of permeabilized and non-permeabilized cells. Images of calcein (**a**) staining were used to select permeabilized (**b**, purple) and non-permeabilized (**b**, pink) cells based on calcein fluorescence intensity to separately extract LUnAR RhoVR1 fluorescence data. Purple circled cells (permeabilized) in **b** show a fluorescence change in response to voltage changes (**c**) whereas pink circled cells (non-permeabilized) show no large fluorescence changes in response to voltage changes (**d**)

As an additional control, perfusing FCCP, which transports protons across membranes down their concentration gradient,[39] rather than [K^+], results in minimal changes in fluorescence (**Figure 3.4.5**). This supports the ER localization of LUnAR RhoVR 1, corroborating colocalization data (**Figure 3.3.3**, **Figure 3.3.4, Figure 3.3.5, Figure 3.3.6**),

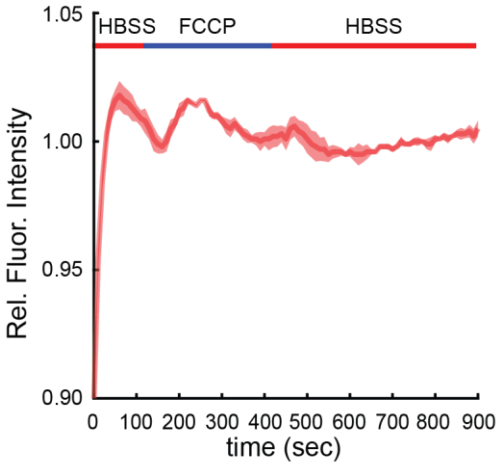

since we previously established that low doses of FCCP (500 nM) cause a change in the mitochondrial membrane potential.[9] It further corroborates that the fluorescence changes we observe upon switching [K^+] result from membrane potential changes in the ER, rather than off-target pH sensing, since the pH of the ER is similar to the cytosol, **Error! Bookmark not defined.** while the pH gradient between the cytosol and other organelles like mitochondria and lysosome is much steeper.[1, 40] Taken together, these results demonstrate that LUnAR RhoVR 1 is able to sense voltage transients in the ER.

Figure 3.4.5 FCCP does not induce large fluorescence changes in LUnAR RhoVR. Corrected LUnAR RhoVR1 fluorescence intensity (red line) +/- SEM (red shading) before (red, left), during (blue), and after (red, right) perfusion of 500 nM FCCP onto cells.

3.5 ER voltage does not change during Ca^{2+} release

Having demonstrated that LUnAR RhoVR1 selective senses ER membrane potential, we move on to use LUnAR RhoVR1 as a functional probe to examine the two physiological processes in which ER membrane potential changes may play a role: Ca^{2+} release from ER stores and electrical coupling between the ER and plasma membranes. We first examined ER voltage changes during Ca^{2+} release. The ER and sarcoplasmic reticulum (SR) are major cellular stores of calcium ions.[41] During various signaling processes, Ca^{2+} channels in the ER/SR are opened and Ca^{2+} is released from these internal stores.[41] Because this represents a major increase in the permeability of the ER membrane to Ca^{2+} and there is a much higher concentration of Ca^{2+} inside the ER than in the cytoplasm, this should result in a decrease in ER membrane potential relative to the cytosol according to the Goldman equation[42] in the absence of movement of other ions:

$$V_{mem} = \frac{RT}{F}\ln\left(\frac{\sum_i^n P_{i+}Z_{i+}[A_{i+}]_{out} + \sum_i^n P_{i-}Z_{i-}[B_{i-}]_{in}}{\sum_i^n P_{i+}Z_{i+}[A_{i+}]_{in} + \sum_i^n P_{i-}Z_{i-}[B_{i-}]_{out}}\right) \qquad \textbf{Equation 3.5.1}$$

Where V_{mem} is the electrical potential difference from the outside of the membrane to the inside, R is the universal gas constant, T is the temperature of the system, F is Faraday's constant, P_{i+} is the permeability of the membrane to a positively charged ionic species, Z_{i+} is the net charge of that species (i.e. +1 for sodium, +2 for calcium, etc.), and $[A_{i+}]$ is the concentration of that species (outside and inside the membrane represented by subscripts). The – subscripts represent the analogous variables for negatively charged

species. If the permeability of Ca^{2+} is much larger than the permeabilities of other ions, as would be the case during Ca^{2+} release, this equation collapses to:

$$V_{mem} = \frac{RT}{F} \ln\left(\frac{[Ca^{2+}]_{out}}{[Ca^{2+}]_{in}}\right) \qquad \textbf{Equation 3.5.2}$$

Thus, if no other ion channels are active during calcium release, the membrane potential across the ER membrane should change from its resting equilibrium state to the calcium equilibrium potential governed by **Equation 3.5.2,** resulting in a hyperpolarization of the ER membrane relative to the cytosol. Physically, what this means is that the movement of Ca^{2+} out of the ER down its concentration gradient should result in a decrease in positive charge in the ER lumen.

Previous reports in skeletal muscle sarcoplasmic reticulum[43] and fragmented sarcoplasmic reticulum[44] have found that sarcoplasmic reticulum membrane potential does not change during Ca^{2+} release. However, the fluorescent reporters used in these experiments have limited time resolution due to their slower kinetics. The genetically encoded voltage indicator (GEVI) used to measure SR membrane potential in intact skeletal muscle is based on Mermaid[45] which has response kinetics of 10s of milliseconds to voltage transients and the internally targeted variant has a response time of 25-150 ms depending on voltage.[45] The synthetic dyes used in previous reports rely on Nernstian redistribution to sense membrane potential transients: too slow to capture rapid voltage transients.[46-47] Potassium may flows into the ER lumen from the cytosol to compensate for the outward flow of Ca^{2+}. However, previous probes used to measure the voltage change were limited in their ability to sense rapid changes in membrane potential by the response times of the probes. VoltageFluors, because of their PeT mechanism, can sense rapid changes in membrane potential,[28, 48] and thus we saw an opportunity to extend the conclusions of prior work by looking for more rapid changes in ER membrane potential in a non-excitable cell line.

Histamine treatment induces Ca^{2+} oscillations in HeLa cells which necessitates release of Ca^{2+} from internal stores.[49] By simultaneously measuring ER membrane potential in HeLa cells with LUnAR RhoVR 1/Cer-TCO at 200 Hz (**Figure 3.5.1a**) and Ca^{2+} oscillations via Oregon Green BAPTA (OGB, **Figure 3.5.1b**), we were able to look for rapid changes in ER voltage that could be linked to Ca^{2+} release. Intact cells were treated with Cer-TCO and LUnAR RhoVR 1 to label ER and OGB (**Figure 3.5.1ab**) and stimulated with histamine to evoke Ca^{2+} release. Fluorescence traces were then aligned so that the steepest increase in OGB fluorescence is synced to t = 0 in all traces (**Figure 3.5.2**). We observe no change from the baseline fluroescence of LUnAR RhoVR during histamine-evoked Ca^{2+} release when examining either individual cells (**Figure 3.5.1c**) or average reponses across multiple trials (**Figure 3.5.1d**).

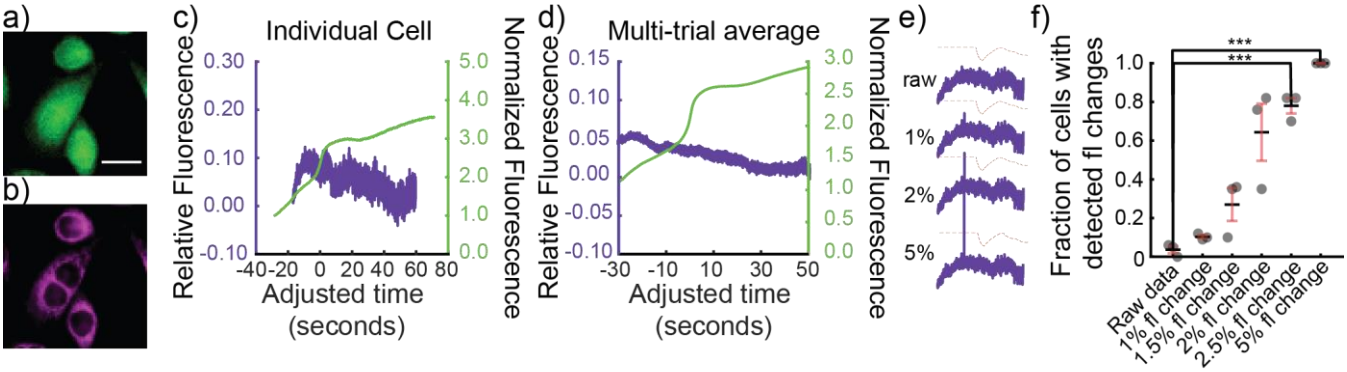

Figure 3.5.1 ER membrane potential does not change during Ca^{2+} release in HeLa cells. **a)** Fluorescence image of HeLa cells treated with Cer-TCO and LUnAR RhoVR 1 to stain the ER. **b)** The same cells were treated with OGB-AM to visualize Ca^{2+} transients. Scale bar is 20 μm.

Plots of LUnAR RhoVR 1 fluorescence (purple) and OGB fluorescence (green) vs time after histamine (100 μM) stimulation from a single HeLa cell 100 μM histamine stimulation (100 μM). Data are for either **c)** a single cell or **d)** the average across 3 different coverslips.

e) adding a fluorescence change of 0%, 1%, 2%, and 5% into the raw trace of a single cell (purple trace) and the threshold for 10 standard deviations above the local average fluorescence (dashed orange trace) used for detection. **f**) Plot of the fraction of individual cells in a single coverslip that have an event detected above the threshold shown in **c** on the raw fluorescence data from histamine trials as well as raw data where a single frame has an added fluorescence change of the amount indicated on the x-axis. *** indicates $p<0.001$ (student's t-test, 2-tailed, unequal variance)

To establish a limit of detection, we developed an automated analysis routine (**Figure 3.5.2**). We examined each cell region of interest (ROI) to search for any cell on a coverslip that has a fluorescence change 10 standard deviations above the noise at any point during the RhoVR recording. We then created artificial positives to test the limit of detection, increasing the fluorescence of an ROI at a single timepoint by 1 to 5% (**Figure 3.5.1**). Then we asked what fraction of cells had detectable single-frame fluorescence changes. The raw data had no cells with a detectable fluorescence change, but the automated analysis could readily detect changes of 2.5% or greater ($p < 0.001$, student's t-test 2-tailed unequal variance, **Figure 3.5.1**). Taken together, these results extend the

current literature hypothesis that voltage changes during Ca^{2+} release from the ER are not electrogenic and are likely compensated for by the movement of other ions into the ER. The more rapid time sensitivity of LUnAR RhoVR1 compared to existing probes rules out rapid voltage transients down to 5 ms in duration and <2.5% ΔF/F. The lower time bound is due to the limits of the image collection rate rather than the limits of probe response kinetics.

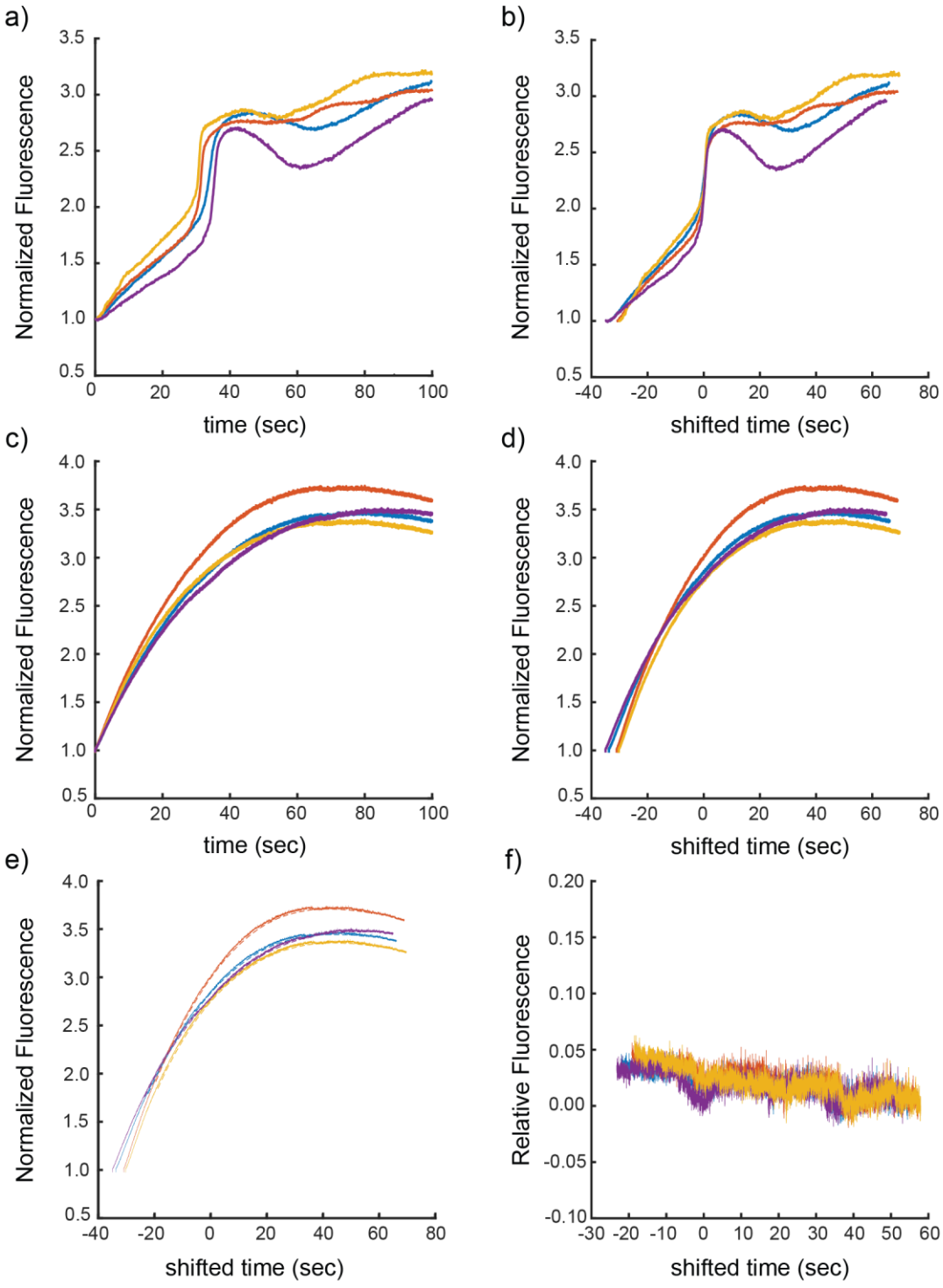

Figure 3.5.2 Time synchronization and average subtraction with and without an artificial pulse establishes limits for voltage transient detection in histamine experiments. Individual cell traces of normalized OGB fluorescence in HeLa cells subjected to histamine stimulation before (**a**) and after (**b**) traces are synchronized in time to align the

traces for future analysis. Individual cell traces of LUnAR RhoVR1 fluoresecence corresponding to unsynchronized calcium traces (**c**) and shifted to match the time shift of the calcium trace from that cell (**d**) needed to synchronize the calcium response with the other cells. **e**) time shifted LUnAR RhoVR1 fluorescence of individual cells (solid line) overlaid with the rolling average used for subtraction (dashed line). **f**) average subtracted LUnAR RhoVR1 fluorescence traces of individual cells; represents dashed line in **e** subtracted from the solid line in **e**.

3.6 ER membrane depolarizes during plasma membrane depolarizations

To further explore the ability of LUnAR RhoVR1 to measure biologically relevant voltage changes, we turned to patch-clamp electrophysiology to examine the electrical relationship between plasma membrane potential and ER membrane potential. A previous report using an internally targeted GEVI gave evidence for electrical coupling between the plasma membrane and the ER in HEK cells and hippocampal neurons.[7] However, these results may be confounded by non-selective localization of the voltage sensor in question. Additionally, the orientation of the previous probe in intracellular membranes is unknown and therefore the direction of fluorescence change cannot be used to determine the direction of the voltage change. We set out to extend these results into another cell line through simultaneous electrical measurements of plasma membrane potential and optical measurements of ER membrane potential. Using whole-cell voltage clamp, we find that induced depolarizing steps in the plasma membrane (**Figure 3.6.1**) are accompanied by depolarization in the ER membrane as observed by decreasing LUnAR RhoVR1 fluorescence (**Figure 3.6.1**). This result establishes the direction of electrical coupling between the plasma membrane and ER membrane in HeLa cells.

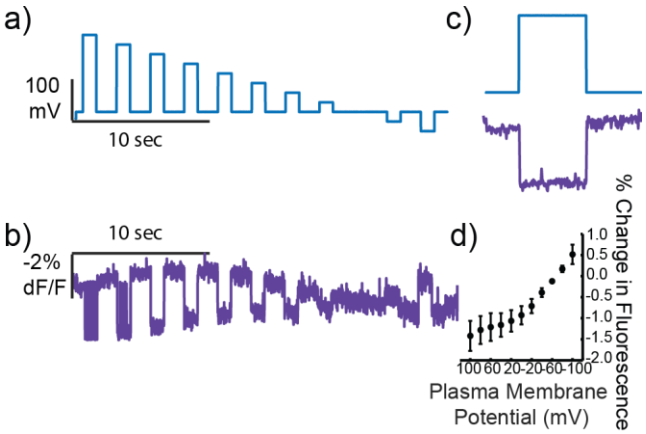

Figure 3.6.1 ER and plasma membrane are electrically coupled in HeLa cells. Representative plasma membrane voltage recordings (**a**), and LUnAR RhoVR1 fluorescence changes (**b**). from HeLa cells voltage clamped to steps 20 mV apart in plasma membrane potential. **c**) expanded plot of voltage and fluorescence from the first pulse in **a** and **b**. **d**) Plot of percent change in fluorescence from fluorescence at -60 mV as a function of plasma membrane potential from n=5 cells voltage clamped as in **a**. Error bars represent +/- standard error of the mean.

3.7 Conclusions and outlook

In this work, we demonstrate a novel small-molecule sensor capable of targeting subcellular membranes. We show that LUnAR RhoVR is capable of targeting the ER and make voltage measurements for two different biologically relevant experiments. The click chemistry targeting approach holds future promise for targeting to other subcellular locations as HIDE probes have been developed for multiple organelles and short HaloTag ligands could enable intracellular genetic targeting. We hope to explore these additional targets in future applications.

3.8 Details of synthesis, characterization, and image analysis

General methods for chemical synthesis and characterization

Chemical reagents and solvents (dry) were purchased from commercial suppliers and used without further purification. Synthesis of meta-bromo-TMR (compound 1), methoxy wire (compound 3), aniline-free wire (compound 7), and BOC-haloamine (compound 23) were carried out as previously reported[7,52,53]. Thin layer chromatography (TLC) (Silicycle, F254, 250 µm) and preparative thin layer chromatography (PTLC) (Silicycle, F254, 1000µm) were performed on glass backed plates pre-coated with silica gel and were visualized by fluorescence quenching under UV light. Flash column chromatography was performed on Silicycle Silica Flash F60 (230–400 Mesh) using a forced flow of air at 0.5–1.0 bar. NMR spectra were measured on Bruker AVB-400 MHz, 100 MHz, AVQ-400 MHz, 100 MHz, Bruker AV-600 MHz, 150 MHz. Variable temperature NMR experiments were measured on the Bruker AV-600 with the assistance of Hasan Celik. Chemical shifts are

expressed in parts per million (ppm) and are referenced to CDCl3 (7.26 ppm, 77.0 ppm) or DMSO (2.50 ppm, 40 ppm). Coupling constants are reported as Hertz (Hz). Splitting patterns are indicated as follows: s, singlet; d, doublet; t, triplet; q, quartet; dd, doublet of doublet; m, multiplet. High-resolution mass spectra (HR-ESI-MS) were measured by the QB3/Chemistry mass spectrometry service at University of California, Berkeley. High performance liquid chromatography (HPLC) and low resolution ESI Mass Spectrometry were performed on an Agilent Infinity 1200 analytical instrument coupled to an Advion CMS-L ESI mass spectrometer. The column used for the analytical HPLC was Phenomenex Luna 5 µm C18(2) (4.6 mm I.D. × 150 mm) with a flow rate of 1.0 mL/min. The mobile phases were MQ-H2O with 0.05% trifluoroacetic acid (eluent A) and HPLC grade acetonitrile with 0.05% trifluoroacetic acid (eluent B). Signals were monitored at 254, 380 and 545 nm over 10 min with a gradient of 10-100% eluent B. The column used for preparative HPLC was Phenomenex Luna 10 µm C18(2) (21.2 mm I.D. x 250 mm) with a flow rate of 30.0 mL/min. The mobile phases were MQ-H2O with 0.05% trifluoroacetic acid (eluent A) and HPLC grade acetonitrile with 0.05% trifluoroacetic acid (eluent B). Signals were monitored at 254 nm over 40 min with a gradient of 30-70% eluent B.

Cell Culture

HeLa cells were plated directly onto 12 mm or 25 mm glass coverslips with no pre-coating. HeLa cells were plated and maintained in Dulbecco's modified eagle medium (DMEM) supplemented with 4.5 g/L D-glucose, 10% FBS and 1% Glutamax. Unless stated otherwise, for loading of all cell lines, 1000x dye stock in DMSO was premixed with 20% pluronic F127 in DMSO and diluted the final indicated concentration of dye and pluronic in 1% casein in dPBS. All imaging experiments were performed in HBSS unless otherwise indicated.

Spectroscopic characterization

For pH studies, a stock solution of RhoVR1 was prepared in DMSO (500 µM) and diluted with PBS (10 mM K2HPO4, 2 mM

KH2PO4, 50 mM Trizma, pH adjusted to indicated value with HCl and NaOH) solution containing 0.10 % (w/w) SDS (1:100-

1:1000 dilution). For quantum yield studies, stock solutions of RhodamineB-tetrazine conjugates and/or RhoVRs were prepared in DMSO (500 µM) and diluted in ethanol with 0.01% HCl. UV-Vis absorbance and fluorescence spectra were recorded using a Shimadzu 2501 Spectrophotometer (Shimadzu) and a Quantamaster Master 4 L-format scanning spectrofluorometer (Photon Technologies International). The fluorometer is equipped with an LPS-220B 75-W xenon lamp and power supply, A-1010B lamp housing

with integrated igniter, switchable 814 photon-counting/analog photomultiplier detection unit, and MD5020 motor driver. Samples were measured in 1-cm path length quartz cuvettes (Starna Cells). Quantum yields were referenced to Rhodamine B in ethanol (0.7)[54]

To determine fluorescence turn-on after reaction with transcyclooctenes, LUnAR RhoVRs (200 µM) were reacted with transcyclooctenes (10 mM) in a 5:1 mixture of water and dioxane until complete consumption of LUnAR RhoVR was observed by LC/MS. Quantum yields were then measured as described above.

Imaging Parameters

Epifluorescence imaging was performed on an AxioExaminer Z-1 (Zeiss) equipped with a Spectra-X Light engine LED light (Lumencor), controlled with Slidebook (v6, Intelligent Imaging Innovations). Images were acquired with either a W-Plan-Apo 20x/1.0 water objective (20x; Zeiss) or a W-Plan-Apo 63x/1.0 water objective (63x; Zeiss). Images were focused onto an OrcaFlash4.0 sCMOS camera (sCMOS; Hamamatsu). Epifluorescence imaging for electrophysiology experiments was performed on an inverted AxioObserver Z-1 (Zeiss), equipped with a Spectra-X Light engine LED light (Lumencor), controlled with µManager (V1.4, open-source, Open Imaging). Images were acquired using a Plan-Apochromat 20/0.8 air objective (20x, Zeiss). Images were focused onto an OrcaFlash4.0 sCMOS camera (sCMOS; Hamamatsu). More detailed imaging information for each experimental application is expanded below. Confocal imaging was performed with a Nikon Inverted Yokogawa spinning disk confocal microscope with 405 nm, 488 nm, 561 nm, and 637 nm laser lines and incubation/CO2 for live-cell imaging controlled via Nikon imaging elements. Images were acquired with a 100x oil objective. In multicolor experiments, filter sets were selected to ensure that bleedthrough contributed <10% of the signal in any given channel by measuring the relative fluorescence of cells stained with a single dye in each excitation/emission path.

For fast LED switching, Lumencor LEDs were controlled via an Arduino box to alternately excite LEDs for the indicated exposure time with ≥3 ms of dropped time in between each frame to allow the camera to read out the fluorescence. The microscope was controlled via HCI image with continuous streaming of frames.

Confocal colocalization of RhoVRs with organelle stains (Fig 3.3.3, 3.3.4, 3.3.5, 3.3.6)

HeLa cells were incubated for 1 hour with 2 µM ceramide-TCO with 0.2% pluronic F127 in 1% casein in dPBS. Cells were then washed 3x with 4.5 g/L D-glucose, 10% FBS and 1% Glutamax and incubated for 1.5 hours with the indicated LUnAR RhoVR with 0.01% pluronic F127 in 1% casein in dPBS. Cells were then washed 3x with 4.5 g/L D-glucose, 10% FBS and 1% Glutamax and incubated for another 2.5 hours. Cells were then incubated for 30 minutes with 1 µM ER tracker green and either 25 nM mitotracker deep red (mitochondria) or 1 µM BeRST (plasma membrane) in HBSS for 30 minutes. Each coverslip was then imaged through a z stack beginning at the cell-coverslip interface and processing upwards through 10 µm total of 0.5 µm steps first in the 637 nm, then the 488 nm, and finally the 561 nm channel. For golgi colocalization, cells were transfected with the GalNAc-BFP plasmid and loaded as above without an organelle stain and then imaged through a z stack of 10 um total of 0.5 um steps first in the 488 nm, then the 561 nm, and finally the 405 nm channel.

Potassium perfusion (Fig 3.4.1, 3.4.2, 3.4.3, 3.4.4)

HeLa cells were incubated for 1 hour with 2 µM ceramide-TCO with 0.2% pluronic F127 in 1% casein in dPBS. Cells were then washed 3x with 4.5 g/L D-glucose, 10% FBS and 1% Glutamax and incubated for 1.5 hours with the indicated LUnAR RhoVR with 0.01% pluronic F127 in 1% casein in dPBS. Cells were then washed 3x with 4.5 g/L D-glucose, 10% FBS and 1% Glutamax and incubated for another 2.5 hours. Cells were then incubated with 250 nM calcein-AM with 0.1% pluronic F127 in 4.5 g/L D-glucose, 10% FBS and 1% Glutamax for 30 minutes. Cells were then loaded with high potassium buffer with 10 µM digitonin and incubated for 30 seconds at 37^{o}C. Cells were then washed 3x with high potassium buffer and then incubated in high potassium buffer for 15 minutes at 37 degrees. Coverslips were then transferred to a perfusion chamber where they were perfused for 1 minute with high potassium buffer, left unperfused for 4 minutes, perfused for 1 minute with either high or low potassium buffer, left unperfused for 4 minutes, perfused again for 1 minute with high potassium buffer, and left unperfused for another 4 minutes. Cells were imaged every 10 seconds for the duration of this procedure. The excitation light was delivered from an LED (0.73 mW/mm^2; 100 ms exposure time) at 542/33 (bandpass) nm and emission was collected with a quadruple emission filter (430/32, 508/14, 586/30, 708/98 nm) after passing through a quadruple dichroic mirror (432/38, 509/22, 586/40, 654 nm LP).

Buffer recipe for potassium perfusion: $CaCl_2$ (2 mM), $MgCl_2$ (2 mM), MgATP (5mM), Glucose (5 mM), HEPES (8 mM), Valinomycin (1 uM), Nigericin (1 uM) at pH 7.4 with:

High potassium: KCl (130 mM), NaCl (10 mM)

Low potassium: KCl (10 mM), NaCl (130 mM)

Histamine stimulation (Fig 3.5.1, 3.5.2)

HeLa cells were incubated for 1 hour with 2 µM ceramide-TCO with 0.2% pluronic F127 in 1% casein in dPBS. Cells were then washed 3x with 4.5 g/L D-glucose, 10% FBS and 1% Glutamax and incubated for 1.5 hours with the indicated LUnAR RhoVR with 0.01% pluronic F127 in 1% casein in dPBS. Cells were then washed 3x with 4.5 g/L D-glucose, 10% FBS and 1% Glutamax and incubated for another 2.5 hours. Cells were then incubated with 1 uM Oregon Green Bapta (OGB) with 0.02% pluronic F127 in 4.5 g/L D-glucose, 10% FBS and 1% Glutamax for 30 minutes. Cells were then washed 1x with HBSS and transferred to a perfusion chamber. Cells were then perfused for 10 seconds with HBSS followed by 90 seconds with 100 µM histamine in HBSS. Cells were imaged continuously using fast LED switching with 17 frames of 2 ms excitation (87 mW/mm^2) at 542/33 (bandpass) nm with 3 ms for camera readout in between followed by 1 frame of 10 ms excitation (14 mW/mm^2) at 475/34 (bandpass) nm with 5 ms for camera readout and emission was collected with a quadruple emission filter (430/32, 508/14, 586/30, 708/98 nm) after passing through a quadruple dichroic mirror (432/38, 509/22, 586/40, 654 nm LP). The frame pattern was looped until the total 100 second acquisition was completed.

Multicolor electrophysiology (Fig 3.6.1)

HeLa cells were incubated for 1 hour with 2 µM ceramide-TCO with 0.2% pluronic F127 in 1% casein in dPBS. Cells were then washed 3x with 4.5 g/L D-glucose, 10% FBS and 1% Glutamax and incubated for 1.5 hours with the indicated LUnAR RhoVR with 0.01% pluronic F127 in 1% casein in dPBS. Cells were then washed 3x with 4.5 g/L D-glucose, 10% FBS and 1% Glutamax and incubated for another 2.5 hours. Cells were then incubated with 500 nM BeRST1 in 4.5 g/L D-glucose, 10% FBS and 1% Glutamax for 30 minutes. Cells were then washed 1x with HBSS and transferred to an attofluor chamber for imaging. Whole-cell, voltage clamp recordings were made with cells held at -60 mV and 1 s hyper- and de- polarizing steps applied from -100 to +100 mV in 20 mV increments. Cells were imaged continuously using fast LED switching with 1 frame of 2

ms excitation (38 mW/mm^2) at 542/33 (bandpass) nm with 3 ms for camera readout in between followed by 1 frame of 2 ms excitation (38 mW/mm^2) at 635/22 (bandpass) nm with 3 ms for camera readout and emission was collected with a quadruple emission filter (430/32, 508/14, 586/30, 708/98 nm) after passing through a quadruple dichroic mirror (432/38, 509/22, 586/40, 654 nm LP). The frame pattern was looped until the total 50 second acquisition was completed.

FCCP perfusion (Fig 3.4.5)

HeLa cells were incubated for 1 hour with 2 µM ceramide-TCO with 0.2% pluronic F127 in 1% casein in dPBS. Cells were then washed 3x with 4.5 g/L D-glucose, 10% FBS and 1% Glutamax and incubated for 1.5 hours with the indicated LUnAR RhoVR with 0.01% pluronic F127 in 1% casein in dPBS. Cells were then washed 3x with 4.5 g/L D-glucose, 10% FBS and 1% Glutamax and incubated for another 3 hours. Cells were then washed 1x with HBSS, and transferred to a perfusion chamber in HBSS. Cells were then imaged under continuous perfusion in HBSS with no additives, vehicle, or FCCP (TCI chemicals) at ~3 mL/min. HBSS was first perfused for 2 minutes followed by FCCP solution for 5 minutes followed by HBSS for 8 minutes. The excitation light was delivered from an LED (0.73 mW/mm^2; 100 ms exposure time) at 542/33 (bandpass) nm and emission was collected with a quadruple emission filter (430/32, 508/14, 586/30, 708/98 nm) after passing through a quadruple dichroic mirror (432/38, 509/22, 586/40, 654 nm LP). Except where indicated otherwise, FCCP was weighed out dry and dissolved in ethanol to make a solution of 500 µM which was then diluted 1000x in HBSS for a final working concentration of 500 nM. Cells were imaged every 10 seconds for 15 minutes at room temperature.

Image analysis

Unless stated otherwise, images were analyzed in ImageJ to extract raw fluorescence values which were then transferred to Excel (Microsoft) or MatLab (MathWorks) for further analysis. ROIs were selected manually to encompass individual cells. Background fluorescence was measured and subtracted from measured fluorescence intensities before intensities were analyzed.

Colocalization analysis (Fig 3.3.3, 3.3.4, 3.3.5, 3.3.6)

ROIs were selected manually to each include contiguous clusters of 1-4 cells. Pearson's values were then assessed individually for each cluster using the coloc2 plugin in ImageJ. Pearson's values for all clusters were then averaged across an individual coverslip. In confocal image stacks, slices that did not contain fluorescence were eliminated before submitting the whole stack for colocalization analysis. Graphs of Pearson's coefficients depict the average Pearson's value as a horizontal bar overlaid with average Pearson's values of a single coverslip. Error bars represent +/- standard error of the mean.

Perfusion analysis (Fig 3.4.1, 3.4.2, 3.4.3, 3.4.4, 3.4.5)

Background subtracted fluorescence intensities for each coverslip were normalized to the average intensity of the first four time points of any perfusion trace. Average traces depict the average normalized fluorescence of the indicated number of coverslips +/- standard error of the mean. For multicolor imaging, ROIs were selected to represent whole cells in the OGB channel or background and these ROIs were used to measure fluorescence in all channels.

For potassium and FCCP experiments, normalized traces were bleach corrected by fitting a subset of initial and final points (t=70-300 and 700-900 for potassium, t=0-120 and 670-900 for FCCP) to a decaying exponential and then normalizing the trace to this fit.

For histamine experiments, LUnAR RhoVR normalized traces were corrected by taking a rolling average of 2000 frames before and 2000 frames after any datapoint subtracting it from that datapoint. Noise was calculated by taking the finding the standard deviation of average subtracted traces taking data from 50 frames before and 50 frames after any point.

Calcium release analysis (Fig 3.5.1, 3.5.2)

Background subtracted fluorescence intensities from individual cells in both the green (OGB) and orange (LUnAR RhoVR) channels were normalized to the average intensity of the first four time points of each cell's trace. An corrected trace was generated by averaging points to either side of a given time point and subtracting this average from the normalized trace to generate a trace that represents the change in average fluorescence.

To align peaks traces from individual cell oscillations to synchronize the calcium transients for analysis, the maximum of the first time derivative, representing the steepest increase in cytosolic calcium concentration, of normalized OGB fluorescence was set to t=0 for each trace and times were adjusted accordingly for each cell's OGB and LUnAR RhoVR fluorescence traces.

To establish the limits of detection of ER voltage transients, a single point in the raw LUnAR RhoVR fluorescence trace was multiplied by 1.0, 1.01, 1.015, 1.02, 1.025, or 1.05 and was subjected to average subtraction as above. A threshold was set to equal 10 times the standard deviation of points 50 points before and 50 points after an individual point and a fluorescence change was considered "detected" if the average subtracted fluorescence was equal or greater to this threshold. Each individual cell on a coverslip was recorded as having either no or 1 or more detected changes and the fraction of cells on each coverslip with detected changes was calculated.

Electrophysiology

Pipettes were pulled from borosilicate glass with filament (Sutter Instruments, Novato, CA), with resistances from 3.5 to 6.5 MΩ with a P97 pipette puller (Sutter Instruments). Pipettes were filled with internal solution of the compositions, in mM: 125 potassium gluconate, 10 KCl, 5 NaCl, 1 EGTA, 10 HEPES, 2 ATP sodium salt, 0.3 GTP sodium salt. EGTA (tetraacid) was prepared as a stock solution in 1 M KOH before addition to the internal solution. Internal solution was pH adjusted to 7.25, and adjusted to 285 mOsmol/L.

Pipettes were positioned with an MP-255 micromanipulator (Sutter Instruments). All voltage step protocols were corrected for a liquid junction potential of -14 mV, determined by the Liquid Junction Potential Calculator in the pClamp software package (Molecular Devices, San Jose, CA).

Electrophysiology recordings were made with an Axopatch 200B amplifier and digitized with a Digidata 1440B digitizer, using the pClamp 10.6 software package (Molecular Devices). Signals were filtered with a 5 kHz low-pass Bessel filter, and correction for pipette capacitance was performed in the cell attached configuration.

Potentials were applied from +100 mV to -100 mV, holding each potential for 1 second, and changing potentials by 20 mV hyperpolarizing steps, with 11 total steps. Cells were held at -60 mV between each step. Patch quality was assessed at the beginning and end

of each recording. Recordings were made for cells with a ratio of membrane resistance (Rm) to access resistance (Ra) of 10:1 at the minimum, and preferably of 30:1, and an Ra value below 30 MΩ. Most cells recorded from had an Rm:Ra ratio of at least 30:1.

Cloning

Plasmid construction for inner membrane HaloTag

For expression in mammalian cells, the construct EGFP-G2S4-HaloTag-HA-CAAX was designed on Benchling into a digested pSNAPf vector backbone (NEB) with a cytomegalovirus (CMV) promoter using a previous HaloTag construct. An EGFP fluorescent protein fused to HaloTag linked with a Glycine-Serine linker. On the C-terminal, an HA epitope tag was added for immunocytochemistry and a CAAX motif sequence was added for endomembrane targeting[51]. All DNA constructs were verified by sequencing and used a Qiagen Miniprep protocol for purification. The following sequences were used (5' to 3').

CMV promoter

GACATTGATTATTGACTAGTTATTAATAGTAATCAATTACGGGGTCATTAGTTCATA
GCCCATATATGGAGTTCCGCGTTACATAACTTACGGTAAATGGCCCGCCTGGCTGA
CCGCCCAACGACCCCCGCCCATTGACGTCAATAATGACGTATGTTCCCATAGTAAC
GCCAATAGGGACTTTCCATTGACGTCAATGGGTGGAGTATTTACGGTAAACTGCCC
ACTTGGCAGTACATCAAGTGTATCATATGCCAAGTACGCCCCCTATTGACGTCAAT
GACGGTAAATGGCCCGCCTGGCATTATGCCCAGTACATGACCTTATGGGACTTTCC
TACTTGGCAGTACATCTACGTATTAGTCATCGCTATTACCATGGTGATGCGGTTTTG
GCAGTACATCAATGGGCGTGGATAGCGGTTTGACTCACGGGGATTTCCAAGTCTC
CACCCCATTGACGTCAATGGGAGTTTGTTTTGGCACCAAAATCAACGGGACTTTCC
AAAATGTCGTAACAACTCCGCCCCATTGACGCAAATGGGCGGTAGGCGTGTACGG
TGGGAGGTCTATATAAGCAGAGCT

EGFP

AGCAAGGGCGAGGAGCTGTTCACCGGGGTGGTGCCCATCCTGGTCGAGCTGGAC
GGCGACGTAAACGGCCACAAGTTCAGCGTGTCCGGCGAGGGCGAGGGCGATGCC
ACCTACGGCAAGCTGACCCTGAAGTTCATCTGCACCACCGGCAAGCTGCCCGTGC
CCTGGCCCACCCTCGTGACCACCCTGACCTACGGCGTGCAGTGCTTCAGCCGCTA
CCCCGACCACATGAAGCAGCACGACTTCTTCAAGTCCGCCATGCCCGAAGGCTAC
GTCCAGGAGCGCACCATCTTCTTCAAGGACGACGGCAACTACAAGACCCGCGCCG
AGGTGAAGTTCGAGGGCGACACCCTGGTGAACCGCATCGAGCTGAAGGGCATCG

ACTTCAAGGAGGACGGCAACATCCTGGGGCACAAGCTGGAGTACAACTACAACAG
CCACAACGTCTATATCATGGCCGACAAGCAGAAGAACGGCATCAAGGTGAACTTC
AAGATCCGCCACAACATCGAGGACGGCAGCGTGCAGCTCGCCGACCACTACCAG
CAGAACACCCCCATCGGCGACGGCCCCGTGCTGCTGCCCGACAACCACTACCTG
AGCACCCAGTCCGCCCTGAGCAAAGACCCCAACGAGAAGCGCGATCACATGGTC
CTGCTGGAGTTCGTGACCGCCGCCGGGATCACTCTCGGCATGGACGAGCTGTACA
AG

G2S4

GGTTCTTCTGGTTCTTCT

HaloTag

ATGGCAGAAATCGGTACTGGCTTTCCATTCGACCCCCATTATGTGGAAGTCCTGGG
CGAGCGCATGCACTACGTCGATGTTGGTCCGCGCGATGGCACCCCTGTGCTGTTC
CTGCACGGTAACCCGACCTCCTCCTACGTGTGGCGCAACATCATCCCGCATGTTG
CACCGACCCATCGCTGCATTGCTCCAGACCTGATCGGTATGGGCAAATCCGACAA
ACCAGACCTGGGTTATTTCTTCGACGACCACGTCCGCTTCATGGATGCCTTCATCG
AAGCCCTGGGTCTGGAAGAGGTCGTCCTGGTCATTCACGACTGGGGCTCCGCTCT
GGGTTTCCACTGGGCCAAGCGCAATCCAGAGCGCGTCAAAGGTATTGCATTTATG
GAGTTCATCCGCCCTATCCCGACCTGGGACGAATGGCCAGAATTTGCCCGCGAGA
CCTTCCAGGCCTTCCGCACCACCGACGTCGGCCGCAAGCTGATCATCGATCAGAA
CGTTTTTATCGAGGGTACGCTGCCGATGGGTGTCGTCCGCCCGCTGACTGAAGTC
GAGATGGACCATTACCGCGAGCCGTTCCTGAATCCTGTTGACCGCGAGCCACTGT
GGCGCTTCCCAAACGAGCTGCCAATCGCCGGTGAGCCAGCGAACATCGTCGCGC
TGGTCGAAGAATACATGGACTGGCTGCACCAGTCCCCTGTCCCGAAGCTGCTGTT
CTGGGGCACCCCAGGCGTTCTGATCCCACCGGCCGAAGCCGCTCGCCTGGCCAA
AAGCCTGCCTAACTGCAAGGCTGTGGACATCGGCCCGGGTCTGAATCTGCTGCAA
GAAGACAACCCGGACCTGATCGGCAGCGAGATCGCGCGCTGGCTGTCGACGCTC
GAGATTTCCGGC

HA

TATCCATATGATGTTCCAGATTATGCT

CAAX motif

AAGATGAGCAAAGATGGTAAAAAGAAGAAAAAGAAGTCAAAGACAAAGTGTGTAAT
TATGTAA

Plasmid construction for GalNAc-BFP

For expression in mammalian cells, the construct pEF-GalNAc-GGS-BFP was designed on Benchling into a double digested plasmid pEF-GalNAc-T2-msGFP provided by Benjamin Glick (Addgene plasmid # 140164; http://n2t.net/addgene:140164; RRID:Addgene_140164) with a eukaryotic translation elongation factor 1 alpha 1 (EF). A golgi marker N-acetylgalactosaminyl transferase 2 (GalNAc) fusion[50] was made with blue fluorescent protein (EBFP) with a glycine serine linker (GGS). All DNA constructs were verified with sequencing and used a Qiagen Miniprep protocol for purification. The following sequences were used (5’ to 3’).

EF-1-alpha promoter

GGCTCCGGTGCCCGTCAGTGGGCAGAGCGCACATCGCCCACAGTCCCCGAGAAG
TTGGGGGGAGGGGTCGGCAATTGAACCGGTGCCTAGAGAAGGTGGCGCGGGGTA
AACTGGGAAAGTGATGTCGTGTACTGGCTCCGCCTTTTTCCCGAGGGTGGGGGAG
AACCGTATATAAGTGCAGTAGTCGCCGTGAACGTTCTTTTTCGCAACGGGTTTGCC
GCCAGAACACAGGTAAGTGCCGTGTGTGGTTCCCGCGGGCCTGGCCTCTTTACGG
GTTATGGCCCTTGCGTGCCTTGAATTACTTCCACCTGGCTCCAGTACGTGATTCTT
GATCCCGAGCTGGAGCCAGGGGCGGGCCTTGCGCTTTAGGAGCCCCTTCGCCTC
GTGCTTGAGTTGAGGCCTGGCCTGGGCGCTGGGGCCGCCGCGTGCGAATCTGGT
GGCACCTTCGCGCCTGTCTCGCTGCTTTCGATAAGTCTCTAGCCATTTAAAATTTTT
GATGACCTGCTGCGACGCTTTTTTTCTGGCAAGATAGTCTTGTAAATGCGGGCCAG
GATCTGCACACTGGTATTTCGGTTTTTGGGGCCGCGGGCGGCGACGGGGCCCGT
GCGTCCCAGCGCACATGTTCGGCGAGGCGGGGCCTGCGAGCGCGGCCACCGAG
AATCGGACGGGGGTAGTCTCAAGCTGGCCGGCCTGCTCTGGTGCCTGGCCTCGC
GCCGCCGTGTATCGCCCCGCCCTGGGCGGCAAGGCTGGCCCGGTCGGCACCAG
TTGCGTGAGCGGAAAGATGGCCGCTTCCCGGCCCTGCTCCAGGGGGCTCAAAAT
GGAGGACGCGGCGCTCGGGAGAGCGGGCGGGTGAGTCACCCACACAAAGGAAA
GGGGCCTTTCCGTCCTCAGCCGTCGCTTCATGTGACTCCACGGAGTACCGGGCGC
CGTCCAGGCACCTCGATTAGTTCTGGAGCTTTTGGAGTACGTCGTCTTTAGGTTGG
GGGGAGGGGTTTTATGCGATGGAGTTTCCCCACACTGAGTGGGTGGAGACTGAAG
TTAGGCCAGCTTGGCACTTGATGTAATTCTCCTTGGAATTTGCCCTTTTTGAGTTTG
GATCTTGGTTCATTCTCAAGCCTCAGACAGTGGTTCAAAGTTTTTTTCTTCCATTTC
AGGTGTCGTGA

GALNACT2

ATGAGGCGGCGCTCGAGGATGCTGCTCTGCTTCGCCTTCCTGTGGGTGCTGGGAA
TCGCCTACTACATGTACTCGGGAGGAGGATCTGCGCTGGCCGGAGGAGCGGGAG
GAGGAGCCGGCAGGAAGGAGGACTGGAATGAAATTGACCCCATTAAAAAGAAAGA
CCTTCATCACAGCAATGGAGAAGAGAAAGCACAAAGCATGGAGACCCTCCCTCCA
GGGAAAGTACGGTGGCCAGACTTTAACCAGGAAGCTTATGTTGGAGGGACGATGG
TCCGCTCCGGGCAGGACCCTTACGCCCGCAACAAGTTCAACCAGGTGGAGAGTG
ATAAGCTTCGAATGGATAGAGCCATCCCTGACACCCGGCATGACCAGTGTCAGCG
GAAGCAGTGGCGGGTGGATCTGCCGGCCACCAGCGTGGTGATCACGTTTCACAAT
GAAGCCAGGTCGGCCCTACTCAGGACCGTGGTCAGCGTGCTTAAGAAAAGCCCG
CCCCATCTCATAAAAGAAATCATCTTGGTGGATGACTACAGCAATGATCCTGAGGA
CGGGGCTCTCTTGGGGAAAATTGAGAAAGTGCGAGTTCTTAGAAATGATCGACGA
GAAGGCCTCATGCGCTCACGGGTTCGGGGGGCCGATGCTGCCCAAGCCAAGGTC
CTGACCTTCCTGGACAGTCACTGCGAGTGTAATGAGCACTGGCTGGAGCCCCTCC
TGGAAAGGGTGGCGGAGGACAGGACTCGGGTTGTGTCACCCATCATCGATGTCAT
TAATATGGACAACTTTCAGTATGTGGGGGCATCTGCTGACTTGAAGGGCGGTTTTG
ATTGGAACTTGGTATTCAAGTGGGATTACATGACGCCTGAGCAGAGAAGGTCCCG
GCAGGGGAACCCAGTCGCCCCTATAAAAACCCCCATGATTGCTGGTGGGCTGTTT
GTGATGGATAAGTTCTATTTTGAAGAACTGGGGAAGTACGACATGATGATGGATGT
GTGGGGAGGAGAGAACCTAGAGATCTCGTTCCGCGTGTGGCAGTGTGGTGGCAG
CCTGGAGATCATCCCGTGCAGCCGTGTGGGACACGTGTTCCGGAAGCAGCACCC
CTACACGTTCCCGGGTGGCAGTGGCACTGTCTTTGCCCGAAACACCCGCCGGGCA
GCAGAGGTCTGGATGGATGAATACAAAAATTTCTATTATGCAGCAGTGCCTTCTGC
TAGAAACGTTCCTTATGGAAATATTCAGAGCAGATTGGAGCTTAGGAAGAAACTCA
GCTGCAAGCCTTTCAAATGGTACCTTGAAAATGTCTATCCAGAGTTAAGGGTTCCA
GACCATCAGGATATAGCTTTTGGGGCCTTGCAGCAGGGAACTAACTGCCTCGACA
CTTTGGGACACTTTGCTGATGGTGTGGTTGGAGTTTATGAATGTCACAATGCTGGG
GGAAACCAGGAATGGGCCTTGACGAAGGAGAAGTCGGTGAAGCACATGGATTTGT
GCCTTACTGTGGTGGACCGGGCACCGGGCTCTCTTATAAAGCTGCAGGGCTGCCG
AGAAAATGACAGCAGACAGAAATGGGAACAGATCGAGGGCAACTCCAAGCTGAGG
CACGTGGGCAGCAACCTGTGCCTGGACAGTCGCACGGCCAAGAGCGGGGGCCTA
AGCGTGGAGGTGTGTGGCCCGGCCCTTTCGCAGCAGTGGAAGTTCACGCTCAAC
CTGCAGCAG

GGS LINKER

GGAGGAAGCGGAGGAAGC

EBFP

ATGAGCAAGGGCGAGGAGCTGTTCACCGGGGTGGTGCCCATCCTGGTCGAGCTG
GACGGCGACGTAAACGGCCACAAGTTCAGCGTGTCCGGCGAGGGCGAGGGCGAT
GCCACCTACGGCAAGCTGACCCTGAAGTTCATCTGCACCACCGGCAAGCTGCCCG
TGCCCTGGCCCACCCTCGTGACCACCCTGAGCCACGGCGTCCAGTGCTTCAGTCG
CTACCCCGACCACATGAAGCAGCACGACTTCTTCAAGTCCGCCATGCCCGAAGGC
TACGTCCAGGAGCGCACCATCTTCTTCAAGGACGACGGCAACTACAAGACCCGCG
CCGAGGTGAAGTTCGAGGGCGACACCCTGGTGAACCGCATCGAGCTGAAGGGCA
TCGACTTCAAGGAGGACGGCAACATCCTGGGGCACAAGCTGGAGTACAACTTCAA
CAGCCACAACGTCTATATCATGGCCGACAAGCAGAAGAACGGCATCAAGGTGAAC
TTCAAGATCCGCCACAACATCGAGGACGGCAGCGTGCAGCTCGCCGACCACTACC
AGCAGAACACCCCCATCGGCGACGGCCCCGTGCTGCTGCCCGACAGCCACTACC
TGAGCACCCAGTCCGCCCTGAGCAAAGACCCCAACGAGAAGCGCGATCACATGGT
CCTGCTGGAGTTCGTGACCGCCGCCGGGATCACTCTCGGCATGGACGAGCTGTA
CAAGTAA

Immunocytochemistry

To detect expression and localization of HaloTag and other protein markers, HeLa cells were fixed with 4% paraformaldehyde in PBS for 10 min and permeabilized (if required) with 0.3% v/v Triton-X100 (Sigma Aldrich) in PBS for 2 min. Blocking was done in 5% w/v bovine serum albumin (BSA; Sigma Aldrich) in PBS for 1 h. Primary antibody was incubated at 4 °C overnight with a nuclear Hoechst stain, followed by AlexaFluor secondary antibody (Life Technologies) at room temperature for 4 h. All antibodies were used at 1:1000 dilution.

Name	**Primary/Secondary**	**Manufacturer**	**Catalog #**	**Isotype**
Anti-HA	Primary	CST	3724S	Rabbit IgG
Anti-rabbit 647	Secondary	Life Technologies	A21244	Goat IgG

Scheme 3.8.1 Structures of compounds used in this study

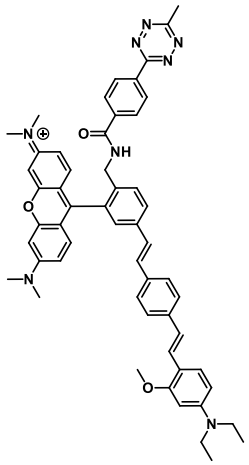

LUnAR RhoVR1

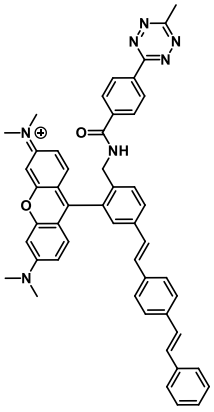

LUnAR RhoVR0

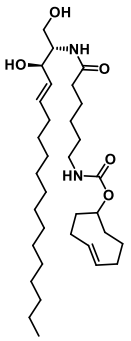

Ceramide-TCO

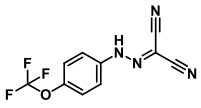

Carbonyl cyanide 4-(trifluoromethoxy)phenylhydrazone (FCCP)

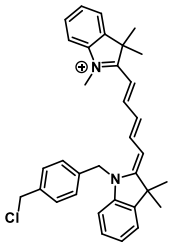

MitoTracker Deep Red

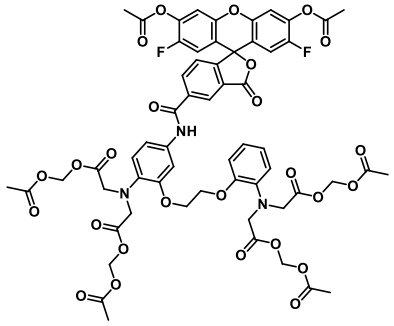

Oregon Green BAPTA

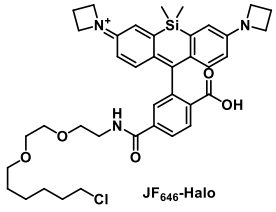

JF_{646}-Halo

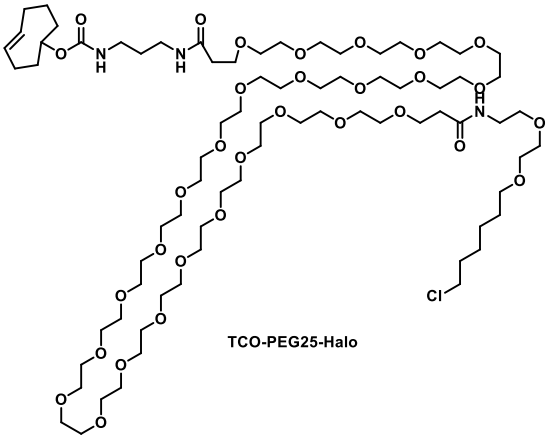

TCO-PEG25-Halo

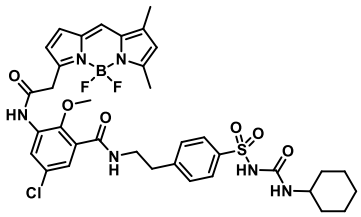

ER Tracker Green

Scheme 3.8.2.

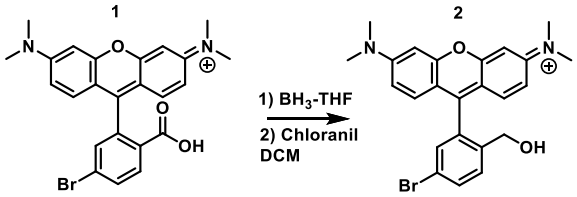

Synthesis of meta-bromo TMR-OH, 2:
Compound **1** (52 mg, 0.11 mmol) was added to a Schlenk flask and evacuated and backfilled 3x with nitrogen. Compound **1** was then dissolved in 0.5 mL anhydrous THF and 1M borane-THF (0.22 mL, 0.22 mmol) was added dropwise and the reaction was then heated to 60^{o}C for 6 hours. The reaction was then quenched with methanol and the solvent evaporated under reduced pressure. The crude product was then immediately redissolved in dichloromethane and chloranil (27 mg, 0.11 mmol) was added and the reaction was stirred for 1 hour. The crude material was then extracted 3x with saturated sodium chloride and the organic layer dried over sodium sulfate, filtered, and concentrated under reduced pressure and then purified by flash chromatography (silica, 10% MeOH in DCM) to yield compound **2** (21 mg, 42% yield)

^{1}H NMR (400 MHz, CD_3Cl) δ 8.13 (d, J = 8.0 Hz, 2H), 7.41 (dd, J = 16.4, 8.0 Hz, 5H), 7.30 (d, J = 8.1 Hz, 2H), 6.88 (s, 2H), 6.83 (s, 1H), 6.76 (d, J = 8.8 Hz, 2H), 6.44 (d, J = 7.9 Hz, 3H), 6.29 (d, J = 8.5 Hz, 1H), 6.17 (s, 1H), 5.90 (d, J = 2.6 Hz, 2H), 5.29 (d, J = 5.8 Hz, 3H), 3.85 (s, 3H), 3.37 (q, J = 6.4 Hz, 4H), 3.17 (s, 2H), 3.11 (s, 3H), 2.93 (s, 12H), 1.17 (t, J = 6.9 Hz, 6H).

Scheme 3.8.3

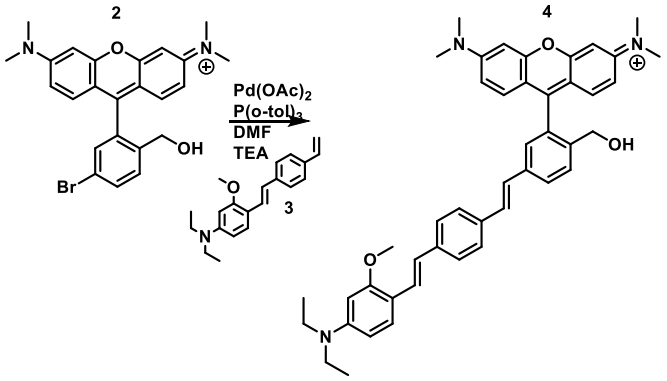

Synthesis of RhoVR1-OH, 4:

Compound **2** (72 mg, 0.16 mmol), compound **3** (55 mg, 0;18 mmol), Palladium II acetate (0.36 mg, 0.0016 mmol), and tri-o-tolyl phosphine (1 mg, 0.003 mmol) were loaded into a dry schlenk flask which was evacuated and backfilled 3x with nitrogen. Reagents were then dissolved in approximately 2 mL anhydrous dimethylformamide and 1 mL anhydrous triethylamine and stirred overnight at 110^{o}C. Reagents were then concentrated under reduced pressure, extracted 5x with 0.1 M HCl, the organic layer dried over sodium sulfate, filtered, and concentrated under reduced pressure. The crude material was purified by flash chromatography (silica, 10% MeOH in DCM) and subsequently purified by preparative HPLC (C18, 30-70% MeCN in H_20 with TFA) to yield compound **4** (21 mg, 19% yield)

^{1}H NMR (400 MHz, CDCl3) δ 7.49 (d, J = 8.1 Hz, 1H), 7.44 (d, J = 2.2 Hz, 1H), 7.42 – 7.34 (m, 3H), 7.10 – 7.06 (m, 1H), 6.99 (s, 1H), 6.96 (d, J = 3.9 Hz, 1H), 6.89 (d, J = 16.4 Hz, 1H), 6.83 (d, J = 8.8 Hz, 2H), 6.49 (s, 2H), 6.44 (d, J = 9.0 Hz, 2H), 6.39 – 6.27 (m, 1H), 6.18 (s, 1H), 5.23 (s, 2H), 5.12 (s, 1H), 3.87 (s, 2H), 3.80 (s, 1H), 3.65 (d, J = 3.6 Hz, 2H), 3.43 – 3.36 (m, 3H), 3.34 (d, J = 7.4 Hz, 4H), 3.12 (d, J = 7.3 Hz, 1H), 2.96 (s, 8H), 1.18 – 1.16 (t, 6H).

Scheme 3.8.4

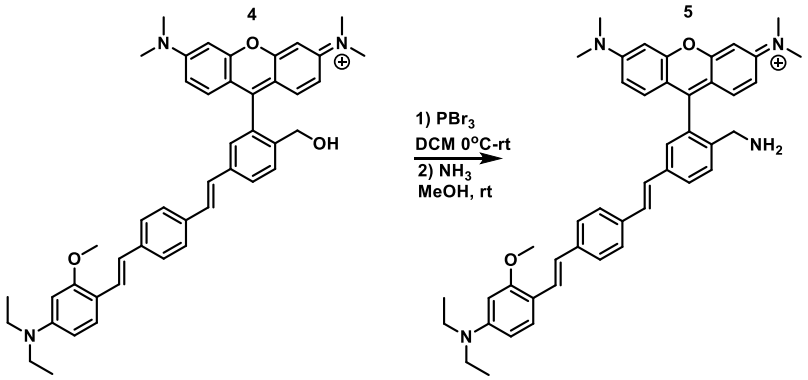

Synthesis of RhoVR1-amine, 5:
Compound **4** (21 mg, 0.031 mmol) was dissolved in approximately 1 mL dichloromethane and cooled to 0°C. 1M Phosphorous tribromide (0.04 mL, 0.04 mmol) was added dropwise and the reaction was allowed to warm to room temperature for 2 hours. The reaction was then quenched with methanol and the crude material concentrated under reduced pressure and redissolved in 2N ammonia in methanol (0.21 mL, 1.5 mmol). The reaction was then stirred overnight at room temperature, concentrated under reduced pressure, and purified via preparative HPLC (C18, 30-70% MeCN in H_2O with TFA) to yield compound **5** (4 mg, 20% yield)

^{1}H NMR (600 MHz, CDCl3) δ 7.46 – 7.41 (m, 3H), 7.37 – 7.30 (m, 3H), 7.28 (d, J = 8.3 Hz, 1H), 7.11 – 7.06 (m, 1H), 6.97 (d, J = 8.4 Hz, 1H), 6.94 (d, J = 13.1 Hz, 1H), 6.89 (d, J = 16.2 Hz, 1H), 6.84 (dd, J = 8.7, 6.2 Hz, 2H), 6.47 (dd, J = 4.4, 2.6 Hz, 2H), 6.43 (ddd, J = 8.7, 4.9, 2.6 Hz, 2H), 6.30 (dd, J = 8.7, 2.5 Hz, 1H), 6.18 (dd, J = 9.1, 2.5 Hz, 1H), 6.09 (dd, J = 8.7, 2.5 Hz, 1H), 4.46 (s, 2H), 3.87 (s, 2H), 3.80 (s, 1H), 3.39 (p, J = 4.5 Hz, 3H), 3.35 – 3.32 (m, 1H), 2.95 (s, 12H), 1.20 (d, J = 2.3 Hz, 4H), 1.18 – 1.15 (m, 2H).

HRMS (ESI+) Calculated for $C_{45}H_{49}N_4O_2$+ $[M]^+$: 677.3850; Found 677.3846

Scheme 3.8.5

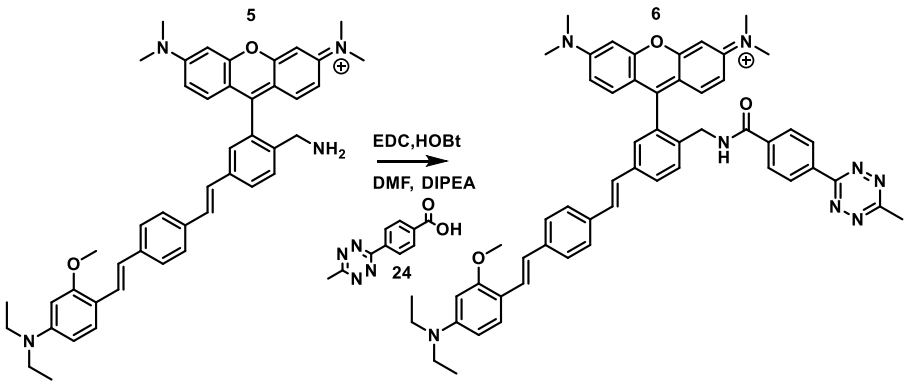

Synthesis of LUnAR RhoVR1, 6:

Compound **24** (19 mg, 0.089 mmol) was dissolved in approximately 1 mL dimethylformamide and diisopropylethylamine (64 µL, 0.37 mmol) was added. The reaction was then cooled to 0°C and EDC (14 mg, 0.089 mmol), HOBt (13 mg, 0.096 mmol) and compound **5** (52 mg, 0.077 mmol) were added and the reaction was stirred at room temperature overnight. The reaction was then concentrated under reduced pressure, redissolved in DMC and extracted 5x with 5% LiCl, and the organic layer dried over sodium sulfate and concentrated under reduced pressure. The crude material was purified by preparative TLC (silica, 5% MeOH in DCM) to yield compound **6** (26 mg, 40% yield)

^{1}H NMR (400 MHz, CDCl3) δ 8.13 (d, J = 8.0 Hz, 2H), 7.41 (dd, J = 16.4, 8.0 Hz, 5H), 7.30 (d, J = 8.1 Hz, 2H), 6.88 (s, 2H), 6.83 (s, 1H), 6.76 (d, J = 8.8 Hz, 2H), 6.44 (d, J = 7.9 Hz, 3H), 6.29 (d, J = 8.5 Hz, 1H), 6.17 (s, 1H), 5.90 (d, J = 2.6 Hz, 2H), 5.29 (d, J = 5.8 Hz, 3H), 3.85 (s, 3H), 3.37 (q, J = 6.4 Hz, 4H), 3.17 (s, 2H), 3.11 (s, 3H), 2.93 (s, 12H), 1.17 (t, J = 6.9 Hz, 6H).

HRMS (ESI+) Calculated for $C_{55}H_{55}N_8O_3$+ $[M]^+$: 875.4392; Found 875.4371

Scheme 3.8.6

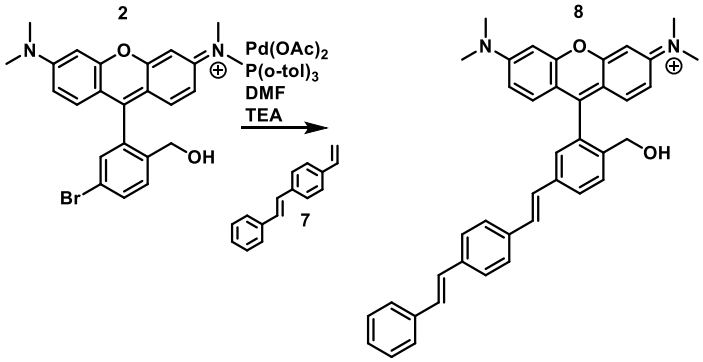

Synthesis of RhoVR0-OH, 8:

Compound **2** (99 mg, 0.22 mmol), compound **7** (58 mg, 0.28 mmol), palladium II acetate (0.5 mg, 0.0022 mmol), and tri o-tolyl phosphine (1.4 mg,0.004 mmol) were added to a dry Schlenk flask which was then evacuated and backfilled 3x with nitrogen. 2 mL anhydrous dimethylformamide and 2 mL anhydrous triethylamine were then added by syringe and the reaction was heated to 110^{o}C and stirred overnight. The reaction was then cooled to 0^{o}C, concentrated under reduced pressure, extracted 5x with 0.1M HCl and dichloromethane, and the organic layer was dried over sodium sulfate and concentrated under reduced pressure. The crude material was purified by flash chromatography (silica, 0-10% MeOH in DCM) to yield compound **8** (108 mg, 85% yield)

^{1}H NMR (400 MHz, MeOD) δ 7.53 (s, 3H), 7.49 (s, 3H), 7.39 (s, 3H), 7.31 (s, 3H), 7.12 (s, 4H), 6.87 (d, J = 8.4 Hz, 2H), 6.56 – 6.50 (m, 4H), 5.29 (s, 2H), 3.00 (s, 12H).

Scheme 3.8.7

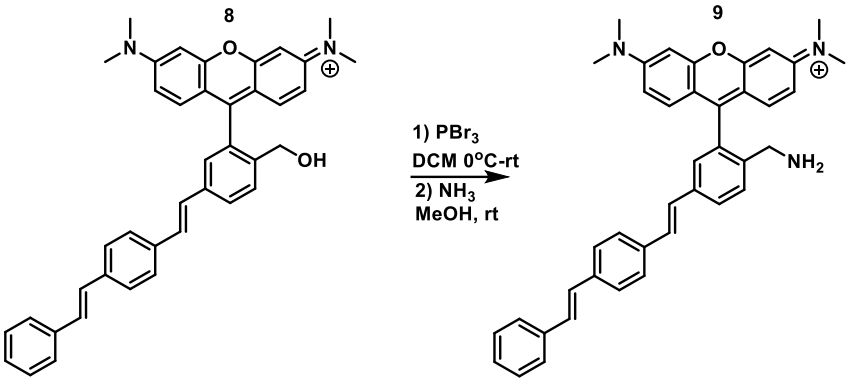

Synthesis of RhoVR0-amine, 9:

Compound **8** (108 mg, 0.19 mmol) was dissolved in approximately 5 mL dichloromethane and cooled to 0°C. 1M Phosphorous tribromide (0.28 mL, 0.28 mmol) was added dropwise and the reaction was allowed to warm to room temperature for 2 hours. The reaction was then quenched with methanol and the crude material concentrated under reduced pressure and redissolved in 0.4 M ammonia in dioxane (24 mL, 19.5 mmol). The reaction was then stirred overnight at room temperature, concentrated under reduced pressure, and purified via flash chromatography (silica, 0-10% MeOH in DCM) to yield compound **9** (13 mg, 12% yield)

^{1}H NMR (400 MHz, CDCl3) δ 8.10 (s, 1H), 7.50 (d, J = 7.9 Hz, 4H), 7.45 (d, J = 7.4 Hz, 2H), 7.40 – 7.35 (m, 4H), 7.08 (s, 4H), 7.02 – 6.96 (m, 2H), 6.83 (d, J = 8.6 Hz, 1H), 6.70 (d, J = 8.7 Hz, 1H), 6.49 – 6.41 (m, 3H), 3.70 (s, 2H), 2.95 (s, 12H).

Scheme 3.8.8

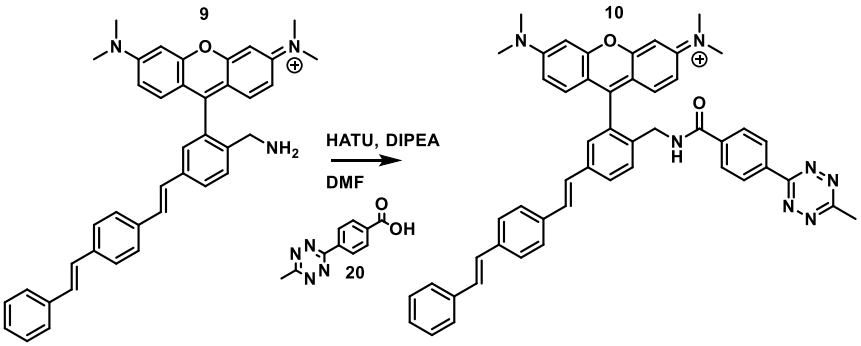

Synthesis of LUnAR RhoVR0, 10:
Compound **9** (13 mg, 0.02 mmol), compound **20** (12 mg, 0.05 mmol), and HATU (28 mg, 0.07 mmol) were dissolve in approximately 1 mL dimethyl formamide and 1 mL diisopropylethylamine and the reaction was stirred for 1 hour. The reaction was then concentrated under reduced pressure, extracted 5x with 0.1M HCl and dichloromethane, the organic layer dried under sodium sulfate and concentrated under reduced pressure. The crude material was purified by preparative TLC (silica, 5% MeOH in DCM) to yield compound **10** (5 mg, 32% yield)

^{1}H NMR (600 MHz, CDCl3) δ 8.43 (d, J = 8.5 Hz, 2H), 7.78 (d, J = 8.5 Hz, 2H), 7.69 – 7.63 (m, 2H), 7.50 – 7.48 (m, 2H), 7.42 (q, J = 8.6 Hz, 4H), 7.35 (t, J = 7.7 Hz, 2H), 7.28 (d, J = 1.7 Hz, 1H), 7.24 (d, J = 9.4 Hz, 3H), 7.06 (d, J = 9.4 Hz, 4H), 6.77 (dd, J = 9.5, 2.5 Hz, 2H), 6.64 (d, J = 2.4 Hz, 2H), 4.36 (d, J = 5.8 Hz, 2H), 3.16 (s, 12H), 3.07 (s, 3H).

HRMS (ESI+) Calculated for $C_{50}H_{44}N_7O_2$+ $[M]^+$: 774.3551; Found 774.3542

Scheme 3.8.9

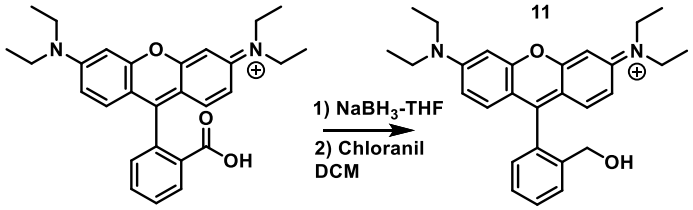

Synthesis rhodamine B alcohol, 11:
Rhodamine B hydrochloride (1.01g, 2.1 mmol) was added to a Schlenk flask and evacuated and backfilled 3x with nitrogen. Rhodamine B was then dissolved in 10 mL anhydrous THF and 1M borane-THF (10.4 mL, 10.4 mmol) was added dropwise and the reaction was then heated to 60^{o}C for 6 hours. The reaction was then quenched with methanol and the solvent evaporated under reduced pressure. The crude product was then immediately redissolved in dichloromethane and chloranil (517 mg, 2.1 mmol) was added and the reaction was stirred for 1 hour. The crude material was then extracted 3x with saturated sodium chloride and the organic layer dried over sodium sulfate, filtered, and concentrated under reduced pressure and then purified by flash chromatography (silica, 10% MeOH in DCM) to yield compound **11** (890 mg, 98% yield)

^{1}H NMR (400 MHz, CDCl3) δ 7.92 (d, J = 7.8 Hz, 1H), 7.51 (td, J = 7.7, 1.3 Hz, 1H), 7.34 (td, J = 7.5, 1.2 Hz, 1H), 7.19 (d, J = 9.5 Hz, 2H), 7.02 (dd, J = 7.5, 1.3 Hz, 1H), 6.79 (dd, J = 9.5, 2.5 Hz, 2H), 6.70 (d, J = 2.4 Hz, 2H), 5.48 (s, 1H), 4.39 (s, 2H), 3.57 (qd, J = 7.3, 2.5 Hz, 8H), 1.28 (t, J = 7.1 Hz, 12H).

Scheme 3.8.10

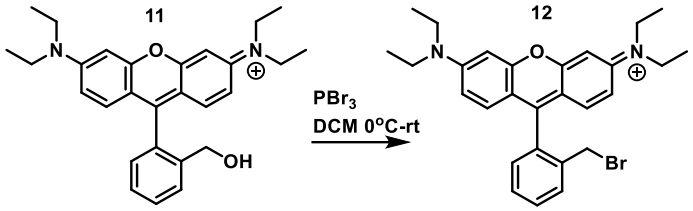

Synthesis of rhodamine B bromide, 12:
Compound **11** (890 mg, 2.1 mmol) was dissolved in approximately 5 mL dichloromethane and cooled to 0°C. Phosphorous tribromide (2.7 mL, 2.7 mmol) was added dropwise and the reaction was allowed to warm to room temperature for 2 hours. The reaction was then quenched with methanol, concentrated under reduced pressure, extracted with DCM and brine and the organic layer dried over sodium sulfate and concentrated under reduced pressure. The crude material was purified by flash chromatography (silica, 10% MeOH in DCM) to yield compound **12** (876 mg, 86% yield)

^{1}H NMR (500 MHz, CDCl3) δ 7.86 (d, J = 7.5 Hz, 1H), 7.84 – 7.66 (m, 2H), 7.37 (t, J = 8.2 Hz, 1H), 7.32 (s, 1H), 7.14 (dd, J = 9.5, 2.4 Hz, 2H), 7.00 (d, J = 2.4 Hz, 2H), 4.40 (s, 1H), 3.85 (q, J = 7.2 Hz, 6H), 1.51 (d, J = 14.3 Hz, 4H).

Scheme 3.8.11

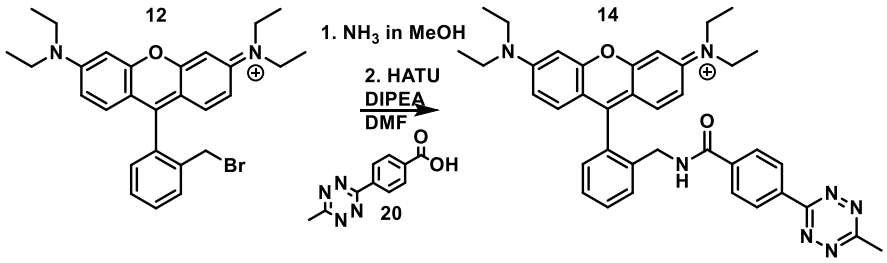

Synthesis of rhodamine B reverse amide, 14:
Compound **12** (376 mg, 0.76 mmol) was dissolved in a 2N solution of ammonia in methanol (19 mL, 38 mmol) and stirred at room temperature for 72 hours. The crude solution was then concentrated under reduced pressure to yield the corresponding amine **13** (68 mg, 21% yield step 1) which was used without further purification. Compound **20** (47 mg, 0.22 mmol), compound **13** (68 mg, 0.16 mmol), HATU (150 mg, 0.39 mmol), and diisopropylethylamine (158 µL, 0.906 mmol) were dissolved in approximately 5 mL dimethylformamide and stirred overnight at room temperature. The crude reaction was then concentrated under reduced pressure, extracted 5x with DCM and 5% LiCl, the organic layer dried over sodium sulfate and concentrated under reduced pressure. The crude material was purified via flash chromatography (silica, 30-50% EtOAc in hexanes) to yield compound **20** (26 mg, 26% yield step 2, 5% overall yield)

^{1}H NMR (400 MHz, CDCl3) δ 9.51 (s, 1H), 8.43 (d, J = 8.2 Hz, 2H), 7.98 (d, J = 8.2 Hz, 2H), 7.80 (s, 1H), 7.59 (s, 1H), 7.52 (s, 1H), 7.43 (s, 1H), 7.12 – 7.07 (m, 2H), 7.00 (s, 1H), 6.73 (s, 3H), 4.46 (d, J = 5.1 Hz, 2H), 3.10 (s, 3H), 2.20 – 2.09 (q, 8H), 1.27 – 1.22 (t, 12H).

Scheme 3.8.12

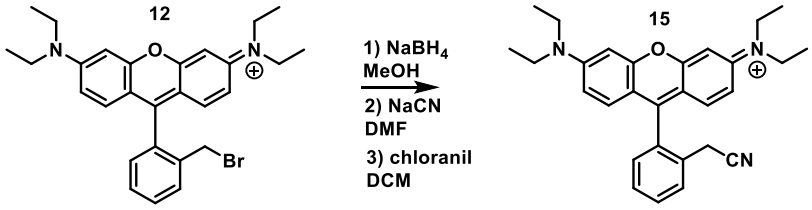

Synthesis of rhodamine B aliphatic nitrile, 15:
Compound **12** (496 mg, 1.0 mmol) was dissolved in 10 mL methanol and cooled to 0^{o}C. Sodium borohydride (196 mg, 5.2 mmol) was added portionwise and the reaction stirred for 10 minutes at room temperature. The reaction was then quenched with saturated ammonium chloride and concentrated under reduced pressure. The crude material was then redissolved in 5 mL dimethylformamide and cooled to 0^{o}C followed by EXTREMELY SLOW (safety first!!) portionwise addition of sodium cyanide (82 mg, 1.7 mmol). The reaction was allowed to warm to room temperature for 2 hours after which it was quenched by saturated sodium bicarbonate and concentrated under reduced pressure. The crude material was redissolved in 10 mL dichloromethane, chloranil (244 mg, 0.99 mmol) was added, and the reaction stirred for 1 hour at room temperature. The reaction was then extracted 3x with brine and the organic layer dried over sodium sulfate and concentrated under reduced pressure (dispose of cyanide waste properly). The crude material was purified by flash chromatography (silica, 10% MeOH in DCM) to yield compound **15** (131 mg, 30% yield)

^{1}H NMR (500 MHz, CDCl3) δ 7.73 (d, J = 7.6 Hz, 1H), 7.65 (td, J = 7.7, 1.4 Hz, 1H), 7.59 – 7.55 (m, 1H), 7.24 (d, J = 1.4 Hz, 1H), 7.09 (d, J = 9.5 Hz, 2H), 6.99 (dd, J = 9.6, 2.4 Hz, 2H), 6.83 (d, J = 2.5 Hz, 2H), 3.65 (q, J = 7.3 Hz, 8H), 3.52 (s, 2H), 1.31 (t, J = 7.1 Hz, 12H).

Scheme 3.8.13

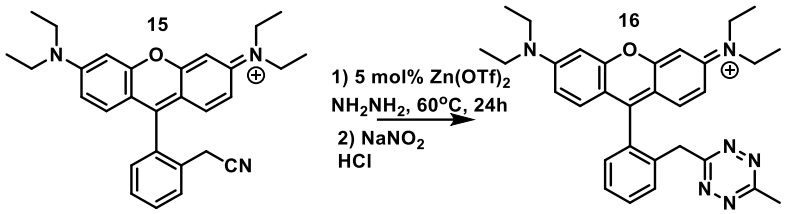

Synthesis of rhodamine B aliphatic tetrazine, 16:
Zinc II trifluoromethanesulfonate (34 mg, 0.094 mmol) was added to a dry two-neck flask and then evacuated and backfilled 3x with nitrogen. Compound **15** (78 mg, 0.18 mmol) was then dissolved in 0.79 mL anhydrous acetonitrile and transferred to the flask. Anhydrous hydrazine (0.28 mL, 8.89 mmol) was then added and the reaction was stirred overnight at 60°C. The reaction was then cooled to room temperature and 1.8 mL 2M aqueous sodium nitrite was added. The reaction was then brought to pH 3 with 1M HCl (USE CAUTION!! NOx GAS PRODUCTION) and extracted with ethyl acetate. The organic layer was dried over sodium sulfate and concentrated under reduced pressure. The crude material was purified by semi-preparative HPLC (C18, 10-100% MeCN in H_2O with TFA) to yield compound **16** (8 mg, 7% yield)

^{1}H NMR (600 MHz, DMSO) δ 7.66 (dt, J = 58.6, 7.7 Hz, 1H), 7.35 (d, J = 8.0 Hz, 1H), 7.16 (d, J = 51.1 Hz, 1H), 7.07 – 6.97 (m, 2H), 6.95 (d, J = 2.4 Hz, 1H), 6.82 (d, J = 9.7 Hz, 1H), 6.53 (s, 2H), 2.09 (s, 2H), 1.24 – 1.05 (m, 12H).

Scheme 3.8.14

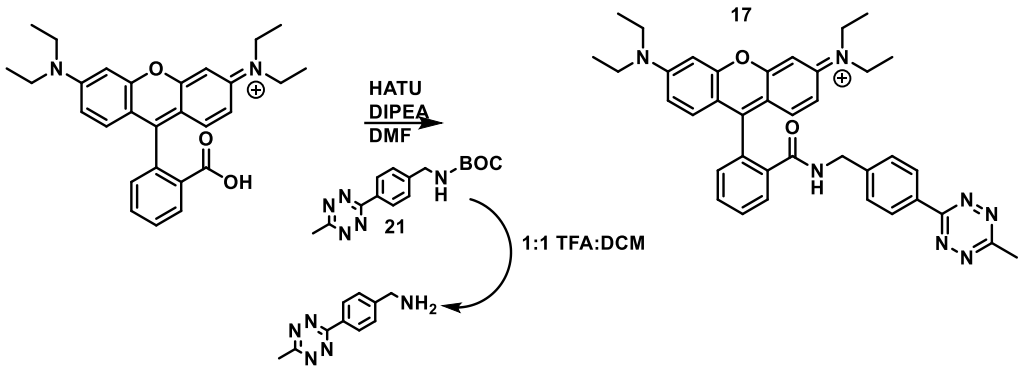

Synthesis of Rhodamine B amide tetrazine, 17:
Compound **21** (25 mg, 0.083 mmol) was dissolved in approximately 2 mL of a 1:1 mixture of TFA and dichloromethane and stirred at room temperature for 2 hours after which the solvent was evaporated under a stream of nitrogen. Rhodamine B (46 mg, 0.10 mmol) was dissolved in approximately 1 mL dimethylformamide and diisopropylethylamine (0.07 mL, 0.42 mmol) and HATU (67 mg, 0.18 mmol) were added and the reaction was stirred at room temperature for 5 minutes. The deprotected compound **21** was dissolved in 500 µL dimethylformamide and the solution was added to the rest of the reagents and the reaction was stirred at room temperature overnight. The reaction was then concentrated under reduced pressure, extracted 5x with 0.1 M HCl and dichloromethane, and then the organic layer was dried over sodium sulfate and concentrated under reduced pressure. The crude material was purified by preparative TLC (silica, ethyl acetate) to yield compound **17** (36 mg, 69% yield)

^{1}H NMR (400 MHz, DMSO) δ 8.10 (d, *J* = 8.3 Hz, 2H), 7.88 (dd, *J* = 5.8, 3.0 Hz, 1H), 7.59 – 7.52 (m, 2H), 7.11 (d, *J* = 8.5 Hz, 3H), 6.22 (d, *J* = 53.9 Hz, 6H), 4.25 (d, *J* = 4.3 Hz, 2H), 3.20 (q, *J* = 7.2 Hz, 8H), 2.97 (s, 3H), 0.94 (t, *J* = 7.0 Hz, 12H).

Scheme 3.8.15

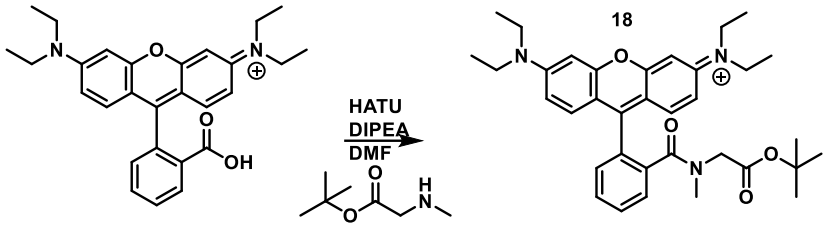

Synthesis of Rhodamine B sarcosine, 18:
Rhodamine B (104 mg, 0.22 mmol), HATU (175 mg, 0.46 mmol), and sarcosine t-butyl ester (56 mg, 0.32 mmol) were dissolved in approximately 0.5 mL dimethylformamide. 181 µL diisopropylethylamine (1.04 mmol) was added and the reaction was stirred overnight at room temperature. The crude reaction was then concentrated under reduced pressure, extracted 5x with 0.1 M HCl and dichloromethane, the organic layer dried over sodium sulfate and concentrated under reduced pressure, and the crude material purified by flash chromatography (silica, 0-10% MeOH in DCM) to give compound **18** (55 mg, 44% yield)

^{1}H NMR (400 MHz, CDCl3) δ 7.74 – 7.59 (m, 4H), 7.38 (d, J = 6.7 Hz, 1H), 7.26 (d, J = 8.9 Hz, 2H), 6.90 (d, J = 9.3 Hz, 2H), 6.76 (s, 2H), 3.81 (s, 2H), 3.61 (dq, J = 14.3, 7.2 Hz, 8H), 2.89 (s, 3H), 2.81 (s, 1H), 1.50 (d, J = 7.2 Hz, 3H), 1.32 (s, 21H).

Scheme 3.8.16

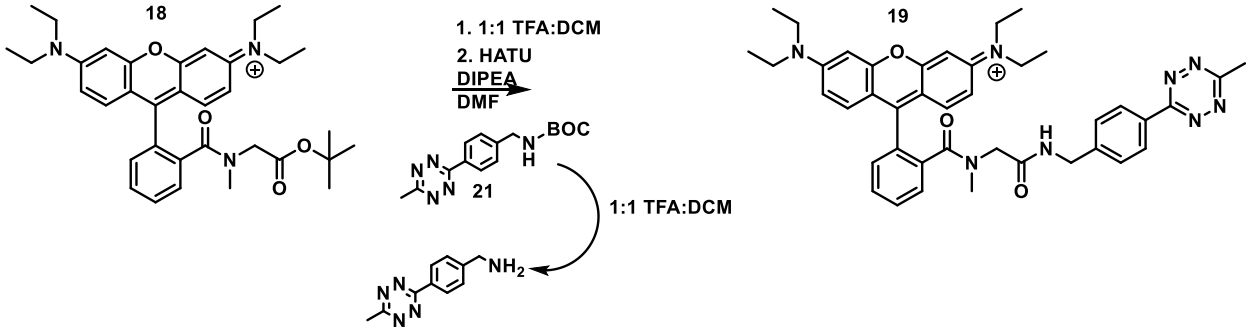

Synthesis of Rhodamine B sarcosine tetrazine, 19:
Compound **18** (92 mg, 0.16 mmol) and compound **21** (50 mg, 0.17 mmol) were stirred separately in approximately 2 mL of a 1:1 mixture of TFA and dichloromethane for 2 hours after which the solvent was evaporated under a stream of nitrogen. The deprotected compounds **18** and **21** were then redissolved in approximately 1 mL dimethyl formamide. HATU (139 mg, 0.37 mmol) and diisopropylethylamine (145 µL, 0.84 mmol) were added and the reaction was stirred overnight at room temperature. The reaction mixture was then concentrated under reduced pressure, extracted 5x with 0.1 M HCl and dichloromethane, and the organic layer dried over sodium sulfate and concentrated under reduced pressure. The crude material was purified by preparative HPLC (C18, 30-70% acetonitrile in water with 0.1% TFA) to yield compound **19** (5 mg, 4% yield)

^{1}H NMR (400 MHz, CDCl3) δ 8.57 (d, J = 7.9 Hz, 2H), 8.13 (s, 2H), 7.81 (d, J = 7.5 Hz, 1H), 7.57 (t, J = 7.4 Hz, 3H), 7.29 (d, J = 5.8 Hz, 4H), 6.70 (s, 2H), 4.58 (d, J = 6.0 Hz, 2H), 4.30 (d, J = 4.7 Hz, 2H), 3.68 – 3.57 (m, 8H), 3.11 (s, 3H), 2.81 (s, 3H), 1.34 (s, 12H).

Scheme 3.8.17

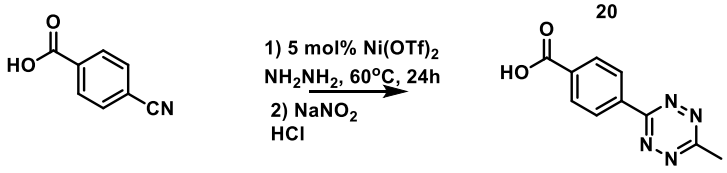

Synthesis of Carboxybenzyl methyl tetrazine, 20:
4-cyanobenzoic acid (96 mg, 0.65 mmol) and nickel II trifluoromethanesulfonate (125 mg, 0.35 mmol) were added to a dry sureseal capped vial which was then evacuated and

backfilled 3x with nitrogen. Anhydrous acetonitrile (0.36 mL, 6.8 mmol) and anhydrous hydrazine (1.07 mL, 34.0 mmol) were added via syringe and the reaction was heated to 60^{o}C and stirred for 24 hours. The reaction was then cooled to room temperature and added to a 1M solution of sodium nitrite (13.6 mL, 13.6 mmol). The reaction was then brought to pH 3 with 1M HCl (USE CAUTION!! NOx GAS PRODUCTION) and extracted with 3x with dichloromethane and brine. The organic layer was dried over sodium sulfate and concentrated under reduced pressure after which the crude material was purified by flash chromatography (silica, 10% MeOH in DCM) to yield compound **20** (47 mg, 32% yield)

^{1}H NMR (400 MHz, DMF) δ 8.68 (d, J = 8.5 Hz, 2H), 8.32 (d, J = 8.5 Hz, 2H), 3.10 (s, 3H).

Scheme 3.8.18

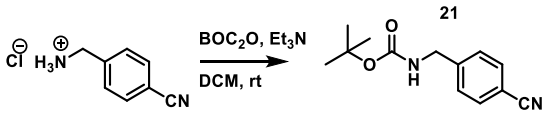

Synthesis of N-BOC 4-cyanobenzylamine, 21:
4-cyanobenzylamine hydrochloride (1.00g, 5.93 mmol) was added to a dry 2-neck flask which was then evacuated and backfilled 3x with nitrogen. The material was then dissolved in anhydrous DCM and triethylamine (1.7 mL, 12.2 mmol) was added via syringe. The reaction was then cooled to 0^{o}C and di-t-butyl dicarbonate (1.61g, 7.35 mmol) was added portionwise. The reaction was allowed to warm to room temperature and stir overnight. The crude reaction was then extracted 3x with brine and the organic layer dried over sodium sulfate and concentrated under reduced pressure to yield compound **21** (1.355g, 98% yield)

^{1}H NMR (300 MHz, DMSO) δ 7.79 (d, J = 8.1 Hz, 2H), 7.52 (t, J = 6.2 Hz, 1H), 7.41 (d, J = 8.0 Hz, 2H), 4.20 (d, J = 6.2 Hz, 2H), 1.39 (s, 9H).

Scheme 3.8.19

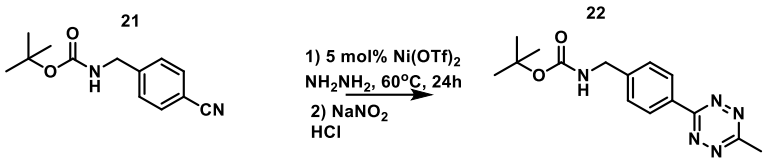

Synthesis of N-BOC benzylamine methyl tetrazine, 22:
Compound **21** (101 mg, 0.44 mmol) and nickel II trifluoromethanesulfonate (79 mg, 0.22 mmol) were added to a dry sureseal capped vial which was then evacuated and backfilled 3x with nitrogen. Anhydrous acetonitrile (0.23 mL, 4.31 mmol), anhydrous hydrazine (0.68 mL, 21.6 mmol) and 0.23 mL anhydrous dimethylsulfoxide were added via syringe and the reaction was heated to 60°C and stirred for 24 hours. The reaction was then cooled to room temperature and added to a 1M solution of sodium nitrite (8.62 mL, 8.62 mmol). The reaction was then brought to pH 3 with 1M HCl (USE CAUTION!! NOx GAS PRODUCTION) and extracted with 3x with dichloromethane and brine. The organic layer was dried over sodium sulfate and concentrated under reduced pressure after which the crude material was purified by flash chromatography (silica, 20% ethyl acetate in hexanes) to yield compound **22** (25 mg, 20% yield)

^{1}H NMR (300 MHz, MeOD) δ 8.41 (d, J = 8.3 Hz, 2H), 7.45 (d, J = 8.4 Hz, 2H), 7.33 – 7.12 (m, 1H), 4.29 (s, 2H), 2.97 (s, 3H), 1.43 (s, 9H).

Scheme 3.8.20

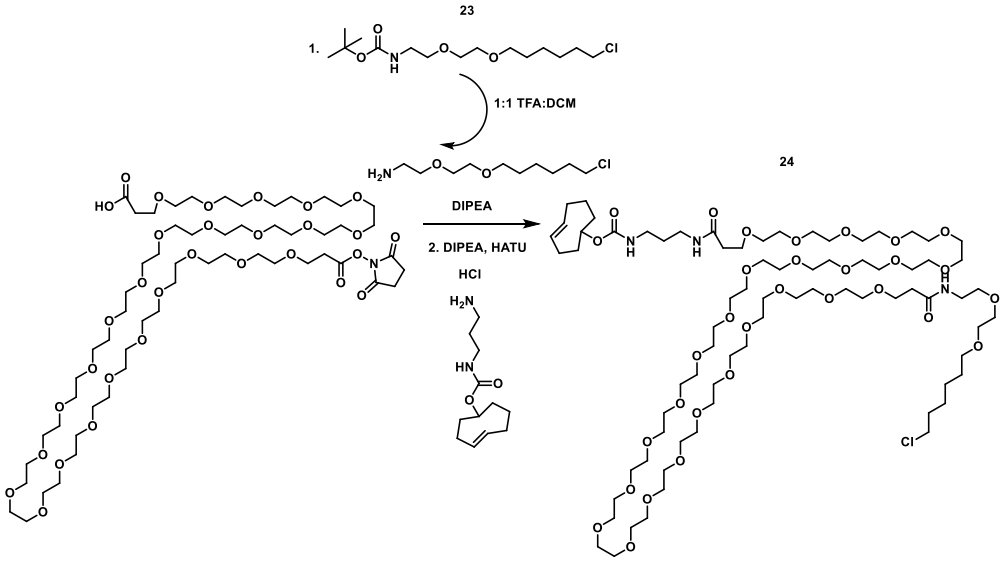

Synthesis of TCO-PEG25-Halo, 24:

23 (13 mg, 0.06 mmol) was dissolved in approximately 1 mL of a 1:1 mixture of TFA:DCM, stirred for 2 hours, and then the solvent was evaporated off under a stream of nitrogen. The material was then redissolved in approximately 1 mL dimethylformamide and NHS-PEG_{25}-acid (66 mg, 0.05 mmol) and diisopropylethylamine (42 µL, 0.24 mmol) were added and the reaction was stirred at room temperature for 2 hours. After 2 hours, TCO-amine (12.5 mg, 0.05 mmol) and HATU (39 mg, 0.11 mmol) were added and the reaction was stirred for another 2 hours at room temperature until complete by LC/MS. The reaction was then concentrated under reduced pressure, extracted 5x with 5% LiCl in water and dichloromethane, the organic layer dried over sodium sulfate and concentrated under reduced pressure. The crude material was purified by preparative HPLC (C18, 30-70%: acetonitrile in water with 0.1% TFA) to yield compound **24** (20 mg, 26% yield)

HRMS (ESI+) Calculated for $C_{76}H_{146}ClN_3NaO_{31}$+ $[M+Na]^+$: 1654.9521; Found 1654.9591

Spectra

Spectrum 3.8.1. LC/MS of 2, meta-bromo TMR-OH

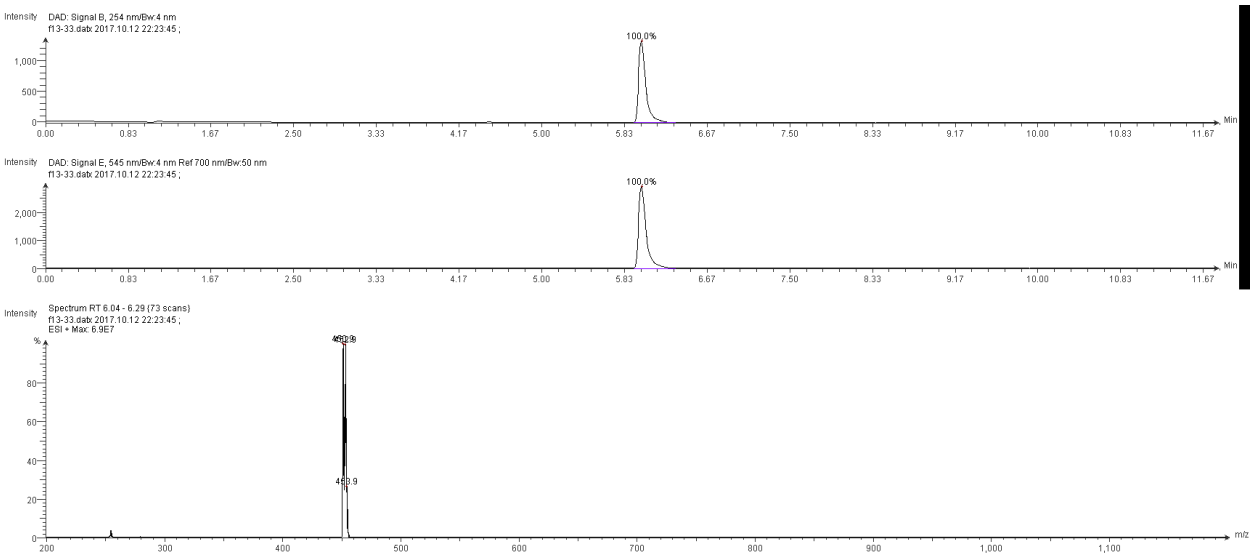

Low resolution ESI+ mass spectrum of 2 (meta-bromo TMR-OH):

Calculated for $[M-^{79}Br]^+$: 451.10
Found: 450.9

Calculated for $[M-^{81}Br]^+$: 453.10
Found: 452.9

Spectrum 3.8.2. ^{1}H spectrum of 2, meta-bromo-TMR-OH

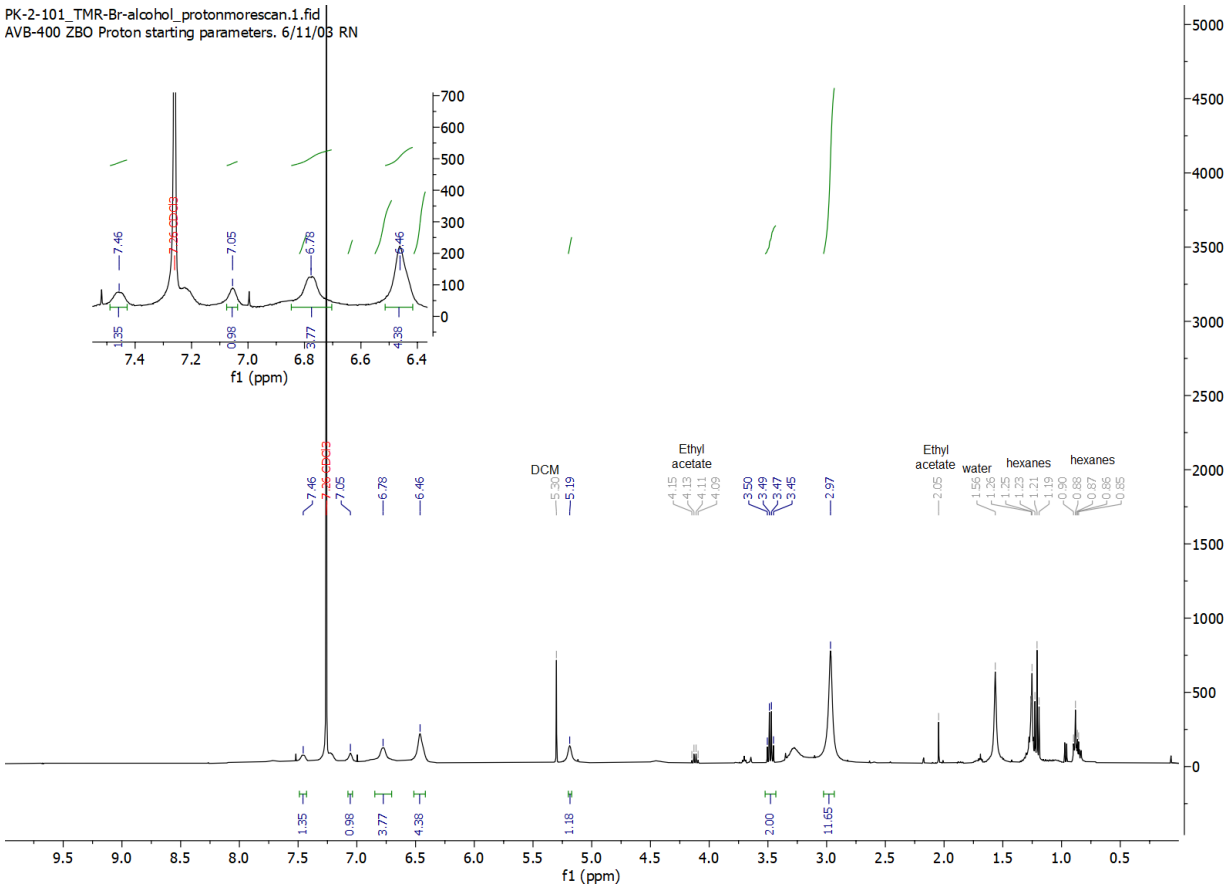

Spectrum 3.8.3. LC/MS of 4, RhoVR1-OH

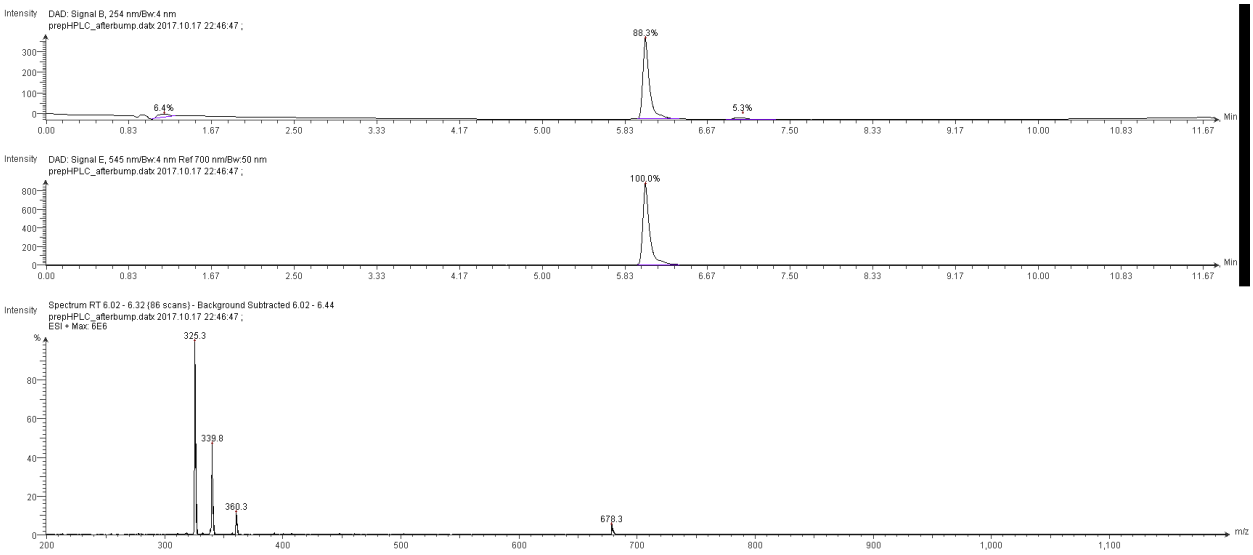

Low resolution ESI+ mass spectrum of 4 (RhoVR1-OH):

Calculated for $[M]^{+}$: 678.37
Found: 678.3

Calculated for $[M+acetonitrile+H]^{2+}$: 360.20

Found: 360.3

Calculated for $[M+H]^{2+}$: 339.69
Found: 339.8

Calculated for $[M+H\text{-ethyl (decomposition on MS)}]^{2+}$: 325.67
Found: 325.3

Spectrum 3.8.4. ^{1}H spectrum of 4, RhoVR1-OH

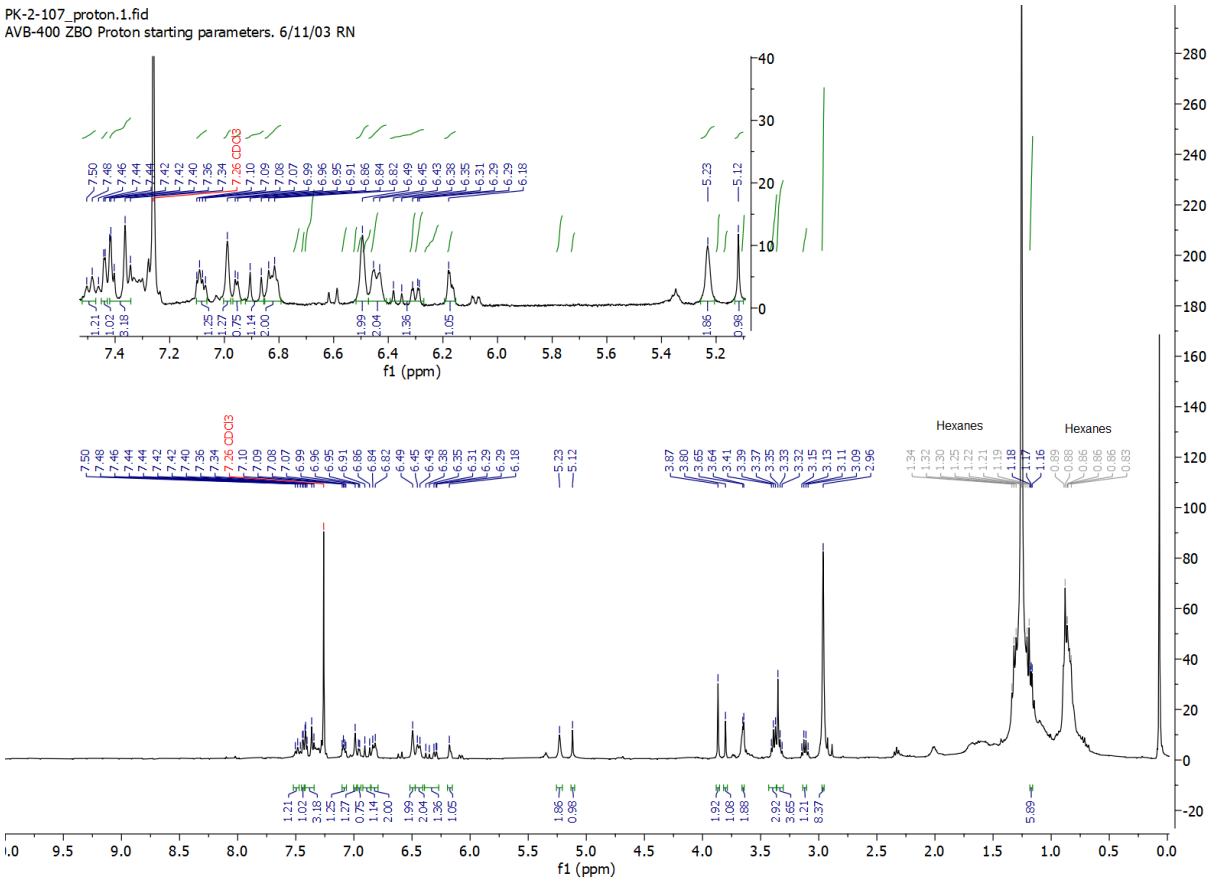

Spectrum 3.8.5. LC/MS of 5, RhoVR1-amine

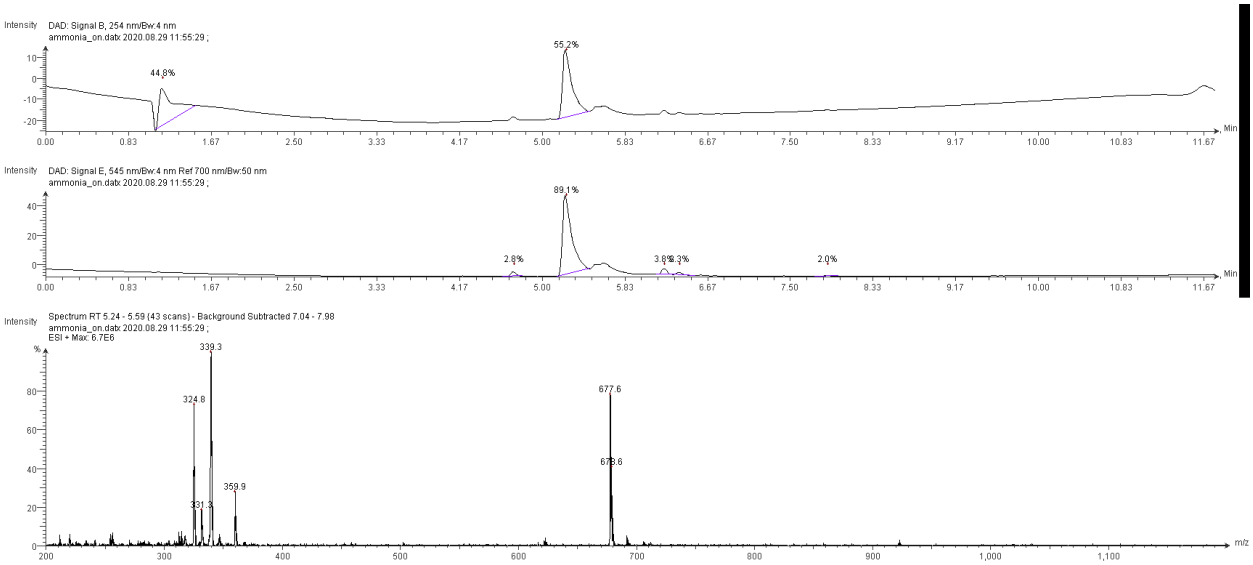

Low resolution ESI+ mass spectrum of 4 (RhoVR1-amine):

Calculated for $[M]^{+}$: 677.39
Found: 677.6

Calculated for $[M+acetonitrile+H]^{2+}$: 359.71

Found: 359.9

Calculated for $[M+H]^{2+}$: 339.20
Found: 339.3

Calculated for $[M+H\text{-}ethyl\ (decomposition\ on\ MS)]^{2+}$: 325.18
Found: 324.8

Spectrum 3.8.6. ^{1}H spectrum of 5, RhoVR1-amine:

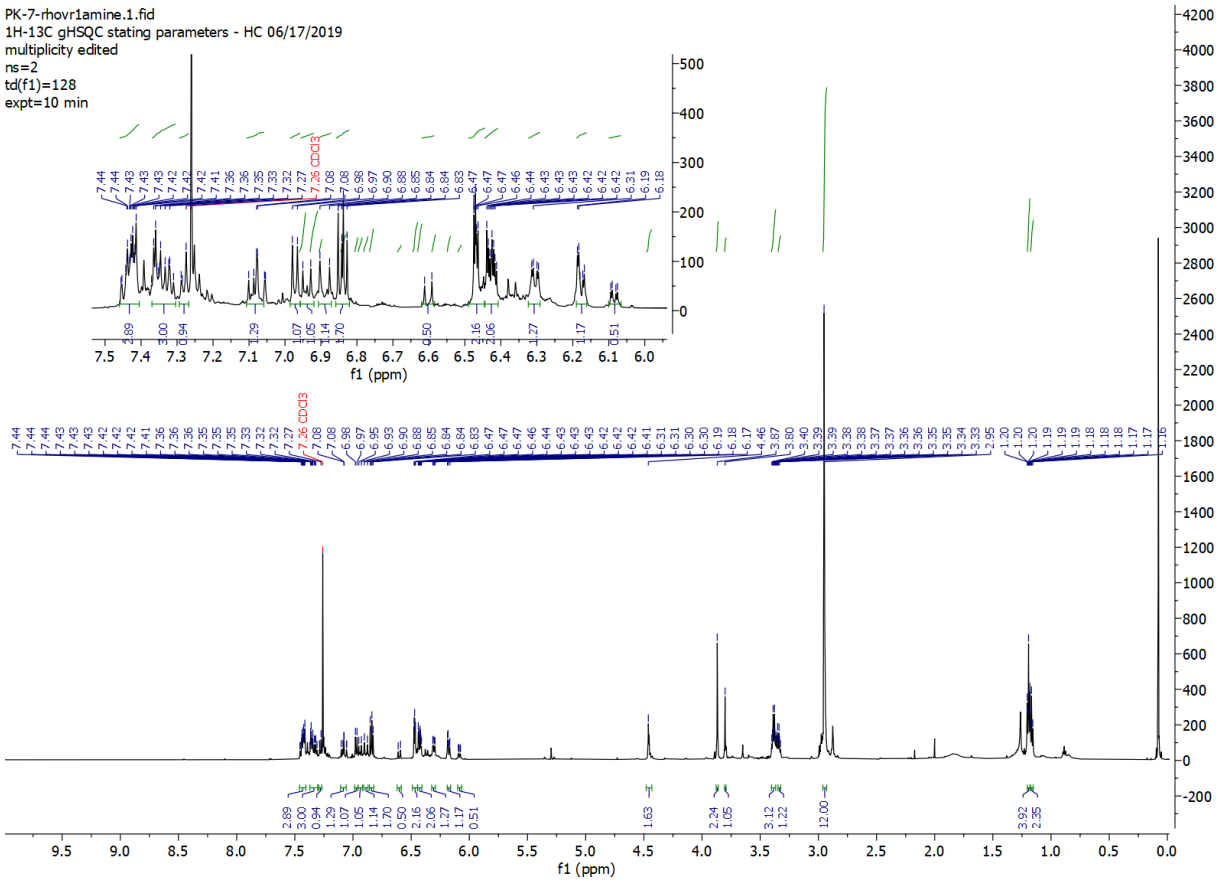

Spectrum 3.8.7. LC/MS of 6, LUnAR RhoVR1:

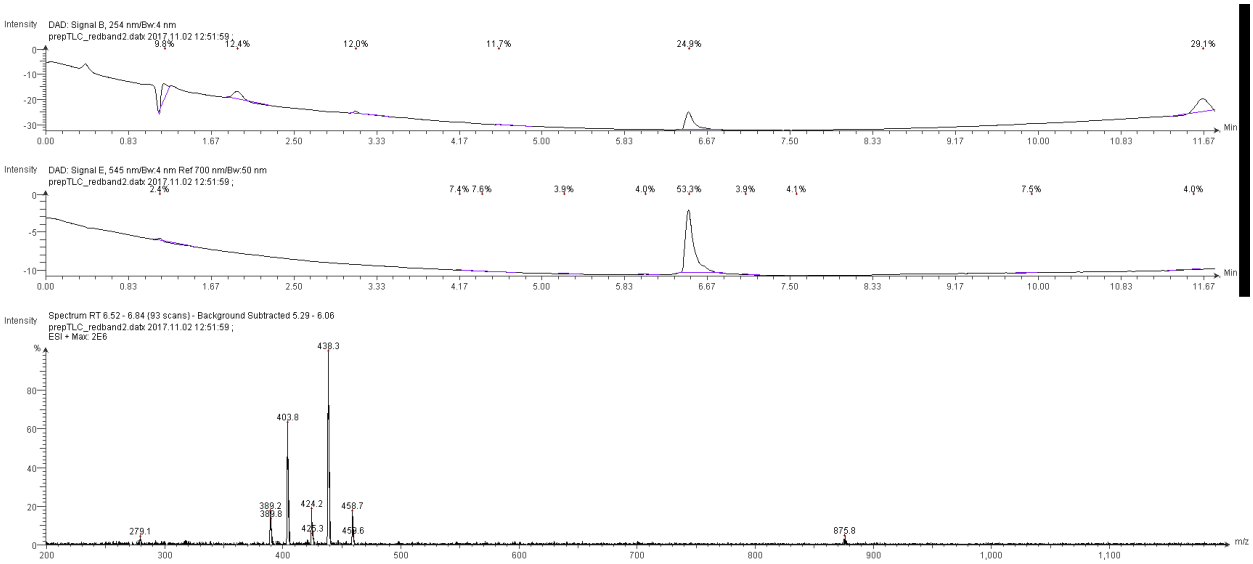

Low resolution ESI+ mass spectrum of 6 (LUnAR RhoVR1):

Calculated for $[M]^{+}$: 875.44
Found: 875.8

Calculated for $[M+acetonitrile+H]^{2+}$: 458.74

Found: 458.7

Calculated for $[M+H]^{2+}$: 438.22
Found: 438.3

Calculated for $[M+H\text{-}ethyl\ (decomposition\ on\ MS)]^{2+}$: 424.21
Found: 424.2

Calculated for $[M+H\text{-}ethyl\ and\ tet\text{-}nitrile\ (decomposition\ on\ LC/MS)]^{2+}$: 389.69
Found: 389.2

Spectrum 3.8.8. ^{1}H spectrum of 6, LUnAR RhoVR1:

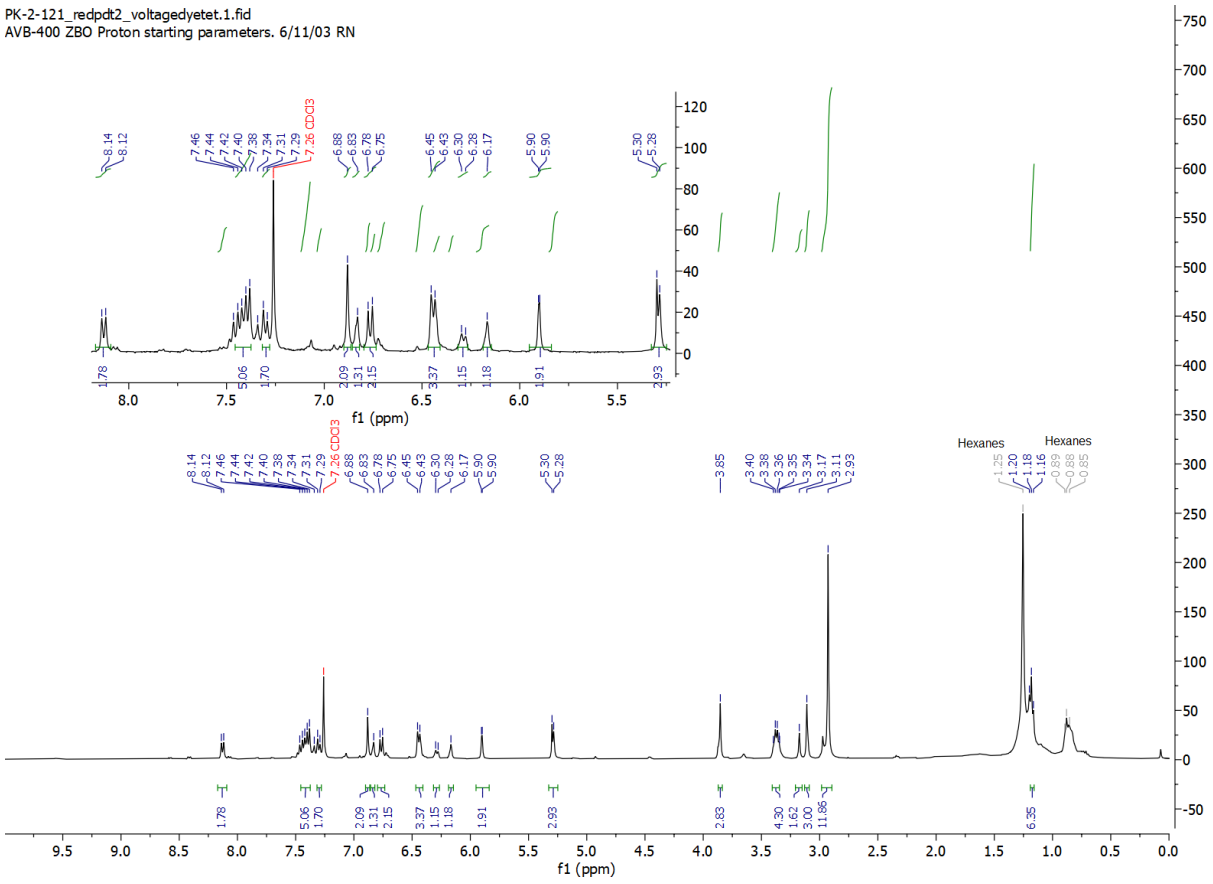

Spectrum 3.8.9. LC/MS of 8, RhoVR0-OH:

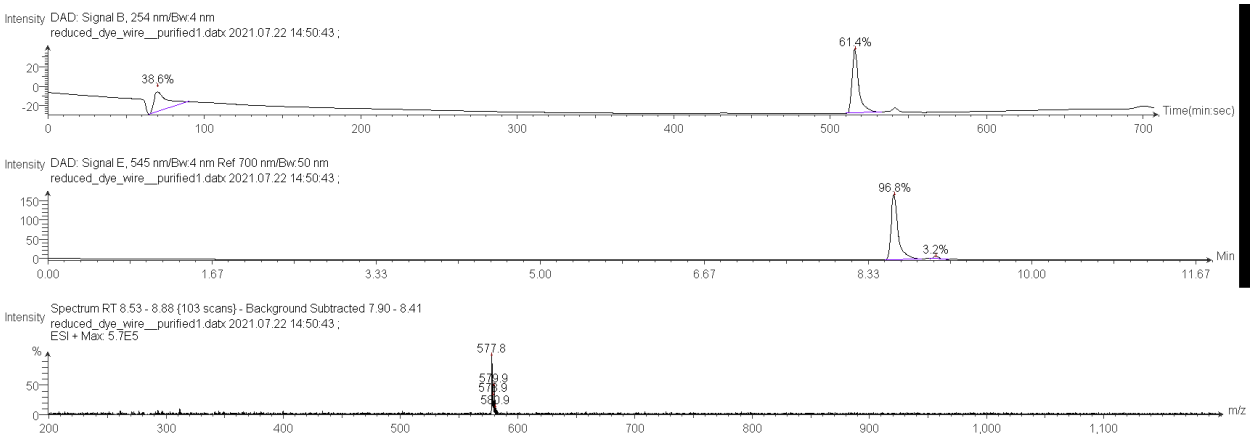

Low resolution ESI+ mass spectrum of 4 (RhoVR1-amine):

Calculated for $[M]^+$: 577.3

Found: 577.8

Spectrum 3.8.10. ^{1}H spectrum of 8, RhoVR0-OH:

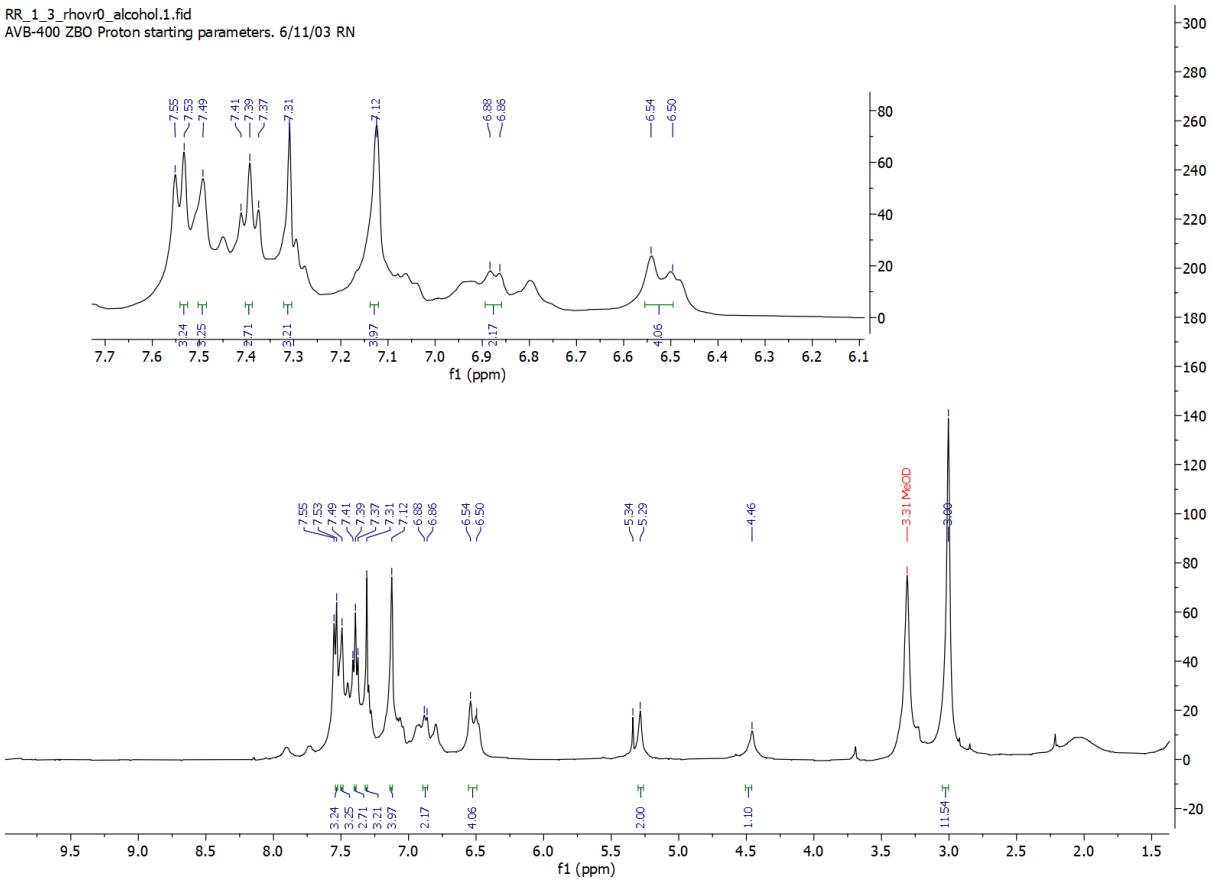

Spectrum 3.8.11. LC/MS of 9, RhoVR0-amine:

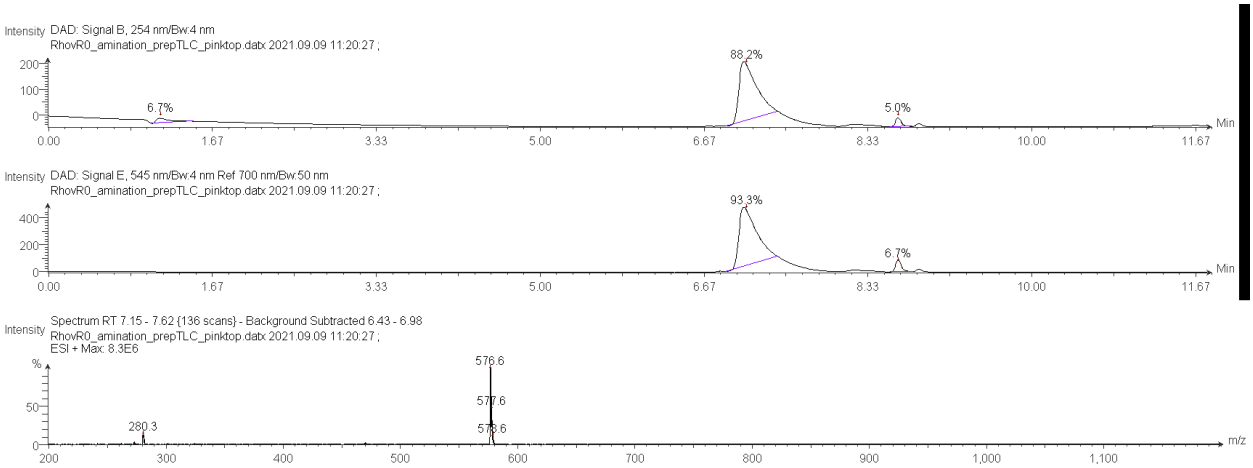

Low resolution ESI+ mass spectrum of 4 (RhoVR1-amine):

Calculated for $[M]^+$: 576.3
Found: 576.6

Spectrum 3.8.12. ^{1}H spectrum of 9, RhoVR0-amine:

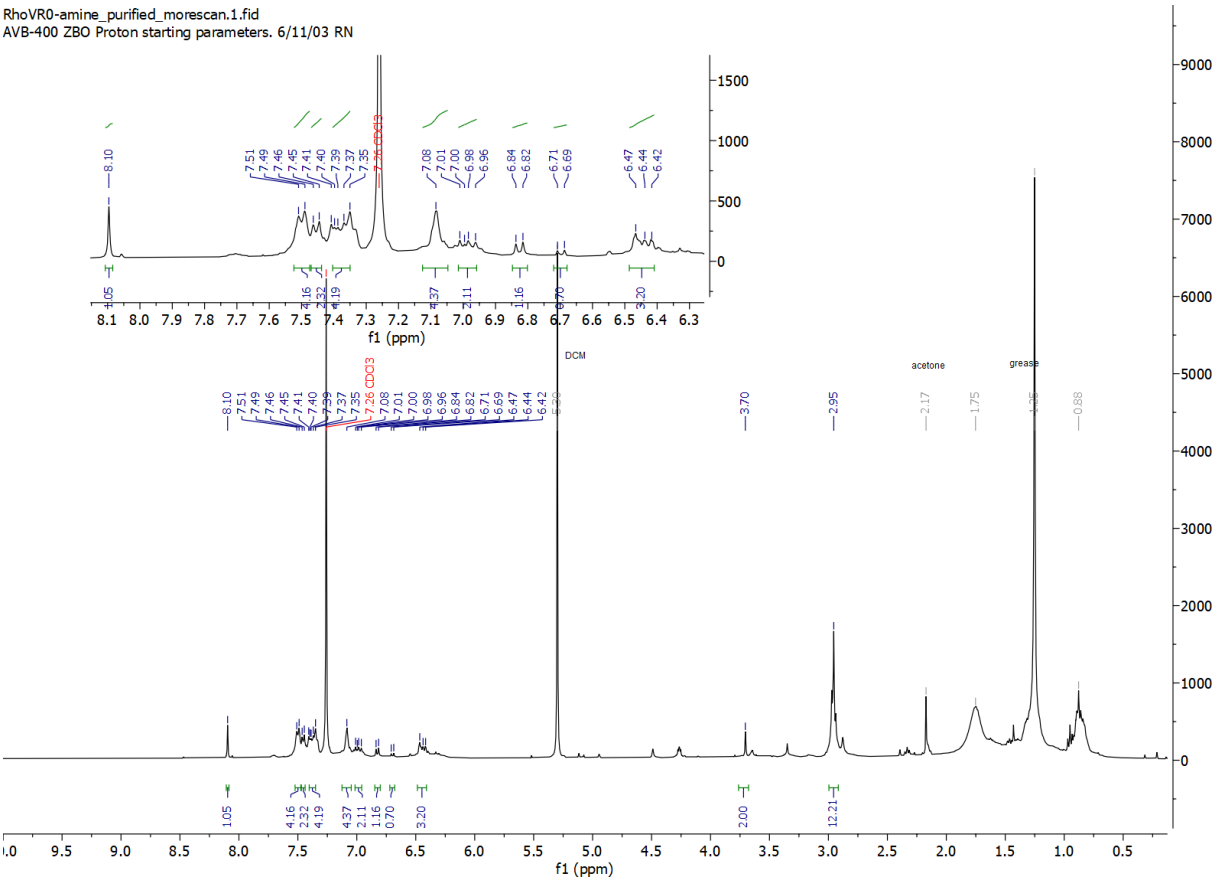

Spectrum 3.8.13. LC/MS of 10, LUnAR RhoVR0:

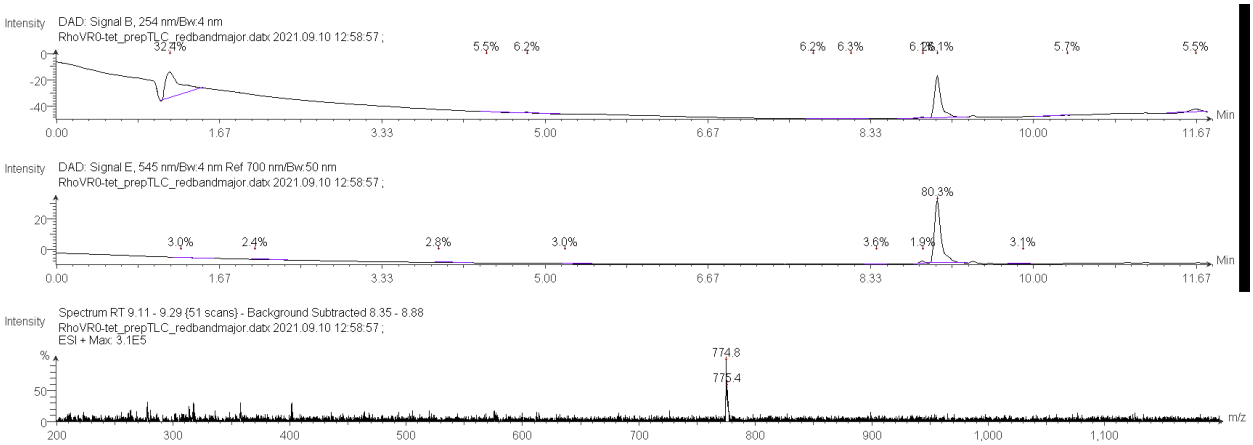

Low resolution ESI+ mass spectrum of 4 (RhoVR1-amine):

Calculated for $[M]^+$: 774.4
Found: 774.8

Spectrum 3.8.14. 1H spectrum of 10, LUnAR RhoVR0:

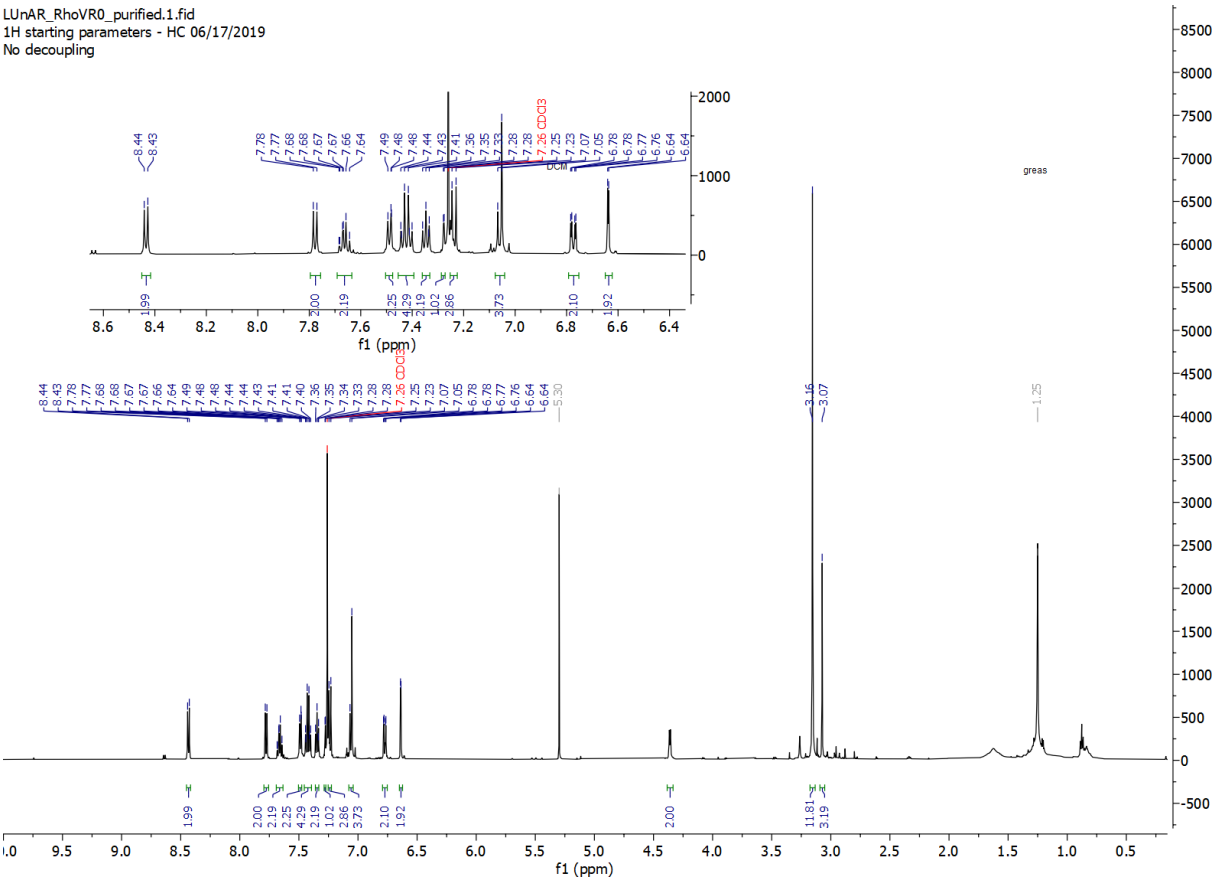

Spectrum 3.8.15. LC/MS spectrum of 11, rhodamine B alcohol:

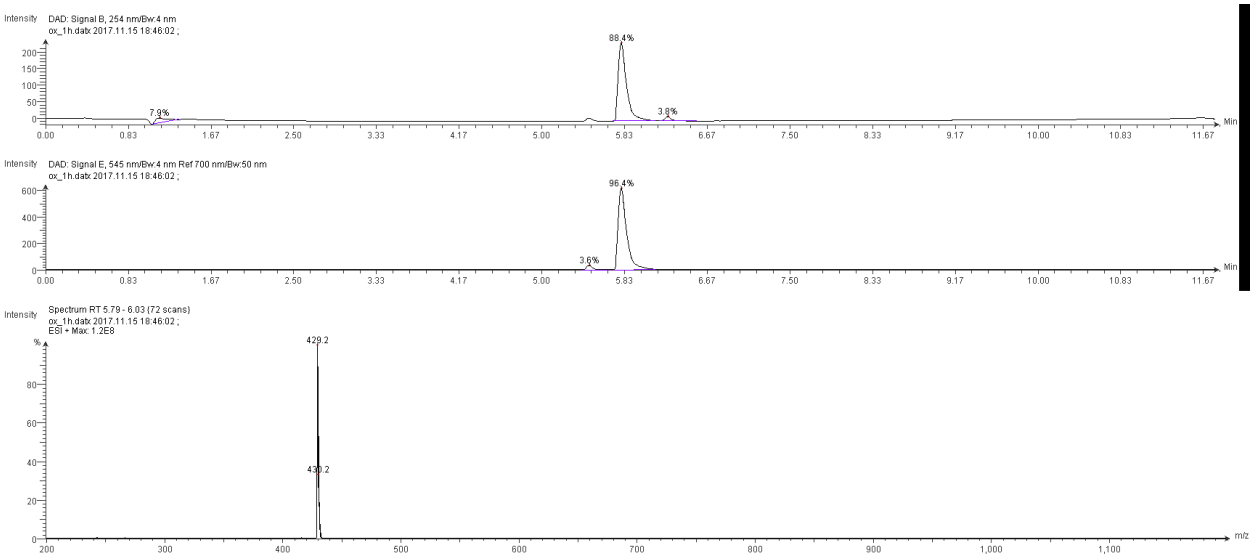

Low resolution ESI+ mass spectrum of 7 (Rhodamine B alcohol):

Calculated for $[M]^+$: 429.25
Found: 429.2

Spectrum 3.8.16. ^{1}H spectrum of 11, rhodamine B alcohol:

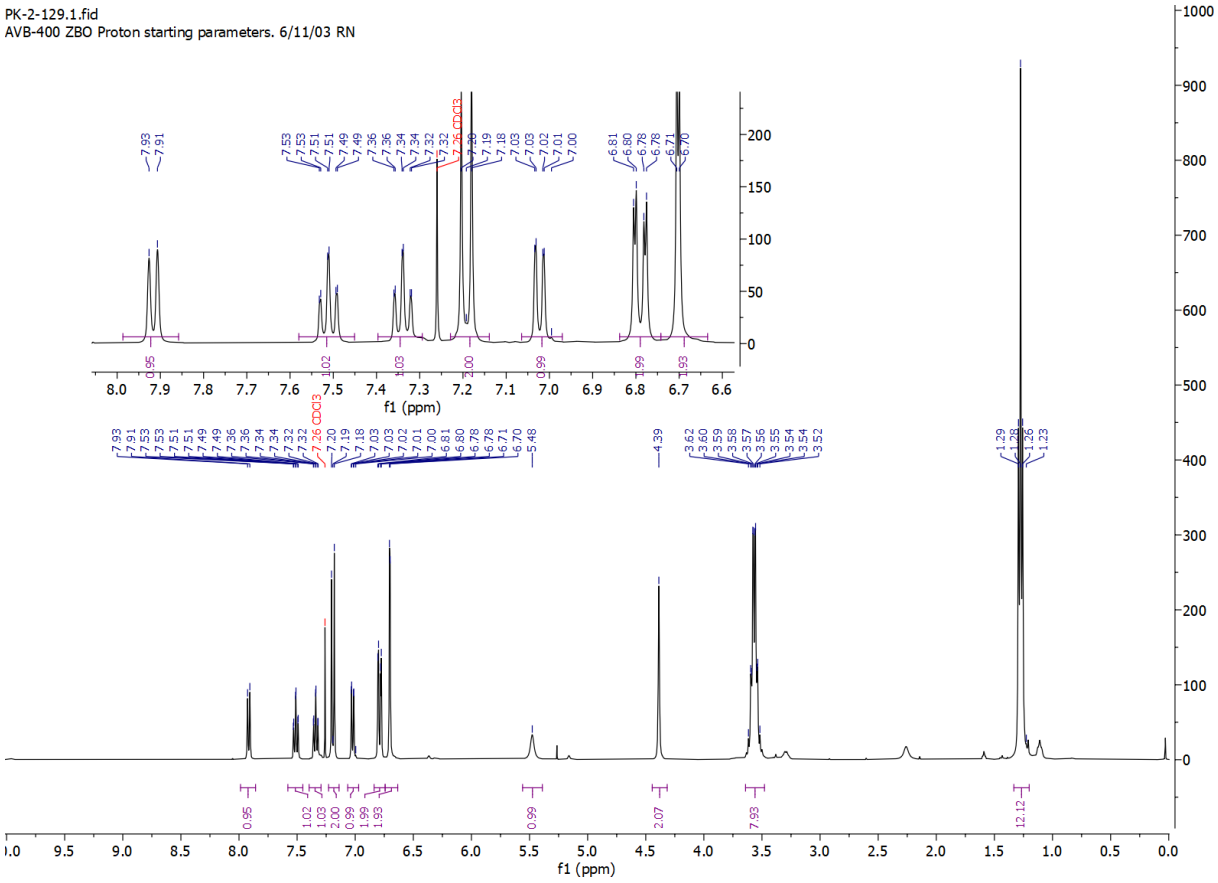

Spectrum 3.8.17. LC/MS spectrum of 12, rhodamine B bromide:

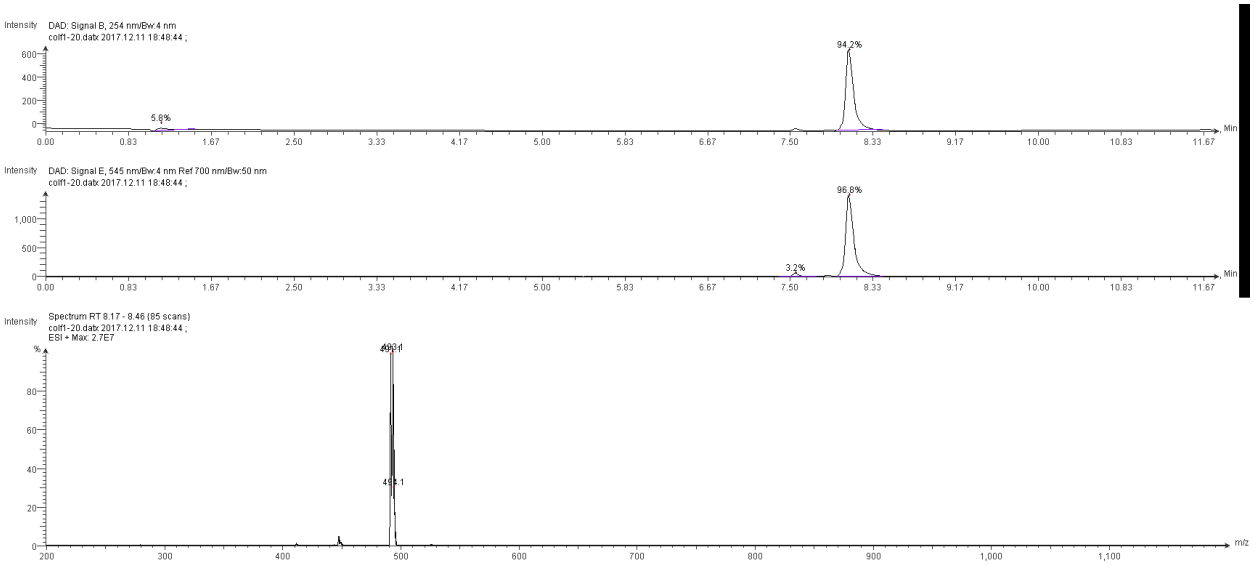

Low resolution ESI+ mass spectrum of 8 (rhodamine B bromide):

Calculated for $[M-^{79}Br]^+$: 491.17
Found: 491.1

Calculated for $[M-^{81}Br]^+$: 493.17
Found: 493.1

Spectrum 3.8.18. 1H spectrum of 12, rhodamine B bromide:

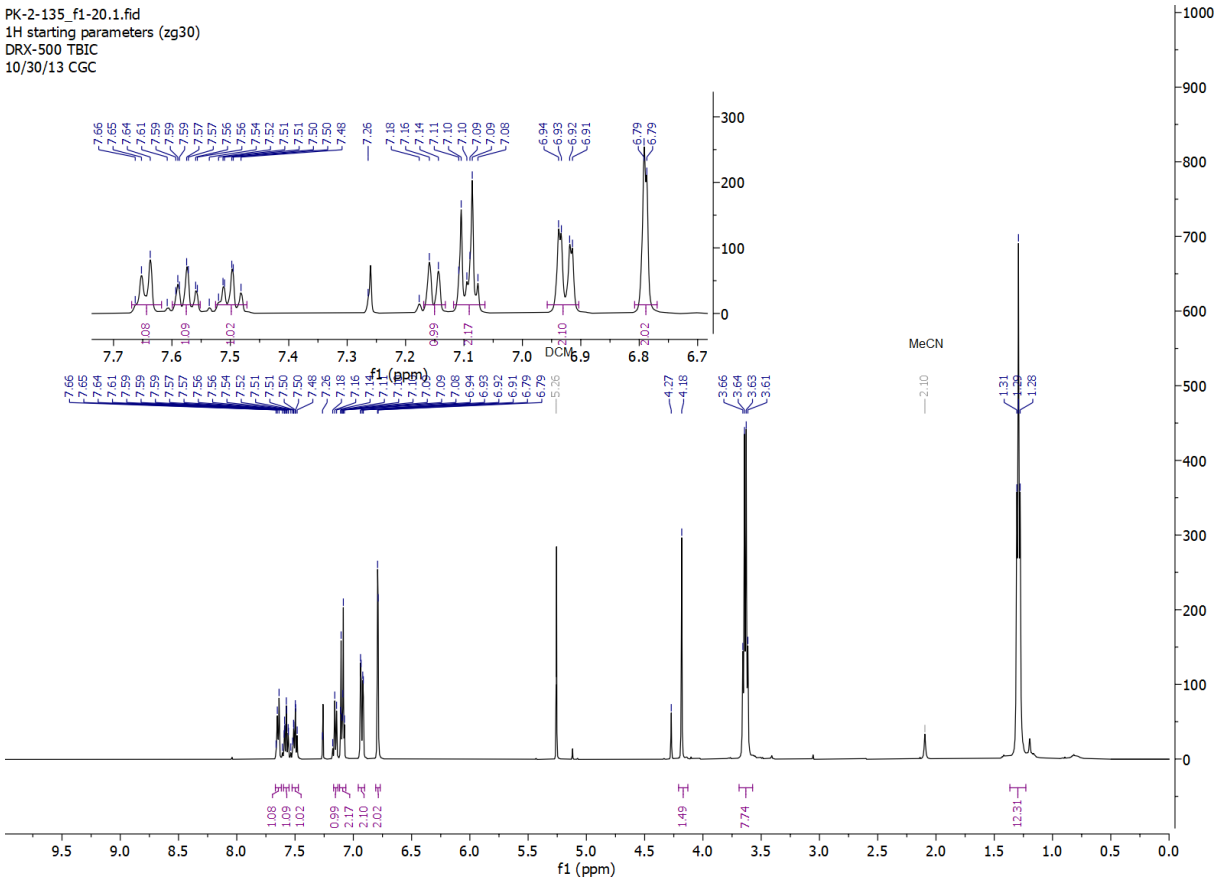

Spectrum 3.8.19. LC/MS spectrum of 14, rhodamine B reverse amide:

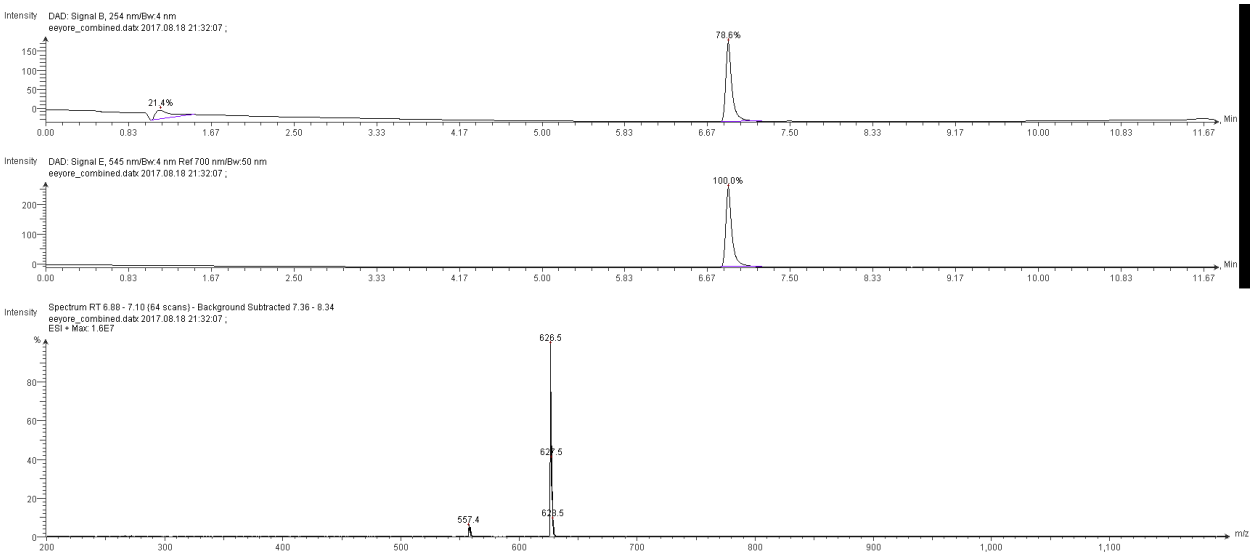

Low resolution ESI+ mass spectrum of 20 (Rhodamine B reverse amide):

Calculated for $[M]^+$: 626.32
Found: 626.5

Calculated for $[M+H\text{-ethyl and tet-nitrile (decomposition on LC/MS)}]^{2+}$: 557.29
Found: 557.4

Spectrum 3.8.20. ^{1}H spectrum of 14, rhodamine B reverse amide:

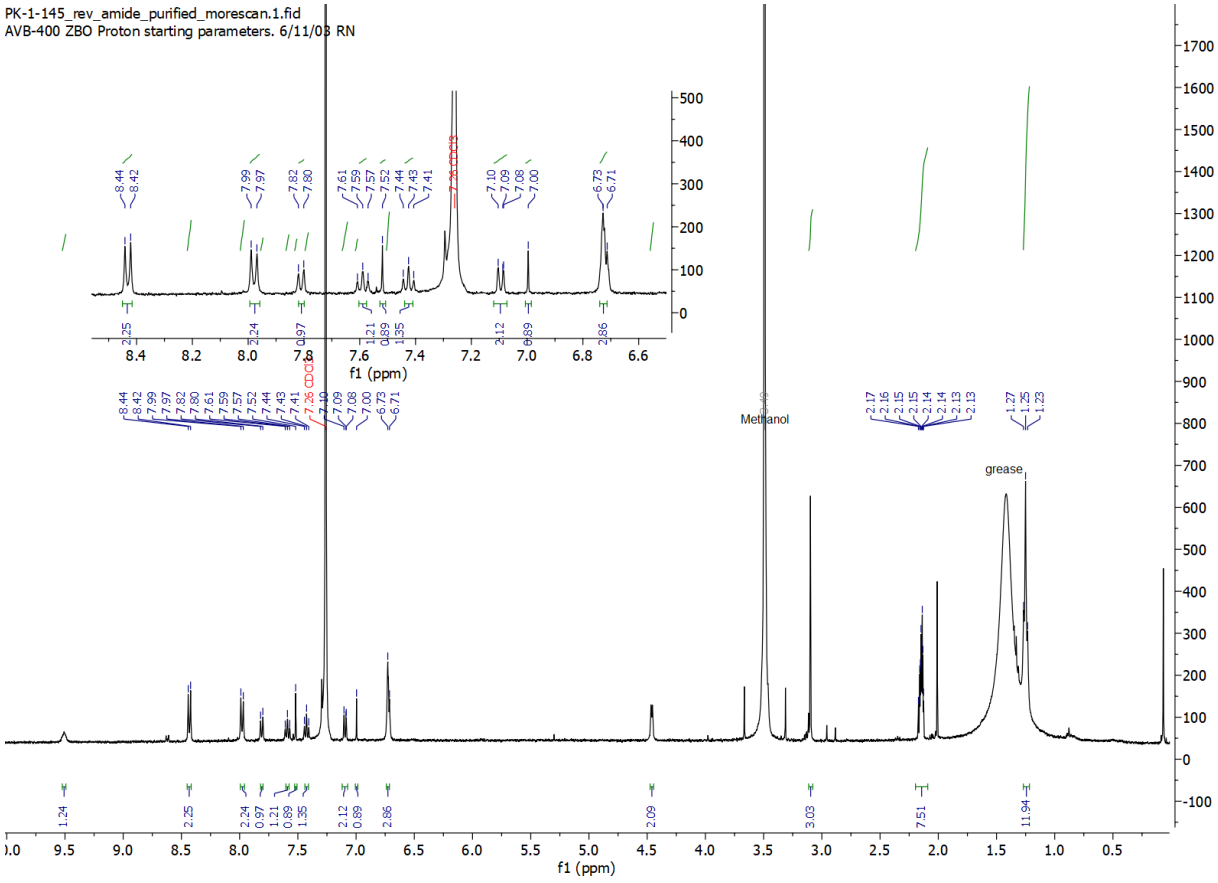

Spectrum 3.8.21. LC/MS spectrum of 15, rhodamine B aliphatic nitrile:

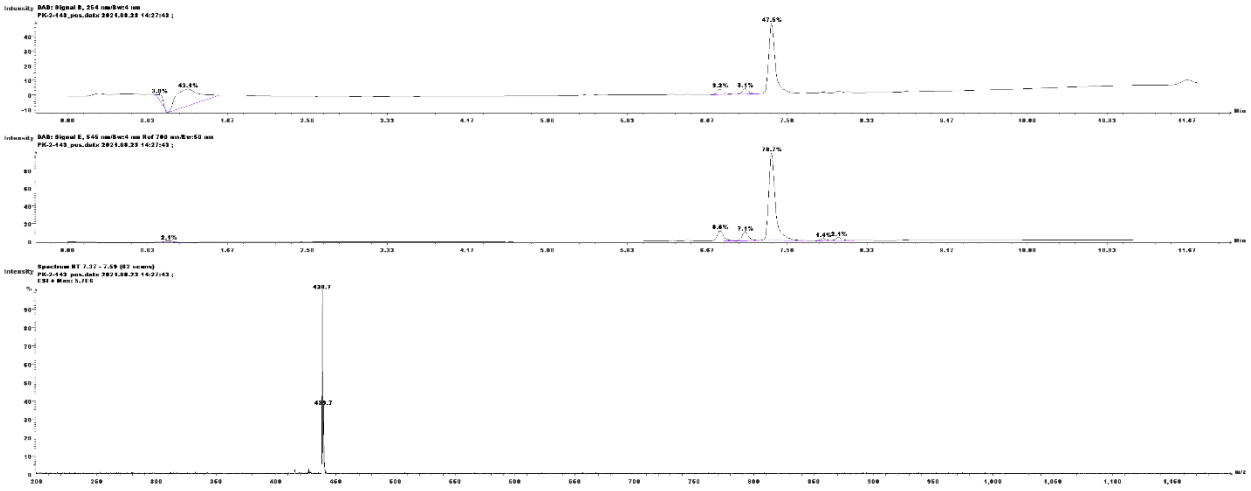

Low resolution ESI+ mass spectrum of 10 (rhodamine B aliphatic nitrile):

Calculated for $[M]^+$: 438.25
Found: 438.7

Spectrum 3.8.22. ^{1}H spectrum of 15, rhodamine B aliphatic nitrile:

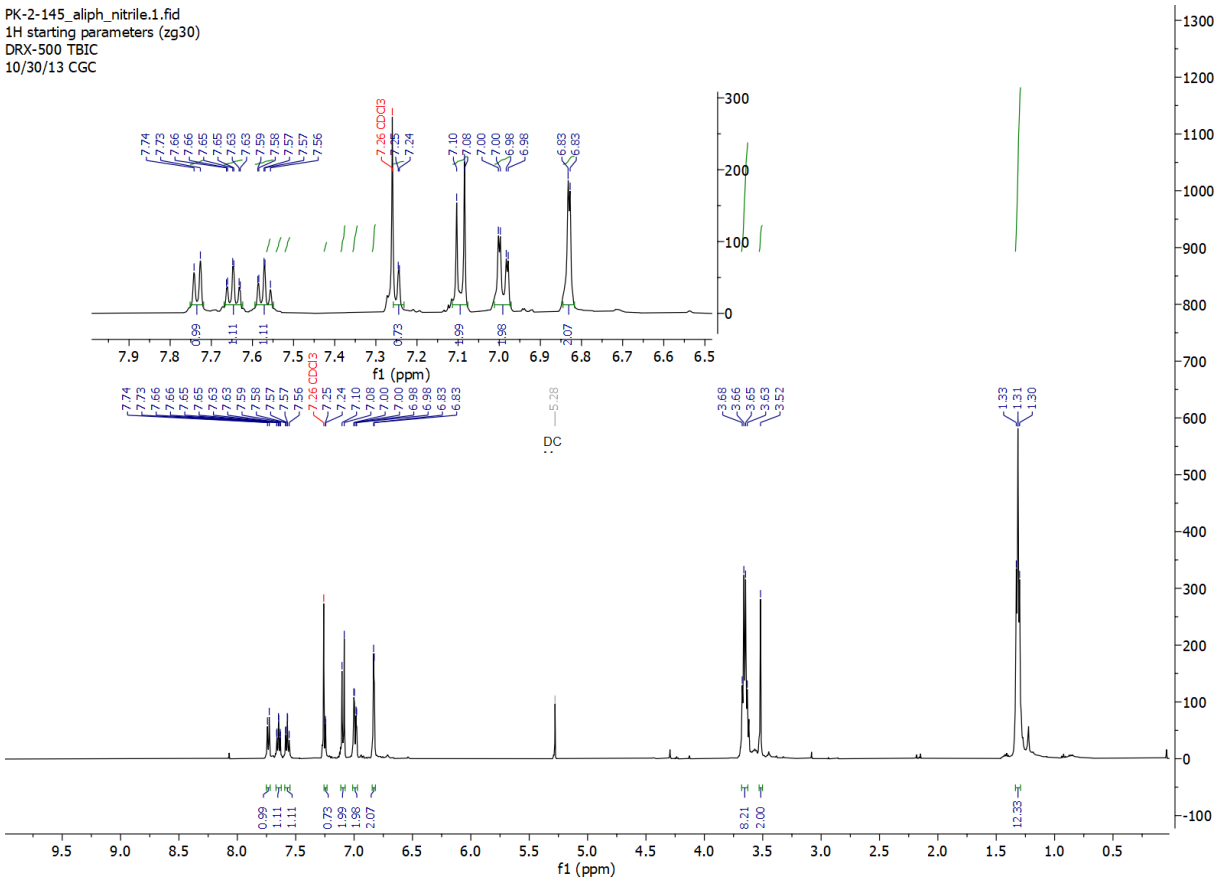

Spectrum 3.8.23. LC/MS spectrum of 16, rhodamine B aliphatic tetrazine:

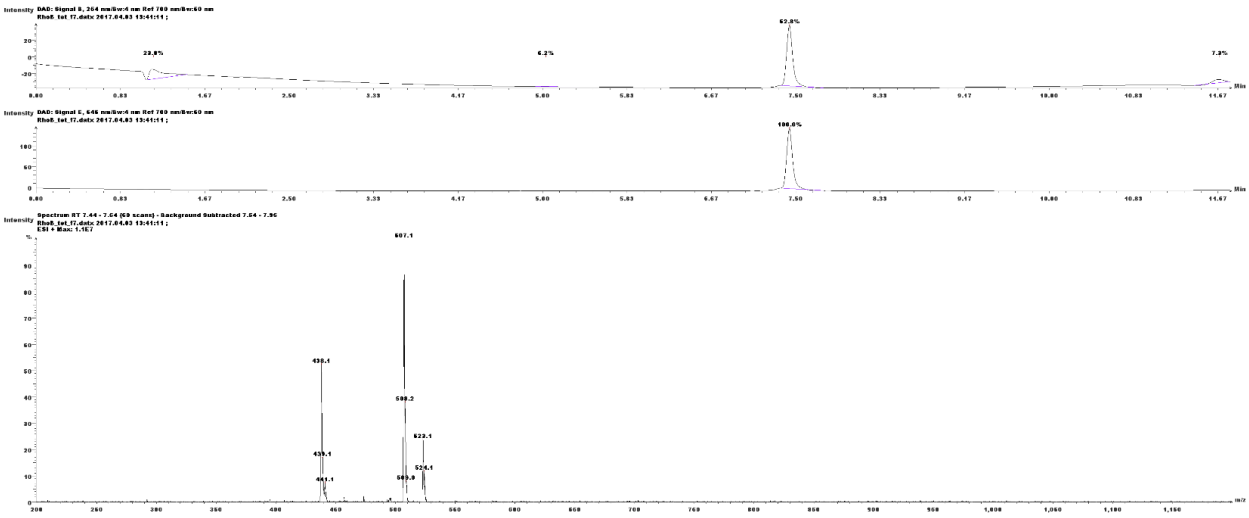

Low resolution ESI+ mass spectrum of 11 (Rhodamine B aliphatic tetrazine):

Calculated for $[M]^+$: 507.29
Found: 507.1

Calculated for $[M+ammonia]^+$: 507.29
Found: 507.1

Calculated for $[M:tet\text{-}nitrile\ (decomposition\ on\ LC/MS)]^{2+}$: 438.25
Found: 438.1

Spectrum 3.8.24. ^{1}H spectrum of 16, rhodamine B aliphatic tetrazine:

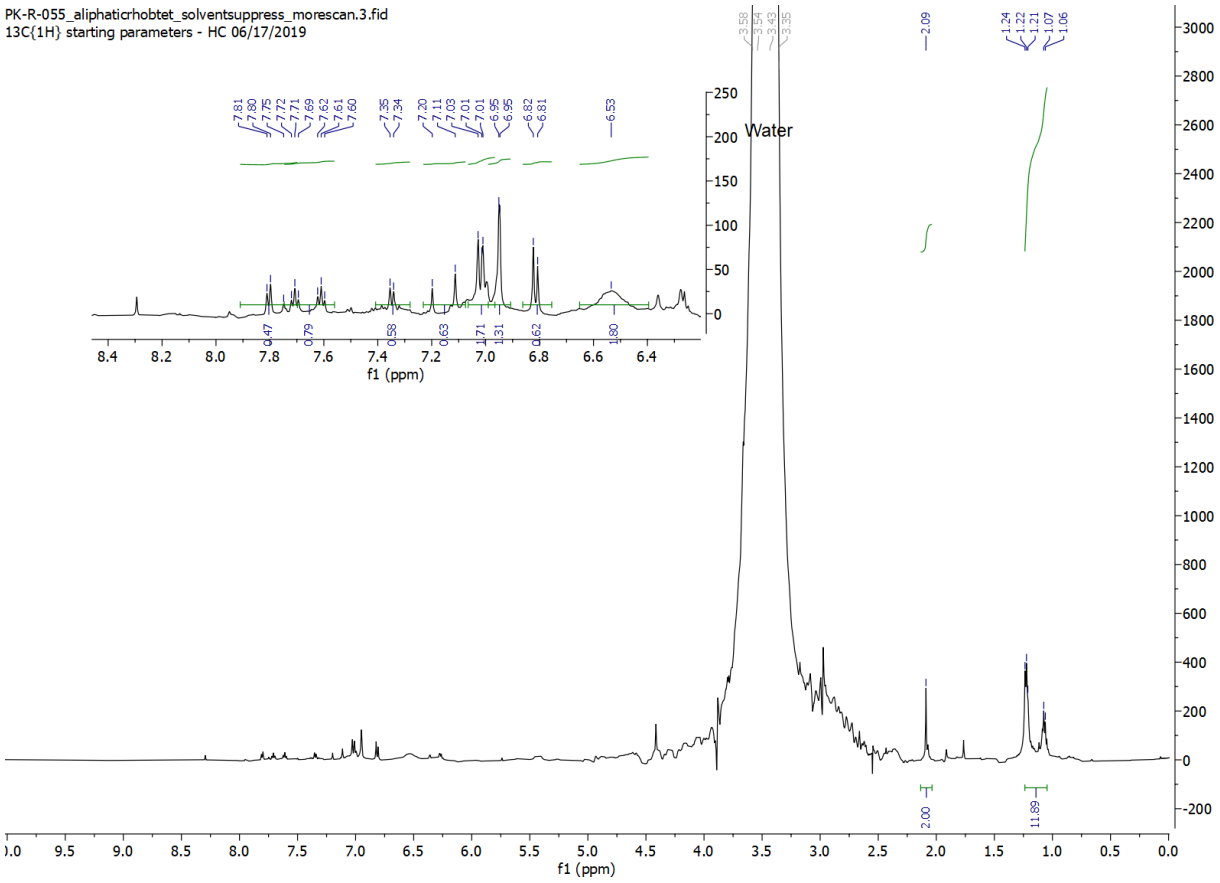

Spectrum 3.8.25. LC/MS of 17, rhodamine B amide tetrazine:

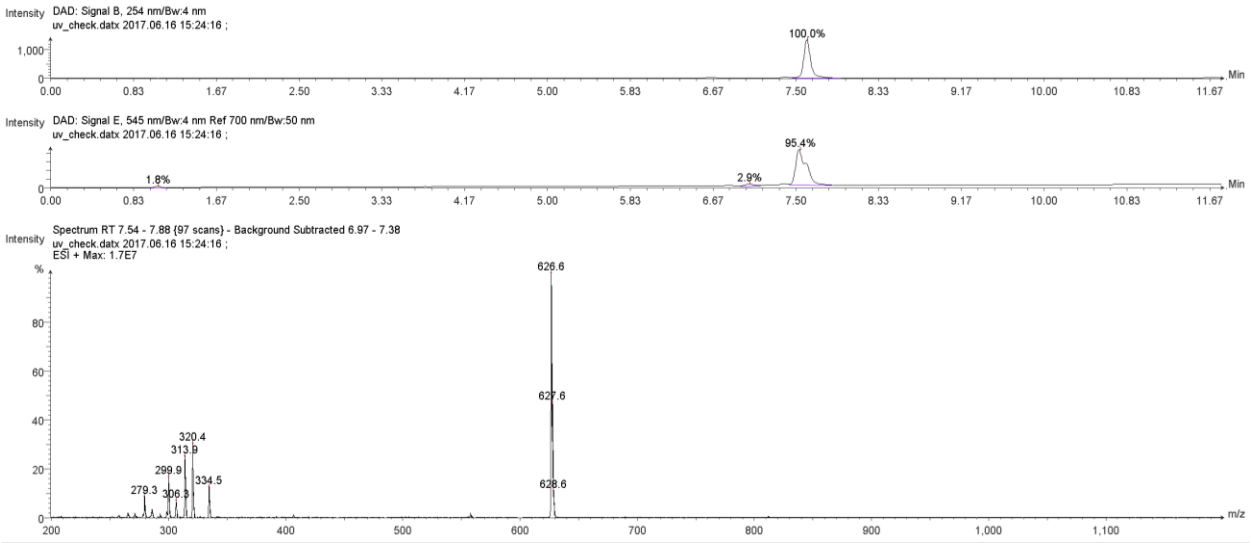

Low resolution ESI+ mass spectrum of **17** (Rhodamine B amide tetrazine):

Calculated for $[M]^{+}$: 626.3
Found: 626.6

Calculated for $[M+H+acetonitrile]^{2+}$: 334.2
Found: 334.5

Calculated for $[M+H+acetonitrile\text{-}ethyl\ (decomposition\ on\ LC/MS)]^{2+}$: 320.2
Found: 320.4

Calculated for $[M+H]^{2+}$: 313.7
Found: 313.9

Calculated for $[M:tet\text{-}nitrile\ (decomposition\ on\ LC/MS)+acetonitrile]^{2+}$: 299.7
Found: 299.9

Calculated for $[M:tet\text{-}nitrile\ (decomposition\ on\ LC/MS)]^{2+}$: 279.1
Found: 279.3

Spectrum 3.8.26. ^{1}H spectrum of 17, rhodamine B amide tetrazine:

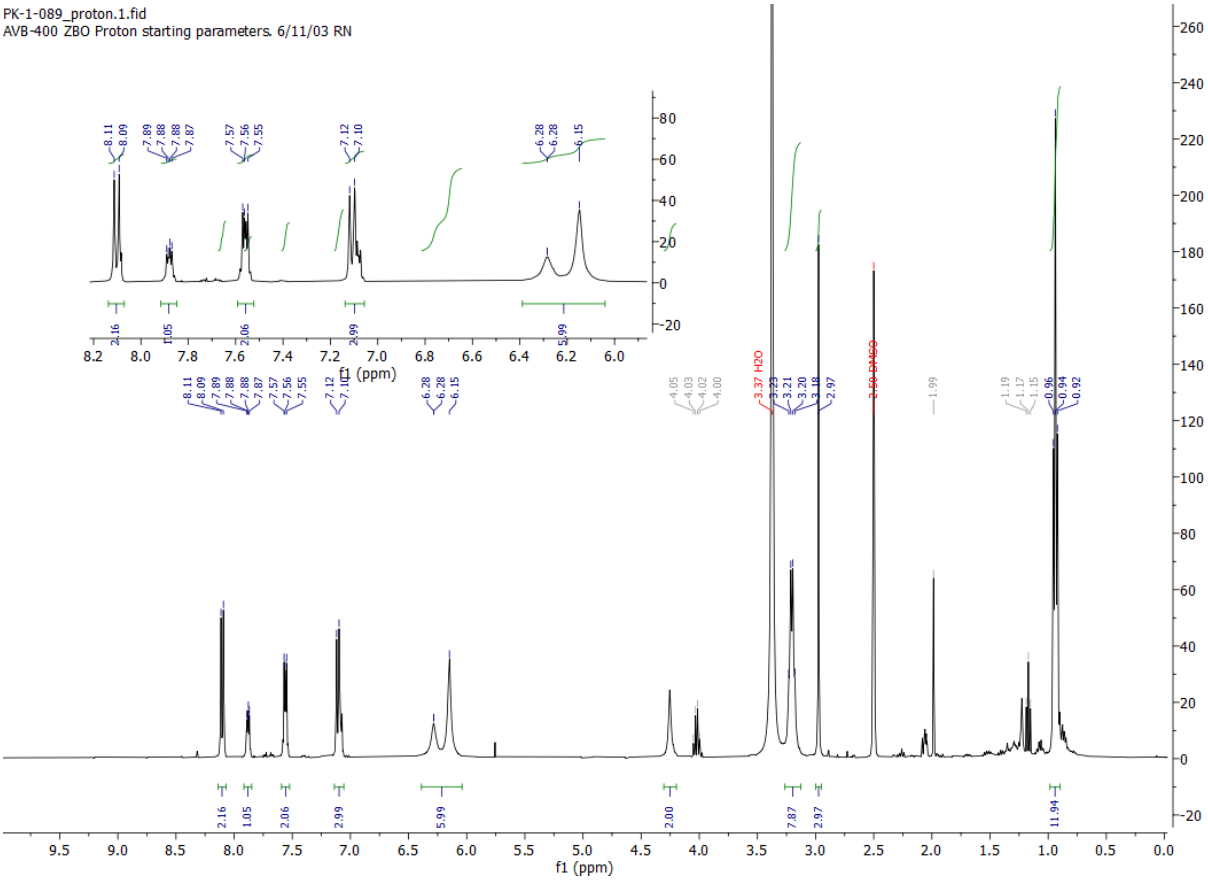

Spectrum 3.8.27. LC/MS of 18, rhodamine B sarcosine:

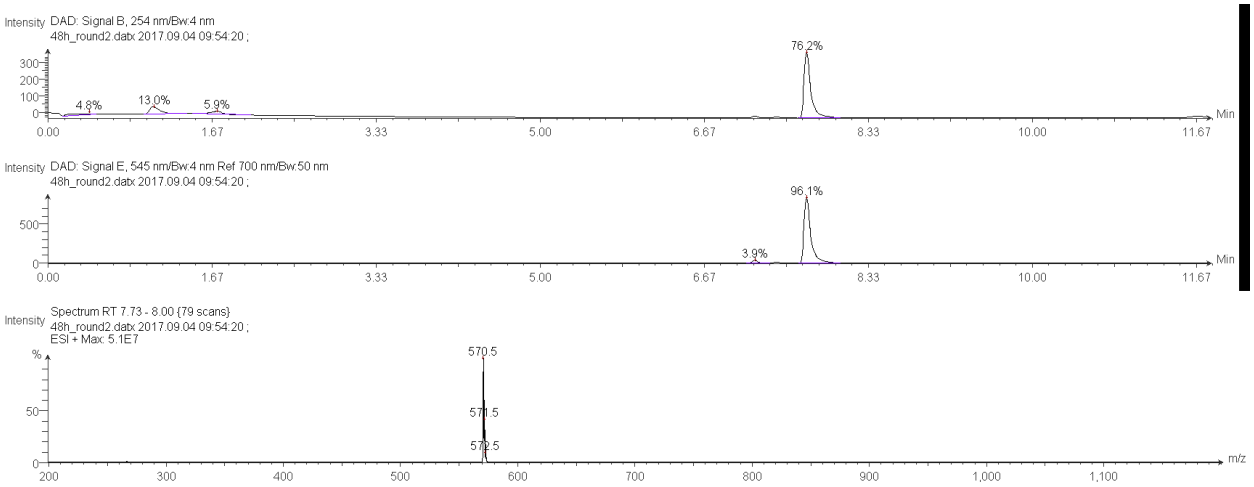

Low resolution ESI+ mass spectrum of **18** (Rhodamine B sarcosine):

Calculated for $[M]^+$: 570.3
Found: 570.5

Spectrum 3.8.28. ^{1}H spectrum of 18, rhodamine B sarcosine:

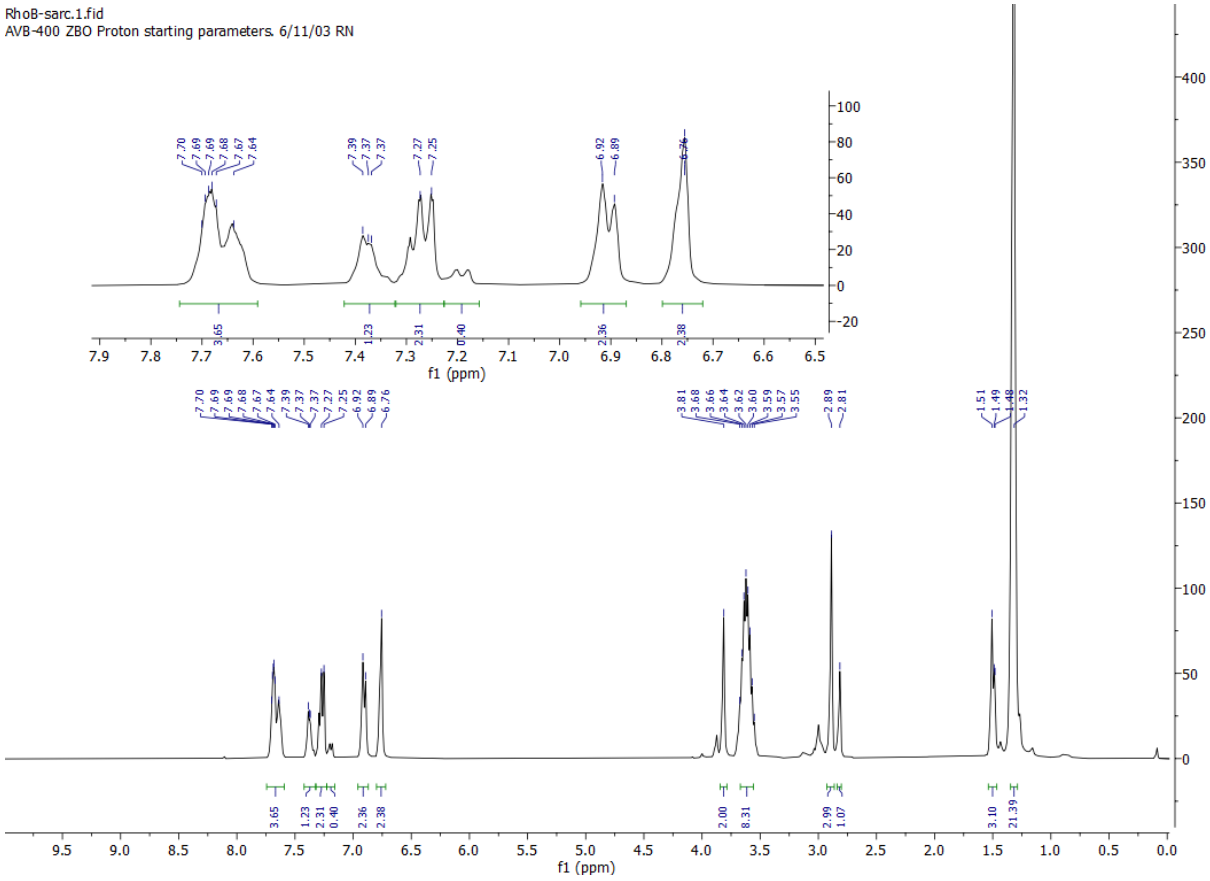

Spectrum 3.8.29. LC/MS spectrum of 19, rhodamine B sarcosine tetrazine:

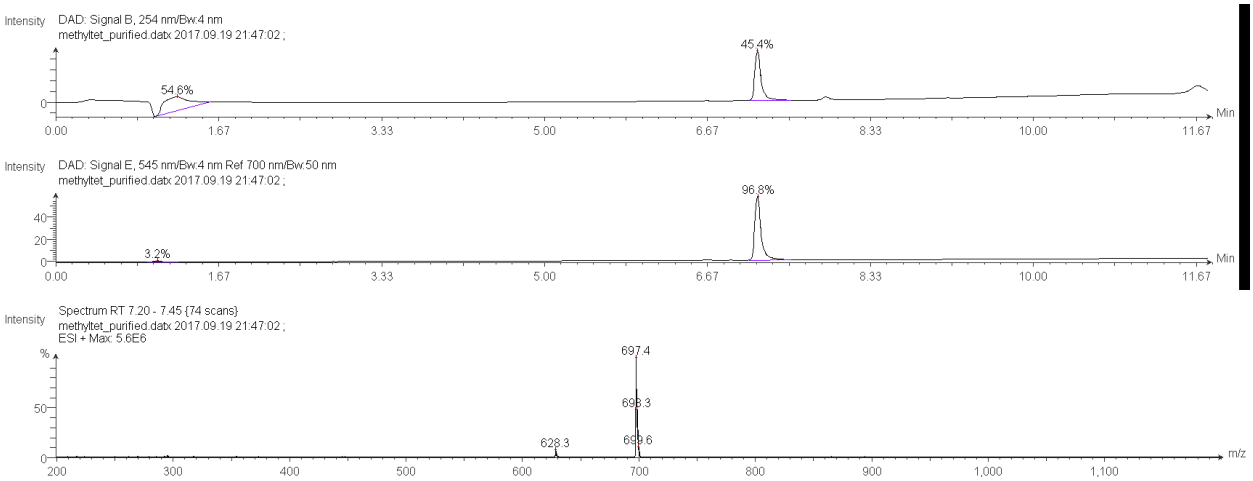

Low resolution ESI+ mass spectrum of **19** (Rhodamine B sarcosine tetrazine):

Calculated for $[M]^+$: 697.4
Found: 697.4

Calculated for [M:tet-nitrile (decomposition on LC/MS)] : 628.3

Found: 628.3

Spectrum 3.8.30. ^{1}H spectrum of 19, rhodamine B sarcosine tetrazine:

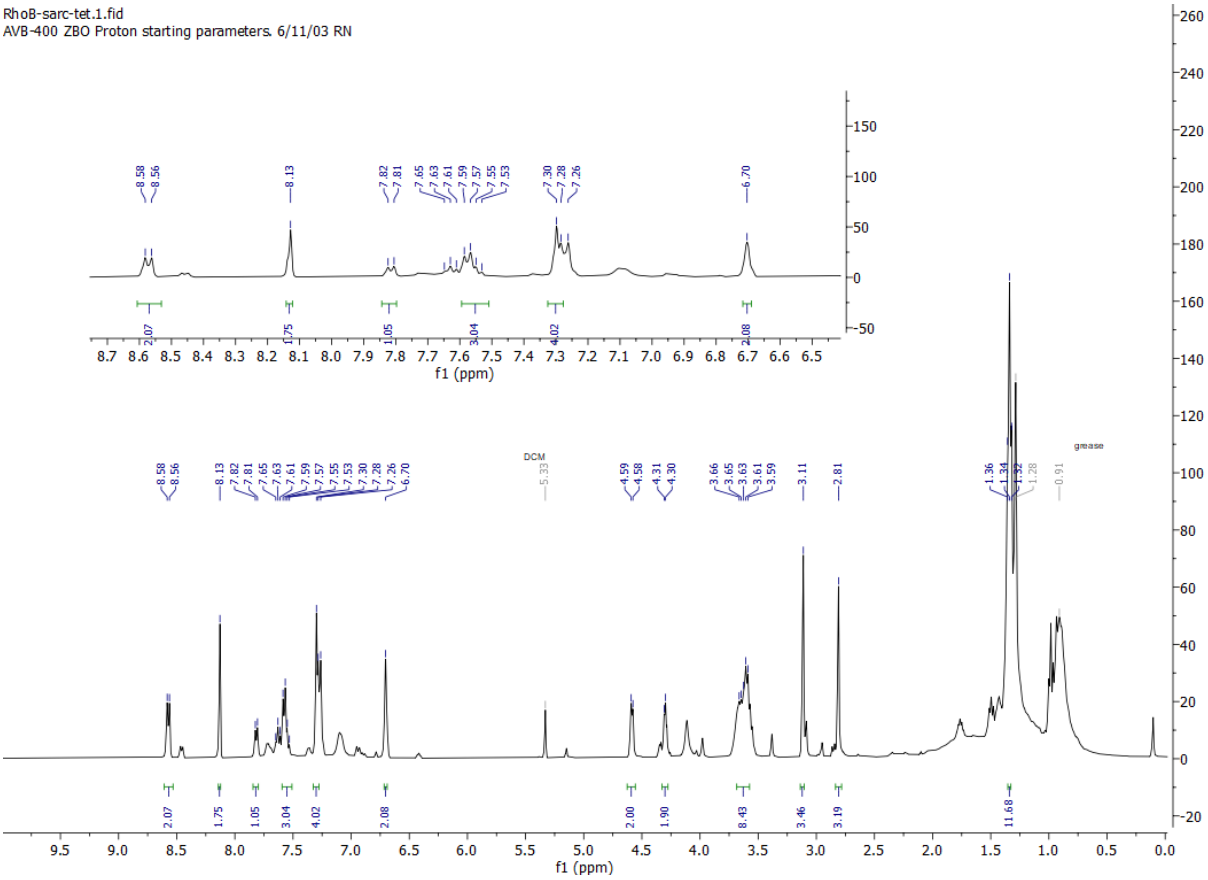

Spectrum 3.8.31. ^{1}H spectrum of 20, benzoic acid methyl tetrazine:

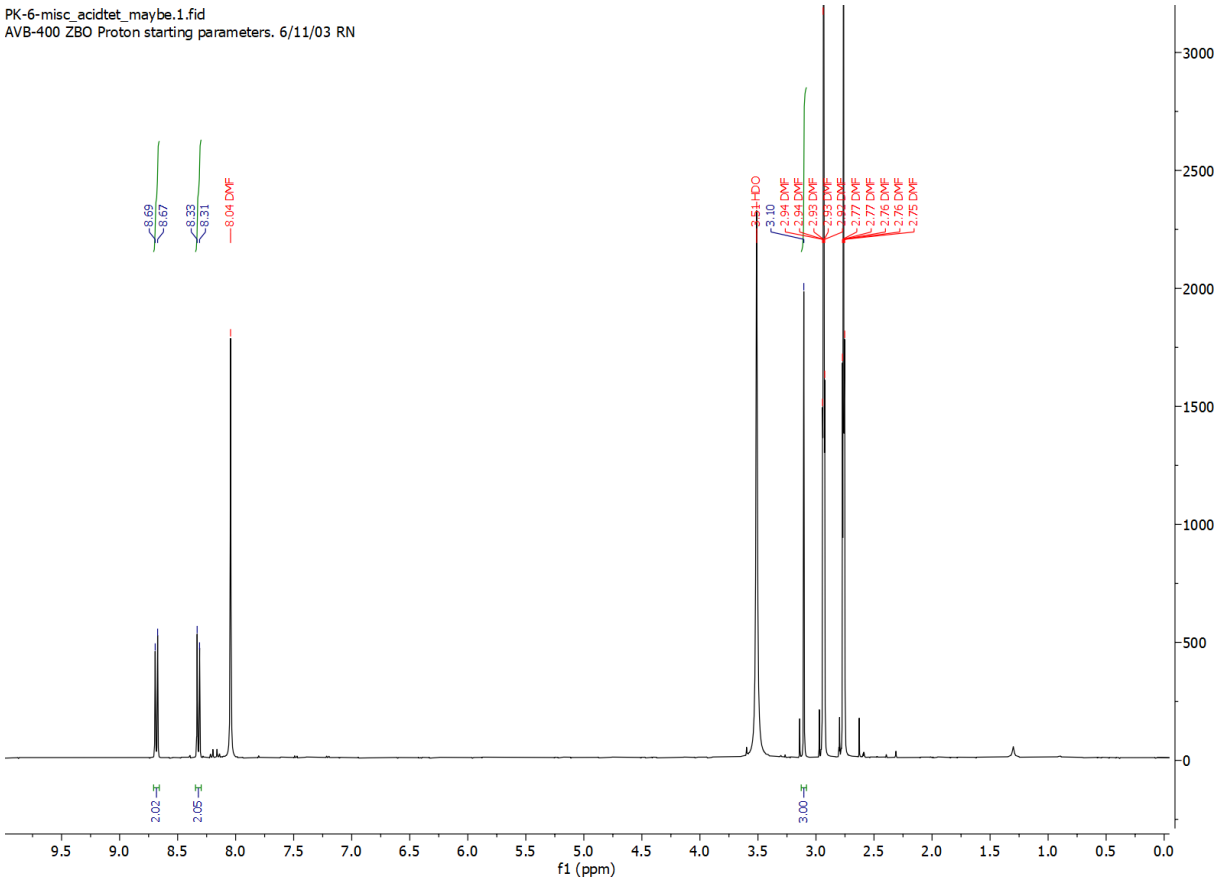

Spectrum 3.8.32. ^{1}H spectrum of 21, N-BOC 4-cyanobenzylamine:

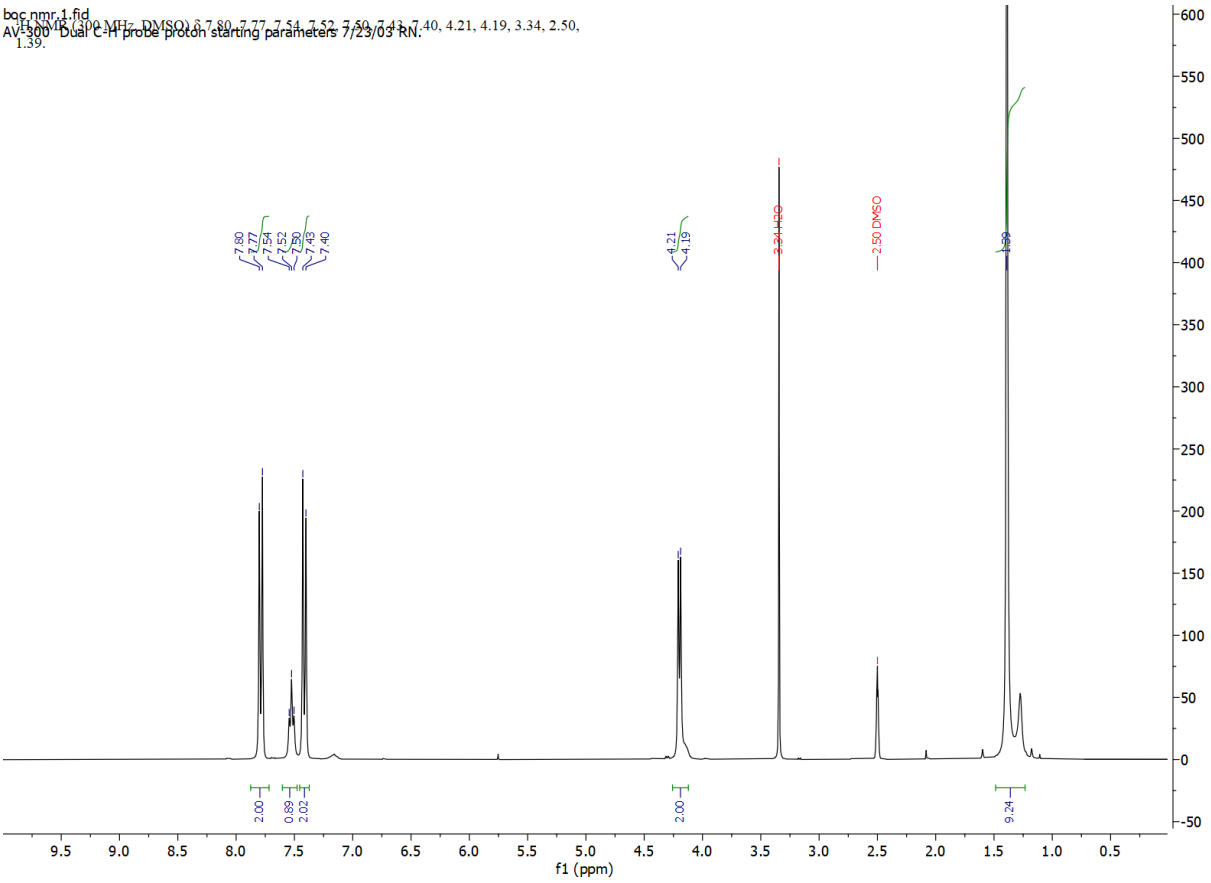

Spectrum 3.8.33. 1H spectrum of 22, N-BOC benzylamine methyl tetrazine:

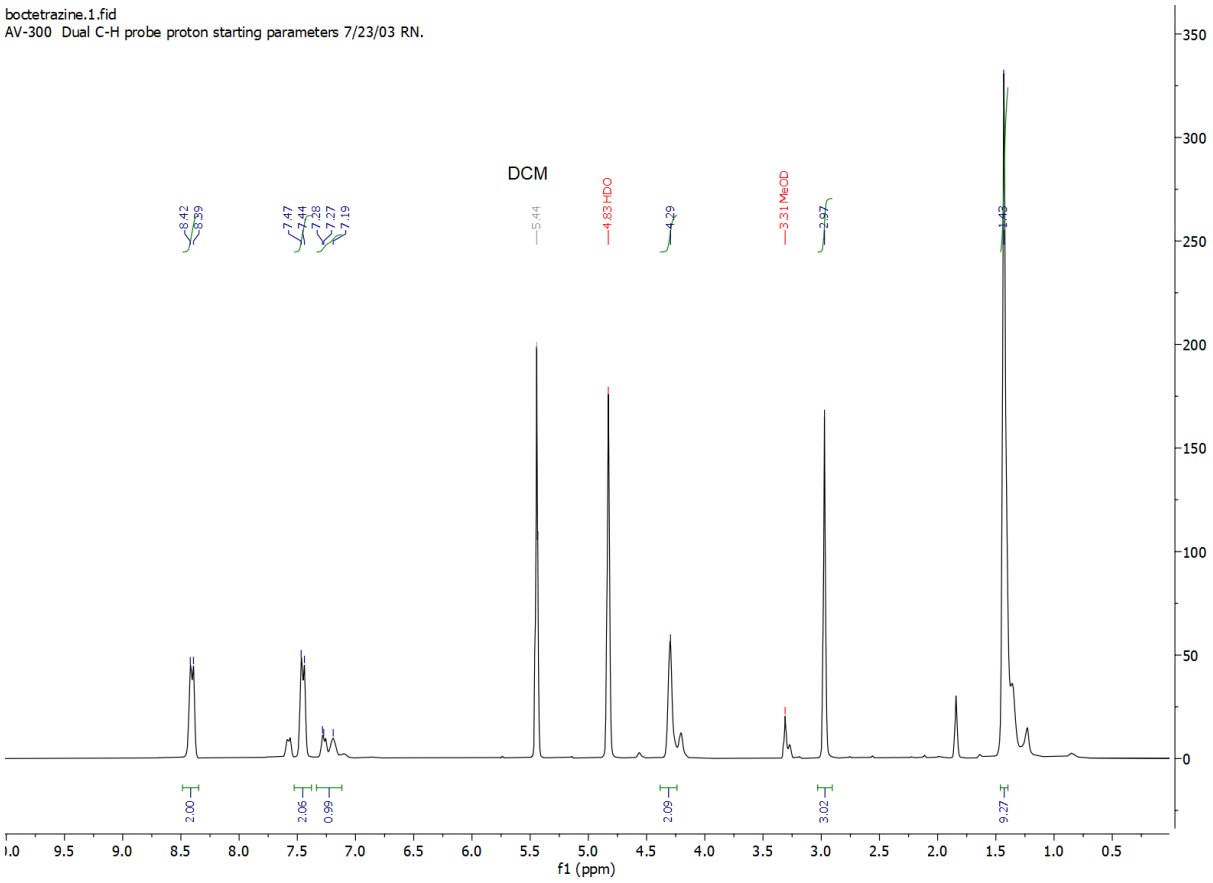

Spectrum 3.8.34. LC/MS spectrum of 24, TCO-PEG$_{25}$-Halo:

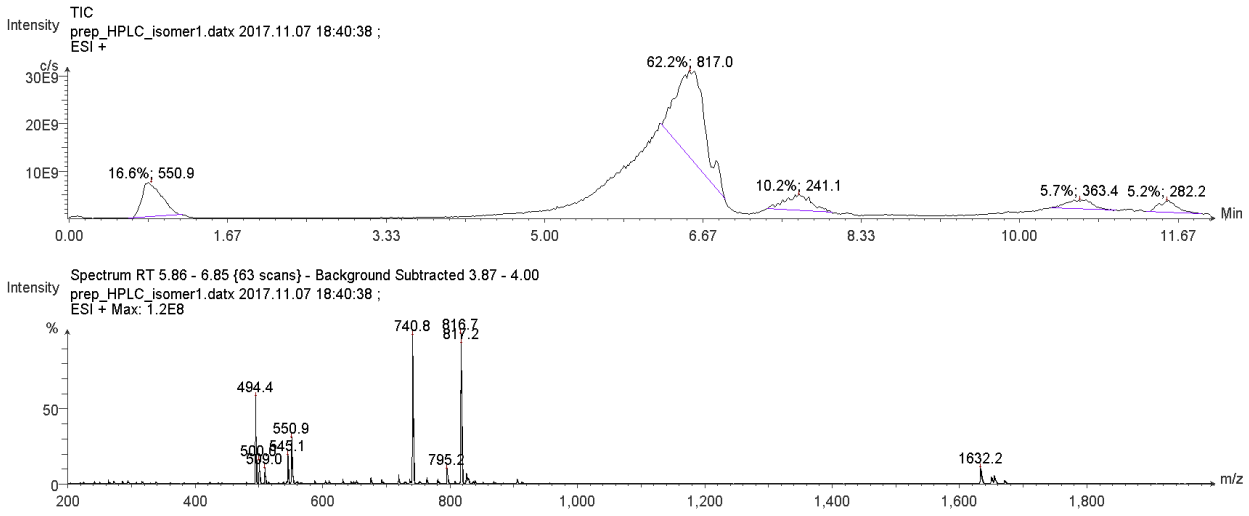

Low resolution ESI+ mass spectrum of **24** (TCO-PEG$_{25}$-Halo):

Calculated for $[M+H]^{+}$: 1633.0
Found: 1632.2

Calculated for $[M+2H]^{2+}$: 817.0
Found: 816.7

Calculated for $[M+2H\text{-carbamate (BOC analog, TFA labile on LC)}]^{2+}$: 741.0

Found: 740.8

Calculated for $[M+2H+Na]^{3+}$: 552.3

Found: 550.9

Calculated for $[M+3H]^{3+}$: 545.0

Found: 545.1

Calculated for $[M+3H\text{-carbamate (BOC analog, TFA labile on LC)}]^{3+}$: 494.3

Found: 494.4

3.9 References

1. Grabe, M.; Oster, G., Regulation of organelle acidity. *The Journal of general physiology* **2001,** *117* (4), 329-44.
2. Kirichok, Y.; Krapivinsky, G.; Clapham, D. E., The mitochondrial calcium uniporter is a highly selective ion channel. *Nature* **2004,** *427* (6972), 360-4.
3. Mak, D. O.; Vais, H.; Cheung, K. H.; Foskett, J. K., Isolating nuclei from cultured cells for patch-clamp electrophysiology of intracellular Ca(2+) channels. *Cold Spring Harbor protocols* **2013,** *2013* (9), 880-4.
4. Zhong, X. Z.; Dong, X. P., Lysosome electrophysiology. *Methods in cell biology* **2015,** *126*, 197-215.
5. Saminathan, A.; Devany, J.; Veetil, A. T.; Suresh, B.; Pillai, K. S.; Schwake, M.; Krishnan, Y., A DNA-based voltmeter for organelles. *Nature nanotechnology* **2021,** *16* (1), 96-103.
6. Matamala, E.; Castillo, C.; Vivar, J. P.; Rojas, P. A.; Brauchi, S. E., Imaging the electrical activity of organelles in living cells. *Communications biology* **2021,** *4* (1), 389.
7. Sepehri Rad, M.; Cohen, L. B.; Braubach, O.; Baker, B. J., Monitoring voltage fluctuations of intracellular membranes. *Scientific reports* **2018,** *8* (1), 6911.
8. Deal, P. E.; Kulkarni, R. U.; Al-Abdullatif, S. H.; Miller, E. W., Isomerically Pure Tetramethylrhodamine Voltage Reporters. *Journal of the American Chemical Society* **2016,** *138* (29), 9085-9088.
9. Klier, P. E. Z.; Martin, J. G.; Miller, E. W., Imaging Reversible Mitochondrial Membrane Potential Dynamics with a Masked Rhodamine Voltage Reporter. *Journal of the American Chemical Society* **2021,** *143* (11), 4095-4099.
10. Johnson, L. V.; Walsh, M. L.; Chen, L. B., Localization of mitochondria in living cells with rhodamine 123. *Proceedings of the National Academy of Sciences* **1980,** *77* (2), 990-994.
11. Zielonka, J.; Joseph, J.; Sikora, A.; Hardy, M.; Ouari, O.; Vasquez-Vivar, J.; Cheng, G.; Lopez, M.; Kalyanaraman, B., Mitochondria-Targeted Triphenylphosphonium-Based Compounds: Syntheses, Mechanisms of Action, and Therapeutic and Diagnostic Applications. *Chemical reviews* **2017,** *117* (15), 10043-10120.
12. Wang, H.; Fang, B.; Peng, B.; Wang, L.; Xue, Y.; Bai, H.; Lu, S.; Voelcker, N. H.; Li, L.; Fu, L.; Huang, W., Recent Advances in Chemical Biology of Mitochondria Targeting. *Frontiers in Chemistry* **2021,** *9* (321).
13. Gao, P.; Pan, W.; Li, N.; Tang, B., Fluorescent probes for organelle-targeted bioactive species imaging. *Chemical science* **2019,** *10* (24), 6035-6071.
14. Tour, O.; Adams, S. R.; Kerr, R. A.; Meijer, R. M.; Sejnowski, T. J.; Tsien, R. W.; Tsien, R. Y., Calcium Green FlAsH as a genetically targeted small-molecule calcium indicator. *Nature chemical biology* **2007,** *3* (7), 423-31.
15. Bannwarth, M.; Corrêa, I. R.; Sztretye, M.; Pouvreau, S.; Fellay, C.; Aebischer, A.; Royer, L.; Ríos, E.; Johnsson, K., Indo-1 Derivatives for Local Calcium Sensing. *ACS chemical biology* **2009,** *4* (3), 179-190.
16. Kamiya, M.; Johnsson, K., Localizable and Highly Sensitive Calcium Indicator Based on a BODIPY Fluorophore. *Analytical Chemistry* **2010,** *82* (15), 6472-6479.

17. Gruskos, J. J.; Zhang, G.; Buccella, D., Visualizing Compartmentalized Cellular Mg2+ on Demand with Small-Molecule Fluorescent Sensors. *Journal of the American Chemical Society* **2016,** *138* (44), 14639-14649.
18. Best, M.; Porth, I.; Hauke, S.; Braun, F.; Herten, D.-P.; Wombacher, R., Protein-specific localization of a rhodamine-based calcium-sensor in living cells. *Organic & Biomolecular Chemistry* **2016,** *14* (24), 5606-5611.
19. Cañeque, T.; Müller, S.; Rodriguez, R., Visualizing biologically active small molecules in cells using click chemistry. *Nature Reviews Chemistry* **2018,** *2* (9), 202-215.
20. Knall, A. C.; Slugovc, C., Inverse electron demand Diels-Alder (iEDDA)-initiated conjugation: a (high) potential click chemistry scheme. *Chemical Society reviews* **2013,** *42* (12), 5131-42.
21. Chen, W.; Wang, D.; Dai, C.; Hamelberg, D.; Wang, B., Clicking 1,2,4,5-tetrazine and cyclooctynes with tunable reaction rates. *Chemical communications (Cambridge, England)* **2012,** *48* (12), 1736-8.
22. Oliveira, B. L.; Guo, Z.; Bernardes, G. J. L., Inverse electron demand Diels–Alder reactions in chemical biology. *Chemical Society reviews* **2017,** *46* (16), 4895-4950.
23. Oliveira, B. L.; Guo, Z.; Boutureira, O.; Guerreiro, A.; Jiménez-Osés, G.; Bernardes, G. J., A Minimal, Unstrained S-Allyl Handle for Pre-Targeting Diels-Alder Bioorthogonal Labeling in Live Cells. *Angewandte Chemie (International ed. in English)* **2016,** *55* (47), 14683-14687.
24. Wieczorek, A.; Werther, P.; Euchner, J.; Wombacher, R., Green- to far-red-emitting fluorogenic tetrazine probes - synthetic access and no-wash protein imaging inside living cells. *Chemical science* **2017,** *8* (2), 1506-1510.
25. Wu, H.; Yang, J.; Šečkutė, J.; Devaraj, N. K., In situ synthesis of alkenyl tetrazines for highly fluorogenic bioorthogonal live-cell imaging probes. *Angewandte Chemie (International ed. in English)* **2014,** *53* (23), 5805-9.
26. Karver, M. R.; Weissleder, R.; Hilderbrand, S. A., Synthesis and Evaluation of a Series of 1,2,4,5-Tetrazines for Bioorthogonal Conjugation. *Bioconjugate Chemistry* **2011,** *22* (11), 2263-2270.
27. Boggess, S. C.; Gandhi, S. S.; Siemons, B. A.; Huebsch, N.; Healy, K. E.; Miller, E. W., New Molecular Scaffolds for Fluorescent Voltage Indicators. *ACS chemical biology* **2019,** *14* (3), 390-396.
28. Lazzari-Dean, J. R.; Gest, A. M.; Miller, E. W., Optical estimation of absolute membrane potential using fluorescence lifetime imaging. *eLife* **2019,** *8*.
29. Deal, P. E.; Liu, P.; Al-Abdullatif, S. H.; Muller, V. R.; Shamardani, K.; Adesnik, H.; Miller, E. W., Covalently Tethered Rhodamine Voltage Reporters for High Speed Functional Imaging in Brain Tissue. *Journal of the American Chemical Society* **2020,** *142* (1), 614-622.
30. Takakura, H.; Zhang, Y.; Erdmann, R. S.; Thompson, A. D.; Lin, Y.; McNellis, B.; Rivera-Molina, F.; Uno, S. N.; Kamiya, M.; Urano, Y.; Rothman, J. E.; Bewersdorf, J.; Schepartz, A.; Toomre, D., Long time-lapse nanoscopy with spontaneously blinking membrane probes. *Nature biotechnology* **2017,** *35* (8), 773-780.
31. Huang, Y. L.; Walker, A. S.; Miller, E. W., A Photostable Silicon Rhodamine Platform for Optical Voltage Sensing. *Journal of the American Chemical Society* **2015,** *137* (33), 10767-76.

32. Scaduto, R. C., Jr.; Grotyohann, L. W., Measurement of mitochondrial membrane potential using fluorescent rhodamine derivatives. *Biophysical journal* **1999,** *76* (1 Pt 1), 469-77.
33. Stewart, M. P.; Langer, R.; Jensen, K. F., Intracellular Delivery by Membrane Disruption: Mechanisms, Strategies, and Concepts. *Chemical reviews* **2018,** *118* (16), 7409-7531.
34. Das, A.; Brown, M. S.; Anderson, D. D.; Goldstein, J. L.; Radhakrishnan, A., Three pools of plasma membrane cholesterol and their relation to cholesterol homeostasis. *eLife* **2014,** *3*.
35. Casares, D.; Escribá, P. V.; Rosselló, C. A., Membrane Lipid Composition: Effect on Membrane and Organelle Structure, Function and Compartmentalization and Therapeutic Avenues. *International journal of molecular sciences* **2019,** *20* (9).
36. Ridsdale, A.; Denis, M.; Gougeon, P. Y.; Ngsee, J. K.; Presley, J. F.; Zha, X., Cholesterol is required for efficient endoplasmic reticulum-to-Golgi transport of secretory membrane proteins. *Molecular biology of the cell* **2006,** *17* (4), 1593-605.
37. Rossi, A. M.; Taylor, C. W., IP(3) receptors - lessons from analyses ex cellula. *Journal of cell science* **2018,** *132* (4).
38. Lichtenfels, R.; Biddison, W. E.; Schulz, H.; Vogt, A. B.; Martin, R., CARE-LASS (calcein-release-assay), an improved fluorescence-based test system to measure cytotoxic T lymphocyte activity. *Journal of immunological methods* **1994,** *172* (2), 227-39.
39. Kalbácová, M.; Vrbacký, M.; Drahota, Z.; Melková, Z., Comparison of the effect of mitochondrial inhibitors on mitochondrial membrane potential in two different cell lines using flow cytometry and spectrofluorometry. *Cytometry. Part A : the journal of the International Society for Analytical Cytology* **2003,** *52* (2), 110-6.
40. Abad, M. F.; Di Benedetto, G.; Magalhães, P. J.; Filippin, L.; Pozzan, T., Mitochondrial pH monitored by a new engineered green fluorescent protein mutant. *The Journal of biological chemistry* **2004,** *279* (12), 11521-9.
41. Carreras-Sureda, A.; Pihán, P.; Hetz, C., Calcium signaling at the endoplasmic reticulum: fine-tuning stress responses. *Cell calcium* **2018,** *70*, 24-31.
42. Goldman, D. E., POTENTIAL, IMPEDANCE, AND RECTIFICATION IN MEMBRANES. *The Journal of general physiology* **1943,** *27* (1), 37-60.
43. Sanchez, C.; Berthier, C.; Allard, B.; Perrot, J.; Bouvard, C.; Tsutsui, H.; Okamura, Y.; Jacquemond, V., Tracking the sarcoplasmic reticulum membrane voltage in muscle with a FRET biosensor. *The Journal of general physiology* **2018,** *150* (8), 1163-1177.
44. Koshita, M.; Hotta, K., Relationship between membrane potential and calcium ion fluxes in the fragmented sarcoplasmic reticulum. *The Japanese journal of physiology* **1981,** *31* (1), 109-20.
45. Tsutsui, H.; Karasawa, S.; Okamura, Y.; Miyawaki, A., Improving membrane voltage measurements using FRET with new fluorescent proteins. *Nature methods* **2008,** *5* (8), 683-5.
46. Beeler, T. J.; Farmen, R. H.; Martonosi, A. N., The mechanism of voltage-sensitive dye responses on sarcoplasmic reticulum. *The Journal of membrane biology* **1981,** *62* (1-2), 113-37.
47. Cabrini, G.; Verkman, A. S., Potential-sensitive response mechanism of diS-C3-(5) in biological membranes. *The Journal of membrane biology* **1986,** *92* (2), 171-82.

48. Beier, H. T.; Roth, C. C.; Bixler, J. N.; Sedelnikova, A. V.; Ibey, B. L., Visualization of Dynamic Sub-microsecond Changes in Membrane Potential. *Biophysical journal* **2019,** *116* (1), 120-126.
49. Vay, L.; Hernández-Sanmiguel, E.; Santo-Domingo, J.; Lobatón, C. D.; Moreno, A.; Montero, M.; Alvarez, J., Modulation of Ca(2+) release and Ca(2+) oscillations in HeLa cells and fibroblasts by mitochondrial Ca(2+) uniporter stimulation. *The Journal of physiology* **2007,** *580* (Pt 1), 39-49.
50. Casler JC, Zajac AL, Valbuena FM, Sparvoli D, Jeyifous O, Turkewitz AP, Horne-Badovinac S, Green WN, Glick BS. ESCargo: a regulatable fluorescent secretory cargo for diverse model organisms. *Mol Biol Cell*. **2020**; 31 (26) 2892-2903.
51. Choy, E.; Chiu, V. K.; Silletti, J.; Feoktistov, M.; Morimoto, T.; Michaelson, D.; Ivanov, I. E.; Philips, M. R. Endomembrane Trafficking of Ras: The CAAX Motif Targets Proteins to the ER and Golgi. *Cell*. **1999**, *98* (1), 69-80
52. Woodford, C.R.; Frady, E.P.; Smith, R.S.; Morey, B.; Canzi, G.; Palida, S.F; Araneda, R.C.; Kristan Jr, W.B.; Kubiak, C.P.; Miller, E.W.; Tsien, R.Y. Improved PeT molecules for optically sensing voltage in neurons. *J. Am. Chem. Soc.* **2015**, *137* (5), 1817–1824
53. Los, G.V.; Encell, L.P.; McDougall, M.G.; Hartzell, D.D.; Karassina, N.; Zimprich, C.; Wood, M.G.; Learish, R.; Ohana, R.F.; Urh, M.; Simpson, D.; Mendez, J.; Zimmerman, K.; Otto, P.; Vidugiris, G.; Zhu, J.; Darzins, A.; Klaubert, D.H.; Bulleit, R.F.; Wood, K.V. HaloTag: A Novel Protein Labeling Technology for Cell Imaging and Protein Analysis. *ACS Chemical Biology* **2008**, 3 (6), 373-382
54. Arbeloa, F.L.; Ojeda, P.R; Arbeloa, I.L. Flourescence self-quenching of the molecular forms of Rhodamine B in aqueous and ethanolic solutions. *J. Luminescence*, **1989** *44* (1-2), 105-112

Chapter 4: Through bond energy and electron transfer in flurophores

With Ryan Roo

4.0 Introduction

When a fluorophore absorbs a photon of a wavelength that matches the energy gap between its ground state and an excited state, an electron gets promoted up an energy level and the fluorophore enters an excited state in which it now carries extra energy that it has taken from that photon. There are many ways in which the excited fluorophore can now release this energy. In a fluorescent molecule, the two most common pathways for loss of this energy are fluorescence, in which a photon of equal or lesser energy to the exciting photon is emitted by the fluorophore, and non-radiative decay, in which the energy is transferred as kinetic energy to the motion of the fluorophore or the atoms and molecules in its environment. The probability that an excited fluorophore will emit a photon rather than transfer energy via other pathways is termed its quantum yield.

In addition to these two typical pathways for energy loss, fluorophores can also "donate" their energy non-radiatively into exciting another "acceptor" molecule into its excited state. The acceptor molecule then behaves as it would if it had been driven to its excited state through other means such as photon absorption. One mechanism by which a fluorophore can transfer its energy is through Resonance Energy Transfer (RET) in which the donor fluorophore transfers its energy through space to the acceptor. The rate of RET depends on the spectral overlap between donor fluorescence emission and acceptor absorption, the distance between the donor and the acceptor, and the relative orientation of the donor and acceptor. The principles governing RET[1] and applications of RET in the design of fluorescent probes[2,3,4] are reviewed extensively elsewhere and are not the focus of this chapter.

A second mechanism by which an excited fluorophore can donate its energy is Through Bond Energy Transfer (TBET) in which the donor fluorophore transfers its energy through bonds to the acceptor. Although the factors governing TBET are poorly understood compared to those that govern RET[2,8], some principles can be concluded from observation of TBET systems. Due to conservation of energy, a donor fluorophore cannot have an emission spectrum that is entirely lower in energy than the absorption spectrum of the acceptor, but beyond this requirement spectral overlap does not need to exist between the donor and acceptor for TBET to occur[5]. What this means in practice is that a donor can be substantially blueshifted compared to an acceptor and TBET will still be observed at rapid rates[6]. Secondly, the bonding structure between the donor and acceptor has a strong impact on the efficiency of TBET, with rigid conjugated, twisted pi systems having extremely rapid TBET rates[7] and little to no TBET observed in purely aliphatic systems[8].

The goal of this chapter is to provide examples of fluorescent probes designed using TBET and analogous through-bond electron transfer systems and explain the principles behind their operation. These principles will then be applied to VoltageFluor systems to provide a computational description of their operation and propose an approach to using these probes for ratiometric measurements of membrane potential.

4.1 Through bond energy transfer for modulation of fluorescence

There are two key approaches used to harnessing TBET in the design of fluorescent probes. The first, and most relevant to the work presented in early chapters of this dissertation, is to attach an acceptor that itself has a very low quantum yield, meaning that when the donor transfers its energy to the acceptor, it will mostly be emitted non-radiatively, leading to a reduction in observed fluorescence of the donor-acceptor conjugate. In practice, this means that the acceptor group has quenched the fluorescence of the donor. This fluorescence can then be unquenched by changing the properties of the quencher through chemical conversion. A common example of this is to use a tetrazine group, which typically has an absorbance maximum around 520 nm, as an acceptor for a green or orange emitting chromophore[7]. The tetrazine group has very little fluorescence, and so efficient energy transfer from the chromophore will lead to a very low observed quantum yield. The tetrazine can then react with strained alkenes to produce a diazine product which absorbs at much bluer wavelengths, thus eliminating TBET from the donor and leading to an increase in observed quantum yield. This allows for targeting of fluorophores to different locations by targeting strained alkenes to these locations with quenched fluorescence from dyes that reside in undesired locations.

Several examples exist of different chromophore-tetrazine linkers with varying efficiencies of fluorescence quenching. The most efficient linkage demonstrated is a single alkene between the chromophore and the tetrazine group. This linkage can lead to observed fluorescence quenching of over 100-fold (greater than 2 orders of magnitude) when using fluorescein, BODIPY, and rhodamine chromophores[9] (**Figure 4.1.1a, compound 1**). Directly coupling the tetrazine to the chromophore via a direct aryl-aryl linkage can achieve fluorescence more moderate fluorescence quenching of around 1-2 orders of magnitude depending on the location of the aryl-aryl linkage[10] (**Figure 4.1.1a, compound 2**). Amide based linkers that include aliphatic groups between fluorophores and tetrazines typically have quenching of 0-1 orders of magnitude[11,12] (**Figure 4.1.1a, compound 3**). **Figure 4.1.1a** summarizes the trend observed across reported literature substrates of linker type vs fluorescence quenching. Rhodamine B based substrates designed and synthesized in this work (see Chapter 3 for full synthetic details) to test the effectiveness of different linkers to tetrazines ortho to the chromophore for fluorescence quenching and turn-on reflect a similar trend (**Figure 4.1.1b**). Only 3-fold quenching is observed when an amide linkage including two aliphatic groups is used (**compound 4**) and only 5-fold quenching is observed when a direct aliphatic attachment to the aromatic system is used (**compound 5**). Changing this direct aliphatic attachment to a direct aryl linkage leads to 10-fold quenching (**compound 6**), demonstrating the increased efficiency of TBET in aromatic vs aliphatic linkages. Amide linkages containing one aliphatic group demonstrate 12-fold quenching (**compounds 7 and 8**), greater than a direct aromatic linkage, which may be due to the increased planarity of the amide attachment compared to the sterically hindered aromatic ring directly ortho to the chromophore which may twist substantially out of plane with the pendant ring it is attached to due to steric hindrance

with the nearby chromophore. All quantum yields are determined in 0.01% HCl to force rhodamines into the open, fluorescent form and avoid confounding effects of lactonization.

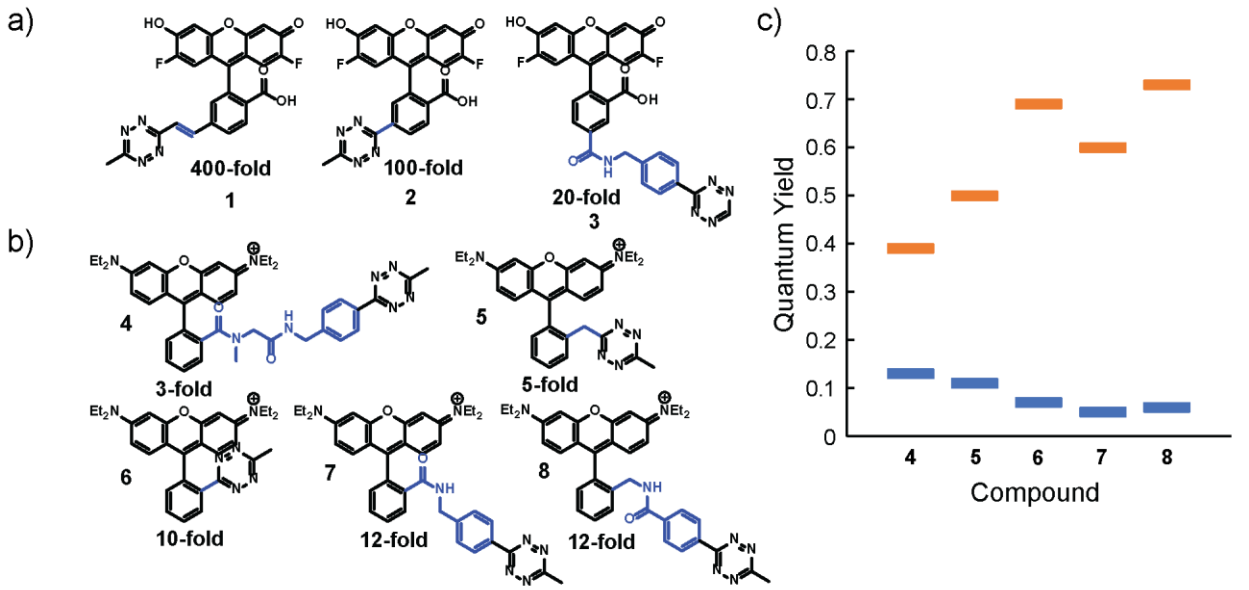

Figure 4.1.1 Representative linkages for TBET in fluorophore-quencher systems

a) Selected examples of linkages (highlighted in blue) between fluoresceins and tetrazines in literature and their relative turn-ons after chemical conversion of the tetrazine. **b**) Novel Rhodamine B-tetrazine conjugates reported in this dissertation and **c**) their fluorescence turn-on after chemical conversion of the tetrazine.

The second approach to utilizing TBET in a fluorescent probe is to design a system in which one chromophore donates its energy to a redshifted acceptor chromophore. This can lead to an overall redshift in fluorescence of the molecule which is desirable in biological applications; additionally, if the fluorescence of the donor or acceptor can be modulated in response to environmental properties or concentration of an analyte, the ratio of donor and acceptor fluorescence can be used as concentration-independent measurement of environmental properties or analyte concentration. Fluorophore-fluorophore TBET systems have been shown using alkyne linkages[13] (**Figure 4.1.2, compound 9**), direct aryl attachment[2] (**Figure 4.1.2, compound 10**) and even rigid fused bicylcic systems[14] (**Figure 4.1.2, compound 11**). The latter system highlights an interesting example of where a rigid but completely aliphatic system demonstrates efficient TBET. Another interesting approach uses TBET between a luciferin and a redshifted fluorophore to redshift the bioluminescence spectrum of the luciferin[15] (**Figure**

4.1.2, compound 12). A representative subset of fluorophore-fluorophore linkages demonstrated in literature are summarized in **Figure 4.1.2**.

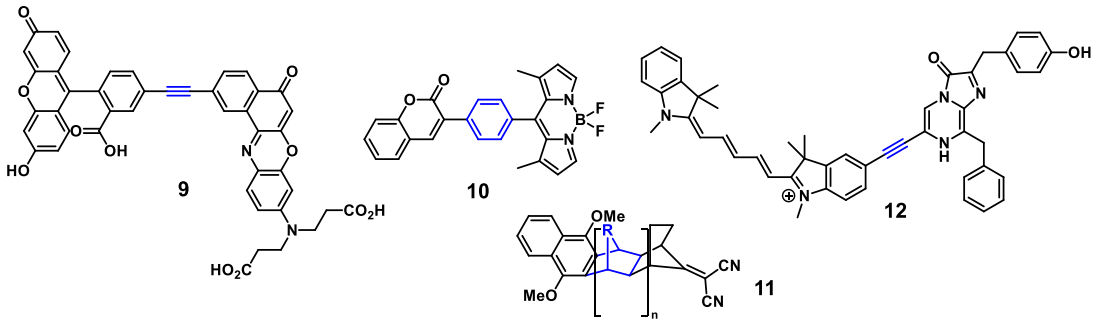

Figure 4.1.2 Representative linkages for TBET in multi-chromophore systems

4.2 Photoinduced through bond electron transfer for modulation of fluorescence

In addition to transferring energy from an excited state donor to an acceptor through bond structures in a single molecule, electrons can transfer through a bond structure from a donor system in a molecule to an acceptor system. In fluorophores, this often manifests as Photoinduced electron Transfer (PeT- not to be confused with Positron Emission Tomography or PET). In PeT, a fluorophore absorbs a photon and enters an excited state. This new excited state now has both a high energy electron that is a more favorable electron donor to an acceptor molecule and an empty “hole” in the orbital from which that electron was excited which is a more favorable acceptor from a donor molecule. If the relative energy levels are favorable, this can lead to two different electron transfer scenarios in a molecule which contains both a fluorophore and another molecular system with a highest occupied molecular orbital (HOMO) and lowest unoccupied molecular orbital (LUMO) similar in energy to that of the fluorophore. In one scenario, donor excited-PeT or d-PeT, the excited state of the fluorophore donates an electron to the LUMO of an acceptor molecule (**Figure 4.2.1abe**). In the second scenario, acceptor excited-PeT or a-PeT, the excited state of the fluorophore acts as an acceptor for an electron from the HOMO of a donor molecule (**Figure 4.2.1acf**). Both types of PeT compete with fluorescence (**Figure 4.2.1d**) as a decay pathway for the excited state of the fluorophore as the electron transfer process itself is non-radiative as well as the eventual reverse electron transfer process to return the fluorophore to the ground state (**Figure 4.2.1cd**)[16].

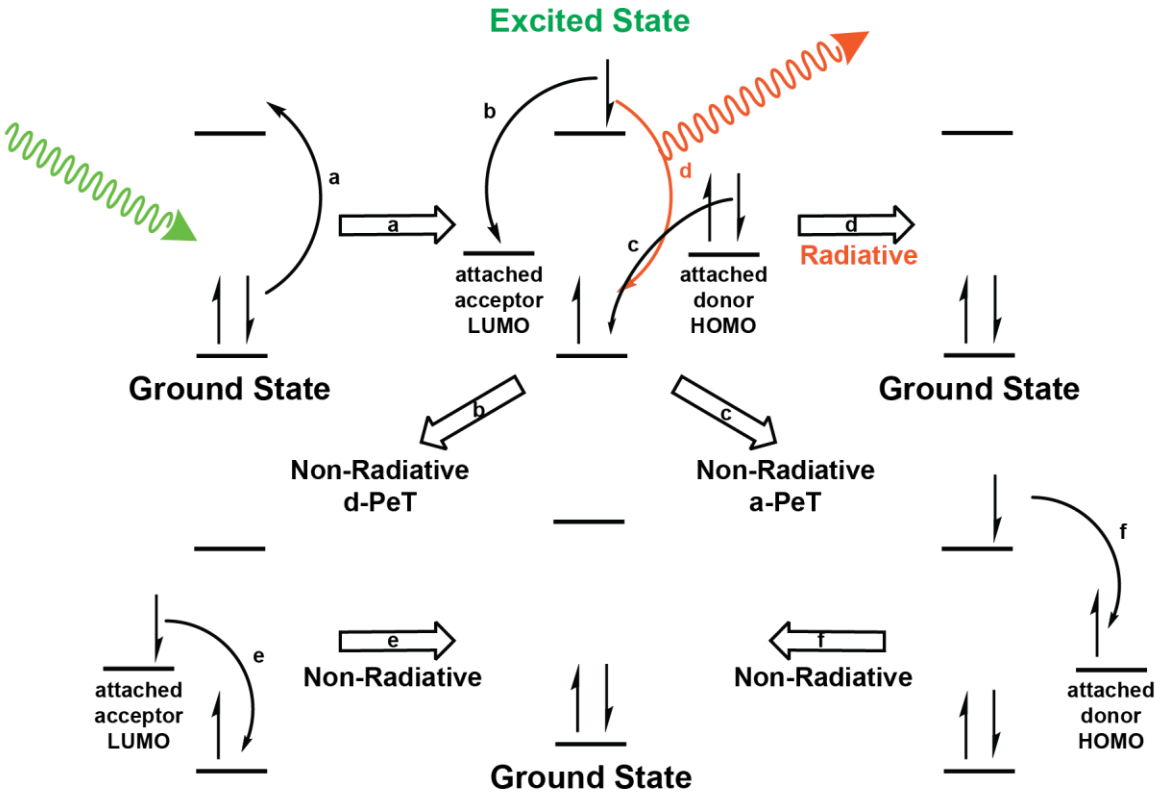

Figure 4.2.1 Photoinduced electron Transfer as a competing process to fluorescence

A fluorophore that has absorbed a photon (**a**) can emit a photon of a redder wavelength (**d**). In the presence of a LUMO of an acceptor of appropriate energy level the excited state can donate an electron to the LUMO (**b**) or, in the presence of a HOMO of a donor of appropriate energy level the HOMO can donate an electron to the now semi-occupied orbital of the fluorophore (**c**). In both these cases, reverse electron transfer non-radiatively restores the ground state (**e,f**)

Thus, if the rate of PeT changes in response to environmental parameters or analyte concentration, the quantum yield of the fluorophore will change as a result according to **Equation 4.2.1**:

$$\Phi_{fl} = \frac{k_{fl}}{k_{fl} + k_{nr} + k_{PeT}} \qquad \textbf{Equation 4.2.1}$$

where Φ_{fl} is the quantum yield of the molecule, k_{fl} is the rate of fluorescence, k_{nr} is the rate of non-radiative decay, and k_{PeT} is the rate of photoinduced electron transfer.

One notable example of the use of a modulation of fluorescence via PeT to provide a fluorescence-based readout of environmental properties is the class of molecules known as VoltageFluors, which localize to plasma membranes in cells and change their fluorescence in response to membrane potential. VoltageFluors consist of a fluorescent dye head linked via a molecular wire to an electron-rich or electron-deficient group that acts as an electron donor or acceptor, respectively. They also have an anionic group that anchors them in an orientation in the membrane that encourages the axis between the dye head and the electron donor/acceptor group to run as parallel as possible to the direction of the electric field (**Figure 4.2.2a**). In order for photoinduced electron transfer to occur, the electron must physically move between the dye head and the attached donor/acceptor through the bonding structure of the molecular wire. Because the electron is a charged species moving through an electric field, the magnitude and direction of the electric field will affect the rate at which the electron moves and thus the rate of PeT and therefore the quantum yield of the molecule (**Figure 4.2.2b**).

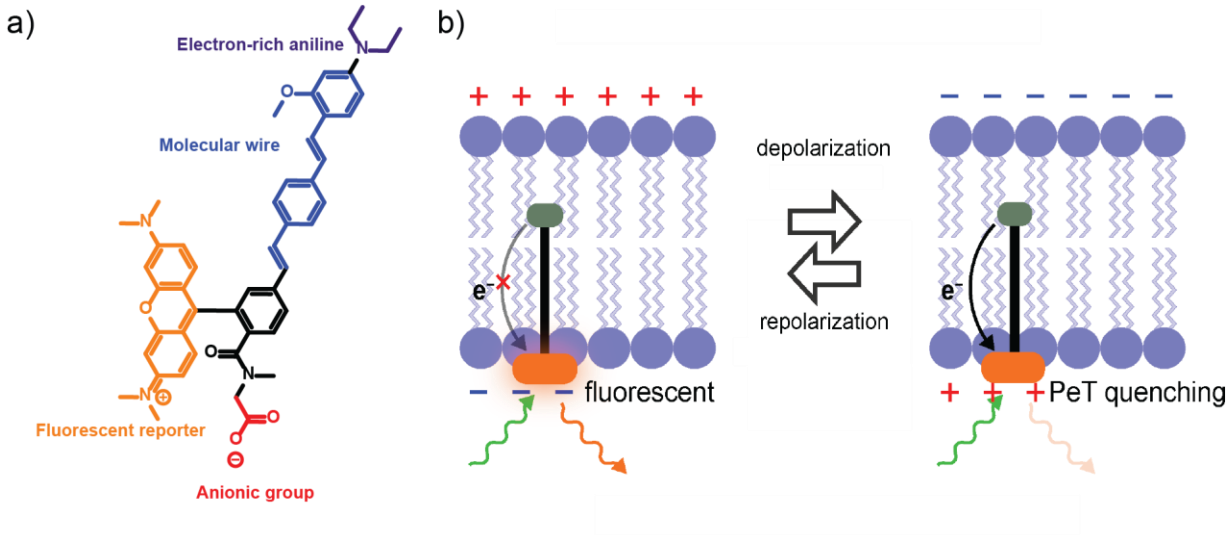

Figure 4.2.2 VoltageFluors operate via a Photoinduced electron Transfer mechanism

a) Structure and components of a representative VoltageFluor. **b**) Differing rates of electron transfer at different membrane potentials lead to changes in VoltageFluor fluorescence which can be used to measure membrane potential

The rate of PeT in a VoltageFluor will be a function of membrane potential but is also a function of static properties of the molecule such as the energy difference between the molecular wire and dye head, orientation in the membrane, and bonding structure of the molecular wire through which the electron passes. The next section uses a computational model to visualize how some of these factors will affect the voltage sensitivity of the VoltageFluor scaffold and compares the observed trends to experimentally derived data.

4.3 Mathematical description of through bond electron transfer

In order to computationally describe the voltage sensitivity of a VoltageFluor, we first need a mathematical model of electron transfer in VoltageFluors in terms of parameters that are either experimentally measurable or computationally predictable. Electron transfer is governed by the Marcus equation[17]:

$$k_{eT} = A * e^{-\frac{\left(\lambda+\Delta G^0_{ET}\right)^2}{4\lambda k_b T}} \quad \textbf{Equation 4.3.1}$$

Where k_{eT} is the rate of electron transfer, A is a constant describing the overall efficiency of that electron transfer, λ is the solvent reorganization energy, ΔG^0_{ET} is the free energy of electron transfer, k_b is the Boltzmann constant, and T is the temperature of the system in Kelvin. For a through-bond electron transfer system, the constant A is described by the equation[18]:

$$A = \sqrt{\frac{\pi}{\hbar^2 \lambda k_b T}} H^2_{DA} \quad \textbf{Equation 4.3.2}$$

where π is the ratio of a circle's circumference to its diameter, $\hbar$ is Planck's constant divided by 2π, and H_{DA} is the electronic coupling between the donor and the acceptor in the electron transfer system. The electronic coupling depends largely on the bonding structure through which the electron will transit and can be modeled by the equation[18]:

$$H_{DA}(r_{DA}) = H^0_{DA} e^{-\frac{\beta}{r_{DA}-r^0_{DA}}} \quad \textbf{Equation 4.3.3}$$

where r_{DA} is the distance between the donor and acceptor on the molecule, r^0_{DA} is the Van der Waals contact distance between the two molecular systems were they to be in direct contact, H^0_{DA} is the electronic coupling between the donor and acceptor at the Van der Waals contact distance, and β is the efficiency of electron transfer through the bonding structure.

When all these equations are considered, π, $\hbar$, and k_b are physical constants which can be easily inputted. r^0_{DA} is a physical property of the atoms involved and can be inputted from tabulated values. The donor-acceptor distance r_{DA} is a geometric property of the molecule that can be calculated from the bond lengths and geometry of the system. H^0_{DA} and λ are difficult parameters to model accurately but can be computationally estimated; these parameters are not the focus of this analysis and placeholder values of appropriate order of magnitude are used for computational modeling. This means that the results presented here are relative descriptors but may not be absolutely accurate. β values are

empirically measured for a variety of different bonding scaffolds and can be inputted directly into a computational model. This leaves ΔG_{ET}^{0} as the only parameter required further description. ΔG_{ET}^{0} can be calculated from the following equation[19]:

$$\Delta G_{PeT} = \Delta E_{ox} - \Delta E_{red} - \Delta E_{0,0} - w \quad \textbf{Equation 4.3.4}$$

where ΔG_{ET}^{0} is re-denoted as ΔG_{PeT} to specify the photoinduced nature of this process, ΔE_{ox} is the oxidation potential of the donor, ΔE_{red} is the reduction potential of the acceptor, $\Delta E_{0,0}$ is the energy required to promote the fluorophore into the excited state, and w is the work required to move the electron from the donor to the acceptor. ΔE_{ox} and ΔE_{red} can be measured via cyclic voltammetry or computationally modeled and $\Delta E_{0,0}$ is simply the energy of a photon whose wavelength equals the absorption maximum of the chromophore. The work required to move the electron can be derived from the basic physics equation:

$$w = q\vec{r} \cdot \vec{E} = qrEcos\theta \quad \textbf{Equation 4.3.5}$$

where $\vec{r}$ is the spatial vector describing the electron's travel and $\vec{E}$ is the vector describing the electric field, and q is simply -1 for an electron's charge. θ is the angle between these two vectors and in practice is the angle at which the VoltageFluor sits in the cell membrane. The magnitude of r is equal to the donor-acceptor distance r_{DA} described above and E is proportional to membrane potential via the equation:

$$E = \frac{V_{mem}}{d_{mem}} \quad \textbf{Equation 4.3.6}$$

where V_{mem} is the membrane potential which is the experimental variable to be measured via measurements of fluorescence intensity and d_{mem} is the thickness of the cell's membrane which is often estimated at 4 nm[20].

4.4 Relationship between through bond electron transfer and fluorescence

Section **4.3** describes the mathematical relationship between membrane potential and the rate of photoinduced electron transfer, but in order to visualize the relationship between membrane potential and changes in fluorescence, we must also show the relationship between changes in the rate of electron transfer and changes in VoltageFluor fluorescence. Recall from earlier that:

$$\Phi_{fl} = \frac{k_{fl}}{k_{fl} + k_{nr} + k_{PeT}} \quad \textbf{Equation 4.2.1}$$

From this equation, it would seem that changes in quantum yield are easily predictable if k_{PeT} can be predicted. However, this is an illusion as k_{nr} and k_{fl} are typically not directly measurable and not easily derivable from Φ_{fl}. In order to have a parameter that is

measurable that encompasses these rates, we turn to fluorescence lifetime in the absence of PeT, which is derived from:

$$\tau_{fl}^{0} = \frac{1}{k_{fl} + k_{nr}} \quad k_{fl}^{0} = \frac{1}{\tau_{fl}^{0}} \quad \textbf{Equations 4.4.1}$$

τ_{fl}^{0} can be determined by either measuring the fluorescence lifetime of a VoltageFluor in the absence of PeT from the wire (i.e. a donor in a fully protonated state) or by measuring the fluorescence of a VoltageFluor derivative analogous to the substrate in question but lacking any electronic modifications on the wire (aniline groups or electron withdrawing groups) that would enable PeT to occur. k_{fl}^{0} is defined for convenience. We can then model the change in fluorescence that will occur with a given change in membrane potential (the proxy for which here is k_{PeT}) through the equation:

$$\Delta\Phi_{fl} = \frac{k_{fl}}{k_{fl} + k_{nr} + k_{PeT2}} - \frac{k_{fl}}{k_{fl} + k_{nr} + k_{PeT1}} \quad \textbf{Equation 4.4.2}$$

Typically, voltage sensitivity of a VoltageFluor is reported as the change in fluorescence relative to the value at a specific membrane potential, usually the resting membrane potential of the cell[21]. This allows us to rewrite **Equation 4.4.2** as:

$$\frac{\Delta\Phi_{fl}}{\Phi_{fl}} = \frac{\frac{k_{fl}}{k_{fl} + k_{nr} + k_{PeT2}} - \frac{k_{fl}}{k_{fl} + k_{nr} + k_{PeT1}}}{\frac{k_{fl}}{k_{fl} + k_{nr} + k_{PeT1}}} \quad \textbf{Equation 4.4.3}$$

From here, it is trivial to show that:

$$\frac{\Delta\Phi_{fl}}{\Phi_{fl}} = \frac{\frac{k_{fl}}{k_{fl} + k_{nr} + k_{PeT2}} - \frac{k_{fl}}{k_{fl} + k_{nr} + k_{PeT1}}}{\frac{k_{fl}}{k_{fl} + k_{nr} + k_{PeT1}}}$$

$$\frac{\Delta\Phi_{fl}}{\Phi_{fl}} = \frac{\frac{1}{k_{fl} + k_{nr} + k_{PeT2}} - \frac{1}{k_{fl} + k_{nr} + k_{PeT1}}}{\frac{1}{k_{fl} + k_{nr} + k_{PeT1}}}$$

$$\frac{\Delta\Phi_{fl}}{\Phi_{fl}} = \frac{k_{fl} + k_{nr} + k_{PeT1}}{k_{fl} + k_{nr} + k_{PeT2}} - \frac{k_{fl} + k_{nr} + k_{PeT1}}{k_{fl} + k_{nr} + k_{PeT1}}$$

$$\frac{\Delta\Phi_{fl}}{\Phi_{fl}} = \frac{k_{fl}^{0} + k_{PeT1}}{k_{fl}^{0} + k_{PeT2}} - 1$$

which now gives us an expression for the change in fluorescence from a reference membrane potential as a function of one measurable parameter and the rate of PeT at the reference membrane potential and the new membrane potential. We now have all the equations we need to visualize the relative sensitivity of VoltageFluors given changes in their structural properties.

4.5 Computational visualization of relative voltage sensitivity trends

The equations described above were written into the following MatLab code:

```
%models dF/F of Voltage Fluors as a function of membrane potential based on
measured and
%calculated PeT parameters

hold on
%clear all;

dEox = 0.129;
dEred = -2.02;
dEoo = 2.38;
dHOMO = -0.231;
%setting up constants for free energy of PeT; can be modified to use
%HOMO-HOMO or LUMO-LUMO gap. Currently set to Evan's values for VF2.1.Cl
%(note that redox potentials are measured in volts but since this is a
%transit of one electron this is directly equivalent to electron volts in
%energy)

r = 2.2;
%aniline-chromophore distance (nm)
Vmem = [-300:0.1:300];
%sets up a vector to calculate kpet for a wide range of membrane potentials

%theta = 35.3;
theta = [0:2.5:90];
weight = [0.0036    0.0101    0.0165    0.0232    0.0299    0.0362    0.0417    0.0442
0.0480    0.0524    0.0544 0.0553    0.0554    0.0535    0.0522    0.0499    0.0491
0.0466    0.0423    0.0371    0.0320    0.0282 0.0239    0.0203    0.0180    0.0162
0.0138    0.0118    0.0097    0.0074    0.0058    0.0042    0.0033 0.0021    0.0011
0.0006         0];

%angle between wire and electric field; should be modeled computationally
%or this program can be modified to calculate this from measured dF/F.
%Currently set to the computationally derived distribution of angles for VF2.1.Cl
```

```
dmem = 4;
%thickness of the membrane in question (nm); 4 nm is a ballpark number. Not
%dubelco's modified eagle media
w = (r.*Vmem./(1000*dmem)).*sum(weight.*cosd(theta));
%w = (r.*Vmem./(1000*dmem)).*cosd(theta);

%calculates work to move electron in PeT (signs and charge accounted for, should be
net positive so watch out
%for cosine range) based on above parameters (takes cosine in degrees);
%1000 in denominator accounts for mV to V conversion
%sanity check: work is positive when Vmem is positive (takes energy to move
%an electron from positive to negative) and work is negative when Vmem is
%negative (electron wants to go from negative to positive)

dGpet = dEox - dEred - dEoo + w;
%dGpet = dHOMO +w;
%Rehm-Weller equation to calculate delta G of PeT as a function of Vmem; we will now
use this to
%calculate kpet as a function of Vmem which we will then use to calculate
%dF/F as a function of Vmem
%+w is because of current sign convention; when work is higher, dGpet should
%become less favorable

HnaughtDA = 10;
%electronic coupling at Van der Waals distance
rnaughtDA = 1.5;
%Van der Waals distance (angstroms)
beta = 0.01;
%coupling efficiency of the wire in question (angstroms^-1)
HDA = HnaughtDA*exp(-beta*(10*r-rnaughtDA));
%calculates donor-acceptor coupling of electron transfer (with correction on r to be in
angstroms); still need to
%poke in literature for best approaches for Van der Waals radius and
%coupling (currently rnaughtDA set to nitrogen radius and HnaughtDA set to
%10 as placeholder (I seem to see this in the 10-100 range).
%Beta set to minimum value for polystyrene wires as a placeholder

hbar = 6.582119569e-16;
%planck's constant over 2 pi because physicists are nerds; also let's keep
%everything in eV since that is useful
kb = 8.617333262e-5;
%Boltzmann constant in eV
T = 310.15;
%Temperature in Kelvin (assuming T=37 degrees for cells)
lambda = 1;
```

```
%solvent reorganization energy; still thinking of the best way to get at
%this (literature? approximations? fitting to known data? currently 1 is a placeholder)
%I seem to see this range from 0.5 to 2ish
kpet = sqrt(pi/(hbar*lambda*kb*T)).*(HDA^2).*exp(-
((lambda+dGpet).^2)./(4*lambda*kb*T));
%at last we have our full kpet calculation from our measured and calculated
%parameters; kpet should be in s^-1

tauprot = 3.5e-9;
%fluorescence lifetime of fully protonated voltagefluor; should be equal to
%1/(kfl+knr) and might be the most tractable experimental way to get at
%those values (currently set to VF2.0Cl lifetime as a placeholder)
kprot = 1/tauprot;
%for variable simplicity later
ref = find(Vmem==-60);
dFoverF = (kprot+kpet(ref))./(kprot+kpet)-1;
%uses kpet to calculate dF/F for that particular voltage step from the
%desired reference voltage (defaults to -60 mV)


Vmempatch = Vmem(2001:4001);
dFoverFpatch = dFoverF(2001:4001);
Vmempatchint0 = Vmempatch + 60;
%selects the range of Vmem and dF/F actually used in our patch experiments
%(-100 mV to +100 mV). Also shifts dF/F values to set -60 mV to 0 dF/F
dFslope = transpose(Vmempatchint0)\transpose(dFoverFpatch);
%finds slope of voltage sensitivity (will be in absolute numbers per 1 mV)
sensitivity = 100*100*dFslope;
%multiply by 100 to get per 100 mV and then another 100 to get percentage;
%this is the dF/F per 100 mV percent value that we typically report

fprintf('dF/F is %g percent per 100mV \n', sensitivity);

dFlinfit = dFslope.*(Vmem+60);
%takes linear fit from above and generates line for plotting

figure(1);
hold on;
plot(Vmem,dFoverF);
plot(Vmem,dFlinfit);
figure(2);
hold on;
plot(Vmem(2001:4001),dFoverF(2001:4001));
plot(Vmem(2001:4001),dFlinfit(2001:4001));
```

```
figure(3);
hold on;
plot(Vmem(2001:4001),log10(kpet(2001:4001)));
```

Script 4.5.1 Computational visualization of voltage sensitivity

Script 4.5.1 takes all the equations presented in the previous two sections and puts them into a script that will generate a plot of change in fluorescence relative to fluorescence at -60 mV as a function of membrane potential for a VoltageFluor with the inputted properties. Currently, the parameters are inputted are accurate for VF2.1.Cl, a common model VoltageFluor due to its primacy. To demonstrate how this visualization works in practice, this section presents three cases in which one property of VF2.1.Cl is changed and the voltage sensitivity of the changed molecule has been reported in literature. The property will be changed in the script to generate relative plots of both VF2.1.Cl voltage sensitivity and voltage sensitivity with the changed parameter.

Case 1: Orientation of the VoltageFluor
In a previous study[22], an additional anionic sulfonate group was appended to VF2.1.Cl and computational modeling predicted the distribution of angles adopted in the cell membrane by VF2.1.Cl and the new disulfonated substrate (**Figure 4.5.1ab**). Generating a plot of voltage sensitivity for VF2.1.Cl and the disulfonated VoltageFluor gives the plots shown in **Figure 4.5.1c**. The reported voltage sensitivities of the two substrates are 30% ΔF/F per 100 mV for the monosulfonated dye and 36% ΔF/F for the disulfonated dye; the predicted sensitivities based on properties inputted into the script are 20% ΔF/F for the monosulfonated dye and 24% ΔF/F for the disulfonated dye which shows the same 20% increase in voltage sensitivity as reported in the measured sensitivities of the substrates. This demonstrates how relative voltage sensitivity can be predicted from dye properties.

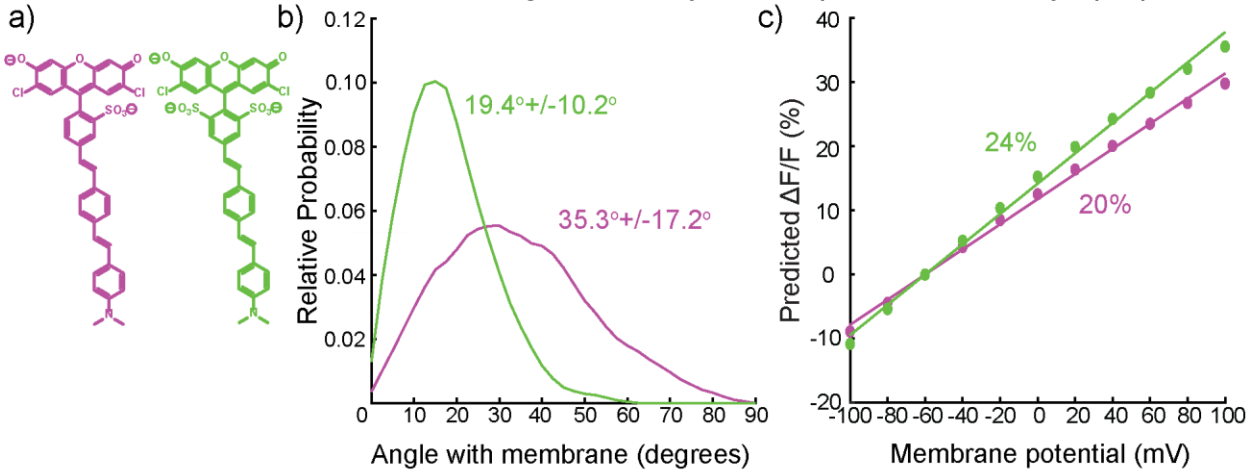

Figure 4.5.1 Relative voltage sensitivity of monosulfonated and disulfonated VF2.1.Cl **a**) Structures and **b**) angular dispersion of monosulfonated (magenta) and disulfonated (green) VF2.1.Cl calculated in previous work[22]. **c**) predicted voltage sensitivity of monosulfonated (magenta) and disulfonated (green) VF2.1.Cl. Dots represent calculated

fluorescence changes from fluorescence at -60 mV from inputted physical parameters for the membrane potentials indicated and lines represent a linear fit to this data. This representation is directly analogous to what would be presented for data measured electrophysiologically.

Case 2: Relative electronics of the donor and acceptor

In a recent study[23], the electron-rich aniline containing wire of VF2.1.Cl was substituted with electron withdrawing wires to reverse the direction of the fluorescence change observed with changes in membrane potential. Inputting the relative donor-acceptor electronics of the nitro, dinitro, cyano, and sulfo substituted wire conjugates (**Figure 4.5.2a**) into the script above gives the plots shown in **Figure 4.5.2b**. The ΔF/Fs per 100 mV of the substrates are -4%, -8%, -0.4%, -0.4%, 0%, and 0% respectively and the predicted ΔF/Fs per 100 mV based on properties inputted into the script are -27%, -15%, -27%, -10%, -2%, and 0%. The trend in predicted voltage sensitivity differs from the trend in measured voltage sensitivity as there is not a clear correlation between a greater magnitude of predicted voltage sensitivity and a greater magnitude of measured voltage sensitivity (**Figure 4.5.2c**).

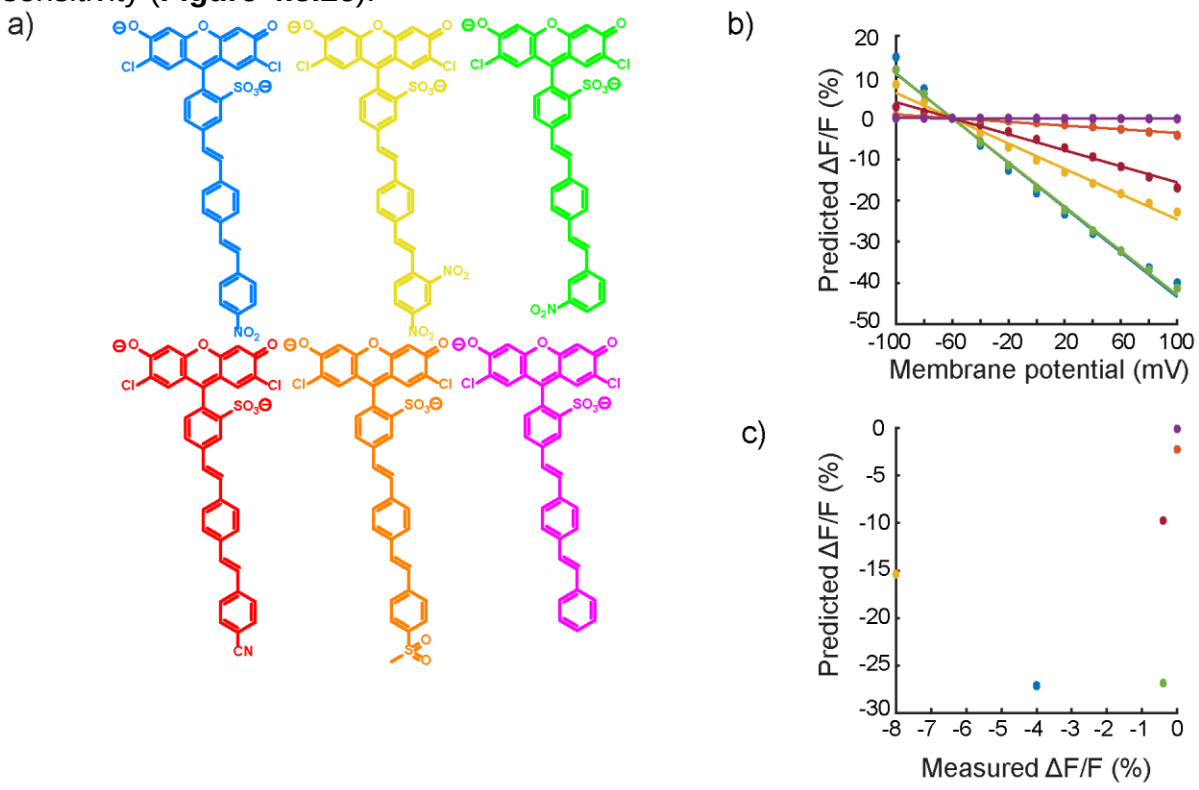

Figure 4.5.2 Relative voltage sensitivity of reverse VFs

a) Structures of VF2.1.Cl derivatives with electron withdrawing wires for a d-PeT rather than a-PeT mechanism **b**) predicted voltage sensitivity of reverse VFs color coded to structures in **a**. Dots represent calculated fluorescence changes from fluorescence at -60 mV from inputted physical parameters for the membrane potentials indicated and lines

represent a linear fit to this data. This representation is directly analogous to what would be presented for data measured electrophysiologically. **c**) Plot of predicted voltage sensitivity vs actual voltage sensitivity for reverse VFs. Colors of plotted points correspond to the line in part **b** from which the calculated sensitivity is taken.

The modeling reveals an interesting deviation from the expected trend. Although it correctly predicts the relative voltage sensitivities of the 4-cyano, 4-methanesulfonyl, and unsubstituted wires and correctly predicts that these will be less sensitive than the nitro substituted substrates, it predicts a much higher voltage sensitivity for the 3-nitro wire and a much lower sensitivity for the 2,4-dinitro wire than what would be expected based on their LUMO-LUMO gaps. The calculated LUMO-LUMO gaps for the 2,4-dinitro wire, 4-nitro wire, and 3-nitro wire are -0.79, -0.58, and -0.33 respectively. A closer examination of the calculated rates of PeT and the shape of the curves for fluorescence change as a function of voltage reveals the reason why. As is expected, the calculated rates of PeT is highest for the 2,4-dinitro and lowest for the 3-nitro substrates (**Figure 4.5.3a**). However, the model predicts that the 2,4-dinitro substrate is too quenched for optimal voltage sensitivity in the physiological range as at membrane potentials around -100 to +100 mV, it is at a very flat part of its response curve. Conversely, the 3-nitro substrate shows an s-shaped curve with an inflection point in the physiological range (**Figure 4.5.3b**), meaning it is in the “goldilocks zone” of PeT for optimal voltage sensitivity (**Figure 4.5.3c**). This means that in this case, the model is predicting rates of PeT for these substrates that are meaningfully higher than what is actually observed. As the only inputs for the model that have changed from the modeling of VF2.1.Cl in **Case 1** are the relative electronics of the dye head and the wire, the prediction of more efficient PeT than is actually observed implies that factors other than electronics have changed between these two substrates. As the nitro groups of these substrates are zwitterionic while the dimethylanilines on VF2.1.Cl species are hydrophobic in comparison, a reasonable hypothesis is that the position and angle of the VoltageFluor in the cell membrane has changed which in turn will affect the rate of PeT. This analysis demonstrates how the computational model presented here can be used to identify when changing one parameter of a VoltageFluor leads to changes in other parameters that must be accounted for when analyzing voltage sensitivity.

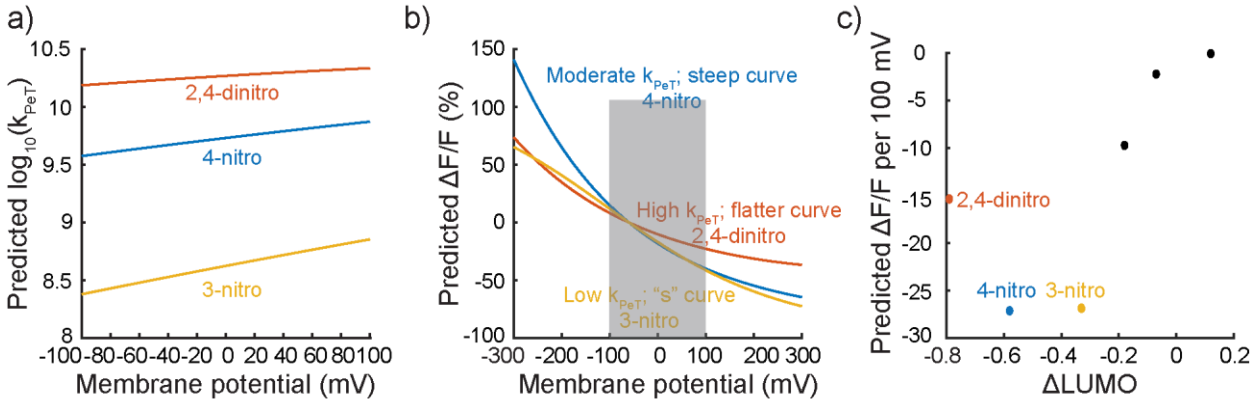

Figure 4.5.3 Computation predicts more quenching than experiment for reverse VFs

a) Computationally calculated rates of PeT for 2,4-dinitro (orange), 4-nitro (blue) and 3-nitro (yellow) substituted reverse VFs. **b**) Computationally calculated change in fluorescence from fluorescence at -60 mV of 2,4-dinitro (orange), 4-nitro (blue) and 3-nitro (yellow) substituted reverse VFs. Grey region represents -100 mV to +100 mV, the physiologically relevant range of membrane potentials. **c**) Plot of calculated voltage sensitivity vs. LUMO-LUMO gap between chromophore and wire for all reverse VFs. Note that the 4-nitro (blue) and 3-nitro (yellow) VFs are predicted to lie near a local extremum.

Case 3: Bond structure of wire-chromophore conjugation

In a previous study[24], the polystyrene wire of VF2.1.Cl was substituted with fluorene containing wires linked via a direct aromatic-aromatic bond between the wire and the chromophore (**Figure 4.5.4a**) to create FVF1. β values for fluorene based molecular wires have been estimated at 0.09[25]. The relative voltage sensitivities were used to predict the relative β value range of the fluorene scaffold to compare to the literature value. β values were predicted by empirically testing a range of β values to match the relative voltage sensitivities at both the minimum reported β value (0.01) and maximum reported β value (0.17) of polystyrene systems[25] until the relative voltage sensitivities of VF2.1.Cl (30%) and FVF1 (5%) matched (6-fold difference) (**Figure 4.5.4bc**). Using this method, the β value range of the hybrid fluorene system was found to be approximately 0.06-0.215 which contains the measured value of 0.09.

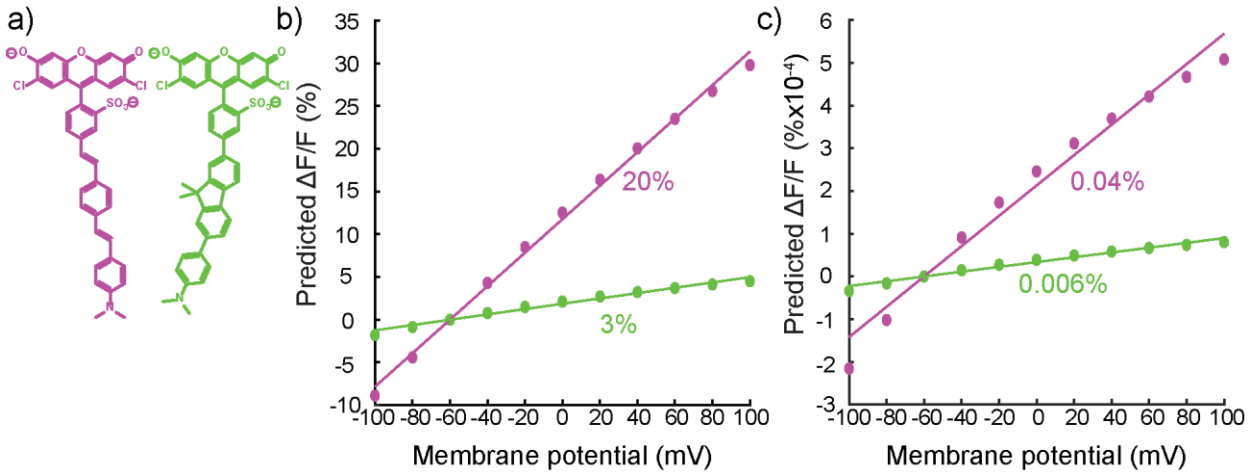

Figure 4.5.4 Calculation of β value range for phenyl-fluorene hybrid wires

a) Structures of VF2.1.Cl (magenta) and FVF1 (green). **b** and **c**) predicted voltage sensitivity of VF2.1.Cl (magenta) and FVF1 (green) assuming β=0.01 for VF2.1.Cl and β=0.06 for FVF1 (**b**) or β=0.17 for VF2.1.Cl and β=0.215 for FVF1 (**c**). Dots represent calculated fluorescence changes from fluorescence at -60 mV from inputted physical parameters for the membrane potentials indicated and lines represent a linear fit to this data. This representation is directly analogous to what would be presented for data measured electrophysiologically.

4.6 Through bond energy transfer as an approach to ratiometric VoltageFluors

To date, the FVF series of VoltageFluors remain the only published system in which the bonding scaffold of the molecular wire differs from the polystyrene scaffold typical for these molecules. Because the efficiency of electron transfer and thus likely TBET is less efficient than that of the polystyrene VoltageFluors, some interesting applications are possible that are not possible with the polystyrene based substrates. The molecular wire is itself a chromophore, and if excited, can transfer its energy to the traditional xanthene dye head via TBET. The TBET process is typically quite efficient and thus when the wire is excited in its absorption spectrum, fluorescence emission of the xanthene dye is predominantly observed rather than mixtures of xanthene and wire fluorescence (**Figure 4.6.1a**). However, the inefficiency of transfer through the hybrid fluorene scaffolds of the FVF series mean that when the VoltageFluor is excited via the wire's absorption spectrum, mixtures of wire and xanthene fluorescence are observed (**Figure 4.6.1b**).

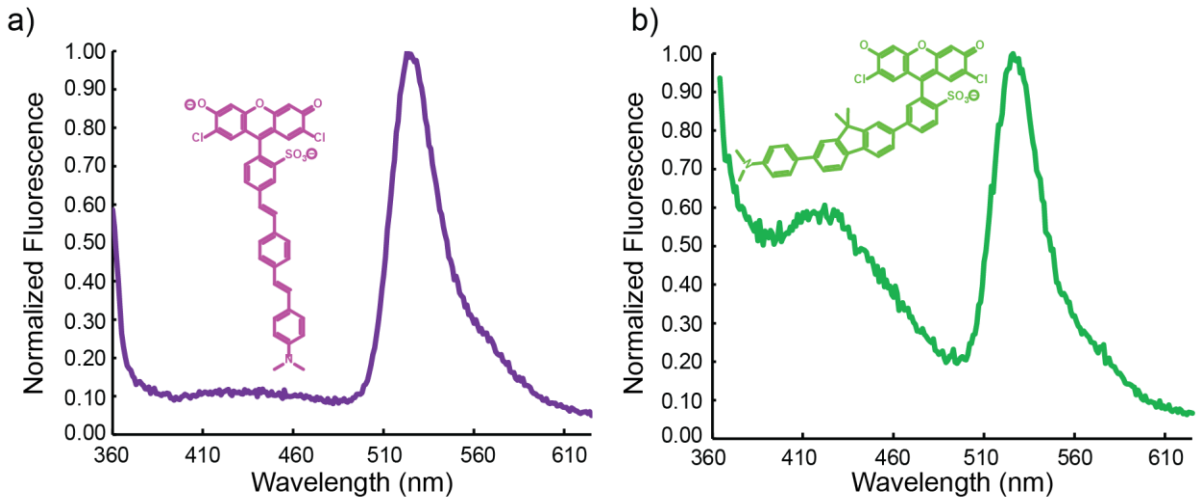

Figure 4.6.1 Through-bond energy transfer in VoltageFluors

Normalized fluorescence spectra in basic pH of VF2.1.Cl (**a**) and IsoFVF1 (**b**) with excitation at 320 nm. IsoFVF1 has a noticeable peak at approximately 420 nm due to wire fluorescence which is lacking in VF2.1.Cl.

Because PeT occurs when the xanthene chromophore enters an excited state rather than as a function of the wire entering an excited state, the wire fluorescence should not be voltage sensitive whereas the fluorescence of the xanthene chromophore will be voltage sensitive; however, both the fluorescence of the wire and the fluorescence of the xanthene chromophore should be proportional to dye concentration. Therefore, by taking the ratio of xanthene fluorescence to wire fluorescence, a concentration-independent measurement of membrane potential will be obtained, which can account for variation in loading concentration between samples. As an initial test to validate this approach, we excited the wire of a dye in the FVF series, isoFVF1, and measured its fluorescence

spectrum as a function of pH; as the aniline gets protonated at lower pHs, PeT will be reduced. We observed that as pH is reduced, the emission of the xanthene chromophore increases as PeT quenching is reduced while wire emission stays relatively static (**Figure 4.6.2a**). This leads to a PeT-sensitive fluorescence ratio between the xanthene chromophore and the wire (**Figure 4.6.2b**). ParaFVF1 was not used for this comparison due to limitations in available dye stocks; however, it would be a more directly analogous comparison and should be explored in future work.

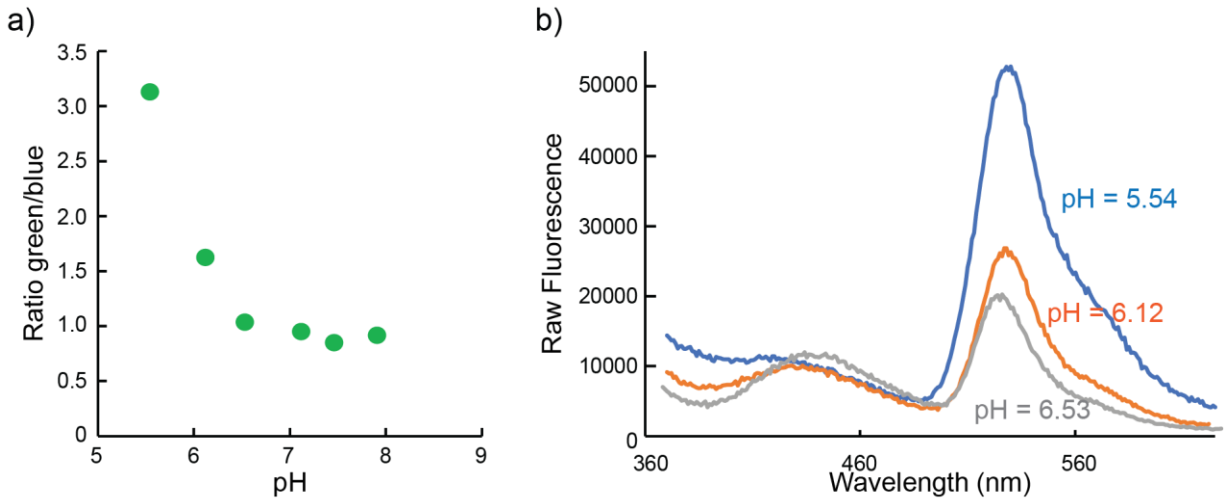

Figure 4.6.2 IsoFVF1 is ratiometric in pH

a) Plot of the ratio of wire fluorescence to fluorescein fluorescence of IsoFVF1. IsoFVF1 was excited at 320 nm and its fluorescence integral measured from 480 to 600 and divided by the fluorescence integral from 360 nm to 460 nm at the indicated pHs. **b**) Representative fluorescence spectra from **a**.

To test if this ratiometric response could be observed in cells, we stained HEK 293T cells with isoFVF1 and imaged their fluorescence in high K+ and low K+ solutions using a violet excitation LED (390/22 nm, 6.68 mW/mm^2, 100 ms exposure) with a (430/32, 508/14, 586/30, 708/98 nm) bandpass filter as an imperfect proxy for wire fluorescence and a cyan excitation LED (475/34 nm,19.7 mW/mm^2,100 ms exposure) with the same bandpass filter as a measurement of xanthene fluorescence. The multiple bandpass filter was used with the violet LED due to the lack of a necessary emission filter to fully select for wire fluorescence and means that TBET induced xanthene fluorescence, which is voltage sensitive, will pollute the wire signal and reduce the observed ratio change with changes in membrane potential. Purchase of proper emission filters would eliminate this problem. High K+ (130 mM K+) solutions depolarize mammalian cells whereas low K+ solutions (5 mM K+, physiological) allow for maintenance of their physiologically relevant membrane potential. We found that examining clusters of cells (n=355 high K+, n=281

low K+) across multiple coverslips (n=4 high K+, n=3 low K+) led to a statistically different difference in fluorescence ratio (**Figure 4.6.3**).

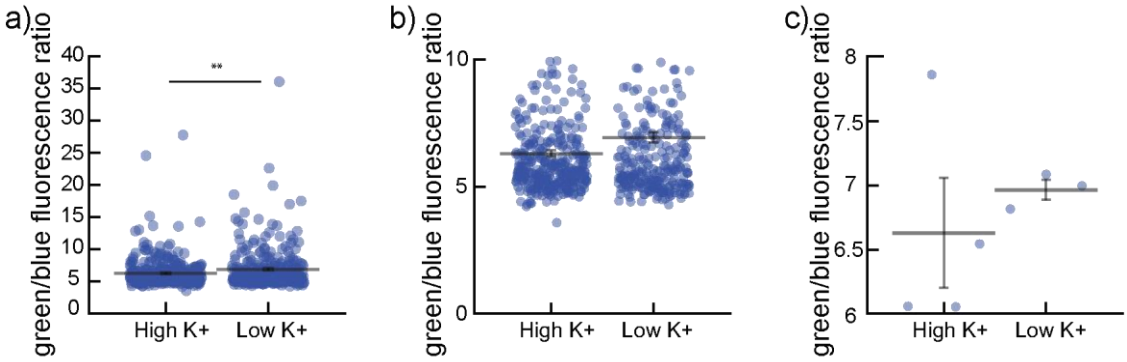

Figure 4.6.3 IsoFVF1 is a ratiometric voltage sensor

a) Scatterplot of background subtracted fluorescence ratios of individual clusters of cells across n=4 (high K+) and n=3 (low K+) coverslips of HEK 293T cells stained with isoFVF1 and then imaged in a solution with the indicated potassium concentration. ** indicates $p<0.01$ (student's t-test, 2-tailed, unequal variance). **b**) Zoomed in region of graph in **a**. **c**) Scatterplot of background fluorescence ratios of averaged across all cells on n=4 (high K+) and n=3 (low K+) coverslips

One would predict that the average fluorescence ratio of cell clusters in the high potassium, depolarized condition, would be higher than that of the low potassium, hyperpolarized condition, because the dye head fluorescence should be less PeT quenched while the wire fluorescence should stay approximately the same. Unexpectedly, the opposite trend is observed, where the hyperpolarized cells have a higher fluorescence ratio (6.9 average) than the depolarized cells (6.3 average), with statistical significance observed when analyzed by clusters of cells (**Figure 4.6.3ab**) but not by individual coverslips due to the presence of one outlier in the high potassium condition (**Figure 4.6.3c**). This suggests that one or both of the following hypotheses is true: 1) collecting emission light from a multiple bandpass filter for "wire" fluorescence is confounding the results and/or 2) the wire is electrochromic, and in the depolarized condition its fluorescence spectrum is more optimal for the imaging setup used and thus the observed wire fluorescence is higher relative to dye fluorescence, increasing the denominator of the ratio and thus decreasing the ratio. Further investigation is needed to elucidate the exact mechanism behind this phenomenon.

4.7 Conclusions and outlook

Through-bond energy and electron transfer are useful phenomena to exploit in the design of fluorescent probes. This chapter describes how through-bond electron transfer can be used to make fluorescent voltage-sensitive indicators (VoltageFluors) and gives a computational description of their properties. VoltageFluors with fluorene-based wires (FVFs) show promise in vitro as a fluorescent indicator that could be a ratiometric sensor of membrane potential. However, although isoFVF1 is a ratiometric voltage sensor in HEK 293T cells, the measured ratio difference between hyperpolarized and depolarized cells is in the opposite direction of what would be predicted based on PeT alone, indicating that further work is needed to fully elucidate the mechanism. Ratiometric VoltageFluors would enable high throughput measurements of membrane potential on systems such as a plate reader which would enable large-scale studies of whether or not a particular perturbation, such as a drug treatment, is affecting membrane potential.

4.8 Details of computation, spectroscopy, and imaging

Computational parameters

Dye	ΔE_{ox}[26]	ΔE_{red}[26]	$\Delta E_{o,o}$	$\Delta LUMO$[23]	$r_{an\text{-}fl}$	θ	β	R^0_{DA}	$T_{VF2.0.Cl}$
VF2.1.Cl	0.129	-2.02	2.38[a]	-	2.2[b]	35.3[c]	0.01[25]	1.5[d]	3.5ns[27]
Disulf	0.129	-2.02	2.38[a]	-	2.2[b]	19.4[c]	0.01	1.5[d]	3.5ns
4-nitro	-	-	-	-0.58	2.2[b]	35.3[c]	0.01	1.5[d]	3.5ns
2,4-dinitro	-	-	-	-0.79	2.2[b]	35.3[c]	0.01	1.5[d]	3.5ns
3-nitro	-	-	-	-0.33	2.2[b]	35.3[c]	0.01	1.5[d]	3.5ns
4-cyano	-	-	-	-0.18	2.2[b]	35.3[c]	0.01	1.5[d]	3.5ns
4-sulf	-	-	-	-0.07	2.2[b]	35.3[c]	0.01	1.5[d]	3.5ns
VF2.0.Cl	-	-	-	+0.12	2.2[b]	35.3[c]	0.01	1.5[d]	3.5ns
FVF1	0.129	-2.02	2.38[a]	-	2.2[b]	35.3[c]	0.09[25]	1.5[d]	3.5ns

a. Calculated from peak absorption wavelength

b. Calculated from bond geometries

c. Distribution[22]

d. set to distance for carbon-nitrogen bond

Matlab code used to generate plots is stored in the following github repository: https://github.com/pklier/Thesis_chapter4/

Spectroscopic characterization

For pH studies, a stock solution of isoFVF1 or VF2.1.Cl was prepared in DMSO (500 μM) and diluted with PBS (10 mM K2HPO4, 2 mM KH2PO4, 50 mM Trizma, pH adjusted to indicated value with HCl and NaOH) solution containing 0.10 % (w/w) SDS (1:100-1:1000 dilution). The dyes were excited at 320 nm and emission measured from 330-650 nm. UV-Vis absorbance and fluorescence spectra were recorded using a Shimadzu 2501 Spectrophotometer (Shimadzu) and a Quantamaster Master 4 L-format scanning spectrofluorometer (Photon Technologies International). The fluorometer is equipped with an LPS-220B 75-W xenon lamp and power supply, A-1010B lamp housing ith integrated igniter, switchable 814 photon-counting/analog photomultiplier detection unit, and MD5020 motor driver. Samples were measured in 1-cm path length quartz cuvettes (Starna Cells)

Cell Culture

Human embryonic kidney 293T (HEK) cells were passaged and plated onto 12 mm glass coverslips pre-coated with Poly-D-Lysine (PDL; 0.1 mg/ml; in 10 mM Na3BO3; Sigma-Aldrich) to provide a confluency of ~50% for imaging. HEK cells were plated and maintained in Dulbecco's modified eagle medium (DMEM) supplemented with 4.5 g/L D-glucose, 10% FBS and 1% Glutamax. Unless stated otherwise, for loading of all cell lines, dyes were diluted in DMSO to 1000x the final indicated concentration and then diluted 1:1000 in HBSS. All imaging experiments were performed in Ben's Imaging Buffer (BIB) which contains 1.26 mM $CaCl_2$, 0.49 mM $MgCl_2$, 0.41 mM $MgSO_4$, 0.44 mM KH_2PO_4, 10 mM HEPES, 0.34 mM Na_2HPO_4, and 5.56 mM D-Glucose with either 5.33 mM KCl and 139.5 mM NaCl (Low K+) or 119.6 mM KCl and 23.6 mM NaCl (High K+).

Imaging Parameters

Epifluorescence imaging was performed on an AxioExaminer Z-1 (Zeiss) equipped with a Spectra-X Light engine LED light (Lumencor), controlled with Slidebook (v6, Intelligent Imaging Innovations). Images were acquired with a W-Plan-Apo 20x/1.0 water objective (20x; Zeiss). Images were focused onto an OrcaFlash4.0 sCMOS camera (sCMOS; Hamamatsu). HEK 293T cells stained with isoFVF1 were imaged in high K+ and low K+ solutions using a violet excitation LED (390/22 nm, 6.68 mW/mm^2, 100 ms exposure) with a (430/32, 508/14, 586/30, 708/98 nm) bandpass filter as an imperfect proxy for wire fluorescence and a cyan excitation LED (475/34 nm,19.7 mW/mm^2,100 ms exposure) with the same bandpass filter as a measurement of xanthene fluorescence.

4.9 References

1. Lakowicz, A. L. *Principles of Fluorescence Spectroscopy*. Springer, **2006**
2. Fan, J.; Hu, M.; Zhan, P.; Peng, X. Energy transfer cassettes based on organic fluorophores: construction and applications in ratiometric sensing. *Chem Soc Rev.* **2013**, *42* (1) 29-43

3. Sekar, R.B.; Periasamy, A. Fluorescence resonance energy transfer (FRET) microscopy imaging of live cell protein localizations. *J Cell Biol*. **2003**, *160* (5), 629-633
4. Yuan, L.; Lin, W.; Zheng, K.; Zhu, S. FRET-based small-molecule fluorescent probes: rational design and bioimaging applications. *Acc Chem Res*. **2013**, *46* (7) 1462-1473
5. Qu, X.; Liu, Q.; Ji, X.; Chen, H.; Zhou, Z,; Shen, Z. Enhancing the Stokes' shift of BODIPY dyes via through-bond energy transfer and its application for Fe(3+)-detection in live cell imaging. *Chem Commun (Camb).* **2012**, *48* (38), 4600-4602
6. Wan, C.W.; Burghart, A.; Chen, J.; Bergström, F.; Johansson, L.B.; Wolford, M.F.; Kim, T.G.; Topp, M.R.; Hochstrasser, R.M.; Burgess, K. Anthracene-BODIPY cassettes: syntheses and energy transfer. *Chemistry*. **2003**, *9* (18), 4430-4441
7. Meimetis, L.G.; Carlson, J.C.; Giedt, R.J.; Kohler, R.H.; Weissleder, R. Ultrafluorogenic coumarin-tetrazine probes for real-time biological imaging. *Angew Chem Int Ed Engl*. **2014**, *53* (29), 7531-7534
8. Loudet, A.; Thivierge, C.; Burgess, K. Through-bond Energy Transfer Cassettes. *Dojin News* **2011**

9. Wu, H; Yang, J; Šečkutė, J; Devaraj, N.K. In situ synthesis of alkenyl tetrazines for highly fluorogenic bioorthogonal live-cell imaging probes. *Angew Chem Int Ed Engl*. **2014**, *53* (23), 5805-5809
10. Wieczorek, A; Werther, P; Euchner, J; Wombacher, R. Green- to far-red-emitting fluorogenic tetrazine probes - synthetic access and no-wash protein imaging inside living cells. *Chem Sci*. **2017**, *8* (2), 1506-1510
11. Devaraj, N.K.; Hilderbrand, S; Upadhyay, R; Mazitschek, R; Weissleder, R. Bioorthogonal turn-on probes for imaging small molecules inside living cells. *Angew Chem Int Ed Engl*. **2010**, *49* (16), 2869-2872
12. Pinto-Pacheco B; Carbery W.P.; Khan, S; Turner, D.B.; Buccella, D. Fluorescence Quenching Effects of Tetrazines and Their Diels-Alder Products: Mechanistic Insight Toward Fluorogenic Efficiency. *Angew Chem Int Ed Engl.* **2020**, *59* (49), 22140-22149
13. Wan, C.W.; Burghart, A; Chen, J; Bergström, F; Johansson, L.B.; Wolford, M.F.; Kim, T.G.; Topp, M.R.; Hochstrasser, R.M.; Burgess, K. Anthracene-BODIPY cassettes: syntheses and energy transfer. *Chemistry* **2003**, *9* (18), 4430-4441
14. Oevering, H.; Paddon-Row, M.N.; Heppener, M.; Oliver, A.M.; Cotsaris, E.; Verhoeven, J.W.; Hush, N.S. Long-Range Photoinduced Through-Bond Electron

Transfer and Radiative Recombination via Rigid Nonconjugated Bridges: Distance and Solvent Dependence. *J. Am. Chem. Soc.* **1987**, *109*, 3258-3269

15. Abe M, Nishihara R, Ikeda Y, Nakajima T, Sato M, Iwasawa N, Nishiyama S, Paulmurugan R, Citterio, D.; Kim, S.B.; Suzuki, K. Near-Infrared Bioluminescence Imaging with a through-Bond Energy Transfer Cassette. *Chembiochem.* **2019**, *20* (15), 1919-1923
16. Ueno, T.; Urano, Y.; Setsukinai, K.; Takakusa, H.; Kojima, H.; Kikuchi, K.; Ohkubo, K.; Fukuzumi, S.; Nagano, T. Rational principles for modulating fluorescence properties of fluorescein. *J Am Chem Soc.* **2004**, *126* (43), 14079-14085
17. Anslyn, E. V.; Dougherty, D.A. Modern Physical Organic Chemistry. *University Science Books*, **2005**

18. Kuss-Petermann, M.; Wenger, O.S. Unusual distance dependences of electron transfer rates. *Phys Chem Chem Phys.* **2016**, *18* (28) 18657-18664
19. Rehm, D.; Weller, A. Kinetics of Fluorescence Quenching by Electron and H-Atom Transfer. *Israel J. Chem.* **1970**, *8*, 259-271

20. Ingólfsson, H.I.; Carpenter, T.S.; Bhatia, H.; Bremer, P.T.; Marrink, S.J.; Lightstone, F.C. Computational Lipidomics of the Neuronal Plasma Membrane. *Biophys J.* **2017**, *113* (10) 2271-2280
21. Miller, E.W.; Lin, J.Y.; Frady, E.P.; Steinbach, P.A.; Kristan, W.B.; Tsien, R.Y. Optically monitoring voltage in neurons by photo-induced electron transfer through molecular wires. *Proc Natl Acad Sci U S A.* **2012**, *109* (6), 2114-2119

22. Kulkarni, R.U.; Yin, H.; Pourmandi, N.; James, F.; Adil, M.M.; Schaffer, D.V.; Wang, Y.; Miller, E.W. A Rationally Designed, General Strategy for Membrane Orientation of Photoinduced Electron Transfer-Based Voltage-Sensitive Dyes. *ACS Chem Biol*. **2017**, *12* (2), 407-413
23. McCann, J.; Benlian, B.; Knudson, I.; Miller, E. Flipping the Switch: Reverse-Demand Voltage-Sensitive Fluorophores. *ChemRxiv* **2021**

24. Boggess, S.C.; Gandhi, S.S.; Siemons, B.A.; Huebsch, N.; Healy, K.E.; Miller, E.W. New Molecular Scaffolds for Fluorescent Voltage Indicators. *ACS Chem Biol.* **2019** *14* (3) 390-396
25. Goldsmith, R.H.; Sinks, L.E.; Kelley, R.F.; Betzen, L.J.; Liu, W.; Weiss, E.A.; Ratner, M.A.; Wasielewski, M.R. Wire-like charge transport at near constant bridge energy through fluorene oligomers. *Proc Natl Acad Sci U S A*. **2005**, *102* (10), 3540-3545
26. Woodford, C.R.; Frady, E.P.; Smith, R.S.; Morey, B.; Canzi, G.; Palida, S.F.; Araneda, R.C.; Kristan, W.B. Jr; Kubiak, C.P.; Miller, E.W.; Tsien, R.Y. Improved PeT molecules for optically sensing voltage in neurons. *J Am Chem Soc*. **2015**, *137* (5), 1817-1824
27. Lazzari-Dean, J.R.; Gest, A.M.; Miller, E.W. Optical estimation of absolute membrane potential using fluorescence lifetime imaging. *Elife*. **2019**, *8*, e44522

Appendix α: A new synthetic route to sulfonated rhodamines for increased water solubility and tissue penetration

Aα.1 Background and motivation

Rhodamine dyes are highly valued in microscopy experiments for their high photostability compared to other fluorophores, high quantum yields, good 2-photon absorption cross section, and synthetic handles for functionalization[1]. However, the lipophilic, cationic nature of rhodamines means that they can be retained in membranes and even pass through them to accumulate in subcellular locations, which poses challenges for applications where dye labeling on the extracellular surface is desired[2]. This also limits their utility for selective labeling in complex tissues, as the dye is likely to have high retention in off-target membranes, reducing the selectivity of targeted staining and hindering full staining of larger samples. Additionally, adding extra functional groups to rhodamines often decreases their solubility in aqueous solution which reduces the effective concentration in a loading solution and often requires surfactants to obtain any substantial amount of dye in solution[3].

A common approach to overcoming this limitation is to add sulfonates to the dye scaffold of interest[4]. Sulfonates are highly acidic and thus are anionic at normal and even acidic physiological pHs. Adding anionic character to a dye improves its water solubility and reduces its propensity to partition into lipid membranes or pass through them into the interior of cells[5]. Sulfonates can be installed through click reactions[6], alkylation of boron on BODIPYs[7], or direct sulfonation of alkyl groups on the chromophore[4,8]. Another common sulfonated dye scaffold is the commercially available AlexaFluor series of dyes which consist of commonly used fluorophores with sulfonates installed at various locations on the fluorophore, typically directly on the aromatic ring[9]. However, only a few AlexaFluor substrates, most notably AlexaFluor 488, are rhodamine based because the synthetic methods used to install the sulfonates are not compatible with many rhodamine scaffolds including the spectrally useful tetraalkylrhodamines as well as rhodamines with substituted pendant rings[10]. This work to produce sulfonated rhodamines initially began with an attempt to extend the AlexaFluor synthesis using direct sulfonation of rhodamine scaffolds to tetramethylrhodamine and rhodamines with a bromine on the pendant ring but neither scaffold showed significant sulfonation (data not shown).

An alternative approach previously reported in patent literature involved synthesis of a tetrasulfonated rhodamine with the sulfonates on the N-alkyl groups[11]. Not only does this scaffold introduce four sulfonates instead of the more typical 1-2 common in other approaches, but it largely maintains the core of the tetraalkylrhodamine scaffold thus preserving the ability to install synthetic handles and additional functional groups on the molecule. The route pursued by the original authors involves synthesizing the relevant doubly sulfonated aminophenol and then pursuing rhodamine syntheses using condensation with aldehydes in acid as is traditional for these substrates (**Figure Aα.1.1a**). However, this means that the sulfonates are carried through the entire synthesis, leading to highly water-soluble intermediates that are difficult to purify and are insoluble in organic solvents, limiting their further derivatization.

An alternative approach involves installing protecting groups on the sulfonates which will mask their anionic character enabling traditional organic synthetic methods to be used for derivatization of the substrates. Protecting a sulfonate typically involves esterifying the sulfonate. These esters can then be unmasked at the end of the synthesis to reveal the final water-soluble rhodamine derivative. Although protecting groups for sulfonates are less common than for other functional groups, methods have been developed over the last several years to examine new sulfonate esters that are robust to many synthetic conditions and selectively cleaved under specific synthetic conditions[12] or even inside of cells[13]. These esters have been used in the synthesis of water-soluble organic dyes[12] but have not been adapted for use in the synthesis of alkylated rhodamine derivatives.

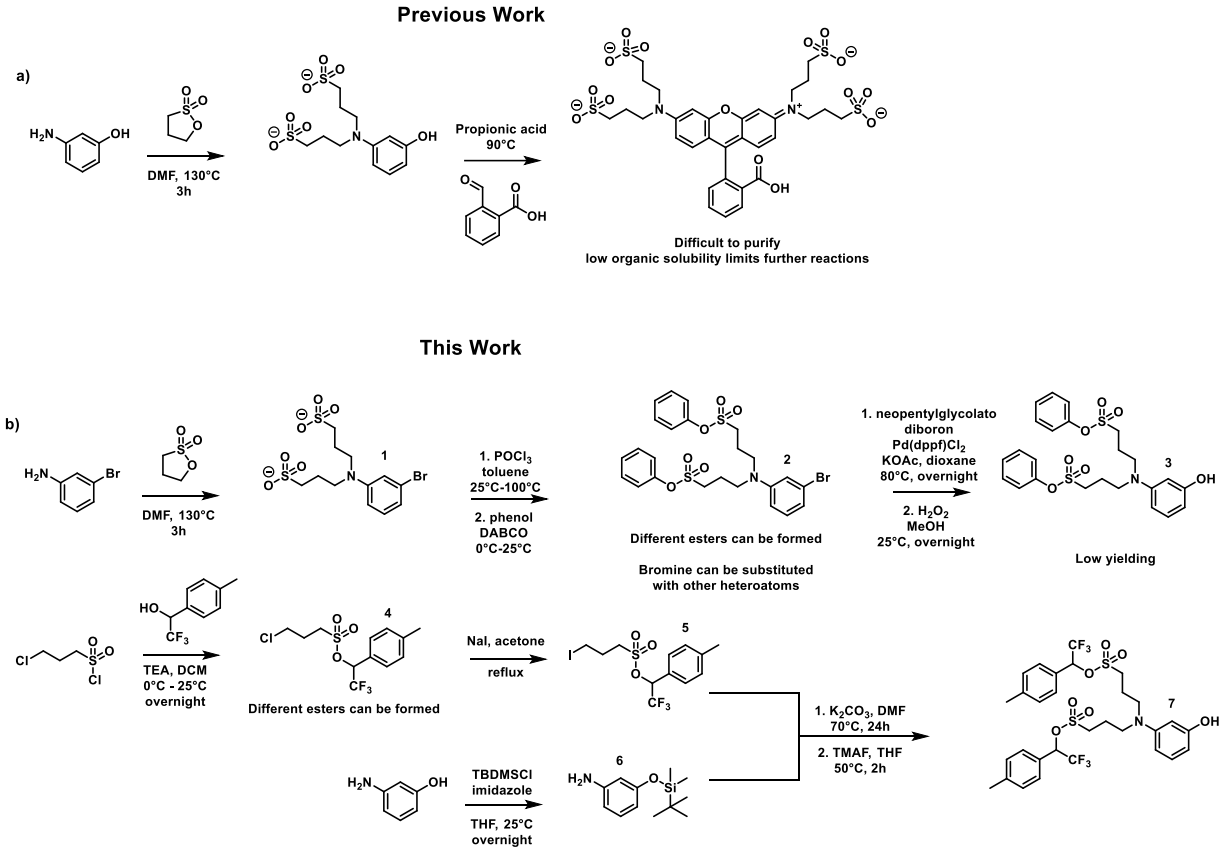

Figure Aα.1.1 Synthetic approaches to tetrasulfonated rhodamines

Synthetic routes tried in literature and this work to synthesize tetrasulfonated rhodamines without (**a**) and with (**b**) the aid of protecting groups.

Two sulfonate esters were selected as protecting groups in the design of the synthetic route reported here. The first, a phenyl ester, is robust to most reaction conditions with the exception of strongly basic conditions[14]. This makes it an ideal protecting group for synthesis involving strongly acidic condensations, but less ideal for synthesis where the final substrate will be base-sensitive. The second is a recently reported sulfonate ester of

2,2,2-Trifluoro-1-p-tolyl-ethanol which is stable to most reaction conditions except strong bases and strong acids. Its reactivity is fairly analogous to the ubiquitous t-butoxycarbonyl protecting group common in peptide synthesis which makes it useful for substrates that will undergo further derivatization via peptide couplings. However, its lability to acidic conditions mean that it is only compatible with mild condensation conditions for rhodamine synthesis.

Two different routes are demonstrated here for generating disulfonated dialkylated aminophenols useful for making sulfonated rhodamines. In the first approach, 3-bromoaniline is first dialkylated with propanesultone to form **compound 1** followed by esterification of the sulfonates to form **compound 2**. The bromine is then converted to an alcohol via boronic ether formation and subsequent hydrolysis and oxidation to form **compound 3**. This route is advantageous because the bromine can be used as a synthetic handle for conversion to other atoms to make different rhodamine derivatives; substitution of the bridgehead oxygen on rhodamines can have dramatic effects on their photophysical properties, in particular their absorption and emission spectra[15]. The second route involves synthesizing an esterified 3-sulfo-1-iodopropane (**compound 5**) which can be used as a pre-esterified alkylating agent for alkylating protected 3-aminophenol (**compound 6**) for generating an aminophenol ready for rhodamine synthesis (**compound 7**). This route is synthetically preferable to the bromination route as it installs the sulfonate ester earlier in the synthesis making purifications of intermediates easier.

In this work, the synthetic route towards the aminophenols is reported. A condensation was attempted using **compound 3**, and although conversion was observed by TLC and fluorescence was observed from the reaction material, the sample was spilled before purification and characterization could be attempted.

Synthetic details for the intermediates synthesized are found at the end of this appendix. These tetrasulfonated rhodamine substrates have great promise in two specific applications relevant to work done in this thesis and related work. Tetrasulfonated rhodamines could be conjugated to a benzylguanine group which would enable genetic targeting via a SNAP tag protein (**Figure Aα.1.2a**). This would be extremely useful in *Drosophila* reporter lines for anatomical studies as the existing tetramethylrhodamine-SNAP conjugates are too lipophilic to penetrate an entire drosophilia brain[16]. Tetrasulfonated rhodamines, because of their enhanced water solubility, should disperse more effectively through the extracellular fluid thus enhancing staining of remote regions of the brain while maintaining the desirable photophysical properties, particularly the high 2-photon absorption cross-section, of tetraalkylrhodamines. A second application is to make a new molecule in the class of photoinduced electron transfer-based fluorescent voltage indicators known as VoltageFluors. Typical VoltageFluors contain an anionic group on the pendant ring of the dye to anchor them in the proper orientation in the membrane for voltage sensing[17]. Moving this anionic group from the pendant ring to the

dye head should allow more of the molecule to insert into and span the membrane thus enhancing its voltage sensitivity (**Figure Aα.1.2b**).

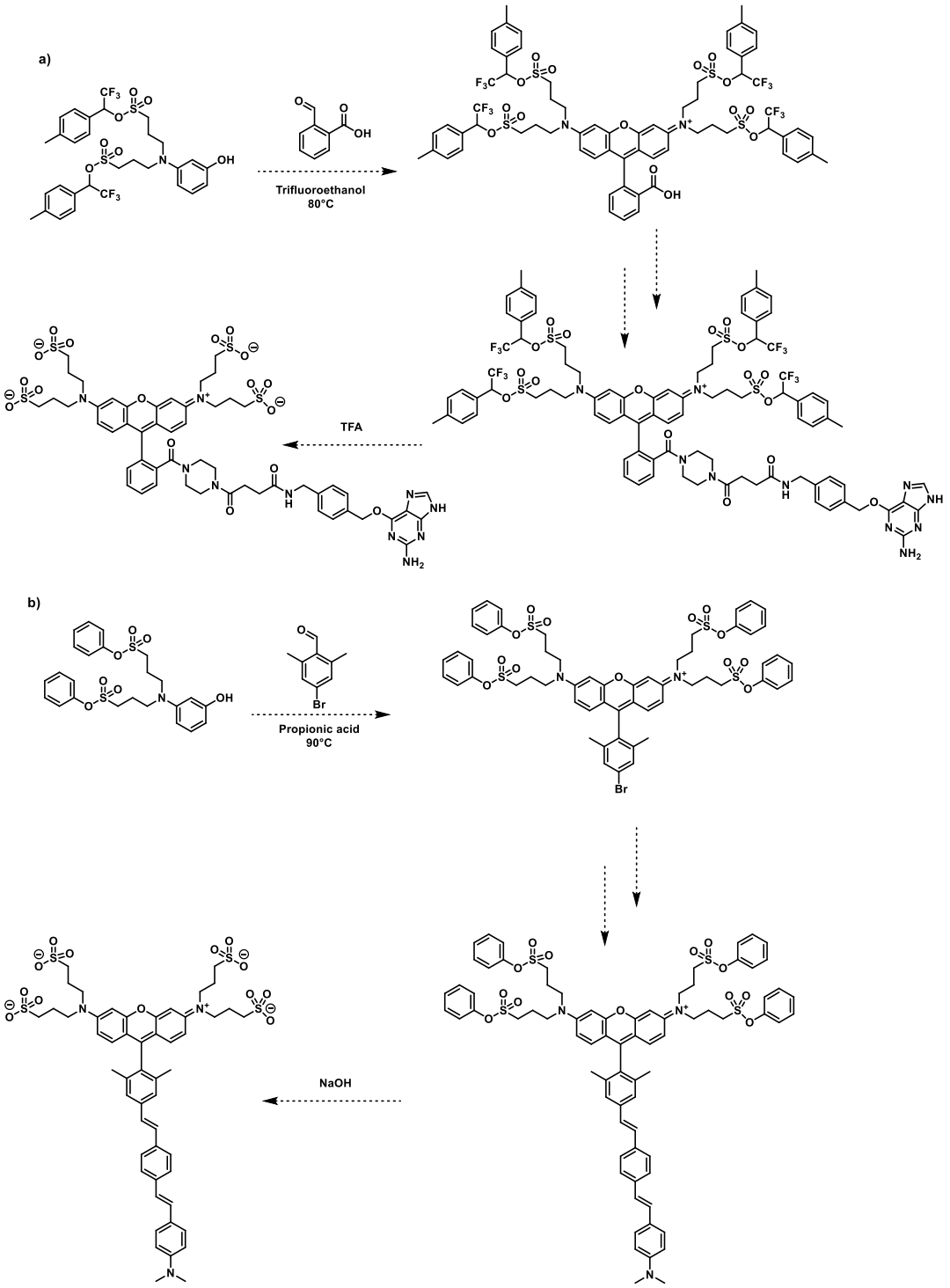

Figure Aα.1.2 Planned future work for applications of tetrasulfonated rhodamines

Planned future synthesis for making tetrasulfonated rhodamines for genetic targeting with SNAP tag (**a**) and for making a water-soluble voltage sensor with anionic orienting groups on the dye head rather than the pendant ring (**b**)

Aα.2 Details of synthesis and characterization

Chemical reagents and solvents (dry) were purchased from commercial suppliers and used without further purification. Compounds **4** and **5** were synthesized according to previously reported procedures[12]. Thin layer chromatography (TLC) (Silicycle, F254, 250 μm) and preparative thin layer chromatography (PTLC) (Silicycle, F254, 1000μm) were performed on glass backed plates pre-coated with silica gel or silica gel with C18 functionalization and were visualized by fluorescence quenching under UV light. Flash column chromatography was performed on Silicycle Silica Flash F60 (230–400 Mesh) or SiliaBond® Functionalized Silica Gels C18 (17%C) Monomeric (40 - 63 μm, 60 Å) using a forced flow of air at 0.5–1.0 bar. NMR spectra were measured on Bruker AVB-400 MHz, 100 MHz, AVQ-400 MHz, 100 MHz, Bruker AV-600 MHz, 150 MHz. Chemical shifts are expressed in parts per million (ppm) and are referenced to CDCl3 (7.26 ppm, 77.0 ppm), DMSO (2.50 ppm, 40 ppm), or D_2O (4.8 ppm). Coupling constants are reported as Hertz (Hz). Splitting patterns are indicated as follows: s, singlet; d, doublet; t, triplet; q, quartet; dd, doublet of doublet; m, multiplet. High-resolution mass spectra (HR-ESI-MS) were measured by the QB3/Chemistry mass spectrometry service at University of California, Berkeley. High performance liquid chromatography (HPLC) and low resolution ESI Mass Spectrometry were performed on an Agilent Infinity 1200 analytical instrument coupled to an Advion CMS-L ESI mass spectrometer. The column used for the analytical HPLC was Phenomenex Luna 5 μm C18(2) (4.6 mm I.D. × 150 mm) with a flow rate of 1.0 mL/min. The mobile phases were MQ-H2O with 0.05% trifluoroacetic acid (eluent A) and HPLC grade acetonitrile with 0.05% trifluoroacetic acid (eluent B). Signals were monitored at 254, 380 and 545 nm over 10 min with a gradient of 10-100% eluent B. The column used for preparative HPLC was Phenomenex Luna 10 μm C18(2) (21.2 mm I.D. x 250 mm) with a flow rate of 30.0 mL/min. The mobile phases were MQ-H2O with 0.05% trifluoroacetic acid (eluent A) and HPLC grade acetonitrile with 0.05% trifluoroacetic acid (eluent B). Signals were monitored at 545 over 20 min with a gradient of 30-70% eluent B.

Scheme Aα.2.1

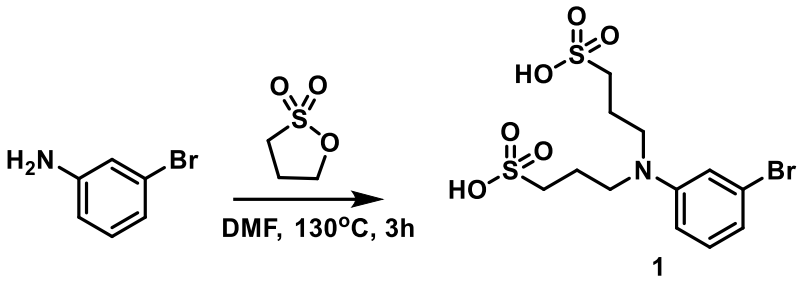

1

Synthesis of 3,3'-[(3-bromophenyl)amino]bis-1-propanesulfonic acid, 1:
3-bromoaniline (5.06g, 29.4 mmol, 1 eq) and 1,3-propanesultone (7.83g, 64.1 mmol, 2.2 eq) were dissolved in 5mL anhydrous dimethylformamide (DMF) and stirred at 130°C under a nitrogen atmosphere for 3 hours. The reaction was then cooled and the solvent removed under reduced pressure and the crude material redissolved in a 1:1 biphasic mixture of dichloromethane (DCM) and water. The aqueous layer was then extracted 3x with DCM and the water removed under reduced pressure. The crude material was then purified by flash chromatography (C18 silica, 10% MeCN in H_2O) to yield compound **1** (6.6g, 54% yield) as a yellow oil.

^{1}H NMR (400 MHz, Chloroform-d) δ 4.51 (q, J = 7.2 Hz, 2H), 4.44 (q, J = 7.1 Hz, 1H), 3.54 (q, J = 7.1 Hz, 3H), 2.91 (dd, J = 7.5, 5.7 Hz, 2H), 2.73 (dd, J = 7.5, 5.8 Hz, 2H), 2.70 – 2.61 (m, 1H), 2.58 (ddd, J = 7.6, 5.8, 1.4 Hz, 1H), 1.48 (s, J = 2.5 Hz, 9H), 1.48 (m, J = 2.5 Hz, 8H), 1.46 – 1.40 (m, 4H), 1.25 (t, J = 7.0 Hz, 5H).

Scheme Aα.2.2

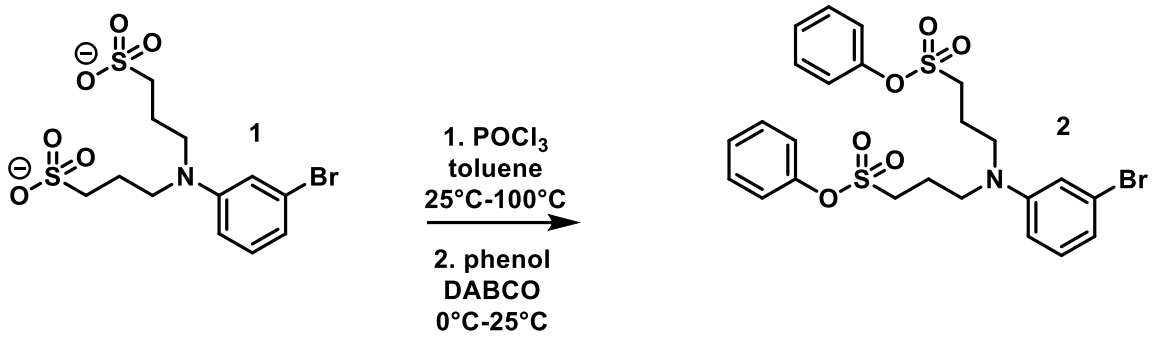

Synthesis of 3,3'-[(3-bromophenyl)amino]bis-1-propanesulfonic acid phenyl ester, 2:

Compound **1** (2.5g, 6.0 mmol) was added to approx. 50 mL toluene and phosphorous V oxychloride (5.6 mL, 60.1 mmol) was added dropwise. The reaction was then heated to 80^{o}C and the reaction was stirred for 4h. The reaction was then concentrated under reduced pressure, redissolved in approximately 5 mL dichloromethane, and phenol (1.26 g, 13 mmol) was added in 2 mL dichloromethane. The reaction was then cooled to 0^{o}C, and DABCO (3.16 g, 28 mmol) was added in 6 mL dichloromethane and the reaction was allowed to warm to room temperature for 4 hours. The reaction was then extracted with saturated sodium bicarbonate, the aqueous layer dried over sodium sulfate and concentrated under reduced pressure, and the crude material purified by flash chromatography (silica, 50% EtOAc in hexanes) to yield compound **2** (212 mg, 6% yield) as a pale yellow oil.

Scheme Aα.2.3

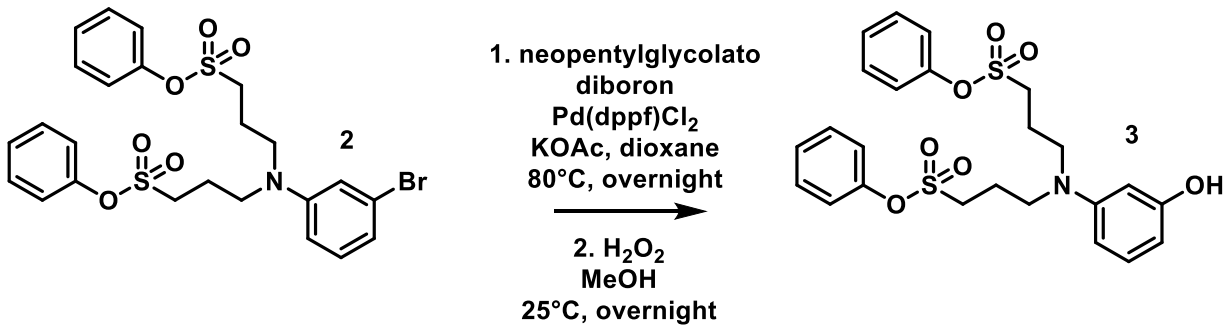

Synthesis of 3,3'-[(3-oxyphenyl)amino]bis-1-propanesulfonic acid phenyl ester:
Compound **2** (212 mg, 0.37 mmol), bis(neopentylglycalato) diboron (95 mg, 0.41 mmol), $Pd(dppf)Cl_2$ (31 mg, 0.04 mmol), and potassium acetate (113 mg, 1.1 mmol) were added to a dry Schlenck flask which was evacuated and backfilled 3x with nitrogen. Dry reagents were then dissolved in 1 mL anhydrous dioxane and the reaction was heated to 80°C and stirred overnight. The reaction was then cooled to room temperature, filtered through celite, and the celite washed with ethyl acetate. The crude material was concentrated under reduced pressure, redissolved in 1 mL methanol, and cooled to 0°C. Hydrogen peroxide (50% in water, 2.1 mL, 0.63 mmol) was then added dropwise and the reaction warmed to room temperature overnight. The reaction was then quenched with 10 mL 1M sodium sulfite, extracted with dichloromethane, and the organic layer dried over sodium sulfate and concentrated under reduced pressure. The crude material was purified by flash chromatography (silica, 0-80% ethyl acetate in hexanes) to yield compound **3** (54 mg, 29% yield) as a tan oil.

Scheme Aα.2.4

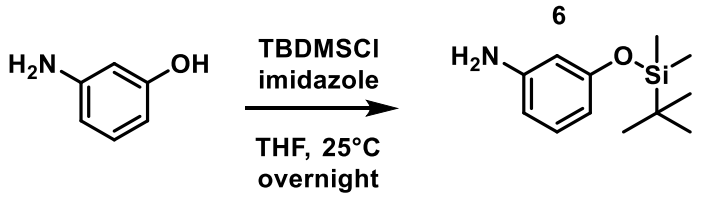

Synthesis of 3-aminophenol TBDMS ether:
Imidazole (4.3 g, 63 mmol) and 3-aminophenol (5.0 g, 46 mmol) were dissolved in 100 mL anhydrous tetrahydrofuran and cooled to 0°C. TBDMSCl (8.3 g, 55 mmol) was added

portionwise over 5 minutes and the reaction was allowed to warm to room temperature overnight. The reaction was then poured into water and extracted 3x with diethyl ether. The ether was then washed 3x with brine, dried over sodium sulfate, and concentrated under reduced pressure. The crude material was purified by flash chromatography (30% ethyl acetate in hexanes) to yield compound **6** (586 mg, 6% yield) as an orange oil.

^{1}H NMR (400 MHz, CDCl3) δ 7.09 (t, J = 8.0 Hz, 1H), 6.40 – 6.33 (m, 2H), 6.29 (t, J = 2.3 Hz, 1H), 3.65 (s, 2H), 1.12 (s, 9H), 0.32 (s, 6H).

Scheme Aα.2.5

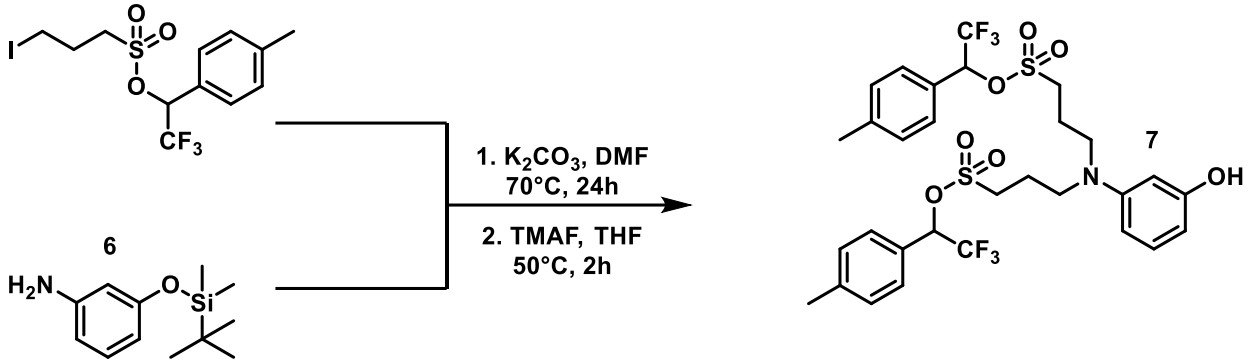

Synthesis of 3,3'-[(3-oxyphenyl)amino]bis-1-propanesulfonic acid trifluoro tolyl ester, 7:

Compound **5** (1.62 g, 3.8 mmol) and compound **6** (217 mg, 1.0 mmol) were transferred to a dry Schlenck flask which was evacuated and backfilled 3x with nitrogen. The reagents were dissolved in 4 mL anhydrous dimethylformamide and potassium carbonate (170 mg, 1.2 mmol) was added. The reaction was heated to 70^{o}C for 24 hours and then poured in water and acidified to pH 1 with 1M HCl. The reaction was then extracted 3x with ethyl acetate and the organic layer dried over sodium sulfate and concentrated under reduced pressure. The crude material was redissolved in tetrahydrofuran and TMAF (109 mg, 1.2 mmol) was added and the reaction was heated to 50^{o}C for 2 hours. Conversion was observed by LC/MS and the reaction was concentrated under reduced pressure into a round bottom flask but has not yet undergone purification.

Spectrum Aα.2.1 LC/MS spectrum of 3,3'-[(3-bromophenyl)amino]bis-1-propanesulfonic acid, 1

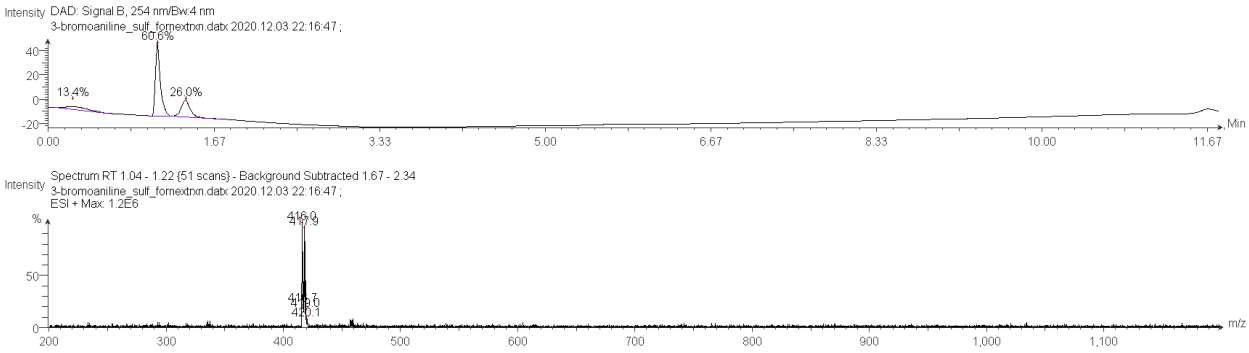

Low resolution ESI+ mass spectrum of 2 (meta-bromo TMR-OH):

Calculated for $[M-^{79}Br+H]^+$: 415.98
Found: 416.0

Calculated for $[M-^{81}Br+H]^+$: 417.98
Found: 418.0

Spectrum Aα.2.2 ^{1}H spectrum of 3,3'-[(3-bromophenyl)amino]bis-1-propanesulfonic acid, 1:

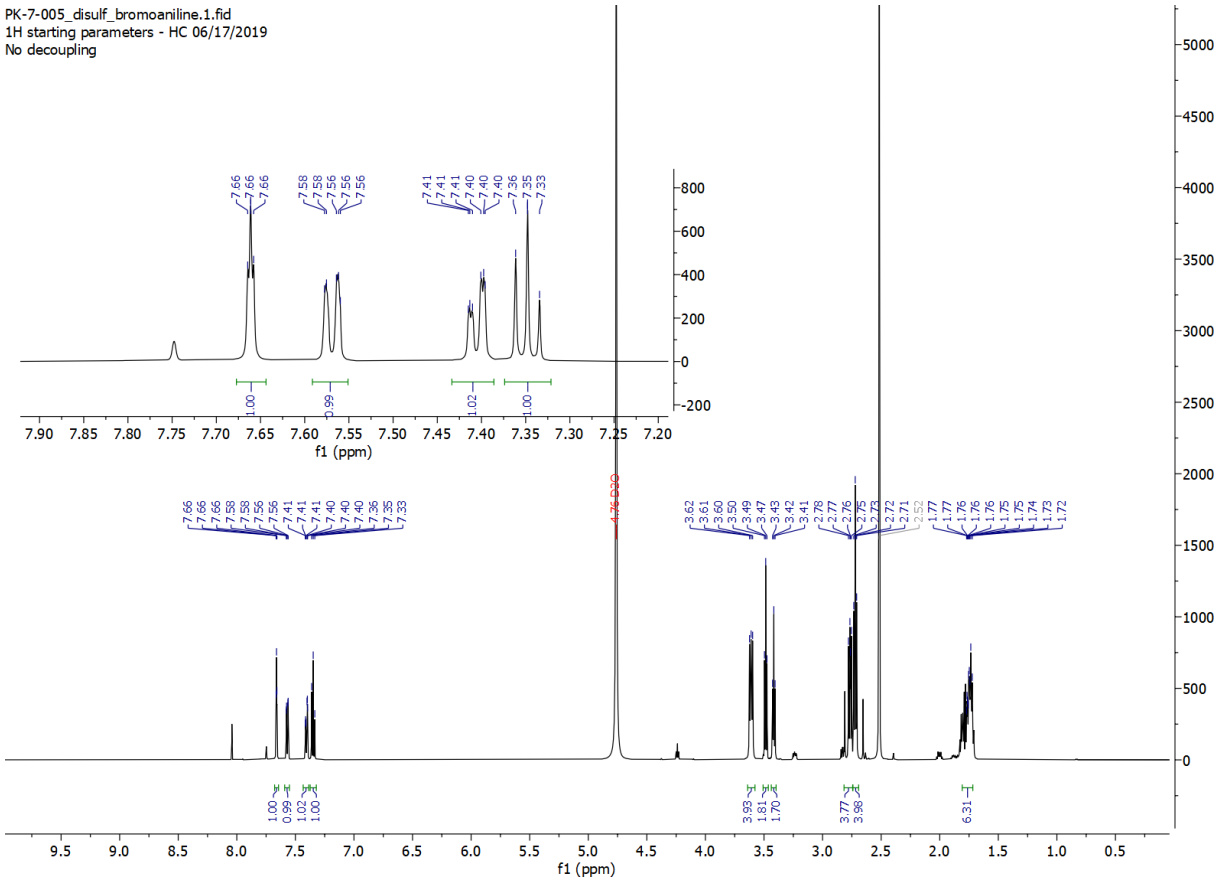

Spectrum Aα.2.3 LC/MS spectrum of 3,3'-[(3-bromophenyl)amino]bis-1-propanesulfonic acid phenyl ester, 2:

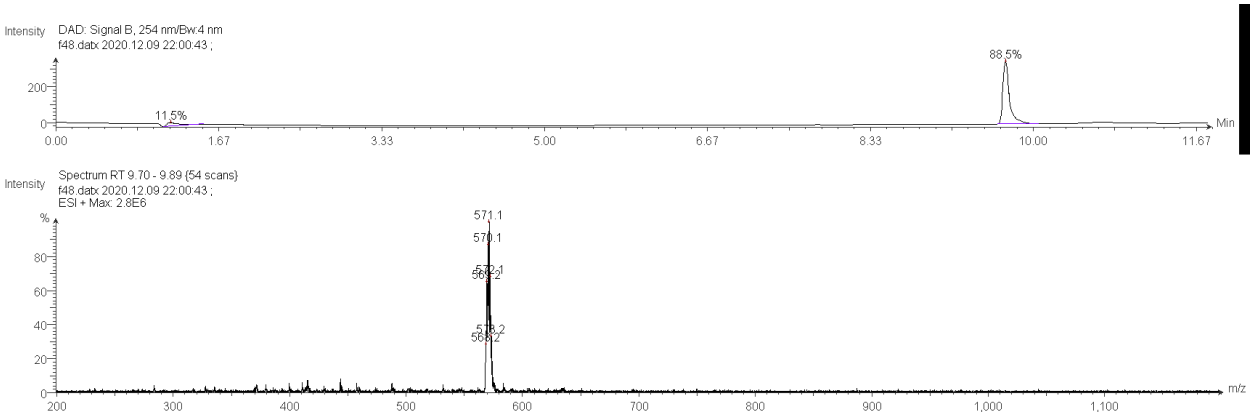

Low resolution ESI+ mass spectrum of 2 (3,3'-[(3-bromophenyl)amino]bis-1-propanesulfonic acid phenyl ester):

Calculated for $[M-^{79}Br+H]^+$: 568.1
Found: 568.2

Calculated for $[M-^{81}Br+H]^+$: 570.0
Found: 571.1

Spectrum Aα.2.4 LC/MS spectrum of 3,3’-[(3-oxyphenyl)amino]bis-1-propanesulfonic acid phenyl ester, 3:

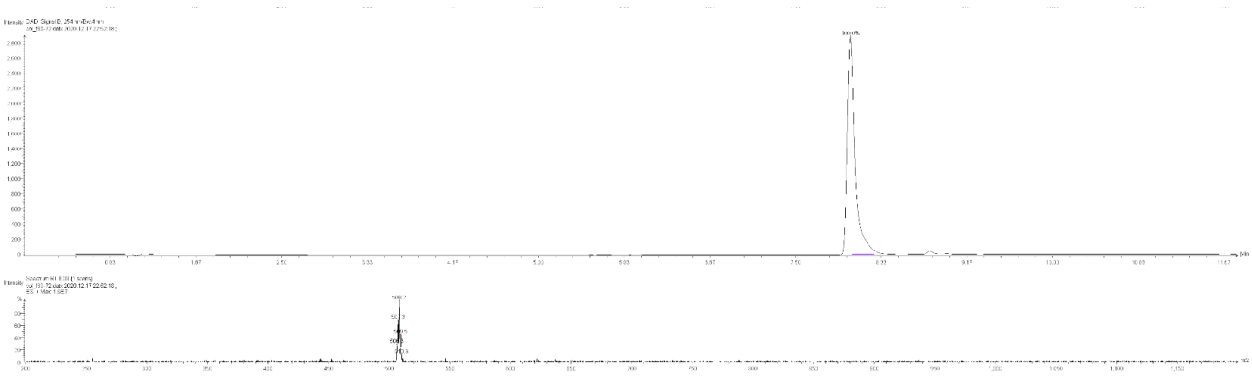

Low resolution ESI+ mass spectrum of 3 (3,3’-[(3-oxyphenyl)amino]bis-1-propanesulfonic acid phenyl ester):

Calculated for $[M+H]^+$: 506.1
Found: 506.3

Spectrum Aα.2.5 LC/MS spectrum of 3-aminophenol TBDMS ether, 6:

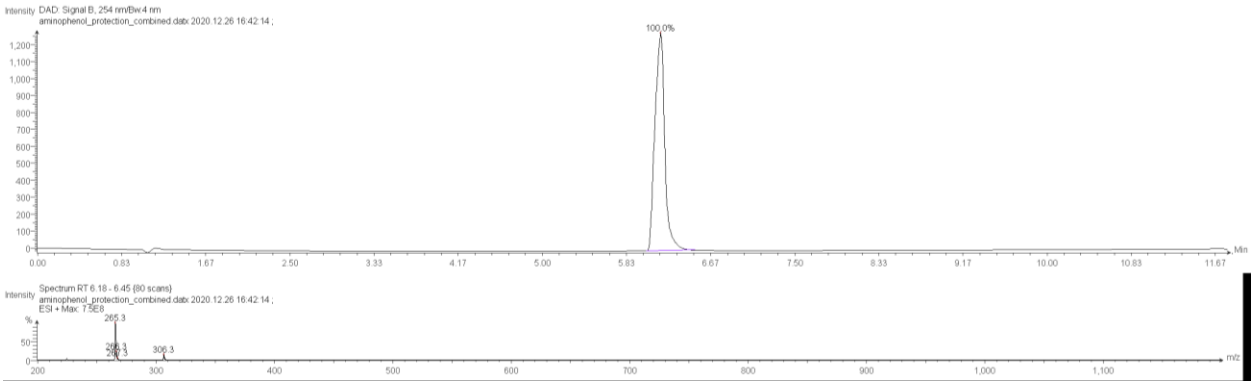

Low resolution ESI+ mass spectrum of 3-aminophenol TBDMS ether, 6:

Calculated for $[M+H+acetonitrile]^+$: 265.2
Found: 265.3

Calculated for $[M+H+2\ acetonitrile]^+$: 306.2

Found: 306.3

Spectrum Aα.2.6 1H spectrum of 3-aminophenol TBDMS ether, 6:

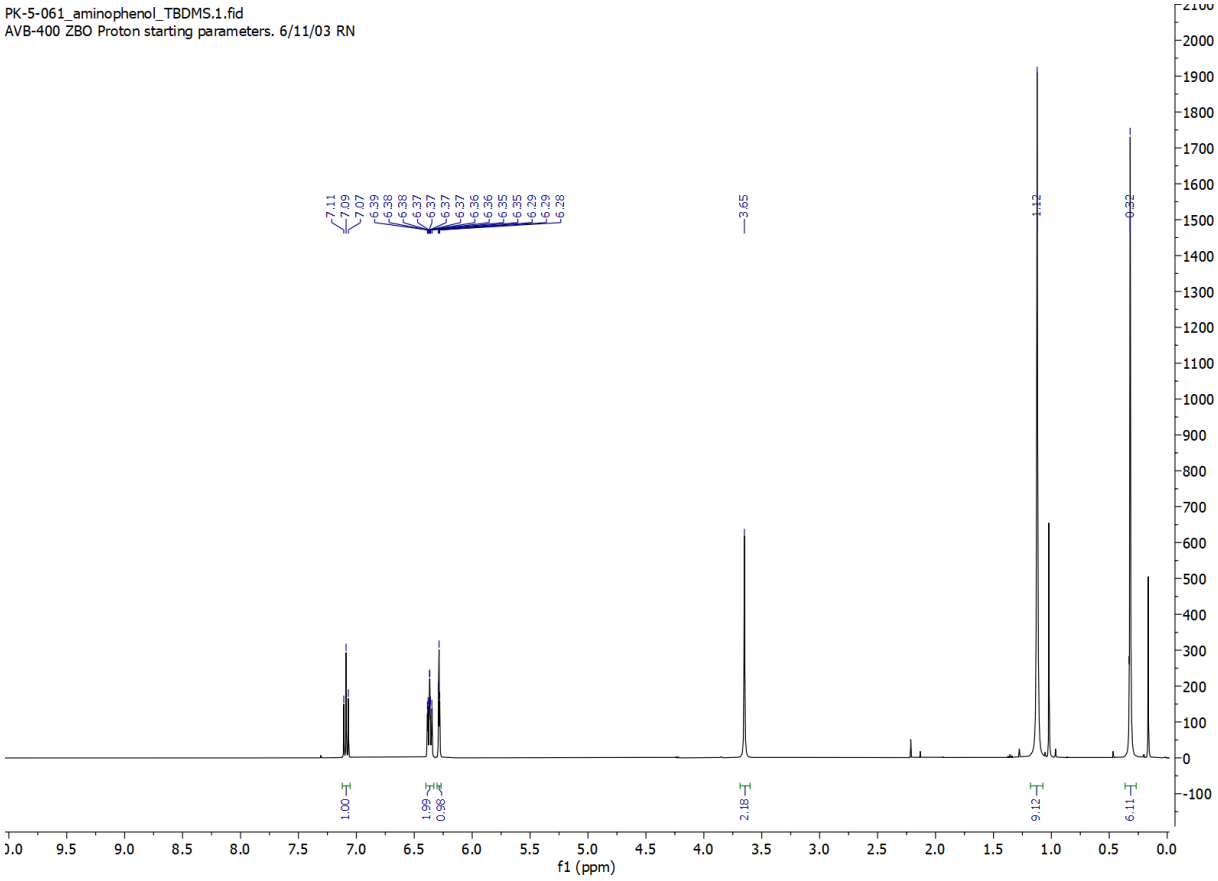

Spectrum Aα.2.7 LC/MS spectrum of crude 3,3'-[(3-oxyphenyl)amino]bis-1-propanesulfonic acid trifluoro tolyl ester, 7:

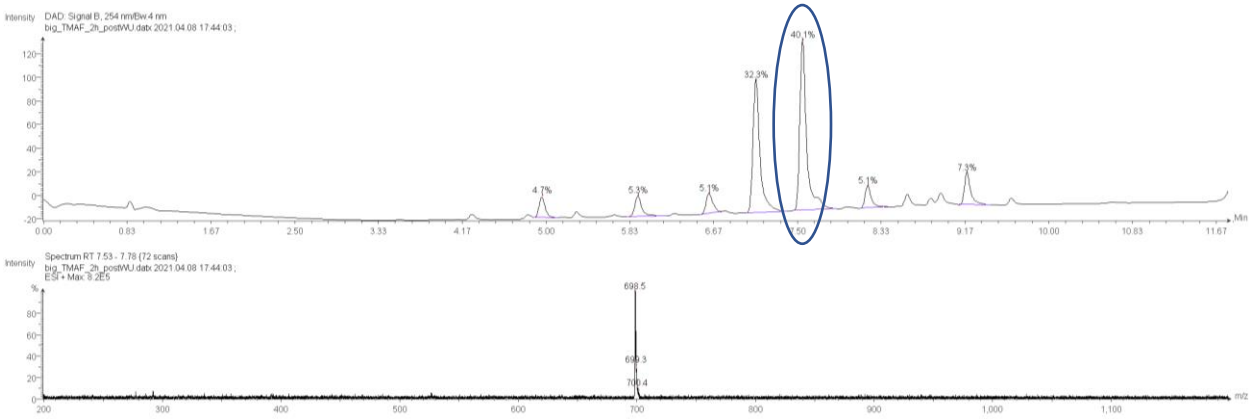

Low resolution ESI+ mass spectrum of (3,3'-[(3-oxyphenyl)amino]bis-1-propanesulfonic acid trifluoro tolyl ester), 7:

Calculated for $[M+H]^+$: 698.2
Found: 698.5

Note: this reaction has not yet been purified. The peak in the circle is the peak from which the mass spectrum is taken, representing the desired product

Aα.3 References

1. Beija, M.; Afonso, C.A.; Martinho, J.M. Synthesis and applications of Rhodamine derivatives as fluorescent probes. *Chem Soc Rev.* **2009**, *38* (8), 2410-2433
2. Scaduto, R.C. Jr; Grotyohann, L.W. Measurement of mitochondrial membrane potential using fluorescent rhodamine derivatives. *Biophys J.* **1999**, *76* (1 Pt 1), 469-477

3. Kirk, M.J.; Benlian, B.R.; Han, Y.; Gold, A.; Ravi, A.; Deal, P.E.; Molina, R.S.; Drobizhev, M.; Dickman, D.; Scott, K.; Miller, E.W. Voltage imaging in *Drosophila* using a hybrid chemical-genetic rhodamine voltage reporter. *Front. Neurosci.* **2021**, *15*, 1494-1503

4. Boyarskiy, V.P.; Belov, V.N.; Medda, R.; Hein, B.; Bossi, M.; Hell, S.W. Photostable, amino reactive and water-soluble fluorescent labels based on sulfonated rhodamine with a rigidized xanthene fragment. *Chemistry*. **2008**, *14* (6), 1784-1792
5. Lichtenfels, R.; Biddison, W.E.; Schulz, H.; Vogt, A.B.; Martin, R. CARE-LASS (calcein-release-assay), an improved fluorescence-based test system to measure cytotoxic T lymphocyte activity. *J Immunol Methods*. **1994**, *172* (2) 227-239
6. Massif, C.; Dautrey, S.; Haefele, A.; Ziessel, R.; Renard, P.Y.; Romieu, A. New insights into the water-solubilisation of fluorophores by post-synthetic "click" and Sonogashira reactions. *Org Biomol Chem*. **2012**, *10* (22) 4330-4336
7. Niu, S.; Ulrich, G.; Retailleau, P.; Harrowfield, J.; Ziessel, R. New insights into the solubilization of Bodipy dyes. *Tetrahedron Letters*. **2009**, *50* (27), 3840-3844

8. Kolmakov, K.; Wurm, C.A.; Hennig, R.; Rapp, E.; Jakobs, S.; Belov, V.N.; Hell, S.W. Red-emitting rhodamines with hydroxylated, sulfonated, and phosphorylated dye residues and their use in fluorescence nanoscopy. *Chemistry*. **2012**, *18* (41) 12986-12998
9. Thermo Fisher (2010): Molecular Probes Handbook, 35-54

10. Park, J.U.; Won, G.K.; Shin, G.R. Method for the preparation of rhodamine derivatives as fluorescent compounds. **2018**, *Patent # KR1921662*

11. Wang, S.S. Dyes and Methods of Marking Biological Material. **2014**, *Patent # US 8,710,244 B2*

12. Pauff, S.M.; Miller, S.C. A trifluoroacetic acid-labile sulfonate protecting group and its use in the synthesis of a near-IR fluorophore. *J Org Chem.* **2013**, *78* (2), 711-716
13. Rusha, L.; Miller, S.C. Design and application of esterase-labile sulfonate protecting groups. *Chem Commun (Camb).* **2011**, *47* (7), 2038-2040
14. Miller, S.C. Profiling sulfonate ester stability: identification of complementary protecting groups for sulfonates. *J Org Chem.* **2010**, *75* (13), 4632-4635
15. Lavis, L.D. Teaching Old Dyes New Tricks: Biological Probes Built from Fluoresceins and Rhodamines. *Annu Rev Biochem.* **2017**, *86*, 825-843

16. Kirk, M.J. et al. Manuscript in preparation

17. Kulkarni, R.U.; Yin, H;, Pourmandi, N.; James, F.; Adil, M.M.; Schaffer, D.V.; Wang, Y.; Miller, E.W. A Rationally Designed, General Strategy for Membrane Orientation of Photoinduced Electron Transfer-Based Voltage-Sensitive Dyes. *ACS Chem Biol.* **2017**, *12* (2); 407-413

Appendix β: Progress towards a new enzymatically uncaged VoltageFluor

With Thomas Masterson

Aβ.0 Introduction

A problem common to many fluorescent probes is their non-specific localization. VoltageFluors, a class of voltage-sensitive fluorescent dyes discussed extensively in this dissertation, suffer from this flaw as in their typical form they stain all cellular membranes to which they are exposed. This poses serious challenges if a researcher wishes to use a VoltageFluor to make optical measurements of membrane potential from a specific cell type in a complex tissue or a specific subcellular organelle.

One approach to circumvent this limitation is to genetically encode a protein such as HaloTag[1], SNAP tag[2], or SpyCatcher[3], that will covalently bind to specific chemical ligands and attach the corresponding ligand to the VoltageFluor that is to be targeted. This will result in the desired VoltageFluor being covalently tethered to the membrane of interest. Although this strategy has proven effective in applications in cell culture, brain slice, and whole drosophilia brains, the total amount of VoltageFluor that can be targeted to the membrane of interest is limited by the number of proteins that the cell has trafficked to that membrane. Additionally, long linkers between the VoltageFluor and the targeting motif are required to give the dye enough tether to reach from the active site of the targeting protein to the membrane, where the dye must insert in order to sense membrane potential. These linkers can increase the retention of VoltageFluor in off-target membranes (see Appendix α) and limit the internalization of the dye, making it difficult to target intracellular membranes (see Chapter 3).

An alternative to covalent enzymatic targeting is enzymatic uncaging, in which a VoltageFluor is “capped” with a group that quenches its fluorescence but can be selectively cleaved by a non-endogenous enzyme. The enzyme can then be expressed to the membrane of interest, allowing for catalytic cleavage of the quenching group and a turn-on in VoltageFluor fluorescence. This strategy has been realized using cyclopropylmethyl esters as a caging group which are selectively cleaved by Porcine Liver Esterase (PLE)[4]. Although this hybrid chemical-genetic uncaging approach does not tether the VoltageFluor to the membrane of interest it does have some advantages over covalent tethering approaches. Because uncaging is catalytic, the amount of VoltageFluor that is uncaged is not limited by the total amount of enzyme expressed. VoltageFluor that stains membranes other than the membrane of interest will remain quenched, so fluorescence from off-target locations will be minimal. Furthermore, the caging groups are often small relative to the overall size of the molecule and can be hydrophobic enough to pass through membranes, enabling enzymatic targeting of subcellular locations.

Existing enzymatic uncaging strategies for VoltageFluors use fluorescein-based VoltageFluors as a scaffold. This work seeks to extend enzymatic uncaging to rhodamine-based scaffolds. This will enable orthogonal uncaging strategies for use in multiple organelles and/or cell types and facilitate subcellular targeting as the existing fluorescein scaffolds do not internalize.

Aβ.1 Design of caged rhodamine-based VoltageFluors

In keeping with standard naming conventions reported in literature for this class of compounds[5,6,7], the caged rhodamines developed for optical measurements of membrane potential on targeted membrane are named **E**nzymatically **U**ncaged **R**eporters for **Op**tical **A**ssessment: **Rho**damine **V**oltage **R**eporters (**EUROpA RhoVRs**). EUROpA RhoVRs are based on a rhodamine 110 scaffold which has free rather than alkylated anilines on the chromophore portion of the molecule. This is crucial as these anilines are the site of caging. The rest of the molecule follows the standard design pattern of previously reported RhoVRs with a molecular wire terminating in an aniline group for voltage sensing and a sarcosine group for anchoring in the membrane. The sarcosine carboxylate can be capped with a labile ester for intracellular targeting[6].

Although many strategies could be used to cage the RhoVR anilines, two stand out as promising initial targets. The first is to cage the anline with a peptide motif that is selectively cleaved by a peptidase[8,9,10,11]. This approach is promising because the sequence of the peptide can be altered flexibly to enable different orthogonal uncaging systems to be developed using peptidases specific for different sequences. The second is to form a diazo bond with a caging group and use a non-endogenous azoreductase to cleave this bond, a strategy that has been demonstrated in literature for subcellular targeting[12]. This appendix primarily focuses on synthetic approaches to the azoreductase strategy.

The retrosynthesis of the diazo-capped EUROpA RhoVR first disconnects the diazo bond with the quencher to work backwards to the uncapped RhoVR **4** (**Scheme Aβ.1.1a**). This molecule can be disconnected through a peptide coupling, aniline deprotection, and Heck reaction to the doubly protected brominated Rhodamine 110 **3** (**Scheme Aβ.1.1b**).

Scheme Aβ.1.1 Retrosynthesis of diazo EUROpA RhoVRs

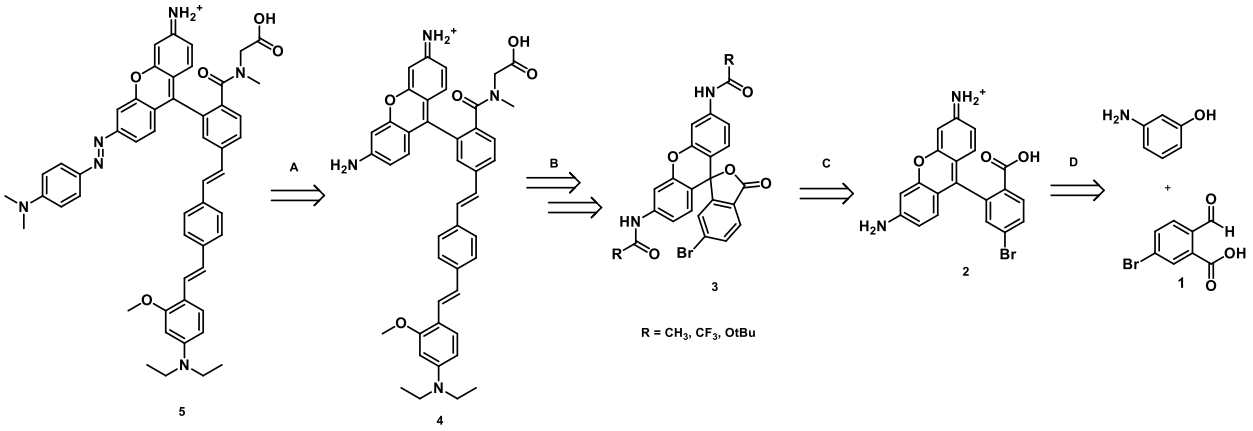

The diprotected compound **3** can be achieved through double amide formation of the brominated dye head **2** (**Scheme Aβ.1.1c**) which can be synthesized through condensation of commercially available 3-aminophenol and the previously reported brominated aldehyde **1**.

Aβ.2 Optimizing condensation for brominated fluorophore

Many procedures exist for the synthesis of rhodamines via the condensation of aminophenols with carbonyl species and thus the first step in the synthesis of EUROpA RhoVRs was to optimize the initial condensation to synthesize the brominated fluorophore **2**. **Table Aβ.2.1** summarizes the conditions used for the synthesis of brominated fluorophore **2** as well as their outcomes.

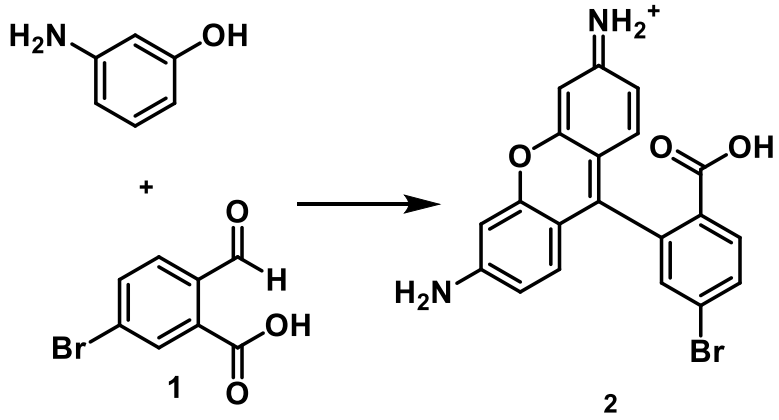

Scheme Aβ.2.1 Reaction scheme for Table Aβ.2.1

Table Aβ.2.1 Synthetic conditions for condensation to form compound 2

Trial	Acid?	Solvent	Temperature	Duration	Yield
1A[1]	Yes	Propionic, PTSA	90° C	18 h	2%
1B	Yes	Propionic, PTSA	110° C	60 h	0.5%

1C	Yes	Propionic, PTSA	110° C	18 h	0 %
2A[13,*]	Yes	Fuming Sulfuric Acid	180° C	18 h	Test
2B	Yes	Fuming Sulfuric Acid, PTSA	180° C	18 h	Reaction Success, isolation failure
2D	Yes	Fuming Sulfuric Acid	180° C	18 h	32.4%
3	No	K10, neat	140° C	5 h	~30% by LCMS
4A[14]	No	TFE : Water, ~4:1	Reflux, ~80° C	48 h	30.7%

4B	No	TFE : Water, ~4:1	Reflux, ~80º C	65 h	49.1%
4C	No	TFE, Water, NaOH	Reflux, ~80º C	18 h, add base, 18 h	25% by LCMS

*Multiple regioisomers were produced as 4-bromo phthalic anhydride was used in lieu of aldehyde **1**

The highest yielding reaction conditions proved to be refluxing aldehyde **1** with an excess of 3-aminophenol in a 4:1 mixture of 2,2,2 trifluoroethanol (TFE) and water for 65 hours, yielding 49% of the theoretical yield of dye head **2**.

Aβ.3 Protection of rhodamine anilines

In order to increase the hydrophobicity of the synthetic intermediates for easier purification as well as eliminate potential catalyst poisoning by the anilines during the planned Heck reaction, attempts were made to protect the aniline groups of compound **2** via amide formation to produce compound **3**. The reaction conditions attempted are summarized in **Table Aβ.3.1**.

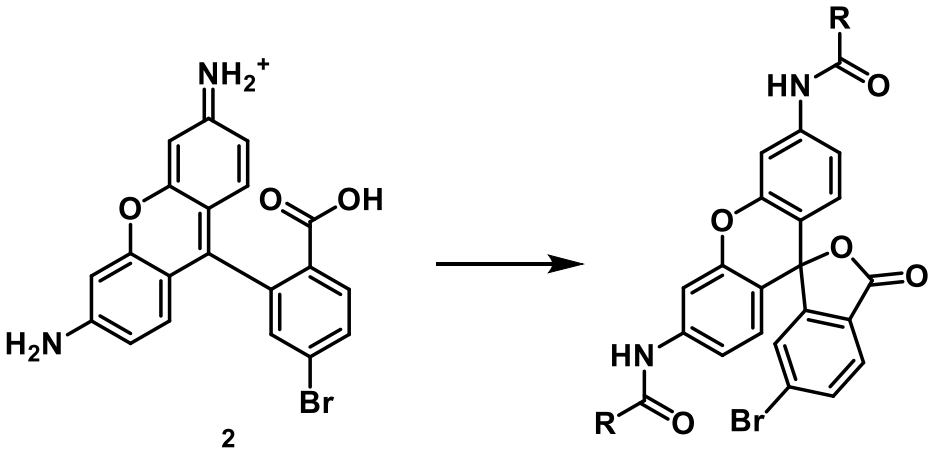

Scheme Aβ.3.1 Reaction scheme for Table Aβ.3.1

Table Aβ.3.1 Synthetic conditions for protection of compound 2

Trial	Reagents	Solvent	Temp	Duration	Yield
	$(\mathrm{Boc})_2\mathrm{O}, 2.2\ \mathrm{eq}$	Water	33°, 80° C	18 h	0% LC/MS
	$(\mathrm{Boc})_2\mathrm{O}, 6\ \mathrm{eq}$	Water, MeOH	75° C	24 h	0% LC/MS
	$(\mathrm{Boc})_2\mathrm{O}, \mathrm{DMAP}, \mathrm{DIPEA}$	MeOH	60° C	18 h	0% LC/MS
	$(\mathrm{Boc})_2\mathrm{O}, \mathrm{DMAP}, \mathrm{DIPEA}$	DMF	60° C	18 h	Inconclusive
	$(\mathrm{Boc})_2\mathrm{O}, \mathrm{DMAP}, \mathrm{DIPEA}$	THF	60° C	18 h	0% LC/MS
	$\mathrm{Acetyl\ Chloride}$	DMF, Pyridine	RT	65 h	16%
	$\mathrm{TFA}, \mathrm{COMU}, \mathrm{DIPEA}$	DMF	RT	5 h	Inconclusive

Overall, none of the protection conditions were particularly successful at efficiently protecting the anilines of compound **2**, so the other planned synthetic reactions were conducted without protection of the aniline groups.

Aβ.4 Synthetic progress towards EUROpA RhoVR

Although the complete synthesis of a diazo-capped EUROpA RhoVR has not been achieved as of this work, the following presents a summary of the reactions that have been achieved in hopes that future work can build on this to finish the synthesis of a EUROpA RhoVR.

Scheme Aβ.4.1 Synthetic progress towards EUROpA RhoVR

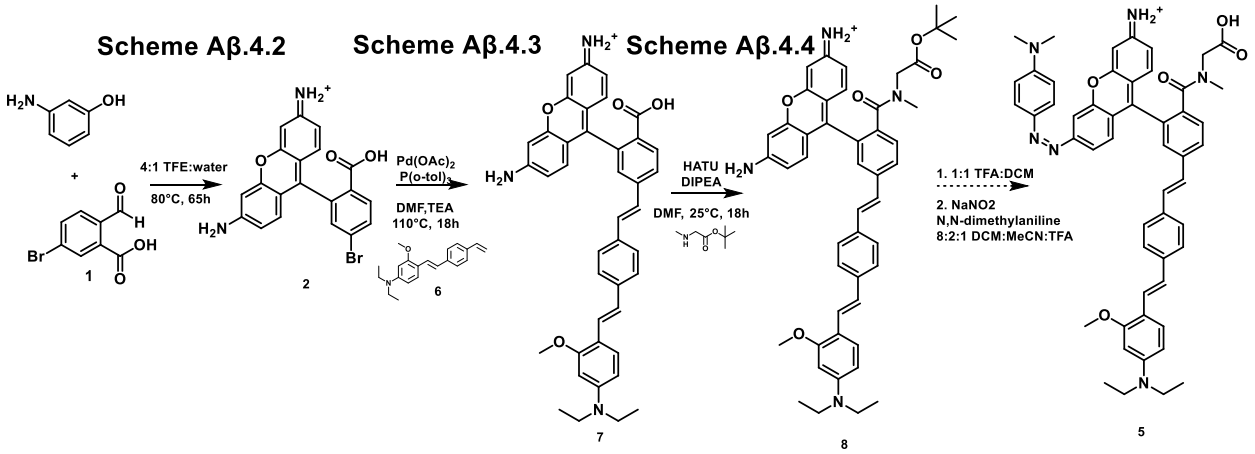

Scheme Aβ.4.2

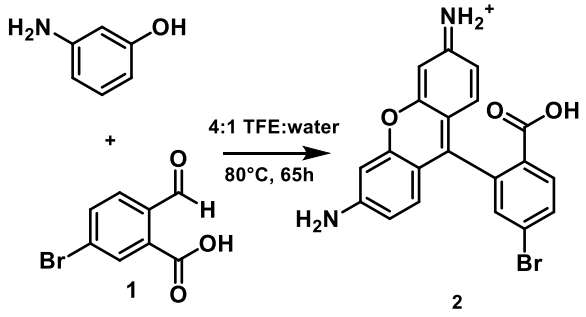

Synthesis of meta-bromo Rhodamine 110, 2

Compound **1** (1000 mg, 4.37 mmol) and 3-aminophenol (1429 mg, 13.1 mmol) were added to a round bottom flask along with TFE (67.8 mL) and water (16.9 mL). A needle with airflow was placed beneath the surface of the solvent, and the reaction was stirred at 80^{o} C for 65 hours. The reaction was then allowed to cool, and solvent was removed *in vacuo*. The solids were purified by column chromatography (15-75% MeOH/EtOAc) on silica gel, and solvent evaporated to yield the purple crystals of **2** (880 mg, 49%).

Scheme Aβ.4.3

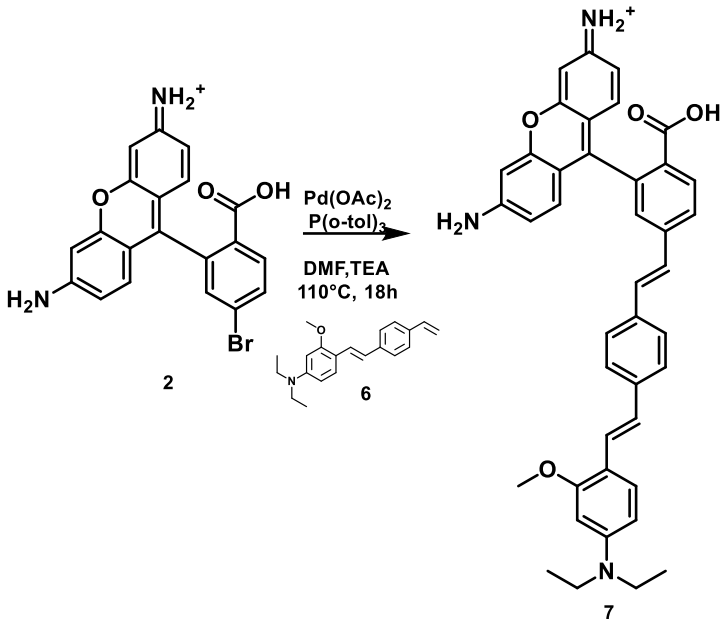

Synthesis of carboxy Rhodamine 110 RhoVR, 7

Compound **2** (88 mg, 0.22 mmol) was added to a Schlenk flask along with catalytic amounts of Bis[tris(2-methylphenyl)phosphine]-palladium (10 mg, 0.02 mmol, 0.1 eq), degassed, and placed under nitrogen. A roughly 1 : 1 solution of DMF and triethylamine was added to a dry 2-neck flask under nitrogen and frozen using liquid nitrogen. The flask was left under vacuum for a few minutes, and nitrogen atmosphere was then replaced. The mixture was allowed to thaw, and the procedure was repeated three times. This solvent mixture (~5 mL) was cannulated into the Schlenk flask, and the solution was stirred at 110^{o} C for 18 hours. The reaction was monitored by LCMS, which suggested conversion of starting material to product **7**. This would be confirmed later following a peptide coupling and successful detection of compound **8**. Solvent was removed *in vacuo* and the resulting solids purified by column chromatography (0-25% MeOH : EtOAc) resulting in a mixture of impurities, dyehead **2,** and product **7**. LC/MS suggested this to have a roughly 1:3 ratio of product (**7**) to dyehead (**2**) using the absorbance trace at 500 nm. Mass of **7** was estimated as 30 mg, with around ~20% yield.

Scheme Aβ.4.4

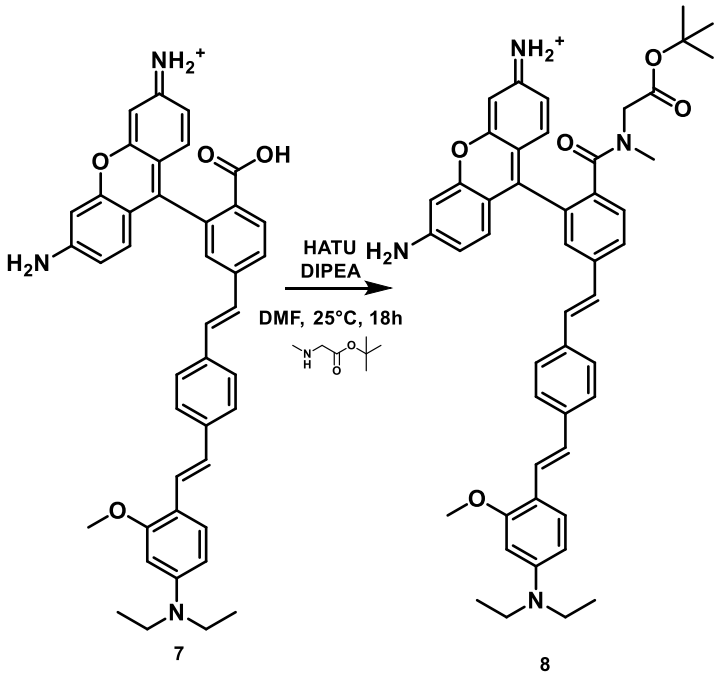

7 8

Synthesis of t-Bu RhoVR green, 8

An impure portion of **7** (50 mg, 0.08 mmol, roughly 1 : 3 ratio of compounds **7** / **2**), equaling roughly 15 mg of pure **7**, N-methyl sarcosine t-Bu ester hydrochloride (36 mg, 0.12 mmol), and HATU (33 mg, 0.09 mmol) were placed in a reaction tube. DMF (3.1 mL) and DIPEA (0.02 mL) were added, and the solution was stirred at room temperature for 3 hours. The solvent was removed *in vacuo* and the resulting solids were tested by LCMS, which indicated that **8** was the minor product (as a result of use of impure substrate). The reaction was purified by preparative thin layer chromatography (8% MeOH/DCM plus 1% triethylamine); however, because of insufficient product mass, **8** was unable to be isolated.

Scheme Aβ.4.5

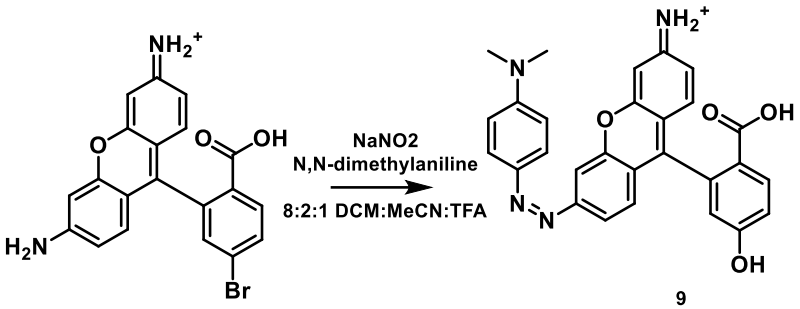

9

Compound **2** (117 mg, 0.29 mmol) was added to a round bottom flask along with water (5 mL), MeCN (5 mL), and TFA (0.1 mL). The solution was stirred, and temperature lowered to 0º C before $NaNO_2$ (37 mg, 0.56 mmol) was added. After an additional 15 minutes, N,N-dimethylaniline was added slowly and stirred for 1 hour at 0º C. An extraction with DCM and water was run, and resulting solids tested by LCMS to reveal significant production of **9**, which was the major product. Yield for the reaction was not determined but can be estimated using LCMS absorbance traces to be above 80%.

Spectra

Spectrum Aβ.4.1 LC/MS spectrum of meta-bromo Rhodamine 110, 2:

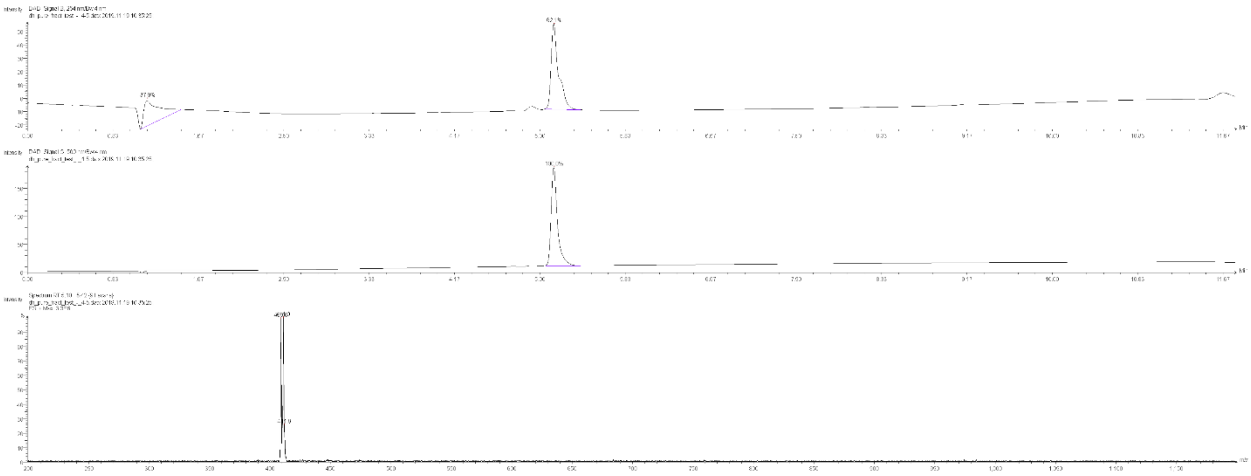

Low resolution ESI+ mass spectrum of meta-bromo Rhodamine 110, 2:

Calculated for $[M-^{79}Br+H]^+$: 409.0
Found: 409.0

Calculated for $[M-^{81}Br+H]^+$: 411.0
Found: 411.0

Spectrum Aβ.4.2 LC/MS of carboxy Rhodamine 110 RhoVR, 7:

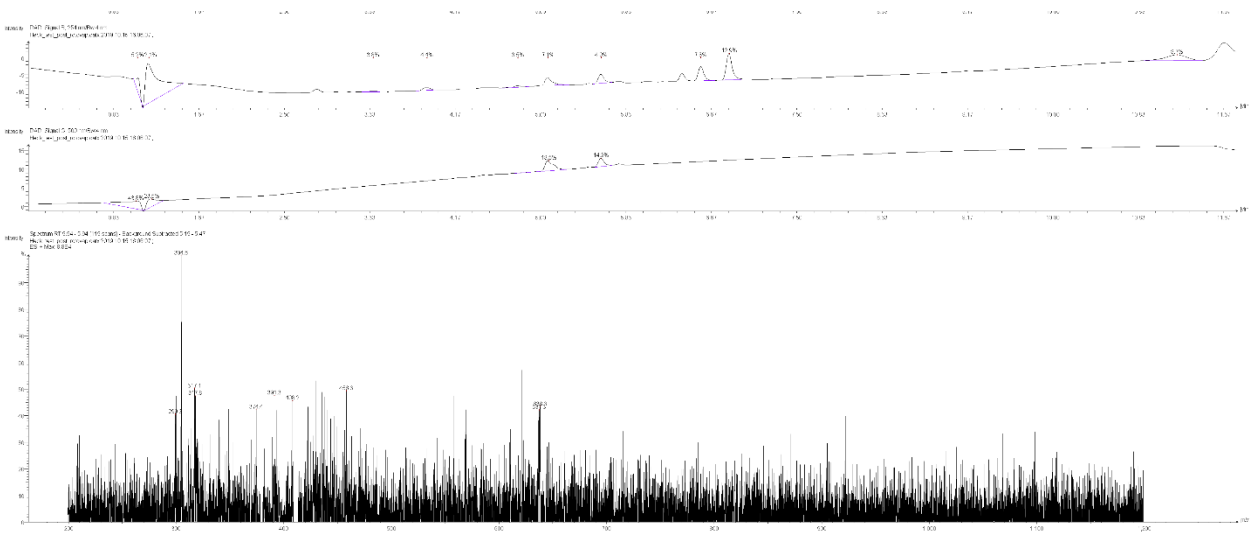

Low resolution ESI+ mass spectrum of carboxy Rhodamine 110 RhoVR, 7:

Calculated for $[M+H]^+$: 636.3
Found: 637.3

Calculated for $[M+2H]^+$: 318.7
Found: 317.8

Note: the pure material from this reaction was not isolated

Spectrum Aβ.4.3 LC/MS of t-Bu RhoVR green, 8:

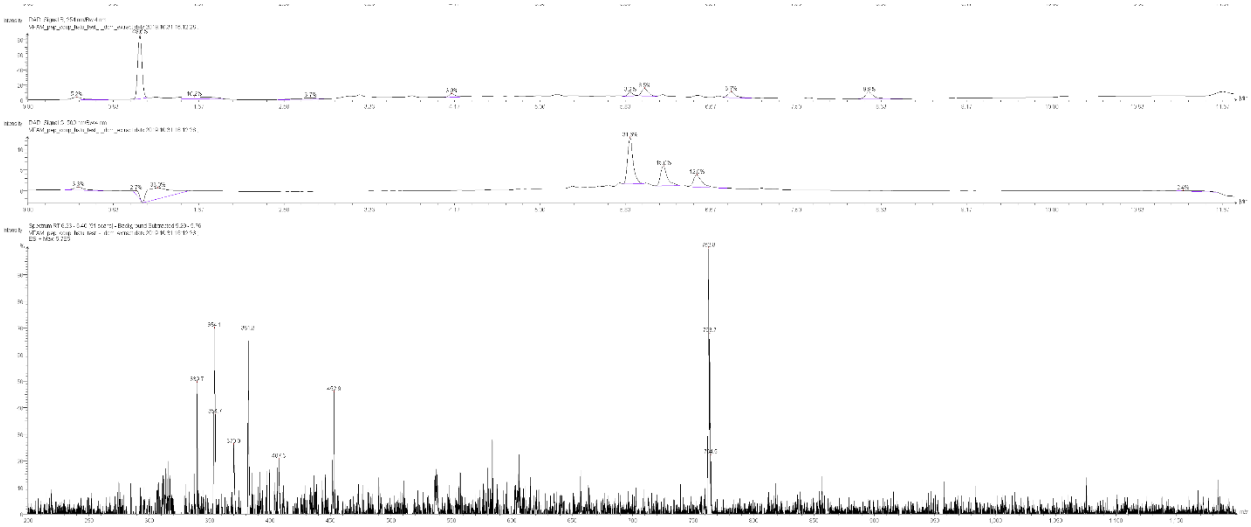

Low resolution ESI+ mass spectrum of meta-bromo Rhodamine 110, 2:

Calculated for $[M+H]^+$: 763.4
Found: 762.8

Spectrum Aβ.4.4 LC/MS of 4-N,N-dimethylaniline diazo meta-Br-Rho110, 9:

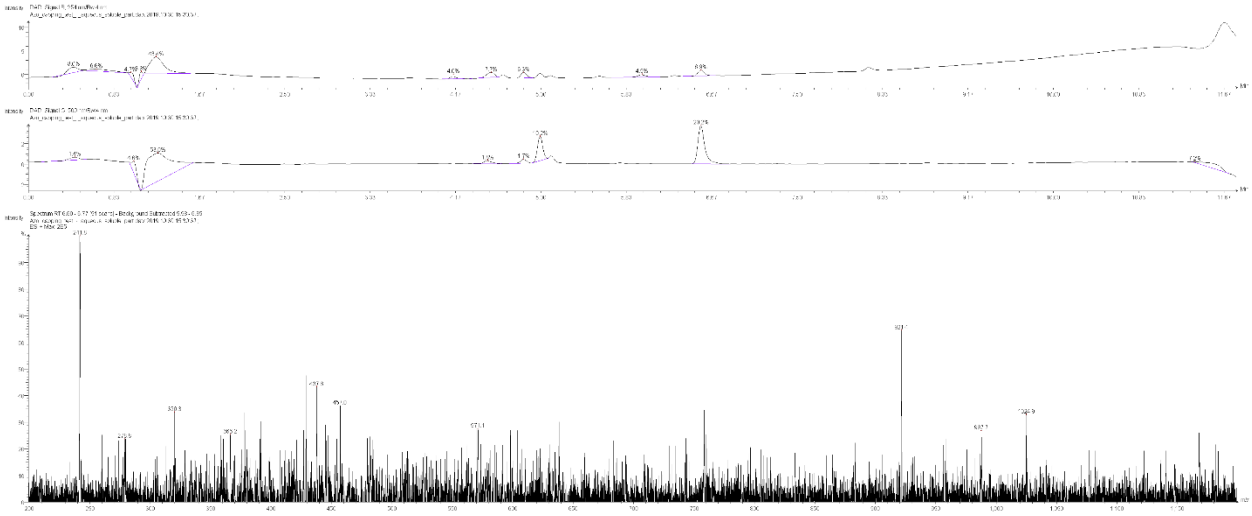

Low resolution ESI+ mass spectrum of 4-N,N-dimethylaniline diazo meta-Br-Rho110, 9:

Calculated for $[M+H]^+$: 240.1
Found: 241.8

Aβ.5 Conclusions and outlook

The work demonstrated herein shows that the synthesis of diazo capped EUROpA RhoVRs is achievable although further purification of synthetic intermediates is required. The results obtained in **Scheme Aβ.4.5** indicate that the Heck reaction should be undertaken before diazo coupling.

The future steps of this project would entail:

1. Finish the synthesis of diazo capped EUROpA RhoVR
2. Keep some of the uncapped intermediate
3. Characterize the fluorescence properties (QY, etc.) of the uncapped intermediate in vitro
4. Characterize the fluorescence properties of the capped EUROpA RhoVR in vitro to measure the overall fluorescence turn-on
5. Uncaged the capped EUROpA RhoVR in vitro using an Azoreductase and measure the overall fluorescence turn-on and kinetics
6. Perform patch-clamp electrophysiology on the uncapped intermediate to measure its voltage sensitivity
7. Clone an azoreductase conjugate targeted to a membrane of interest and evaluate fluorescence turn-on in cells

Alternately, by capping the dye with a peptide sequence in the final step rather than a diazo quenching group, the dye can be uncaged by a peptidase selective for that sequence and a similar set of future steps would result in a novel uncaging system for VoltageFluors.

Aβ.6 References

1. Deal, P.E.; Liu, P.; Al-Abdullatif, S.H.; Muller, V.R.; Shamardani, K.; Adesnik, H.; Miller E.W. Covalently Tethered Rhodamine Voltage Reporters for High Speed Functional Imaging in Brain Tissue. *J Am Chem Soc.* **2020**, *142* (1), 614-622
2. Benlian, B.R. et al. Manuscript in preparation
3. Grenier, V.; Daws, B.R.; Liu, P.; Miller, E.W. Spying on Neuronal Membrane Potential with Genetically Targetable Voltage Indicators. *J Am Chem Soc.* **2019**, *141* (3), 1349-1358
4. Liu, P.; Grenier, V.; Hong, W.; Muller, V.R.; Miller E.W. Fluorogenic Targeting of Voltage-Sensitive Dyes to Neurons. *J Am Chem Soc.* **2017**, *139* (48), 17334-17340
5. Deal, P.E.; Kulkarni, R.U.; Al-Abdullatif, S.H.; Miller E.W. Isomerically Pure Tetramethylrhodamine Voltage Reporters. *J Am Chem Soc.* **2016** *138* (29) 9085-9088

6. Klier, P.E.Z.; Martin, J.G.; Miller, E.W. Imaging Reversible Mitochondrial Membrane Potential Dynamics with a Masked Rhodamine Voltage Reporter. *J Am Chem Soc.* **2021**, *143* (11), 4095-4099
7. Klier, P.E.Z. et al. Manuscript in preparation

8. Grimm, J.B.; Heckman, L.M.; Lavis, L.D. The chemistry of small-molecule fluorogenic probes*. Prog Mol Biol Transl Sci*. **2013**, *113*, 1-34
9. Grant, S.K.; Sklar, J.G.; Cummings, R.T. Development of novel assays for proteolytic enzymes using rhodamine-based fluorogenic substrates. *J Biomol Screen*. **2002**, *7* (6), 531-540
10. Kuriki, Y.; Kamiya, M.; Kubo, H.; Komatsu, T.; Ueno, T.; Tachibana, R.; Hayashi, K.; Hanaoka, K.; Yamashita, S.; Ishizawa, T.; Kokudo, N.; Urano, Y. Establishment of Molecular Design Strategy To Obtain Activatable Fluorescent Probes for Carboxypeptidases. *J Am Chem Soc*. **2018**, *140* (5), 1767-1773
11. Hug, H.; Los, M.; Hirt, W.; Debatin, K.M. Rhodamine 110-linked amino acids and peptides as substrates to measure caspase activity upon apoptosis induction in intact cells. *Biochemistry*. **1999**, *38* (42), 13906-13911.
12. Shin, N.; Hanaoka, K.; Piao, W.; Miyakawa, T.; Fujisawa, T.; Takeuchi, S.; Takahashi, S.; Komatsu, T.; Ueno, T.; Terai, T.; Tahara, T.; Tanokura, M.; Nagano, T.; Urano, Y. Development of an Azoreductase-based Reporter System with Synthetic Fluorogenic Substrates. *ACS Chem Biol.* **2017**, *12* (2), 558-563
13. Brem, S.; Schlücker, S. Surface-Enhanced Raman Spectroscopy and Density Functional Theory Calculations of a Rationally Designed Rhodamine with Thiol Groups at the Xanthene Ring. *The Journal of Physical Chemistry* C **2017**, *121* (28), 15310–15317
14. Dwight, S. J.; Levin, S. Scalable Regioselective Synthesis of Rhodamine Dyes. *Organic Letters* **2016**, *18* (20), 5316–5319